# Hierarchical self-assembly, interpolymer complex formation and phase states in biopolymeric soft matter systems

Thesis submitted to the Jawaharlal Nehru University
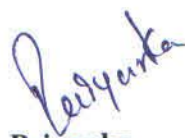for the award of the degree of

## Doctor of Philosophy

## PRIYANKA



**SCHOOL OF PHYSICAL SCIENCES**

**JAWAHARLAL NEHRU UNIVERSITY**

**NEW DELHI-110067**

**2019**

## DECLARATION

I hereby declare that the work carried out in this thesis entitled "Hierarchical self-assembly, interpolymer complex formation and phase states in biopolymeric soft matter systems" is entirely original. It was carried out by me in School of Physical Sciences, Jawaharlal Nehru University, New Delhi, India under the supervision of Prof. H. B. Bohidar. I further declare that it was not formed the basis for the award of any diploma, membership or similar title of any university or institution.

**Priyanka**

School of Physical Sciences

Jawaharlal Nehru University

New Delhi-110067, India

**Prof. H. B. Bohidar**

Thesis Supervisor

School of Physical Science

Jawaharlal Nehru University

New Delhi-110067, India

**Prof. S. Patnaik**

Dean

School of Physical Science

Jawaharlal Nehru University

New Delhi-110067, India

DEDICATED
TO
MY PARENTS
FOR THEIR ENDLESS LOVE
&
ENCOURAGEMENT...

# ACKLOWLEDGEMENT

# HIERARCHICAL SELF-ASSEMBLY, INTERPOLYMER COMPLEX FORMATION AND PHASE STATES IN BIOPOLYMERIC SOFT MATTER SYSTEMS





**SCHOOL OF PHYSICAL SCIENCES**

**JAWAHARLAL NEHRU UNIVERSITY**

# TABLE OF CONTENTS

# 2 Chapter 2: Materials and Methods

# 3 Interaction of zein nanoparticles with different polyelectrolytes

## [PART-A]

## 3.1 Aanomalous Dispersion and Hydrophobic Aggregation of Zein Nanoparticles

## [PART-B]

## 3.2 Mixing ratio dependent complex coacervation versus bicontinuous gelation of pectin and in-situ zein nanoparticles

CHAPTER 1

INTRODUCTION

**OVERVIEW**

This chapter discusses the soft matter science, and proteins and polyelectrolytes in particular which gives the motivation, and help formulates the importance of present thesis with some basic concepts.
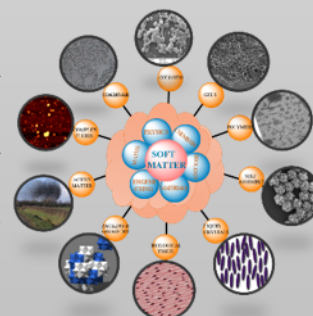
## 1.1 SOFT MATTER: INTRODUCTION AND MOTIVATION OF THESIS

Fundamental understanding of phase stability of soft materials is necessary due to their flexible and interesting behaviour. Soft matter intermediate between solids and liquids which make these materials very interesting. Soft condensed matter is the study of soft system, often composed of at least two components [de Gennes, 1991]. Examples are foams, emulsion, colloids, gels, polymer etc. Soft matter consists of organic molecules weakly interacted through secondary forces counter balanced by thermal fluctuations with their structure and properties strongly effected by external stimuli and interface effects. On the basis of kinetic energy, soft and hard matters can be distinguished. Soft condense matter system are those where we have statistical number of particles and the relevant energy are of the order of thermal energy, $k_BT$, where $k_B$ is Boltzmann constant and T is absolute temperature. The elastic modulus of soft matter is sixth order of magnitude smaller than that of atomic and molecular solids. Therefore, they are extremely fragile against mechanical stress and are easily destroyed [Kleman et al, 2007]. Due to soft and flexible behaviour these have interesting properties. Thermal

fluctuation, bending energy and local curvature plays important role in determining properties of soft matter [Mezzenga et al, 2005]. Self-assembly and phase separation are the most attractive phenomenon shown by these materials. Self-assembly of soft materials can be exploited to create an array of mesoscopic structures for various applications. Weak ordering caused by noncovalent interactions are involved in such structures thus, thermal energy plays an important role during the phase transition of different degrees of order. Energy dissipated in self-assembly of soft materials occurs due to fluctuation of particle density or molecular orientation that result in Brownian motion which is comparable to thermal energy. As we know weak noncovalent bonds are broken and re-formed by thermal energy, hence thermal energy has dramatic impact on soft matter [Hamley, 2003]. As there is weak interaction involved between molecules, transition between different states can be driven by change in physical conditions like pH and temperature. There is a variety of phase transition between different structures of soft matter. The phase stability of soft matter can be explained by using a phase diagram as is shown in Fig. 1.1. This phase diagram shows multiple phase depending upon the selective physical parameters like ionic strength, temperature, pH, concentration, mixing ratio, kind of interactions etc. It produces either bicontinous phase or droplet pattern in soft material [Tanaka et al, 2005; Butler, 2002].
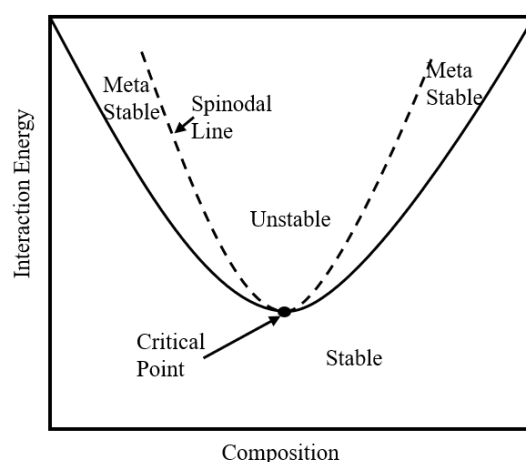


**Fig. 1.1:** Phase diagram for soft materials.

In a typical discrete system, the pattern gets coarsened in order to lower the interface energy and domain shape is determined by the force acting on the interface. Phase separation can also produce a network pattern in soft matter. Recent progress in soft matter research arises many questions like nature of interactions involved, process of phase separation, gel formation, phase stability formation etc. and the pursuit for new experimental tools that allows for characterization of their soft solids and complex fluids over a large region of time and length scales is available these days. In this thesis polyampholyte proteins (colloids) have been taken as the model system to study the phase stability and interparticle interactions through various means, and in some systems including binary solvent and introduction of polyelectrolytes may result in various polymeric phases. The significance of science and technology in soft matter field is summarized in Fig. 1.2.
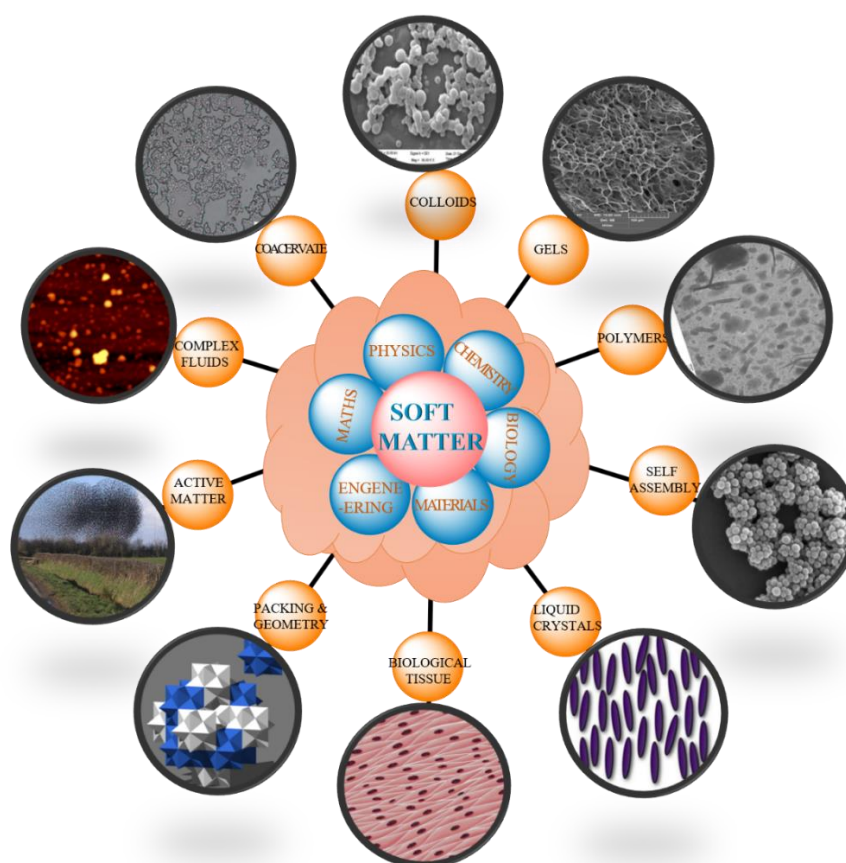
**Fig. 1.2:** Significance of soft matter in various field of science and technology.

## 1.2 OBJECTIVES OF THE THESIS

My thesis broadly has three folds:

(i)     Preparation and characterization of protein nanoparticles and their stability as function of different physical parameters.

(ii)    Phase behaviour study of protein-polyelectrolyte complexes.

(iii)   Application of polymeric phase (gel) for drug delivery.

## 1.3 BIOPOLYMERS

Biopolymers are polymeric biomolecules produced by living organisms, biopolymers form larger structure from covalently bonded monomeric units. On the basis of monomeric unit and structure of biopolymers, these are classified as:

(i) Nucleotide monomer and long polymer, Polynucleotide e.g. DNA and RNA

(ii) Amino acids and short polymer, polypeptide e.g. gelatin, insulin, ferritin, albumin, etc.

(iii) Linearly bonded polymeric carbohydrate structures, Polysaccharides, e.g. agar, pectin, chitosan, etc.

There is one major difference between biopolymer and synthetic polymers, biopolymers do have well defined secondary structure. Primary structure is the sequence in which these monomeric units are arranged. Proteins do have secondary and tertiary structures which are responsible of their biological function, and there are derived from their primary structure, while in case of synthetic polymer, they have much simple, more random and stochastic structure which leads to mass distribution. All biopolymers of a type say one specific protein are all alike, they all contain similar amino acid sequences and number of residues, plus all have same mass this phenomenon is called polydispersed, in contrast, polydispersity is commonly encountered in synthetic polymers. As a result, biopolymers have monodispersity index of nearly one. The convention for a polypeptide is to list its constituent's amino acids

residues as they occur from the amino to the carboxylic acid terminus where the amino acids residues are always joined by peptide bonds. Protein though used colloquially to refer to any polypeptide to larger or fully functional forms and can consists of several polypeptide chains as well as single chains. Protein can also be modified to include non-peptide components such as saccharides chains [Hamley, 2003].

## 1.3.1 POLYMERIC PHASE STATES

### 1.3.1.1 Sol

Polymer dissolve in solution termed as polymeric solution. They can be classified on the basis of concentration:

(i)      Dilute

(ii)     Overlap

(iii)    Semi-dilute

de Gernnes et al proposed overlap concentration (c*) to distinguish dilute from semi-dilute solution. Overlap concentration for three-dimensional system is given by $c^* \sim N R_g^{-3}$, where $R_g$ and N are the radius of gyration and degree of polymerisation respectively [Aral et al, 2003]. While Cotton et al defines c* as $c^* \sim \frac{3M}{4\pi N_A R_g^3}$, where $N_A$ and M are the Avogadro number and polymer molecular weight respectively [Storm et al, 2005]. Various solution phases are schematically shown in Fig. 1. 3.
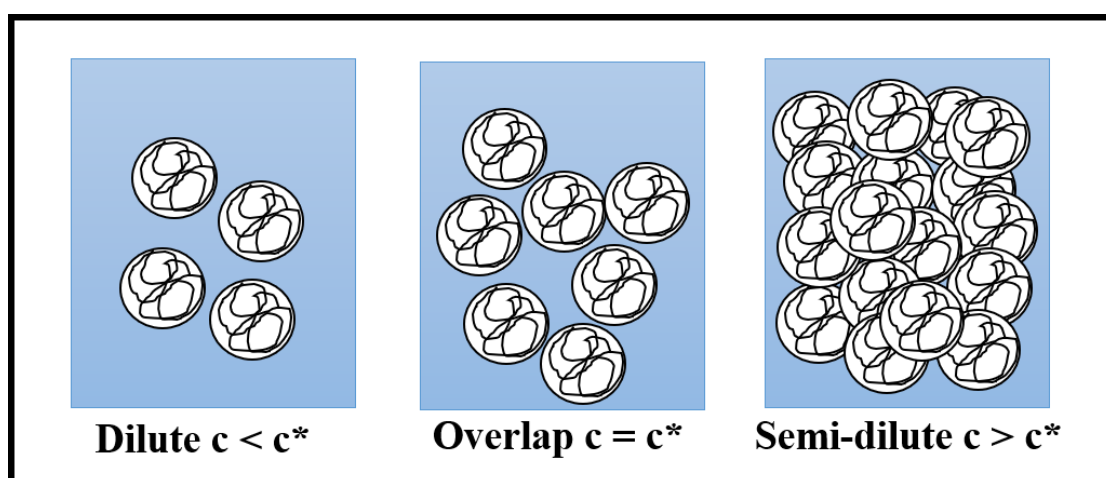


**Fig. 1.3:** Various polymeric solution phases.

For the condition c>>c* i.e. highly concentrated polymeric solution may lead to viscoelastic (viscous as well as elastic behaviour) materials which also behave as melt phase.

**1.3.1.2 GEL**

These are defined to be space filling or percolating network of particles which are formed when sufficient amount of particle concentration results in net attract. The interaction of colloids either through long- or short-range attraction at low solid volume fraction lead to the formation of gels. In the gels, the colloidal particles are arrested by the nearest neighbours and result in the formation of a structured percolated network. The time of self-assembly where the system stops flowing is termed as "gelation point". At the gelation point the system percolates and fraction of bonds were formed which are in agreement with the Flory theory. After a certain time, the system is found to get trapped into a metastable state of minimum free energy and becomes non-ergodic. The leading mechanism for gelation of gels is the attraction. The formation of colloidal gels results from the formation of fractal clusters, which form space filling networks and the connectivity present in the system determine the viscoelastic properties of these gels [Trappe et al, 2004; Zaccarelli et al, 2007]. In the case of dilution test, the arrested state remains solid due to the attractive bonds between the particles which cannot be altered through solvent and led to conclude that the dominant interaction in gels is attractive.

Gels are polymeric cross-linked network swollen in a solvent medium, the solvent prevents the polymer network from collapsing into a compact mass and the network remains in the liquid. Polymeric gel can be classified in two categories with respect to their network's nature:

(i)     Chemical gels: Network formed by covalent bond.

(ii)    Physical gel: Undergoes reversible gelation by externally-induced topological changes of chains.
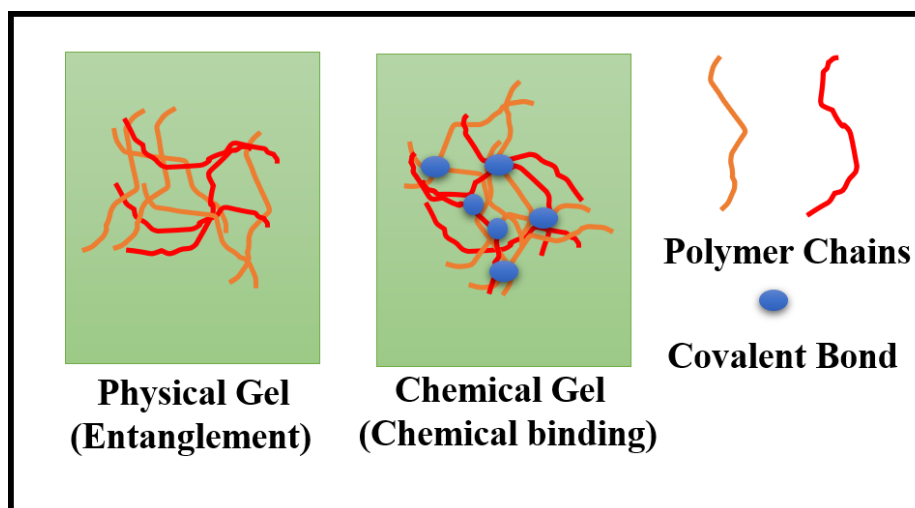
**Fig. 1.4:** Schematic of physical and chemical gel.

**1.3.1.3 COACERVATE**

The phenomenon of coacervation embodies associative interaction between a wide variety of polyelectrolyte-polyelectrolyte, polyelectrolyte-polyampholyte, and polyampholyte-polyampholyte pairs [Bungenberg de Jong, 1949; Doublier et al, 2000]. Coacervation in polymers/biopolymers is a unique type of associative interaction that provokes a phase separation in the homogenous solution leading to the formation of two distinct liquid phases, one polymer-rich, and another mostly containing the supernatant [Gouin, 2004]. This process is driven by various interactions occurring between the polymers via hydrophobic, electrostatic, polarization-induced attractive and hydrogen bonding forces [Boral et al, 2010]. Complex coacervation in some cases is followed by two-step nucleation, and then kinetic growth causing the origin of soluble or insoluble complexes [Klassen, 2010]. Kinetics of phase separation in the coacervation process has been discussed by many theoretical models such as Overbeek [Overbeek et al, 1957], Veis [Veis, 1961], Nakajima [Nakajima et al, 1972], Tainaka [Tainaka, 1980], and Gupta and Bohidar [Gupta et al, 2010]. This process is influenced by many parameters: polymer mixing ratio, pH, temperature, ionic strength, nature of the solvent etc. the effect of interactions, ionic concentration and temperature which is summarized in Fig. 1.5.
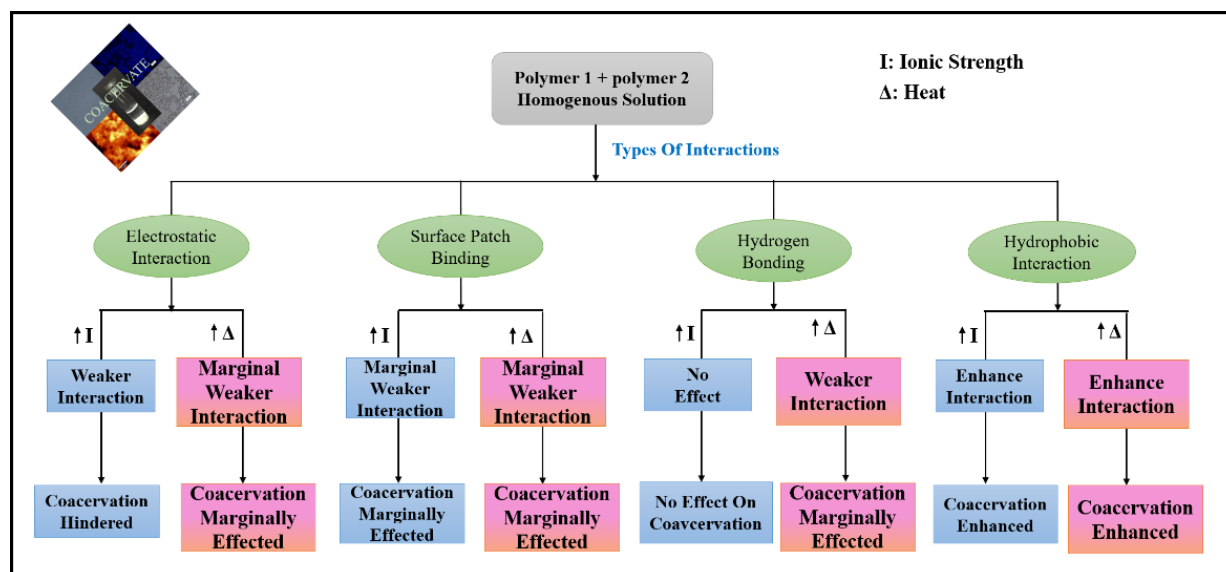
**Fig. 1.5:** Factors influence process of complex coacervation [Pathak et al, 2017].

Coacervates of protein-protein, DNA-protein and protein-polysaccharide systems get much consideration due to their intrinsic potential in generating newer biomaterials, and these often act as model systems to explain self-assembly in soft matter [Kayitmazer et al, 2010; Tiwari et al, 2010]. Protein and polysaccharide coacervates have found many applications such as carrier materials for encapsulation of drugs and essential oils [Meng et al, 2018; Reineccius 2018].

Complex coacervation also can be explained on the basis of the change of the pH of the complex solution as shown in Fig.1.6. There is a structured complex formation of intermolecular complexes in coacervates:

(i)     $pH_c$:  pH at which associated interaction take place which results in a soluble-complexes, Critical pH ($pH_c$).

(ii)    $pH_\phi$: pH at which soluble complex coalesce to results a liquid-liquid phase separation leads to coacervation, coacervation transition pH ($pH_\phi$).

(iii)    $pH_{prep}$: pH at which large insoluble complexes driven the solution to liquid-solid phase separation.
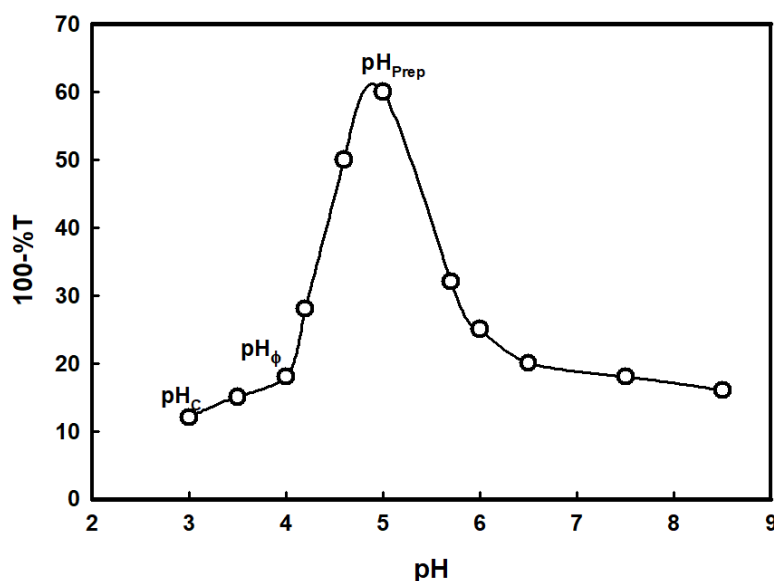
**Fig. 1.6:** Typical titration profile showing various transitions of biopolymers complex (BSA-βlg complex) at their critical pH value. [Pathak et al, 2017]

## 1.3.2 POLYELECTROLYTES AND POLYAMPHOLYTES

Polyelectrolytes are water soluble polymers carrying ionizable groups (positive or negative) along the polymer chain [Dobrynin et al 2004, Barrat et al 1995]. These ionizable groups dissociate water, making the polymer charged. Charged molecular chain plays an important role in defining structure, stability and the interaction of various molecular assemblies. Many biological polyelectrolytes such as Pectin, Agar and DNA (both polyanionic) and chitosan (polycationic) are few examples of polyelectrolytes, in this thesis we focus on polyanionic molecules. They have various applications, generally related to adjusting flow and stability properties of aqueous solutions, coacervates, and gels. Some polymers containing both positive and negative charged repeating groups are called polyampholytes. Most of the proteins belong to this category. Zein and Elastin, are examples of polyampholytes which were used in this thesis. In the aqueous solution, the net charge on polyampholytes depends upon the pH of the solution. The number of positive and negative charge sites on the polymer equal at a specific pH that is the net charge becomes zero is called isoelectric point, symbolized by pI. Fig. 1.7

represents schematic of polyelectrolyte and polyampholyte structures. Proteins and polyampholytes interact with each other to form complexes, which can have widely varied stoichiometries, architectures and phase states.



POLYCATION POLYANION POLYAMPHOLYTE
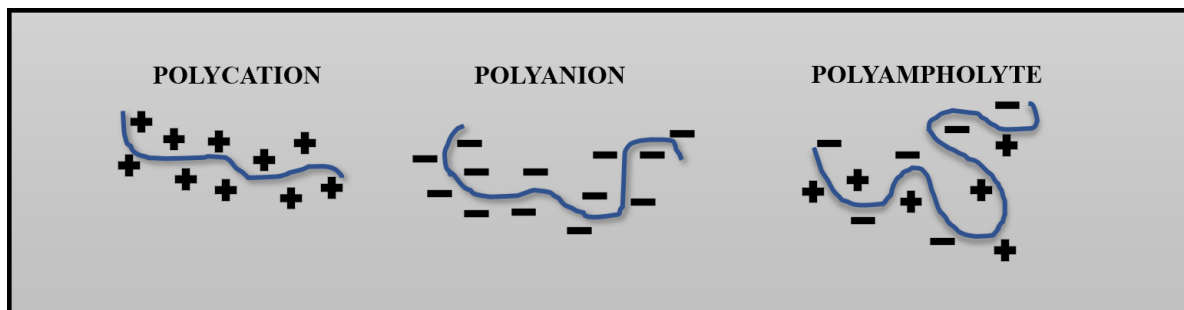
**Fig. 1.7:** Schematic picture of polycation, polyanion and polyampholytes.

Depending on the degree of dissociation of polyelectrolytes in aqueous medium, these are classified as weak and strong. Ionizable groups on strong polyelectrolytes are fully dissociated when dissolved in water, whereas those on weak electrolyte are dissociated only upon neutralization. Polyelectrolytes have been the focus of research for several decades where theoretical and experimental investigations have made the major progress made in this area. Polyelectrolytes and polyampholytes used in this thesis were:

**1.3.2.1 PECTIN**

Pectin a polysaccharide which is mostly heterogeneous in terms of both chemical structure and molecular weight with its chemical composition varying with its source and conditions of extraction. The typical molecular structure is shown in Fig. 1.8. Pectin is a hydrophilic polysaccharide (anionic polyelectrolyte) extracted from plant cell walls and consists of esterified D-galacturonic acid residues in an (1-4) chain, and is associated with $pK_a=$ 3.5. Pectin and its derivatives have found many applications in food industry and in pharmaceutical formulations. Pectin are classified into high (HM) and low methoxy (LM) carbohydrates based on the extent to which their methyl groups get esterified, where the reference degree of methylation is either above or below 50%, respectively. Pectin has bad thermal stability and low mechanical properties but it can be improved by bind with other

biopolymers. Therefore, pectin is used in paradigm matrices to encapsulate specific materials and for delivery in a controlled manner. In literature, pectin has been used as colon-specific drug delivery for a long time. Low methoxy pectin is expected to increase the efficiency of encapsulation [Glinsky et al, 2009; Kohn 1987; Munarin et al, 2012].
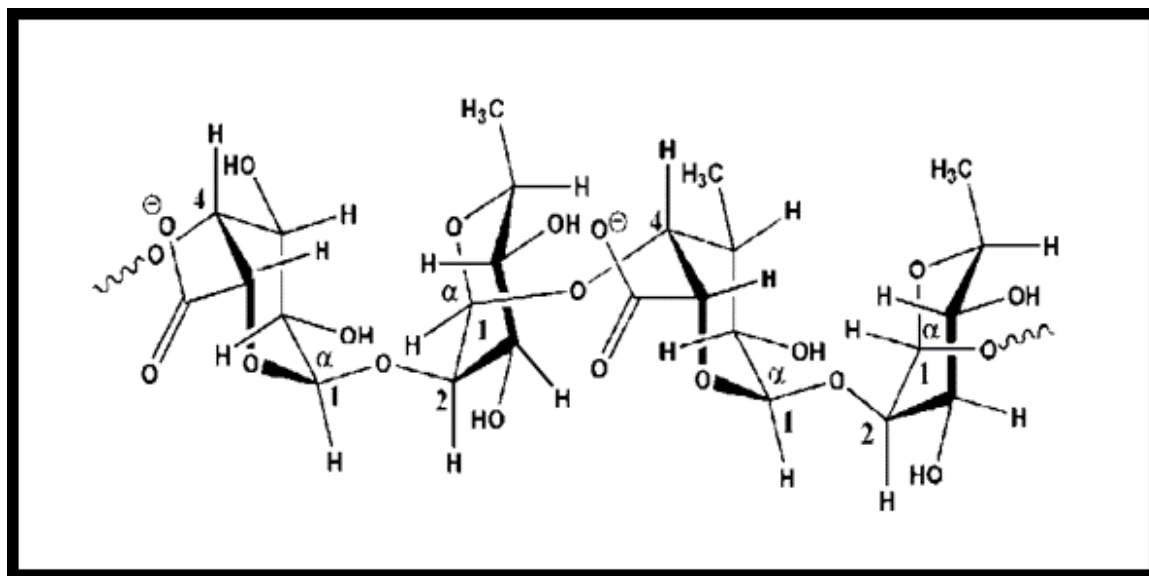


**Fig. 1.8:** Molecular structure of pectin.

### 1.3.2.2 AGAR

Agar (MW=300 kDa, polysaccharide, which occurs as structural carbohydrate in the cell walls of agarophytes algae) is a hydrophilic colloid with agarose and agaropectin constituting the two major fractions, and this yellowish odourless powder material is easily soluble in hot water. The gel-forming biopolymer is extracted from marine green development of Rhodophyceae, for example, Gelidium sp. (linear polymer comprising a repeating unit of the disaccharide, 3-connected $\beta$-d-galactose and 4 associated 3,6-anhydro-α-1-galactose developments) [Freile-Pelegrín et al, 1997; Falshaw et al, 1998]. Due to its extraordinary gelation properties and exceptional saturation limit, agar has been among the principal biomaterials for many food processing and biomedical applications [Francavilla et al, 2013; Garrido et al, 2016]. Further, in comparison to proteins, these materials are additionally alluring

for tissue regeneration application because of their absorptive, good surface-to-volume fraction and, most important similarity in outline with basic extracellular network [Mohajer et al, 2017; Bao et al, 2010].
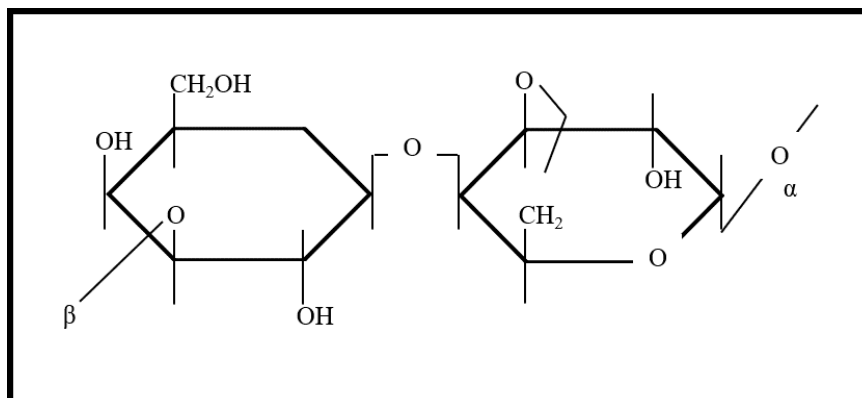


**Fig. 1.9:** Molecular structure of agar.

**1.3.2.3 DNA**

dsDNA is formed by a condensation reaction between phosphate and hydroxyl group., where H-bonding occurs between distinctive bases of DNA. A and T bases have two hydrogen bonds, and G and C have three hydrogen bonds which is shown in Fig.1.10. dsDNA is composed of tenfold helix. DNA is one of the polyelectrolytes having the highest linear charge density, its association with other biomolecules is of considerable interest [Smith, 1997]. Binding of DNA to proteins and oppositely charged spherical macroions has revealed interesting results [Mrevlishvili, 2005]. Kaya et al. compared the relative binding between ssDNA and dsDNA complexes with collagen and concluded that the structure of fibrils formed in the complexes showed remarkable dependence on the DNA form [Kaya et al, 2005]. Nguyen and Shklovskii [Nguyen et al, 2001] examined the phase diagram of DNA and positively charged colloidal macroions in dispersion and observed the following:

(i) At low colloid concentration, the DNA–colloid complexes were negatively charged with DNA wrapping the colloids

(ii)  At high colloid concentration, the complexes showed charge reversal and revealed positive charge. We also studied the phase diagram of DNA and polycations (PCs) and observed that the complex charge state was decided by the DNA: PC charge ratio.
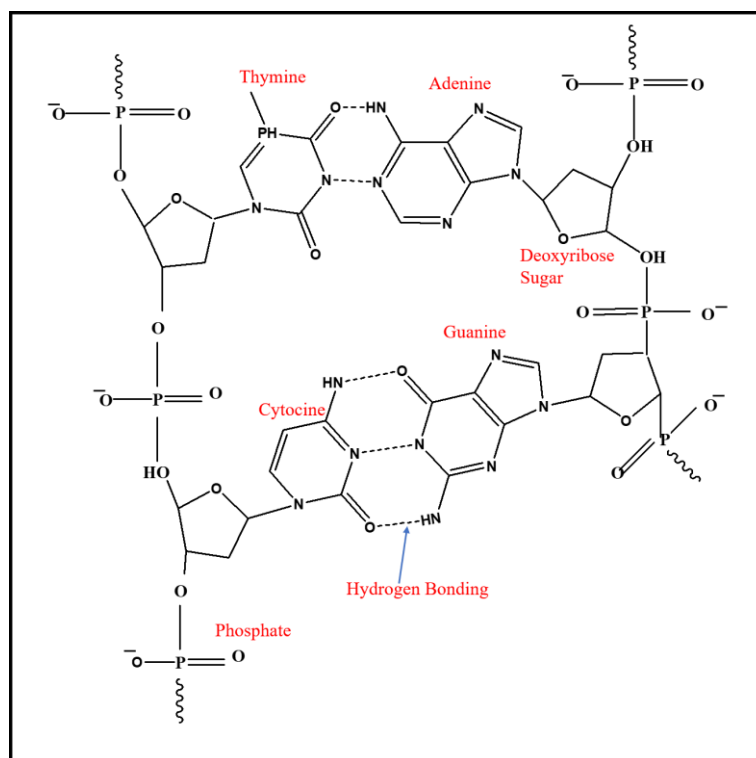


**Fig. 1.10:** Molecular structure of DNA.

**1.3.2.4 ZEIN**

The hydrophobic biopolymer zein (having special water solubility properties) is a major capacity protein inferred from corn and it is solely found within the endosperm that has been considered as a model bio-macromolecule and it may account for 35-60% of total protein content. The presence of more than 50% of amino acids like leucine, proline, alanine, and phenylalanine in the primary structure of this protein makes this biopolymer water insoluble. Zein is biodegradable, biocompatible, bears high thermal resistance, and is hydrophobic in nature. It has revealed low water uptake value and zein films exhibit good mechanical property, so it is used in food and pharmaceutical products as edible coatings. Zein is classified on the

basis of its molecular weight as follows: (i) α-zein (MW = 21-25 kDa), (ii) $\beta$-zein (MW = 17-18 kDa), (iii) γ-zein (MW = 27 kDa) and, (iv) δ-zein (MW = 10 kDa) [Anderson et al, 2011]. Tertiary structure of zein encloses tandem helical units which is linearly stacked by glutamine-rich turns and is stabilized by hydrogen bonds as shown in Fig. 1.11 (a) [Matsushima et al, 1997]. Besides, zein compromises of both hydrophilic and hydrophobic amino acid residues and this protein can self-assemble to form nanoparticles of size in the range of 80-200 nm through pH control, liquid-liquid dispersion, solution enhanced dispersion, and phase separation processes, and it has found applications in controlled release of hydrophobic drugs [Lai et al, 2011]. Coacervates of zein has been utilized to encapsulate and release Gitoxin in a controlled manner. Because of its biological origin, desirable physiochemical properties, self-assembly ability, hydrophobicity and its typical size of 100-500 nm nanoparticles, zein has been magnificently used a carrier for controlled encapsulation and release of fat-soluble compounds. Plant-based protein nanoparticle explored for prodrug by participating with stimuli-responsive components could respond to many factors such as temperature, pH, enzyme, light and bio-reducible environment. Being of its good biodegradability, they undergo hydrolytic or enzymatic degradation in the biological environment into nontoxic by-product, that makes zein a direct and rapid carrier of drugs better than synthetic polymers and animal proteins [Luo et al, 2014].
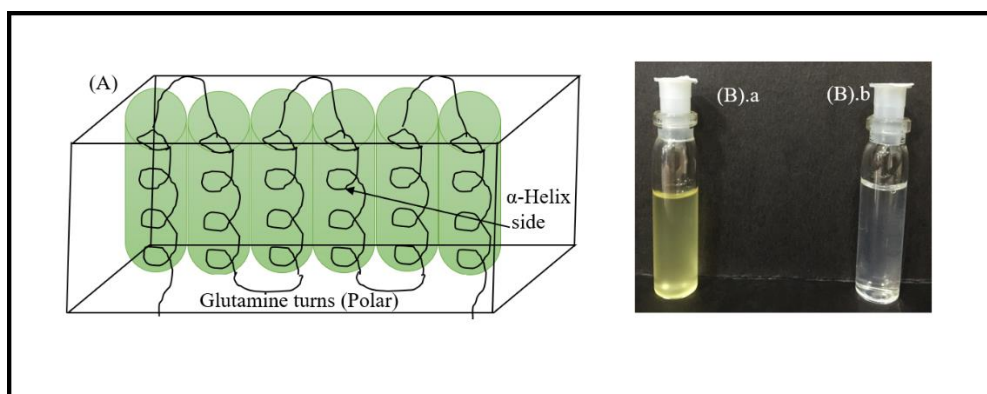


**Fig. 1.11:** (A) Tandem helical structure of zein. (B.a) Zein in ethanol: water (80:20 % v/v) binary solvent (B.b) Zein nanoparticle by liquid liquid dispersion method.

## 1.3.2.5 ELASTIN

Elastin is an important structural protein which plays significant role in providing elasticity to wide variety of tissues in living system. Elastin, a hydrophobic fibrous protein, is one of the smart biopolymers found in the human body with unusual properties. It imparts elastic properties of stretch and reversible recoil to vertebrate tissues including major blood vessels, lungs and skin. Tropoelastin forms the monomeric precursor for elastin which is soluble, non-glycosylated and highly hydrophobic. Tropoelastin undergoes self-aggregation, and phase separation in a process called coacervation to form elastin. This process is driven by the temperature and sodium chloride concentration that provides the optimal condition for the subsequent cross-linking [Sell et al, 2010; Zou et al, 2011]. Elastin has outstanding mechanical properties due to regular alternance of hydrophobic regions rich in glycine, alanine, valine and leucine and of hydrophilic domains rich in alanine and lysine residues. The hydrophobic sequences give elasticity while the hydrophilic ones confer to the protein resistance to rupture and fatigue. Elastin and its derived peptides have found to be promising biomaterials with wide range of applications in therapeutics, because it is a major component of extra cellular fluid. Since it is chemically inert, it shows unusual viscoelastic properties. Needless to mention, it has found potential use in bioengineering and biomedical applications. Elastin is an important extracellular matrix protein that is responsible for extensibility and elastic recoil properties of connecting tissues, arterial walls, skin lung parenchyma, and blood vessels [Herrero-Vanrell, 2005]. Elastin coacervation has drawn much attention in the past and it has been mostly recognized that the insoluble fraction of elastin, tropoelastin, is mostly responsible for causing coacervation. A coherent picture of elastin coacervation that has emerged so far concludes the following [Yeo et al, 2011]: (i) coacervation occurs primarily due to hydrophobic cooperative association of tropoelastin, (ii) the number, sequence, and contextual arrangement of hydrophobic domains are important, (ii) coacervation is an entropic driven endothermic

process, and (iii) it is closely associated with increased β-structures in hydrophobic and α-helices in cross-linking domains.

## 1.4 FORCES AND INTERACTION

Various kind of forces are responsible for stabilizing of the polymer and colloids in suspension.

### 1.4.1 ELECTROSTATIC INTERACTION

The most widely recognized interactions which plays an important role in providing stability to the dispersion and occur between all types of molecules in the dispersed and continuous phase is the electrostatics or coulombic interaction. These interactions depend on the nature or characteristics of the surface as well as the medium for example pH, ionic strength, temperature etc. As the colloidal particles carry electrical charge, thus their stability and the properties are affected by these interactions. Some of the particles are known to have unevenly distributed surface charge so this heterogeneity of charge results in alteration in the electrostatic interactions at molecular level. In the case of only van der Waals forces the dispersed particles may precipitate and aggregate, but it doesn't happen in most cases due to the presence of long-range repulsive forces. An ionizable particle or a macromolecule in solvent which itself contains mobile ions remains or are in equilibrium due to the balance between electrostatic and Brownian forces. The surface of the particle dispersed in medium brought two charging mechanism either by adsorption of ions from the solution and by dissociation or ionization of surface group. Electrical double layer is formed by these surrounded charges but these charges carried by double layer prevail for certain distance from particle centre and gradually decay with increasing distance. Electrical double layer of two liked charged particles overlap as they approach each other, and this results in strong repulsion. These electrostatic repulsions fall off as an exponential function of distance and the range is of order of double layer thickness. Due to the balance between electrostatic and Brownian force, the charged colloids in the solvent

remain in equilibrium. The two regions which exist are the one Stern layer where ions are immobile and are present in immediate proximity to the particles, and the other region in between shear plane and Stern plane where ions are mobile and are farther away from particles.
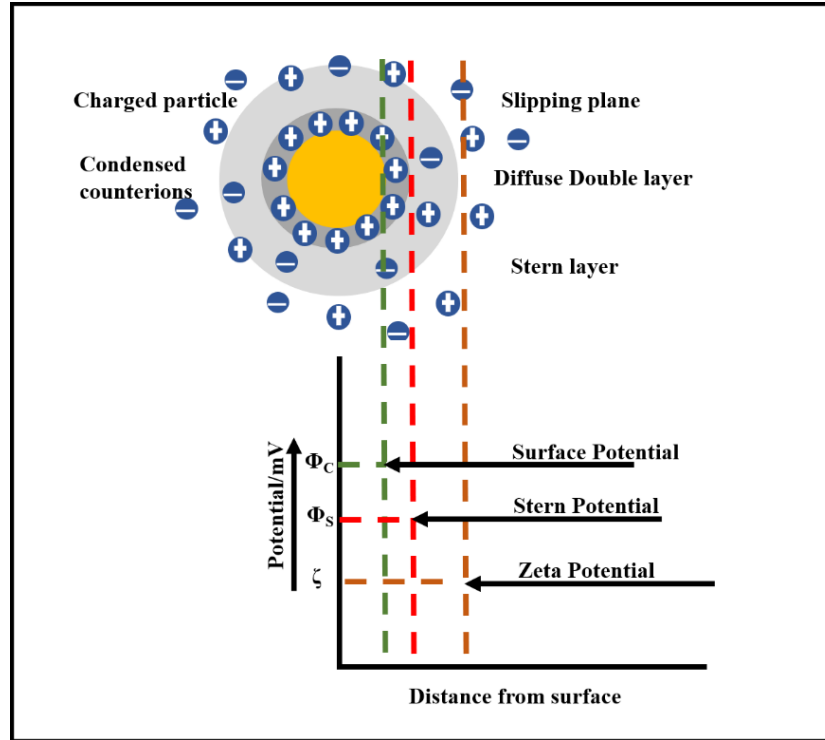


**Fig. 1.12:** Illustration of double layer for different potentials.

The two regions are shown in Fig. 1.12 with the variation in potential for positively charged particle as a function of distance. The Stern layer thickness defined by Bjerrum length $l_B$ defined as,

$$l_B = \frac{q^2}{4\pi\varepsilon k_B T} \tag{1.1}$$

The Coulombic interaction can screen in the electrolyte medium according to Debye Huckel theory with Debye screening length given by,

$$\kappa^{-1} = \left(\frac{\varepsilon k_B T}{4\pi q^2 n}\right)^{\frac{1}{2}} \tag{1.2}$$

where $\varepsilon$, $k_B$, q, T and n are the dielectric constant, the Boltzmann constant, elementary charge, temperature and concentration of mobile ions, respectively. Contribution of electrostatic interaction for protein-polyelectrolyte complex formation first discussed by Tiebackx in the

gelatin with gum acacia system, the stability of the complex increases with salt concentration [Tiebackx et al, 1922]. Veis–Aranyi et al [1960] offered a model for coacervation between Type-A and Type-B gelatin molecules, generally mentioned to as dilute phase aggregation model which undermined the electrostatic interactions [Dickinson et al, 1998] and postulated the formation of complex coacervates through solute–solvent interactions.

### 1.4.2 SURFACE PATCH BINDING

Surface patch binding has been observed between two biopolymers with same surface net charge polarity. Polyelectrolyte interact with protein even on the "wrong side" of isoelectric point (pI) because protein are polyampholytes have small patches of anisotropic charge distribution on its surface, which localized with higher charge density. So, ion-ion repulsion overcome by ion-dipole interaction as shown in Fig. 1.13. SPB has been realized in a wide range of protein-polyelectrolyte systems where the polyelectrolyte selectively binds to the oppositely charged location (segment) of the protein surface overcoming repulsion arising from similarly charged segment. Such interactions often lead to complex coacervation and liquid-liquid phase separation in complex polyelectrolyte solutions.
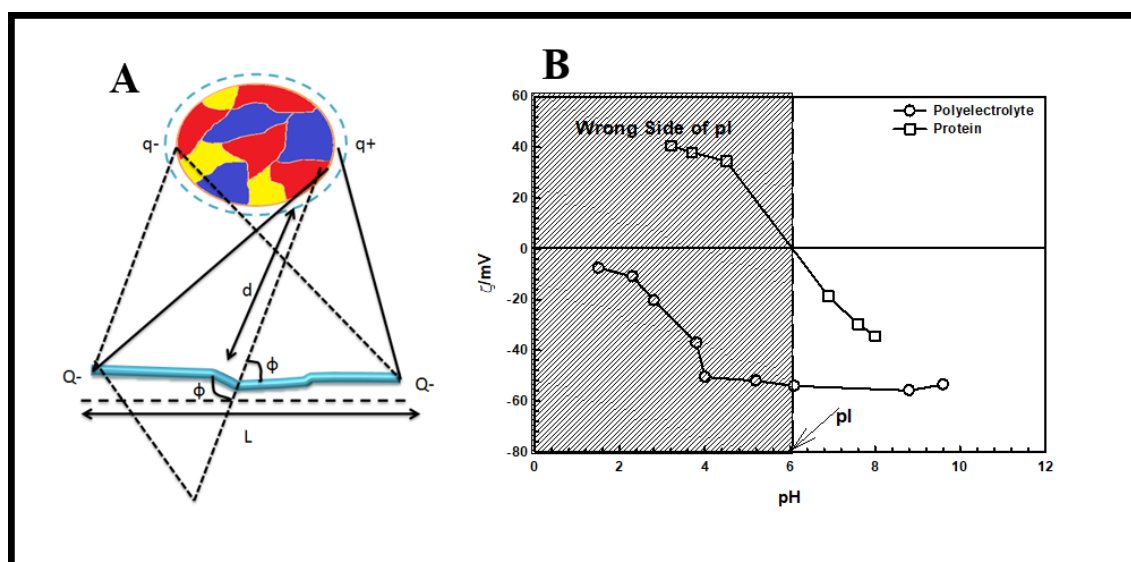


**Fig. 1.13:** (A) Interaction potential for spherical shape protein and rod shaped polyelectrolyte system under surface patch binding and (B) Zeta potential profile for protein (zein) and polyanion (pectin). Shaded region in (B) depicts both biopolymers having similar net charge. Binding in this region is referred to as surface patch binding [Kaushik et al, 2018].

The concept of "wrong side" pI introduced by Paul Dubin and co-workers in the complex formation of BSA protein with polyelectrolyte poly (diallyldimethylammonium chloride) PDADMAC [Kaibara et al, 2000; Yan et al, 2013; Antonov et al, 2010; Seyrek et al, 2003]. The microstructure, phase boundaries and binding affinity have been systematically examined in the complex system. Rubinstein and co-worker [Bowman et al, 1997] give theory in which protein act as dipole in surface patch binding to account for repulsive and attractive interaction with polyelectrolyte as shown in Fig. 1.12.

The inetraction potential between protein (as dipole) and polyelectrolyte (as rod) using Debye-Huckel approximation given by [Ohshima, 1995],

$$U_{Elec}(ij) = \frac{Q_i q_j}{4\pi\varepsilon_o\varepsilon_r r_{ij}}\ln\left(\frac{\frac{L}{2}+r_{ij}}{r_{ij}}\right)e^{-kr_{ij}} \tag{1.3}$$

### 1.4.3 van der Waal Interactions

van der Waal interactions are short range and attractive forces of electromagnetic origin arises due to the dipole-dipole interaction between molecule either through permanent or induced dipoles. The fluctuation of the electron around the atomic nuclei give rise to dipoles which results in attraction between two atoms. These forces fall off as an inverse power of separation between the particles with the comparable range to the particle size. These are mostly operative between non-polar molecules where the electrostatics interaction is minimum and becomes strong at short range. van der Waals interaction in which intermolecular and intramolecular interactions occurs due to the transient dipoles is called London dispersion forces. London forces are weaker than ionic interaction, hydrogen bonding or permanent dipole interaction. These forces are the only attractive intermolecular forces between neutral particles. London forces become stronger as particle becomes larger due to increased polarizability owing to more dispersed electron clouds. They are attractive at large distances and become repulsive at shorter

distances because of overlapping electron's orbitals (Pauli's exclusion principle) and this behaviour is well explained through Lennard-Jonnes (L-J) potential (Fig. 1.14).
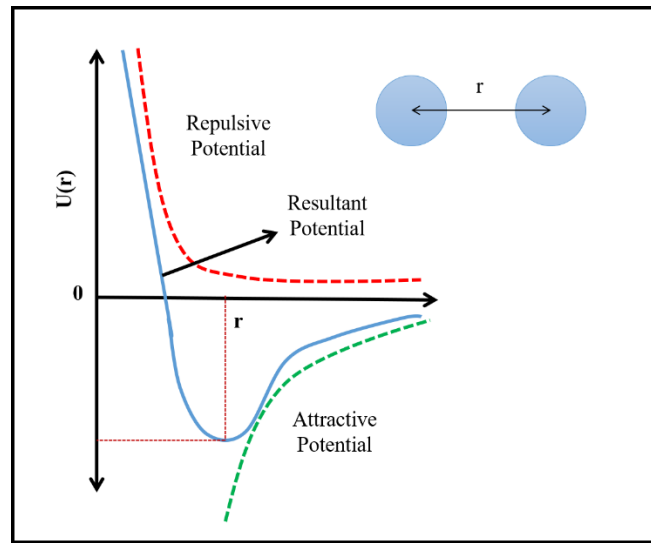


**Fig. 1.14:** Lennard-Jonnes potential between two particles.

Hamacker and de Boer [Hamaker, 1937; de Boer, 1936] determined the forces acting between colloidal objects theoretically with the assumption of pairwise addition of interatomic dispersion energies while neglecting the effect of the neighbour's ones on the interaction between the pairs of the atoms. They demonstrated that the addition of the dispersed energies leads to the range of colloidal interaction of the order of their dimensions nevertheless the fact is that atomic forces range is of atomic dimensions order. Suppose the interaction between two spheres of radii a and b, separated by a distance r, the interaction energy according to Hamaker approximation will be given by

$$V_A(r) = \frac{A_H}{12}\left(\frac{x}{x^2+xy+x} + \frac{x}{x^2+xy+y} + 2ln\left(\frac{x^2+xy+x}{x^2+xy+x+y}\right)\right) \tag{1.4}$$

where $x = \frac{r}{a+b}$, $y = \frac{a}{b}$, and $A_H$ is the Hamaker constant.

For the colloidal particle of same radius i.e., a = b = d, then

$$V_A(r) = \frac{A_H}{6}\left(\frac{d^2}{r^2+4rd} + \frac{2d^2}{(r+2d)^2} + ln\left(1 - \frac{4d^2}{(r+2d)^2}\right)\right) \tag{1.5}$$

From eqn 1.5 potential energy is directly proportional to Hamaker constant (material constant) and separation distance between spheres and inversely proportional to their radius. $A_H$ is given by the equation,

$$A_H = A_{11} + A_{22} - A_{12} \tag{1.6}$$

where $A_{11}$, $A_{22}$, and $A_{12}$ are Hamaker constant for particle, medium and between particle and medium, respectively. For any material i, the relation between the Hamaker constant and London dispersion constant $\beta_{ii}$ with number of molecules or atoms per unit volume $q_i$ is given by,

$$A_{ii} = \pi q_{ii}^2 \beta_{ii} \tag{1.7}$$

The polarizability of molecule and atoms is related to $\beta_{ii}$ with value in the range of $10^{-78} - 10^{-76}$ $Jm^6$.

For r $\ll$ d i.e. the limit of close approach where sphere is sufficiently large compared to distance between spheres then eqn 1.5 become,

$$V_A \cong -\frac{A_H d}{12r} \tag{1.8}$$

This imply particle coagulation will take place if particle approaches very close to each other. Overlapping of colloidal particle prohibited due to Born repulsion (As two surfaces into close contact, the van der Waal force between them continuously increasing and then at a point electron cloud of the two surfaces begin to overlap, that give rise to repulsive force also termed as hard-core repulsion) which make the system a hard sphere potential separated by r < d, here r is centre to centre distance. Irreversible aggregation will take place when the van der Waals potential is finite (due to strong Born repulsion between electron) at contact but very large compared to the thermal energy.

### 1.4.4 DLVO THEORY

Deraguin, Landau, Verwey and Overbeek (DLVO) proposed a classical theory for the stability of colloidal particles in suspension. DLVO theory is based on the assumption that force between the two colloidal surfaces in a suspension is addition of the electrostatic repulsive force due to double layer and attractive London-van der Waals forces. The electrostatic repulsive potential ($V_{El}$) between two interacting particles is determined on the basis of Poisson-Boltzmann equation and the integral of dispersion interactions over the volume of the particles give attractive van der Waal potential ($V_{vdW}$), addition of these attractive and repulsive potential give total potential of DLVO ($V_{DLVO}$),

$$V_{DLVO} = V_{El} + V_{vdW} \qquad (1.9)$$

The height of the potential barrier in the energy profile defines the stability and its small value describe the particle overcome the barrier and to cause aggregation.

### 1.4.5 HYDROPHOBIC INTERACTIONS

The interaction between hydrophobes to exclude water is called "hydrophobic interactions". In protein folding, the hydrophobic part of large macromolecules (proteins) arrange themselves to minimize the water contact by using hydrophobic interaction. Figure 1.15 describes these phenomena using a schematic diagram. When hydrophobe is dispersed in water, the hydrogen bond between water molecules are broken increasing its free energy and then water molecule forms new hydrogen bond with cage like structure called Clathrate cage around the hydrophobe to minimize contact with water. These alignments make the hydrophobe system more ordered but the water structure more disordered which give positive change to entropy ($\Delta S$), which make Gibb's free energy ($\Delta G = \Delta H - T \Delta S$) negative and so the mixing of hydrophobes in water though not spontaneous but viable at suitable conditions [Dickinson, 1998].
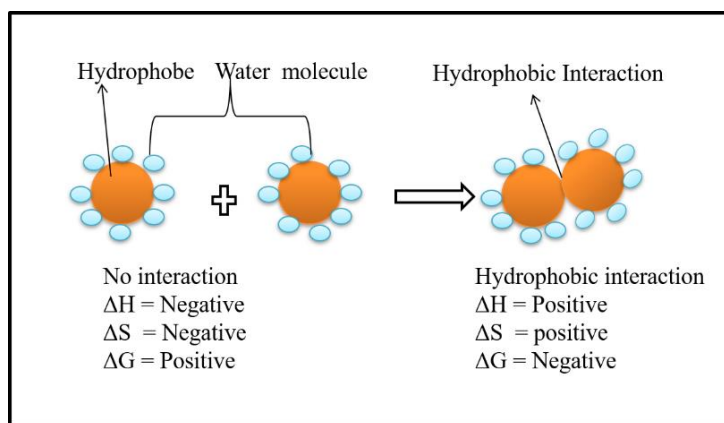
**Fig. 1.15:** Hydrophobic interaction between two molecules.

As we know these hydrophobe interact to minimize the water contact so during these processes the clathrate cage is broken and hydrophobe restructure themselves to form new clathrate cage transiently. In this process, the total number of structured waters around hydrophobes reduced which increases the entropy of the system and thus, this process occurs spontaneously.

## 1.5 PROTEIN-POLYELECTROLYTE INTERACTIONS

The investigation of the interaction between polyelectrolyte (PE) and proteins remains one of the most important research fields in biophysics. It is well-established that proteins and PEs could form complexes, coacervates/precipitates and gel at certain conditions as shown in the Fig. 1.16, driven by non-specific and non-covalent interactions, primarily electrostatic interactions [Xia et al, 1994; Carlsson et al, 2001].
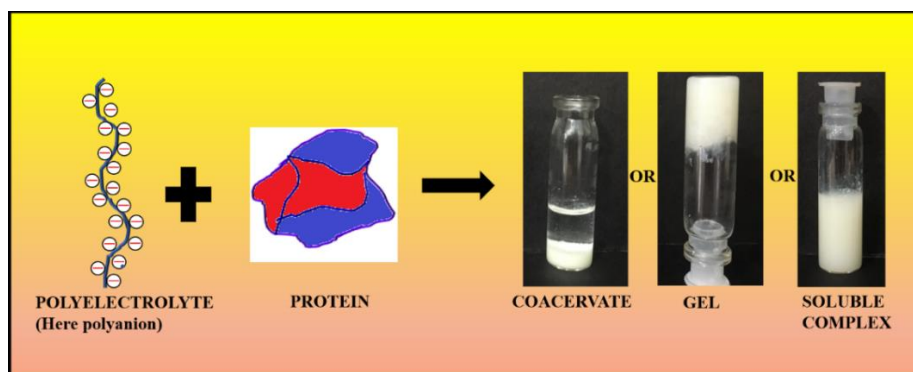


**Fig. 1.16:** Schematic diagram of interaction between polyelectrolyte (polyanion) and protein which result in different phases of complexation.

Compared with specific binding between biomolecular pairs with complementary epitopes such as biotin–avidin and antigen–antibody, the protein–PE complexation is a promising prospect in building a multi-functional biomedical scaffold via a flexible and cost-effective approach. In this way, the structure of the protein–PE complex could be tailored by modulating protein–PE interactions, satisfying the needs for various applications such as biosensing [Wang et al, 2011], pharmacology [Alvarez-Lorenzo et al, 2013], protein separation [Chen et al, 2009], and tissue engineering [Araujo et al, 2014]. Furthermore, a thorough understanding of the protein–PE interaction could help identify vascular circulation and toxicology of PE-based biomaterials because they would be exposed to various proteins/biomolecules such as human serum albumin (HSA), trypsin (TRP), and haemoglobin (Hb) of different content in vivo, known as the opsonization effect [Koegler et al, 2011]. By modulating key parameters related to protein–PE binding, such as surface charge, hydrophobicity, and chain flexibility, the biocompatibility of the newly developed PE-based materials could be assessed and optimized.

## 1.6 THERMODYNAMICS OF COMPLEXATION

From electrostatic interaction, unlike charges attract and like charges repel each other. Coulomb's law gives precise value for such interaction in a vacuum. The interaction energy U(r) is given by

$$U_{12}(r_{12}) = \frac{q_1 q_2}{4\pi\varepsilon_o r_{12}} \tag{1.10}$$

Where $q_1$ and $q_2$ are charges and $r_{12}$ is the distance between them and $\varepsilon_o$ is vacuum permittivity. Bringing two oppositely charged ions closer is always energetically favourable, according to Coulomb's law.

For interaction between molecules, we consider it as dipole and higher multipoles with an arbitrary charge distribution. Electrostatic energy for the molecular charge densities $\rho(\vec{r})$ can be expanded as collection of point charges [Evans et al, 1999],

$$U_{12}(r_{12}) = \int \rho(\vec{r})\,\psi_2(\vec{r})d^3\vec{r} = \frac{1}{4\pi\varepsilon_o r_{12}}\iint \frac{\rho_1(\vec{r})\rho_2(\vec{r}')}{|\vec{r}-\vec{r}'|}d^3\vec{r}d^3\vec{r}' \qquad (1.11)$$

Where $\rho_i(\vec{r})$ and $\psi_i(\vec{r})$ is the signed charge density and electrostatic potential around species $i$. Electrostatic interaction energy can split into attractive and repulsive interactions for clarity.

The situation is more intricate for aqueous solutions. It's very difficult to calculate electrostatic energy between ions, water molecules and polyelectrolytes. Therefore, dielectric medium is taken into account in place of vacuum permittivity using first approximation. The solvent response ($\varepsilon_r$), involves both entropy contribution and energy because of that electrostatic energy is actually a solvated ions free energy [Evans et al, 1999].

In aqueous solution separation between charges is small so this approximation doesn't hold for long due to hydration effects and specific ion interactions out there generic electrostatics start to play a role. Disregarding these limitation, electrostatic energy for polymer, particle, any charged particle or combination in aqueous medium, using an effective permitivity [Evans et al, 1999].

$$U_{el} = \frac{1}{2}\int_V \rho(\vec{r})\psi(\vec{r})dV = \frac{\varepsilon_r\varepsilon_o}{2}\int_V \left(\vec{\nabla}\psi\right)^2 dV \qquad (1.12)$$

where $\vec{\nabla}\psi$ is the gradient of electrostatic potential. Complexation or complex coacervation will favoured or not by elctrostatic energy depends on the gradient of electrostatic potential and will vary with salt conentration also depend on the chemical composition of macroions.

In case of charged polymers and macroions in aqueous medium surrounded by double layer which is accumulated and co-ions are depleted. At this state entropy is lowered compared to which all counterions are randomly mixed. When two oppositely charged macroions formed complex than double layer cancel out to certain extent and the counterions are free in the form

of mobile ion as shown in Fig. 1.17 that leads to an increase in entropy and hence free energy decreases.

Complexation free energy include both the effect of counterion entropy and effect of electrostatic energy. Assuming, the volume doesn't change and in typical experimental system keeping number of molecules and temperature constant, the Helmholtz free energy F is the characterstics thermodynamic quantity given by,

$$\Delta F_{el} = \Delta U_{el} - T\Delta S_{el} \tag{1.13}$$

The Gibb's free energy $\Delta G$ is the required quantity and $P\Delta V$ has to be taken into account for the affected volume [Theodoor et al, 1990]. At room temperature, for aqueous solution the difference between change in the Gibb's free energy and Helmholtz free energy is very less [Lyklema, 1991]. Usually in this thesis, we consider volume is not affected with fixed number of molecules ions, therefore, the Helmholtz free energy is the thermodynamic quantity.
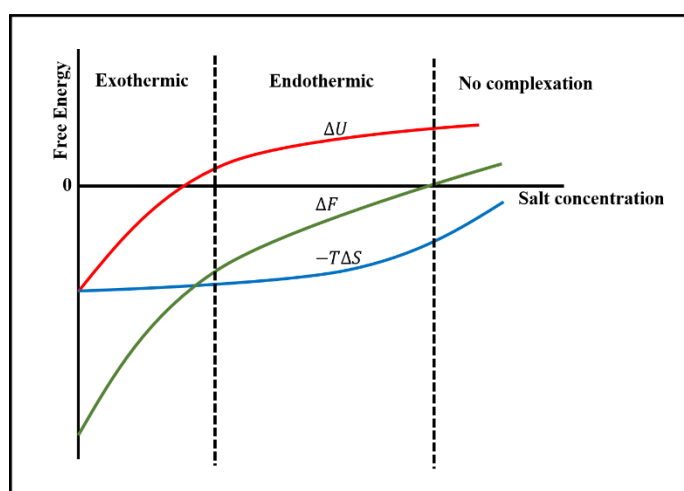


**Fig. 1.17:** Schematic picture showing the hypothesised effect of salt on total free energy of complexation (ΔF), the separate contribution of the electrostatic energy (ΔU), and the ion release entropy (ΔS). (Gucht, et al, 2011)

The entropy change associated with complexation is conquered by the release of counterions that were confind by double layer, therefore entropy is positive. The counterions concentration inside double layer higher than in bulk solution in the case of low salt concentration and the entropy increase upon complexation is large. With ionic strength the

entropy gain of counterion release become less, approaching zero in the limit of very high ionic strength [Gucht et al, 2011].

At low ionic strength, the electrical double layer are thick and dilute and the average distance between opposite charge is large, while the polyelectrolyte complexes are dense which reduce the average distance between opposite charges upon complexation and therefore the electrostatic energy will decrease. In the case of high ionic concentration, the electrical double layer is reduced, and therefore, decreace in electrostatic energy due to unconfined counterions is not compensated by a decrease in electrostatic energy because of newly formed macroion complexes. Which give change in energy positive and the complexation is endothermic.

## 1.7 OUTLINE OF THE THESIS

- Chapter 1 gives a brief introduction of the thesis work also discuss different problem in details. This thesis has five chapter with specific studies discussed below:

- Chapter 2 discusses the different materials used to accomplish the objective of the thesis. Protein used were zein and elastin and polyanion used were agar, pectin and dsDNA. This chapter gives sample preparation used in the work in detail. Also describes the different techniques used for characterizing the materials and to study different phase behaviour.

- Chapter 3 discusses the characterization of plant protein zein and its inetraction with different polyelctrolytes.

- Chapter 4 discusses the study of pH responsive zein-pectin hydrogel for doxorubicin drug delivery.

- Chapter 5 discusses the characterization and phase behaviour of animal protein elastin in aqueous and binary solvent. Also elastin interaction with strong polyanion.

The thesis is concluded with remark on future challenges, and a list of publications arising from this work.

## 1.9 REFERENCES

1.  Alvarez-Lorenzo, C., Blanco-Fernandez, B., Puga, A. M., & Concheiro, A. (2013). Crosslinked ionic polysaccharides for stimuli-sensitive drug delivery. *Advanced drug delivery reviews*, *65*(9), 1148-1171.

2.  Anderson, T. J., & Lamsal, B. P. (2011). Zein extraction from corn, corn products, and coproducts and modifications for various applications: a review. *Cereal Chemistry*, *88*(2), 159-173.

3.  Antonov, M., Mazzawi, M., & Dubin, P. L. (2009). Entering and exiting the protein−polyelectrolyte coacervate phase via nonmonotonic salt dependence of critical conditions. *Biomacromolecules*, *11*(1), 51-59.

4.  Aral, C., & Akbuga, J. (2003). Preparation and in vitro transfection efficiency of chitosan microspheres containing plasmid DNA: poly (L-lysine) complexes. *J Pharm Pharm Sci*, *6*(3), 321-326.

5.  Araujo, J. V., Davidenko, N., Danner, M., Cameron, R. E., & Best, S. M. (2014). Novel porous scaffolds of pH responsive chitosan/carrageenan-based polyelectrolyte complexes for tissue engineering. *Journal of Biomedical Materials Research Part A*, *102*(12), 4415-4426.

6.  Bao, X., Hayashi, K., Li, Y., Teramoto, A., & Abe, K. (2010). Novel agarose and agar fibers: Fabrication and characterization. *Materials Letters*, *64*(22), 2435-2437.

7.  Barrat, J. L., & Joanny, F. (1996). Theory of polyelectrolyte solutions. *Advances in Chemical Physics: Polymeric Systems*, *94*, 1-66.

8.  Boral, S., & Bohidar, H. B. (2010). Effect of Ionic Strength on Surface-Selective Patch Binding-Induced Phase Separation and Coacervation in Similarly Charged Gelatin−Agar Molecular Systems. *The Journal of Physical Chemistry B*, *114*(37), 12027-12035.

9.  Bowman, W. A., Rubinstein, M., & Tan, J. S. (1997). Polyelectrolyte− Gelatin Complexation: Light-Scattering Study. *Macromolecules*, *30*(11), 3262-3270.

10. Bungenberg de Jong, H. G. (1949). Complex colloid systems. *Colloid science*, *2*, 335-432.

11. Butler, M. F. (2002). Mechanism and kinetics of phase separation in a gelatin/maltodextrin mixture studied by small-angle light scattering. *Biomacromolecules*, *3*(4), 676-683.

12. Carlsson, F., Linse, P., & Malmsten, M. (2001). Monte Carlo simulations of polyelectrolyte− protein complexation. *The Journal of Physical Chemistry B*, *105*(38), 9040-9049.

13. Chen, J., Lin, Y., & Jia, L. (2015). Preparation of anionic polyelectrolyte modified magnetic nanoparticles for rapid and efficient separation of lysozyme from egg white. *Journal of Chromatography A*, *1388*, 43-51.

14. De Boer, J. H. (1936). The influence of van der Waals' forces and primary bonds on binding energy, strength and orientation, with special reference to some artificial resins. *Transactions of the Faraday Society*, *32*, 10-37.

15. de Gennes, P. G. (1991). Nobel lecture--soft matter.

16. Dellacherie, E. (1991, April). Bio-specific water-soluble polymer-protein complexes for biological applications. *Abstract in American chemical society*, 201, 321-poly.

17. Dickinson, E. (1998). Stability and rheological implications of electrostatic milk protein–polysaccharide interactions. *Trends in Food Science & Technology*, *9*(10), 347-354.

18. Dobrynin, A. V., Colby, R. H., & Rubinstein, M. (2004). Polyampholytes. *Journal of Polymer Science Part B: Polymer Physics*, *42*(19), 3513-3538.

19. Doublier, J. L., Garnier, C., Renard, D., & Sanchez, C. (2000). Protein–polysaccharide interactions. *Current opinion in Colloid & interface Science*, *5*(3-4), 202-214.

20. Evans, D. F., & Wennerström, H. (1999). The colloidal domain: where physics, chemistry, biology, and technology meet.

21. Falshaw, R., Furneaux, R. H., & Stevenson, D. E. (1998). Agars from nine species of red seaweed in the genus Curdiea (Gracilariaceae, Rhodophyta). *Carbohydrate Research*, *308*(1-2), 107-115.

22. Francavilla, M., Pineda, A., Lin, C. S., Franchi, M., Trotta, P., Romero, A. A., & Luque, R. (2013). Natural porous agar materials from macroalgae. *Carbohydrate polymers*, *92*(2), 1555-1560.

23. Freile-Pelegrín, Y., & Robledo, D. (1997). Influence of alkali treatment on agar from Gracilaria cornea from Yucatan, Mexico. *Journal of applied Phycology*, *9*(6), 533.

24. Glinsky, V. V., & Raz, A. (2009). Modified citrus pectin anti-metastatic properties: one bullet, multiple targets. *Carbohydrate research*, *344*(14), 1788-1791.

25. Gouin, S. (2004). Microencapsulation: industrial appraisal of existing technologies and trends. *Trends in food science & technology*, *15*(7-8), 330-347.

26. Gupta, A., & Bohidar, H. B. (2005). Kinetics of phase separation in systems exhibiting simple coacervation. *Physical Review E*, *72*(1), 011507.

27. Hamaker, H. C. (1937). The London—van der Waals attraction between spherical particles. *physica*, *4*(10), 1058-1072.

28. Hamley, I. W. (2003). Nanotechnology with soft materials. *Angewandte Chemie International Edition*, *42*(15), 1692-1712.

29. Herrero-Vanrell, R., Rincon, A. C., Alonso, M., Reboto, V., Molina-Martinez, I. T., & Rodriguez-Cabello, J. C. (2005). Self-assembled particles of an elastin-like polymer as vehicles for controlled drug release. *Journal of Controlled Release*, *102*(1), 113-122.

30. Kaibara, K., Okazaki, T., Bohidar, H. B., & Dubin, P. L. (2000). pH-induced coacervation in complexes of bovine serum albumin and cationic polyelectrolytes. *Biomacromolecules*, *1*(1), 100-107.

31. Kantor, Y., & Webman, I., *Phys. Rev. Lett.,* 152 (1985) 1891-1894.

32. Kaya, M., Toyama, Y., Kubota, K., Nodasaka, Y., Ochiai, M., Nomizu, M., & Nishi, N. (2005). Effect of DNA structure on the formation of collagen–DNA complex. *International journal of biological macromolecules*, *35*(1-2), 39-46.

33. Kayitmazer, A. B., Seeman, D., Minsky, B. B., Dubin, P. L., & Xu, Y. (2013). Protein–polyelectrolyte interactions. *Soft Matter*, *9*(9), 2553-2583.

34. Klassen, D. (2010). *Associative phase separation in admixtures of pea protein isolates with gum Arabic and a canola protein isolate with iota-carrageenan and alginate* (Doctoral dissertation, M. Sc. Thesis) Saskatoon, SK: University of Saskatchewan).

35. Kleman, M., & Laverntovich, O. D. (2007). *Soft matter physics: an introduction*. Springer Science & Business Media.

36. Koegler, P., Clayton, A., Thissen, H., Santos, G. N. C., & Kingshott, P. (2012). The influence of nanostructured materials on biointerfacial interactions. *Advanced drug delivery reviews*, *64*(15), 1820-1839.

37. Kohn, R. (1987). Binding of divalent cations to oligomeric fragments of pectin. *Carbohydrate research*, *160*, 343-353.

38. Lai, L. F., & Guo, H. X. (2011). Preparation of new 5-fluorouracil-loaded zein nanoparticles for liver targeting. *International journal of pharmaceutics*, *404*(1-2), 317-323.

39. Luo, Y., & Wang, Q. (2014). Zein-based micro-and nano-particles for drug and nutrient delivery: A review. *Journal of Applied Polymer Science*, *131*(16).

40. Lyklema, J. (1991). Fundamentals of colloid and interface science. *Vol. II*.

41. Matsushima, N., Danno, G. I., Takezawa, H., & Izumi, Y. (1997). Three-dimensional structure of maize α-zein proteins studied by small-angle X-ray scattering. *Biochimica et Biophysica Acta (BBA)-Protein Structure and Molecular Enzymology*, *1339*(1), 14-22.

42. Meng, X., Perry, S. L., & Schiffman, J. D. (2018). *U.S. Patent Application No. 15/725,465*.

43. Mezzenga, R., Schurtenberger, P., Burbidge, A., & Michel, M. (2005). Understanding foods as soft materials. *Nature materials*, *4*(10), 729.

44. Mohajer, S., Rezaei, M., & Hosseini, S. F. (2017). Physico-chemical and microstructural properties of fish gelatin/agar bio-based blend films. *Carbohydrate polymers*, *157*, 784-793.

45. Mrevlishvili, G. M., & Svintradze, D. V. (2005). Complex between triple helix of collagen and double helix of DNA in aqueous solution. *International journal of biological macromolecules*, *35*(5), 243-245.

46. Munarin, F., Tanzi, M. C., & Petrini, P. (2012). Advances in biomedical applications of pectin gels. *International journal of biological macromolecules*, *51*(4), 681-689.

47. Nakajima, A., & Sato, H. (1972). Phase relationships of an equivalent mixture of sulfated polyvinyl alcohol and aminoacetalyzed polyvinyl alcohol in microsalt aqueous solution. *Biopolymers: Original Research on Biomolecules*, *11*(7), 1345-1355.

48. Nguyen, T. T., & Shklovskii, B. I. (2001). Complexation of DNA with positive spheres: phase diagram of charge inversion and reentrant condensation. *The Journal of Chemical Physics*, *115*(15), 7298-7308.

49. Ohshima, H. (1995). Electrophoresis of soft particles. *Advances in colloid and interface science*, *62*(2-3), 189-235.

50. Overbeek, J. T. G., & Voorn, M. J. (1957). Phase separation in polyelectrolyte solutions. Theory of complex coacervation. *Journal of Cellular and Comparative Physiology*, *49*(S1), 7-26.

51. Pathak, J., Priyadarshini, E., Rawat, K., & Bohidar, H. B. (2017). Complex coacervation in charge complementary biopolymers: Electrostatic versus surface patch binding. *Advances in colloid and interface science*, *250*, 40-53.

52. Reineccius, G. (2019). Use of proteins for the delivery of flavours and other bioactive compounds. *Food hydrocolloids*, *86*, 62-69.

53. Sell, S. A., Wolfe, P. S., Garg, K., McCool, J. M., Rodriguez, I. A., & Bowlin, G. L. (2010). The use of natural polymers in tissue engineering: a focus on electrospun extracellular matrix analogues. *Polymers*, *2*(4), 522-553.

54. Seyrek, E., Dubin, P. L., Tribet, C., & Gamble, E. A. (2003). Ionic strength dependence of protein-polyelectrolyte interactions. *Biomacromolecules*, *4*(2), 273-282.

55. Smith, A. E., Bellware, F. T., & Silver, J. J. (1967). Formation of nucleic acid coacervates by dehydration and rehydration. *Nature*, *214*(5092), 1038.

56. Storm, C., Pastore, J. J., MacKintosh, F. C., Lubensky, T. C., & Janmey, P. A. (2005). Nonlinear elasticity in biological gels. *Nature*, *435*(7039), 191.

57. Tainaka, K. I. (1980). Effect of counterions on complex coacervation. *Biopolymers: Original Research on Biomolecules*, *19*(7), 1289-1298.

58. Tanaka, H., Araki, T., Koyama, T., & Nishikawa, Y. (2005). Universality of viscoelastic phase separation in soft matter. *Journal of Physics: Condensed Matter*, *17*(45), S3195.

59. Theodoor, J., & Overbeek, G. (1990). The role of energy and entropy in the electrical double layer. *Colloids and Surfaces*, *51*, 61-75.

60. Tiebackx, F. W. (1922). Ist die Gelatine-Gummiarabikumflockung ein chemischer oder ein kolloidchemischer Proze\?. *Colloid & Polymer Science*, *31*(2), 102-103.

61. Tiwari, A., Bindal, S., & Bohidar, H. B. (2008). Kinetics of protein− protein complex coacervation and biphasic release of salbutamol sulfate from coacervate matrix. *Biomacromolecules*, *10*(1), 184-189.

62. Trappe, V., & Sandkühler, P. (2004). Colloidal gels—low-density disordered solid-like states. *Current opinion in colloid & interface science*, *8*(6), 494-500.

63. Van der Gucht, J., Spruijt, E., Lemmers, M., & Stuart, M. A. C. (2011). Polyelectrolyte complexes: bulk phases and colloidal systems. *Journal of colloid and interface science*, *361*(2), 407-422.

64. Veis, A., & Aranyi, C. (1960). Phase separation in polyelectrolyte systems. I. Complex coacervates of gelatin. *The Journal of Physical Chemistry*, *64*(9), 1203-1210.

65. Wang, Y., Zhang, S., Du, D., Shao, Y., Li, Z., Wang, J., ... & Lin, Y. (2011). Self-assembly of acetylcholinesterase on a gold-nanoparticles–graphene nanosheet hybrid for organophosphate pesticide detection using polyelectrolyte as a linker. *Journal of Materials Chemistry*, *21*(14), 5319-5325.

66. Xia, J., & Dubin, P. L. (1994). Protein-polyelectrolyte complexes. In *Macromolecular complexes in chemistry and biology* (pp. 247-271). Springer, Berlin, Heidelberg.

67. Yan, Y., Kizilay, E., Seeman, D., Flanagan, S., Dubin, P. L., Bovetto, L., ... & Schmitt, C. (2013). Heteroprotein complex coacervation: bovine β-lactoglobulin and lactoferrin. *Langmuir*, *29*(50), 15614-15623.

68. Yeo, G. C., Keeley, F. W., & Weiss, A. S. (2011). Coacervation of tropoelastin. *Advances in colloid and interface science*, *167*(1-2), 94-103.

69. Zaccarelli, E. (2007). Colloidal gels: equilibrium and non-equilibrium routes. *Journal of Physics: Condensed Matter*, *19*(32), 323101.

70. Zou, Y., & Zhang, Y. (2011). The orthotropic viscoelastic behavior of aortic elastin. *Biomechanics and modeling in mechanobiology*, *10*(5), 613-625.

# CHAPTER 2

## MATERIALS AND METHODS

**OVERVIEW**

This chapter describes various used techniques in details. In order to investigate the phase stability of proteins and their interaction with polyanions techniques like the turbidity, electrophoresis, light scattering, viscometer, and, rheology were extensively used. TEM, SEM, AFM and optical microscopy were used to study the morphology and structure of nanoparticles, gels and coacervates for various direct visualizations. UV-VIS absorption spectroscopy was also used for primary characterization of the samples.
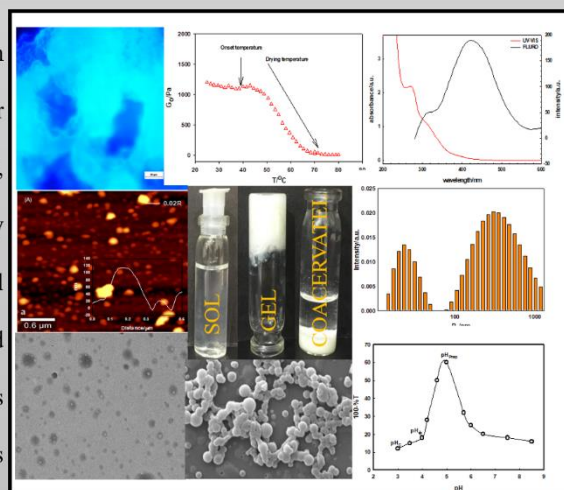
## 2.1 MATERIALS

In this thesis proteins used for study were of two types one plant protein (zein, spherical) and other animal (elastin, rod) protein. Zein resourced from endosperm of maize plant with molecular weight ≈ 20 kDa, purity ≥ 95 %, and containing mostly α-fraction was purchased from Sigma-Aldrich, U.S.A. Two types of elastins were used: soluble and insoluble. Water soluble elastin (salt free, lyophilized powder) resourced from bovine neck ligament was purchased from Sigma-Aldrich, USA, with product number E6527 and CAS no. 9007-58-3. Sodium chloride was brought from CDH, India. Insoluble elastin (CAS No. 9007-58-3) from Bovine neck ligament used in this thesis was purchased from Sigma-Aldrich, USA. Insoluble elastin was provided as a whitish lyophilized powder with a molecular weight of 60 kDa.

Polyelectrolytes used to interaction with protein (in this thesis) were agar, pectin and DNA. Purified lypholyzed agar (MW ≈ 300 kDa) was provided in the form of a powder by CSMRI (India) and ethanol was purchased from Merck (Germany). Pectin (M.W. ≈ 50-150 kDa, methoxy content < 9 %, ≤ 10 % moisture and ≥ 74% Galacturonic acid) sourced from citrus and Salmon testes sodium salt dsDNA with 2000 base pair (MW= $1.6 \times 10^6$ Da) 41.2%, % GC content were purchased from Sigma Aldrich USA. Table 2.1 provides a list of physical properties of biopolymers used in this work.

**Table. 2.1:** Physical properties of protein and polyelectrolytes.

| | Properties | Zein* | Elastin** | Pectin*** | Agar**** | DNA***** |
|---|---|---|---|---|---|---|
| 1 | Molecular weight/kDa | 18-20 | 50-70 | 59-150 | 300 | 1600 |
| 2 | Hydrodynamic Size/nm | 80-120 | 150-200 | 300 | 100 | 700-800 |
| 3 | Conformation | Sphere | Rod | Stiff Chain | Stiff chain | Helical |
| 4 | Persistence length/nm | -- | -- | 10 | 6 | 50 |
| 5 | pI | 6.2 | 4.8-5 | -- | -- | -- |
| 6 | Zeta Potential/mV | 37 | 8 | -50 | -20 | -55 |
| 7 | Polyelectrolyte nature | Polyampholyte | Polyampholyte | Polyanion | Polyanion | Polyanion |

*Zein [Li, 2011; Zhong, 2009], Elastin** [Kaushik et al, 2019], Pectin*** [Joshi et al, 2016; Ventura, 2013], Agar**** [Boral, 2010; Djabourov, 1989] and DNA***** [Pandey et al, 2017]

Alcohol used were only ethanol, analytical grade brought from Merck, Germany. Salt used were calcium chloride and sodium chloride. Calcium chloride dihydrate ($CaCl_2.2H_2O$) and analytical grade ethanol were brought from Merck, Germany.

To proceed for drug delivery from gel, drug used was Doxorubicin Hydrochloride (Cas number 25316-40-9) were brought from Sigma Aldrich, USA. Hydrochloric acid AR grade was purchased from SD Fine Chem Limited (India).

Protein and polyelectrolyte concentration are expressed in % (w/v), ethanol concentration is denoted in % (v/v) and salt concentration in molar. All chemicals were of analytic grade, and these were used without further purifications. All procedures were performed at room temperature 25 $^0$C unless otherwise stated.

## 2.2 CHARACTERIZATION TECHNIQUE

In this chapter, I have described various techniques in details. The technique used to investigate the phase stability of proteins and its interaction with polyanion includes the turbidity, electrophoresis, light scattering, viscometer, rheology, and surface tension. Technique like TEM, SEM, AFM and optical microscopy were also used to study the morphology and structure of nanoparticles, gels and coacervates for various direct visualization. UV-VIS absorption spectroscopy was used for initial characterization of samples.

## 2.2.1 SCATTERING TECHNIQUE

## 2.2.1.1 LIGHT SCATTERING

Light scattering technique plays an important role in the study of physical properties of the systems specially in their solution phase. Such techniques are also used to study various dynamics and phase transition in the complex fluids. Necessary condition for scattering principle is that size of scattered particle should be of the order of incident electromagnetic radiation wavelength. Monochromatic beam of laser light impinges on the sample and is scattered into a detector as shown in Fig. 2.1. Scattering volume is the intersection between the scattered and incident beam. Scattered light radiation generated by an accelerated charge when the molecule in the scattered volume is exposed to the electric field. In the case of solution, molecules due to collision and thermal interaction by solvent molecules shows rotational, translational and vibrational motion. Because of this, molecular position randomly changes and there is fluctuation in scattered light in time about an average. The rate of spontaneous

fluctuations decay to equilibrium directly proportional to the dynamics of molecule. Whether phenomenon is elastic (Rayleigh), inelastic (Raman), or quasi-elastic (Rayleigh-Brillouin) is determined by the change in the energy of incident and scattered radiation. Dynamic and static light scattering embraces elastic scattering.
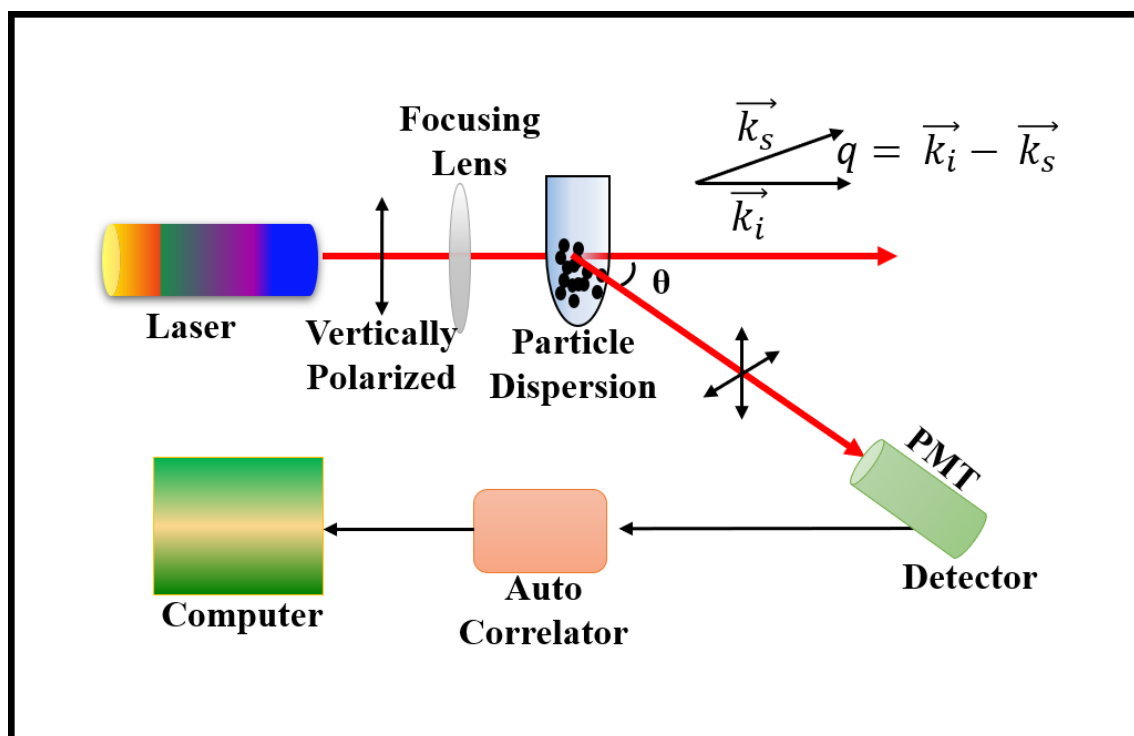


**Fig. 2.1:** Schematic for light scattering.

Physical properties of a biopolymer like its radius of gyration, second virial coefficient of chemical potential and molecular weight are determined by static light scattering (SLS).

Transport properties like bending modes and diffusion coefficient of the biopolymer under different physical conditions are determined by dynamic light scattering (DLS). Table 2.2 listed the different scattering technique used to find out the properties of the system.

**Table 2.2:** Scattering technique used to probe the different length scale.

| S. No. | Scattering Techniques | Length scale accessible (nm) |
|--------|----------------------|------------------------------|
| 1. | Light scattering | 5-500 |
| 2. | Neutron scattering | 1-50 |
| 3. | X-ray scattering | 0.1-0.5 |
| 4. | Electron scattering | <0.5 |

In this thesis light scattering and neutron scattering were used to determine the relaxation and structural properties of the systems.

Instrument used to perform light scattering was PhotoCor (USA) for dynamic and static light scattering which was operated in multi-tau mode. The light scattering spectrometer was mounted on a Newport vibration free optical table. Scattering angle was set according to the requirement of experiment, excitation source was He: Ne laser (35 mW) with laser wavelength 632.8 nm. The time scale spanned 8 decades from 0.5 µs to 10 s. The samples were emptied into borosilicate glass cell and placed inside the thermostat. The thermostat consists of two temperature-controlled shell, the inner and the external one where the temperature were stabilized using PID controller and external circulator (chiller), respectively. The detector, used to collect the light scattered through the samples, was photomultiplier which positioned at right angle to the laser source. The fluctuating intensity data was compiled using digital correlator device which compared the intensity of two signals over a short period of time. The picture of the dynamic and static light scattering instrument used is shown in Fig. 2.2. Non-linear regression analysis of the measured intensity correlation functions was done to determine particle size histogram.



**Fig. 2.2:** PhotoCor (USA), light scattering instrument.

## 2.2.1.1.1 DYNAMIC LIGHT SCATTERING

Dynamic light scattering (DLS) also called as photon correlation spectroscopy (PCS) or quasi-elastic light scattering (QELS) is a perfect tool for the determination of size distribution and particle size. This characterization method employs the measurement of the time resolved scattered light intensity from solute particles dispersed in a solution at a fixed angle 90° and analysed through autocorrelator [Chu 1974; Burchard et al, 1980; Brown 1980; Benedek 1968; Berne et al, 2000]. The random motion of the solute particles exhibits Brownian motion or diffusion due to non-compensated impacts of solvent molecules and the scattering from the solution provide a randomly fluctuating intensity pattern which is oscillating round an average value. Hydrodynamic radius ($R_h$) is evaluated using Stokes-Einstein equation using diffusion coefficient (D) which is related to frequency or relaxation time of an intensity correlation function of the scattered light. However, the validity is limited to spherical particles and low concentration. The robustness of the results was decided through either sample to sample accuracy or through data reproducibility within the same sample. The variance between the calculated and measured base line was not allowed to exceed beyond $\pm 0.1\%$.

The quantitative information related to physical properties of the system was extracted from the intensity fluctuations using the intensity autocorrelation function $g_2(t)$ given by [Berne et al, 1976],

$$g_2(\tau) = \frac{\langle I(\tau')\, I(\tau'+\tau)\rangle}{\langle I(\tau')\rangle^2} \qquad (2.1)$$

where $\tau$ is the time separation between light scattering events in the sample also called correlation time (delay time).

The electric field autocorrelation function $g_1(\tau)$ is given by:

$$g_1(\tau) = \frac{\langle E(\tau')\, E^*(\tau'+\tau)\rangle}{\langle E(\tau')E^*(\tau')\rangle} \;\rightarrow\; \frac{\langle E(\tau')\, E^*(\tau'+\tau)\rangle}{\langle E(\tau')\rangle^2} \qquad (2.2)$$

This intensity and electric field correlation are related to each other through Siegert's relation given by,

$$g_2(\tau) = C_1 + C_2|g_1(\tau)|^2 \tag{2.3}$$

where $C_1$ is the baseline of the correlation function defines as $|g_1(t)||_{t\to\infty} = C_1$ and $C_2$ defines the spatial coherence factor that depend on the detector area, the optical alignment and the scattering properties of the system.

In case of solution, the electric field correlation function having number of particles undergoing Brownian motion is given by

$$g_1(\tau) = \sum_i C_i e^{-\Gamma_i \tau} \tag{2.4}$$

$\Gamma_i$ is the relaxation frequency characterizing different relaxation modes present in the system including translational, rotational diffusion etc.

The relaxation modes $\Gamma$i and diffusion coefficient related to the $i^{th}$ particle through the relation $\Gamma_i = D_i q^2$ and using Stokes-Einstein equation the hydrodynamic size ($R_h$) can be calculated using,

$$R_h = \frac{k_B T}{6\pi\eta_o D} \tag{2.5}$$

where $k_B$ is the Boltzmann constant, D is translational diffusion coefficient, $\eta_0$ is the solvent viscosity, and T is absolute temperature.

The hydrodynamic radius of the particle evaluated through DLS, measure of its size and may depict the shape of the particle. Since the diffusion velocity of the particle is inversely proportional to the hydrodynamic size in eqn. (2.5), so the small size particles diffuse faster than larger particles [Chu 1974; Burchard et al, 1980; Brown 1980; Benedek 1968; Berne et al, 2000].

**2.2.1.1.2 ANALYSIS OF NON-ERGODIC SYSTEMS**

The above discussion using Siegert's relation was used for the ergodic (sol) system where time average property is same as ensemble average property. However, Pusey and Van

Megen found that this relation fails in case of gel where the scattering centers were fixed and able to execute limited Brownian motion about its mean position [Pusey et al, 1989]. Due to this localization of the scattering centres the system was found to trapped in a restricted region of phase space whose locations and extend are determined by the average positions of the scatterers and the magnitude of their displacements and such system are termed as "non-Ergodic" system. This problem can be solved by many ways for example by rotating the sample to probe the entire phase space, expand the incident beam to increase the scattering volume and/or extracting the non-ergodic contribution from the measured data as a heterodyne contribution [Coviello et al, 1997].

The problem of the non-ergodicity in the samples were resolved using the general approach given by Coviello et al where the intensity correlation function is related to electric field correlation function through the equation as [Coviello et al, 1997]

$$g_2(\tau) = 1 + \beta'[2X(1-X)g_1(\tau) + X^2[g_1(\tau)]^2] \qquad (2.6)$$

where $\beta'$ is an instrumental factor whose value is less equal than 1, in our case it is 0.33. The value of X lies between 0 and 1, $X^2$ and 2X(1-X) denotes the homodyne and heterodyne contribution. It is based on the partially heterodyne dynamic light scattering due to the significant heterodyne contribution which is noticed while undergoing transition from sol state to gel state. The value of X = 1 describes full homodyne contribution while for X < 1 the heterodyne contribution become dominant. The value of X is 1 for ergodic system and thus Siegert's relation is found to valid.

For the arrested state X < 1, then 2X(1-X) term makes finite contribution and thus accounted for the linear term pre-factor of $g_1(\tau)$ was found to be larger than the quadratic second term for many cases are given by

$$g_1(t) \approx \frac{g_2(\tau)-1}{[2\beta'(X(1-X))]} \qquad (2.7)$$

The intercept of $g_2(\tau)$-1 versus delay time (t) at t $\rightarrow$ 0 is $\beta'[2X-X^2]$.

### 2.2.1.1.3 RELAXATION DYNAMICS

Polymers particles are found to form different disordered states like glass and gels [Kantor et al, 1985; Krall et al, 1998; Krall et al, 1997]. Crowding of non-interacting particles at high volume fraction result in a glass while strong attraction between the particles lead to formation of gels at low volume fraction. The transition from liquid-like to solid-like behaviour depends on the strength of the interparticle attraction and volume fraction of the particles. A variable which is of utmost importance for describing the suspensions dynamics is the particle density time correlation function in which the information related to the microscopic relaxation timescales in the material is encoded. A twostep decay consisting of fast and slow relaxation process is observed in the correlation function of most suspension where the fast relaxation provides information about local rearrangement of the particles and the slow relaxation represent structural relaxation process. A complex behaviour is observed in certain far away from the equilibrium systems and the correlation function is found to depend explicitly on the age of the systems. This aging time of the system is termed as waiting time. The behaviour exhibited by the systems undergoing dynamical arrest where the slow relaxation time shows the increasing behaviour with waiting time is known to be aging behaviour. This aging dynamics in the arrested system is induced by the formation of particle aggregates. The correlation function from aged samples are fitted using two step relaxation process model which include a fast exponential, and a slow stretched exponential relaxation behaviour given in eqn. 2.8. The fast and slow relaxation process is related to single particle diffusion and cooperative motions, respectively. Aging effect leads to the dynamics of relaxation of glasses become slower. It is the complex relaxation phenomenon in the arrested states through its free energy landscapes so as to reduce its free energy towards the thermodynamic ground state. A typical dynamic structure factor relaxation is given by [Abou et al, 2001]

$$g_2(q,\tau) = A\, e^{(-\Gamma_f \tau)} + (1 - A)e^{(-(\Gamma_s \tau)^\beta)} \tag{2.8}$$

where $\beta$ is stretch exponent, $\Gamma_f$ and $\Gamma_s$ are fast and slow mode relaxation frequency, A and (1-A) are the amplitudes.

### 2.2.1.1.4 STATIC LIGHT SCATTERING

In SLS, solute particle is taken as stationary but particle motion taken into account because of that phase factor of scattered radiation. The scattered light intensity attuned for background scattering and normalized to a reference solvent gives the Rayleigh ratio $R_s(q)$ (ratio of scattered to the incident light intensity) given as [Berne, et al, 1976; Burchard, 1992],

$$\frac{1}{R_s(q)}\frac{4\pi^2 n^2 \left(\frac{dn}{dc}\right)^2}{N_A \lambda^4} = \frac{1}{P(q).\langle M \rangle} + 2B'c \tag{2.9}$$

where c is the concentration of macromolecules, $N_A$ is Avogadro's number, B' is second virial coefficient (describing inter-particle interactions in solution), P(q) is a particle shape factor, and <M> is the weight averaged molecular weight of macromolecule in the solution. When the particle size is small compared to the wavelength of laser light then particle acts as a "point scatter" and then shape doesn't find relevance in scattering i.e. P(q)=1. When size becomes comparable to laser light wavelength then P(q) can approach a quadratic function of qRg and these scattering profiles were used to determine radius of gyration (Rg). The angular dependence is needed to obtain the molar mass and size for all the particle measurements. For the random coil in the very low scattering angle limit i.e. Guinier Region, P(q) is given as

$$P(q) \cong 1 - \frac{q^2 R_g^2}{2} \tag{2.10}$$

The static factor is the Fourier transformation of the correlation function pair which gives the probability to finding the particle at r, assuming that particle is present at the origin. The picture of the light scattering instrument PhotoCor which was used for dynamic and static light scattering is shown in Fig. 2.2.

## 2.2.1.2 SMALL ANGLE NEUTRON SCATTERING

To study internal structure of the coacervate and gel samples were subjected to SANS technique used as probe. This experiment involves scattering of a monochromatic beam of neutrons from the nuclei of scatterer and measuring the scattered neutron intensity I(q) as function of the scattering wave vector q. SANS spectrometer uses neutron with wavelength approximate wavelength ~ 0.5 nm and lower scattering angles of order ~ 1-$10^0$, that is why this technique is called small angle neutron scattering [Lovesey 1992; Squires 1987]. Neutron can be produced by many sources like radioscope, accelerator reactor, photoneutron, spallation and nuclear reactor. Neutron produced from nuclear reactor has flux ~1014 $cm^{-2}$ and position of sample at ~ 107 $cm^{-2}$. The basic setup for SANS divide in three main parts (as shown in Fig. 2.3)

(a) Monochromator: Used to monochromatized white beam of neutron from nuclear reactor. Wavelength was about 5-15 %.

   Types: Velocity selector or double crystal monochromator or filter monochromator

(b) Collimator: used to achieve small scattering angles. For this purpose, few meters long collimators have been used.

(c) Detector: As neutrons are neutral so they detected through indirect method. Firstly, charged particle produced in the detection medium through by neutrons from nuclear reaction and then they are detected. For SANS generally $^3$He position sensitive detectors (PSDs) used. PSDs allowed simultaneous recording of data over a8 large angular range [Aswal et al, 2000; Kohlbrecher et al, 2000].
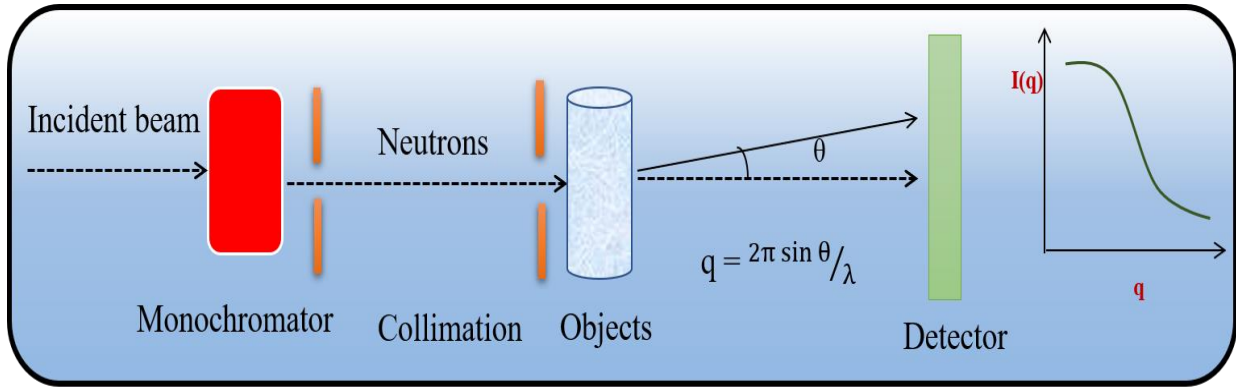
**Fig. 2.3:** Schematic diagram of SANS.

Microscopic structure studies for this thesis has been done at two places (i) Paul Scherrer Institute (PSI), Villigen Switzerland they have spallation source for neutron, the wavelength of neutron was 8 $A^0$ with a resolution of 10%. The scattered neutrons form the samples were detected by using a large ($96 \times 96$ cm$^2$) area $^3$He detector. All the samples (2 mm thick and 0.7 ml quartz cell) were measured at two sample-to-detector distances of 2 and 8 m to cover a q range of 0.07 - 2.5 nm$^{-1}$. and (ii) Bhabha Atomic Research Centre (BARC), Mumbai, India with nuclear reactor source for neutron reactor (Dhruva reactor), neutron passed through 0.7 ml and 2 mm thick quartz cell carrying the sample [Aswal et al, 2000].

For data analysis, the static structure factor profile, I(q) *vs* q for the samples was measured which clearly showed a considerable change in correlation intensity. In order to determine various physical parameters, the data was empirically treated in the following manner. The entire data was first fitted to 1/I(q) *vs* q$^2$, and $1/\sqrt{I(q)}$ *vs* q$^2$ functions which did not prove successful. In the next step, data was divided into three different q-regimes with boundary defined by cross-over wave vector q$^*$ and q$^{**}$ with respective length scale L* ($\frac{2\pi}{q^*}$) and L** ($\frac{2\pi}{q^{**}}$) for the determination of various physical parameters on the basis of model independent best fitting functions. These are,

    (i)    Low-q region: Fitted by power law ($I(q) = I_{PL}(o)\, q^{-\alpha}$), where exponent α defines the geometry of the scattering moiety present in a given system. For

instance, α= 1, 2 and 4 correspond to geometrical shapes of rod, Gaussian coil, and hard sphere conformations [Bohidar et al, 2004].

(ii)    Intermediate q region: Fitted by Debye –Bueche $\left(I(q) = \frac{I_{DB}(o)}{(1+\xi^2 q^2)^2}\right)$ [Debye et al, 1949] or Ornstein- Zernike Relation $\left(I(q) = \frac{I_{OZ}(0)}{1+\xi^2 q^2}\right)$ [Okana 1978], where ξ is the mesh size represent the size of heterogeneity present in the system.

(iii)   High-q region: Guinier -Porod relation $\left(I(q) = I_{GP}(o) exp\left(-\frac{R_c^2 q^2}{2}\right)\right)$, $R_c$ is the cross-sectional radius of the scattering moiety [de Gennes 1985].

## 2.2.2 SPECTROSCOPY TECHNIQUE

Spectroscopy is the study of interaction of matter with radiation. It gives the information about chemical and molecular structure of system. Interaction of matter with radiation is controlled by electric multipole and electric polarizability. Spectroscopy techniques mostly based on process such as scattering, absorption and transmission of electromagnetic radiation. Spectroscopy used for this thesis are UV-VIS, Fluorescence, and FTIR.

### 2.2.2.1 UV-VIS SPECTROSCOPY

UV-VIS spectroscopy is also referred to as absorption spectroscopy, and uses shorter wavelength of range 190-900 nm. In this wavelength range, absorption of electromagnetic radiation occurs due to excitation of bonding and non-bonding electrons of molecule or ions. Therefore, graph of absorbance vs wavelength gives the sample absorption spectrum. Wavelength corresponding to the maximum absorption gives the information about the molecule and also absorption is proportional to the quantity of species absorbing the light. UV-VIS spectroscopy very useful probe of conformational changes occurring in biopolymers. Working principle of UV-VIS spectroscopy is shown in Fig. 2.4. Quantitative measurements based on the Beer-Lambert law which state that the absorption is directly proportional to the

path length and concentration of absorbing species in the solution and is mathematically

defined as [Swinehart, 1962]

$$A = \ln [I/I_o] = \varepsilon cl \qquad (2.11)$$

where, I and $I_o$ intensity of transmitted and incident light respectively, $\varepsilon$ is absorptivity

of sample, c is concentration of the sample, and l is optical path length of the light covered

through the sample.
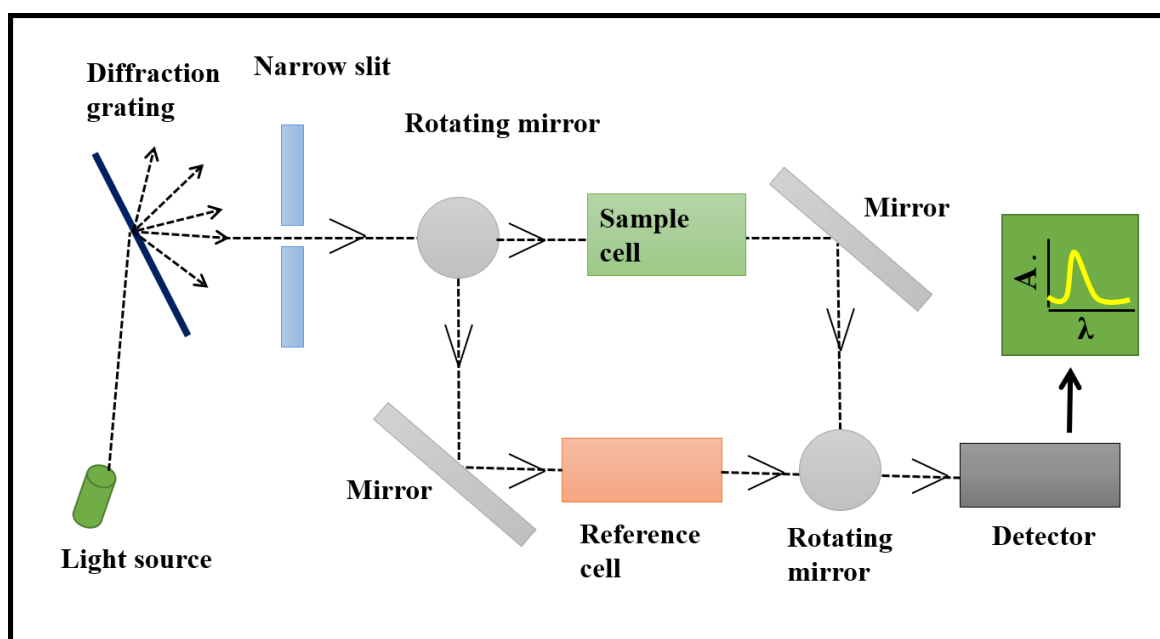


**Fig. 2.4:** Schematic for working of UV-VIS spectroscopy.

In this thesis Cary-60 spectrophotometer of Aglient Tecchnologies, USA was used.

The physical picture of UV-VIS spectrophotometer instrument represents in Fig. 2.5 which

have been used for this thesis.

**Fig. 2.5:** Photo of Cary-60 UV-VIS spectrophotometer.

## 2.2.2.2 FLUORESCENCE SPECTROSCOPY

The emission of light through substance through electronically excited states due to chemical reactions, subatomic motion, electrical charge or stress on a crystal termed as luminescence. Luminescence can be divided into two categories fluorescence and phosphorescence on the basis of transition accompanying change in spin state.
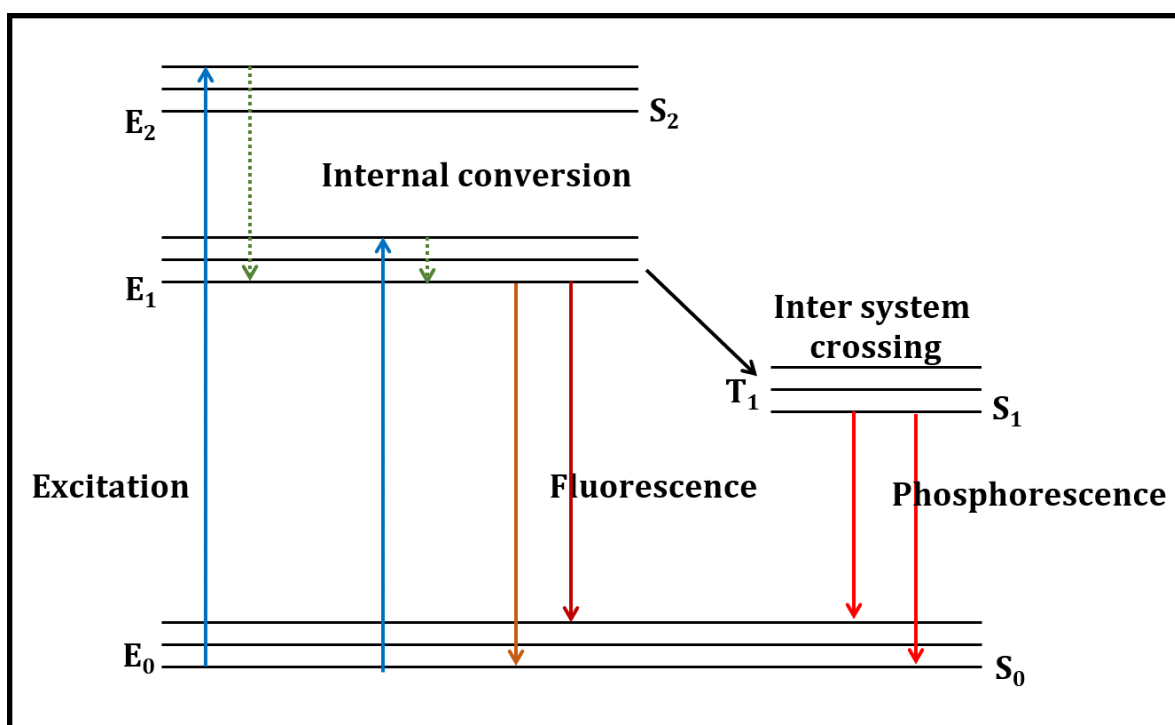


**Fig. 2.6:** Schematic diagram for fluorescence using Jablonski diagram.

Fluorescence absorbed light of shorter and different wavelength comparative to emitted wavelength from molecule and the emission of light break at the moment removing of irradiating light. While in case of phosphorescence substance continue to emit even after removing irradiating. This process is summarized in a Jablonski diagram [Lankchowick et al, 2002] as shown in Fig. 2.5.

Molecule absorbs light (hv) from the ground state which promotes one electron from molecular orbit to the vibrational sub level of first excited state of molecular orbit or to the othe higher excited state. When electron jumps from excited state to ground state it emits radiation of longer wavelength and lower energy than hv, called fluorescence radiation.
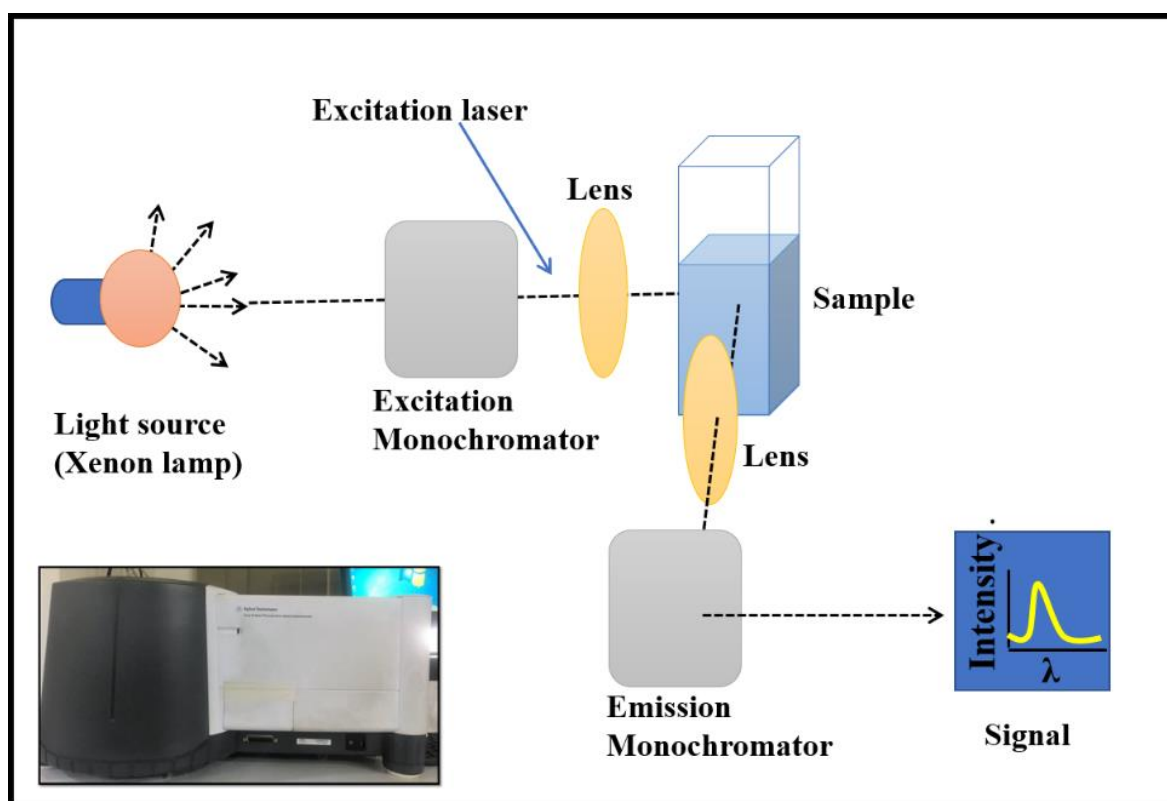


**Fig. 2.7:** Schematic diagram of working of fluorescence with inset physical image of the Varian Cary Eclipse fluorescence spectrophotometer instrument.

Instrument used for fluorescence in this thesis were fluorescence measurements were done on a Varian Cary Eclipse fluorescence spectrophotometer (Agilent, USA). Schematic diagram and physical image for fluorescence showed in Fig. 2.6.

## 2.2.2.3 FOURIER TRANSFORM INFRARED SPECTROSCOPY

FTIR is an analytical and non-destructive technique based on absorption of electromagnetic spectrum in infra-red region by the molecule which correspond to the particular bond. Therefore, spectrum through FTIR is represent of a fingerprint of system. FTIR give information about the rotational and vibrational motion of the molecular structure and chemical bonding which make this technique more useful for analysis of organic and inorganic materials [Colthup et al, 1975] such as lubricants, polymers, paints, cleaning agents, resins etc. the typical range for FTIR is mid IR region (600-4000 cm$^{-1}$).
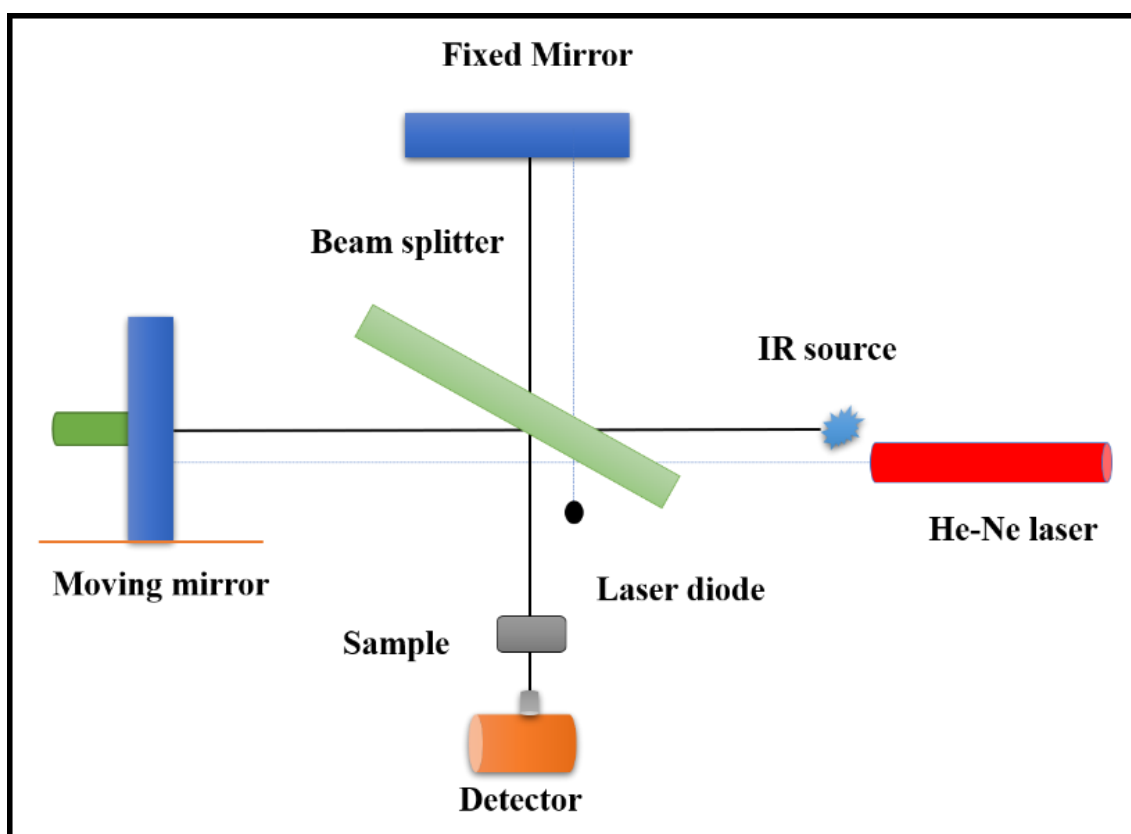


**Fig. 2.8:** Schematic diagram for working principle of FTIR.

The FTIR instrument consists of light emitting source (radiation source), light passed through the interferometer and then incident on the sample as shown in Fig. 2.8. The interferometer divides the incident light and generates an optical path difference between the

beams followed by their recombination to produce interference signals. Detectors detect signals passed through the sample for final measurements and then they are analysed in the computer by Fourier transforming of these signals and then required spectrum is obtained. The sample absorbs all the characteristics wavelength of its spectrum.

FTIR has the ability to transmit and reflect the IR radiation which make it more important to visualizing the sample image. FTIR imaging is very much complimentary to light microscopy but through FTIR we can get information about the molecular composition.

## 2.2.2.4 CIRCULAR DICHROISM

Circular dichroism is a spectroscopy technique used to determine the secondary structure of biological polymers mostly proteins within the range of 170-700 nm wavelength. Proteins are sensitive to physical parameters like its environment, ionic strength, temperature, pH and interaction with other molecules etc., so does its secondary structure. CD spectroscopy used to determine how the secondary structure is affected by physical parameter. In CD technique proteins interact with circularly-polarized light. Circularly-polarized light absorbance consists of left ($\varepsilon_L$) and right ($\varepsilon_R$) circularly- polarized light. Left and right circularly- polarized light components interacts with amino acids resulting in ellipse of polarization which is characterized as molar ellipticity of the protein, $[\theta] = 3300 \, (\varepsilon_L - \varepsilon_R)$ where $\theta$ is in degree $cm^{-1}$ $mole^{-1}$ and varies with wavelength to find out CD spectrum [Cheng et al, 2009]. Circular dichroism (CD) spectra were recorded in this thesis on an Applied Photo physics Chirascan instrument (USA) to estimate the secondary structure of proteins.

**Fig. 2.9:** Photo of Applied Photo physics Chirascan instrument (USA).

## 2.2.3 MICROSCOPY TECHNIQUE

### 2.2.3.1 SCANNING ELECTRON MICROSCOPE

Scanning electron microscope (SEM) [Goodhew et al, 2014] is an imaging technique which used highly focused energy electron for scanning the sample. The interaction of sample with the electron leads to emission of back and secondary scattered electron and then these emitted electrons used for imaging the sample in nanometre scale as shown in Fig. 2.10. The high energy beam electron undergoes either elastic or in-elastic scattering while hit the sample and enter the at the atom layer. Elastically scattered electrons losses minimum energy and called as backscattered electron while in-elastically scattered electrons has low energy because they lose significant amount of energy so known as secondary electrons. As secondary electrons emitted from close to the surface of the sample so it will give high resolution images of the sample surface and thus can reveal the details even of the size less than 1 nm.

The instrument used for scanning electron microscopy (SEM) imaging in this thesis was SEM, Zeiss, EVO-40 instrument as shown in the inset image of Fig. 2.10. Electron bean generated by electron gun fitted with tungsten filament cathode and focused by condenser lens to spot a diameter in range of manometer. Deflector plate used to pass electron beam to scan the sample. SEM images provide information about the topography, compositional and morphological information.
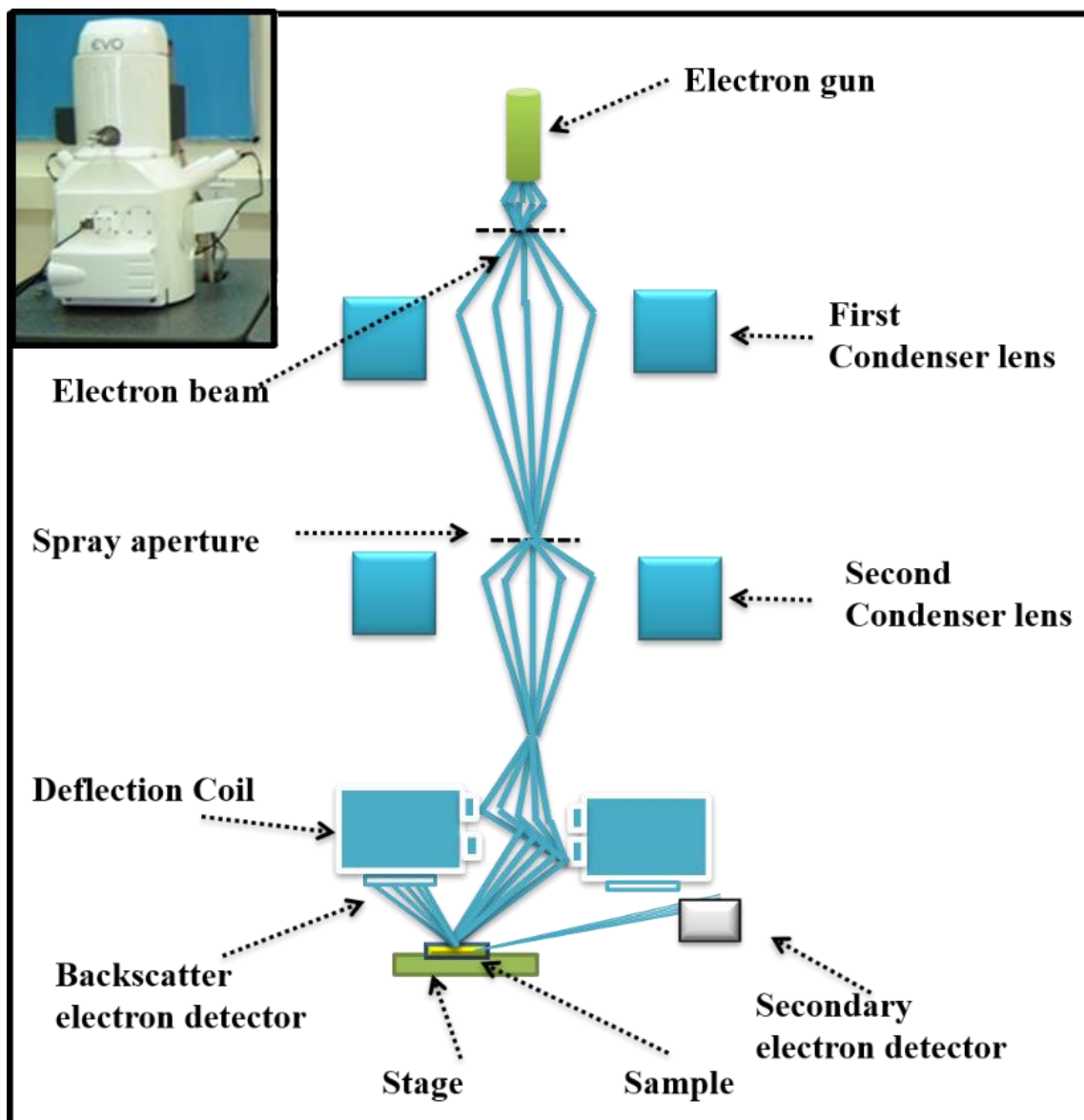


**Fig. 2.10:** Schematic diagram for SEM with inset photo of SEM, Zeiss, EVO-40 instrument.

Sample for SEM imaging prepared by drop-cast of samples over cover slip and kept sample for drying in desiccator for 24 hrs and followed by gold coating using high vacuum evaporation or by low vacuum spin coating for electrically non-conductive samples.

## 2.2.3.2 TUNNELING ELECTRON MICROSCOPE

TEM is used to determine the morphology, size and uniformity of nanoparticles in the interior of the samples. Its high magnification properties make it very important tool for biological, material and medical science [Goodhew et al, 2014]. TEM instrument constituents of an electron source, condensers, vacuum chamber, sample stage, electromagnetic lenses, fluorescent screen and chamber. Electron wavelength of TEM describe by de-Broglie wavelength and that can be achieved by acceleration angstrom.
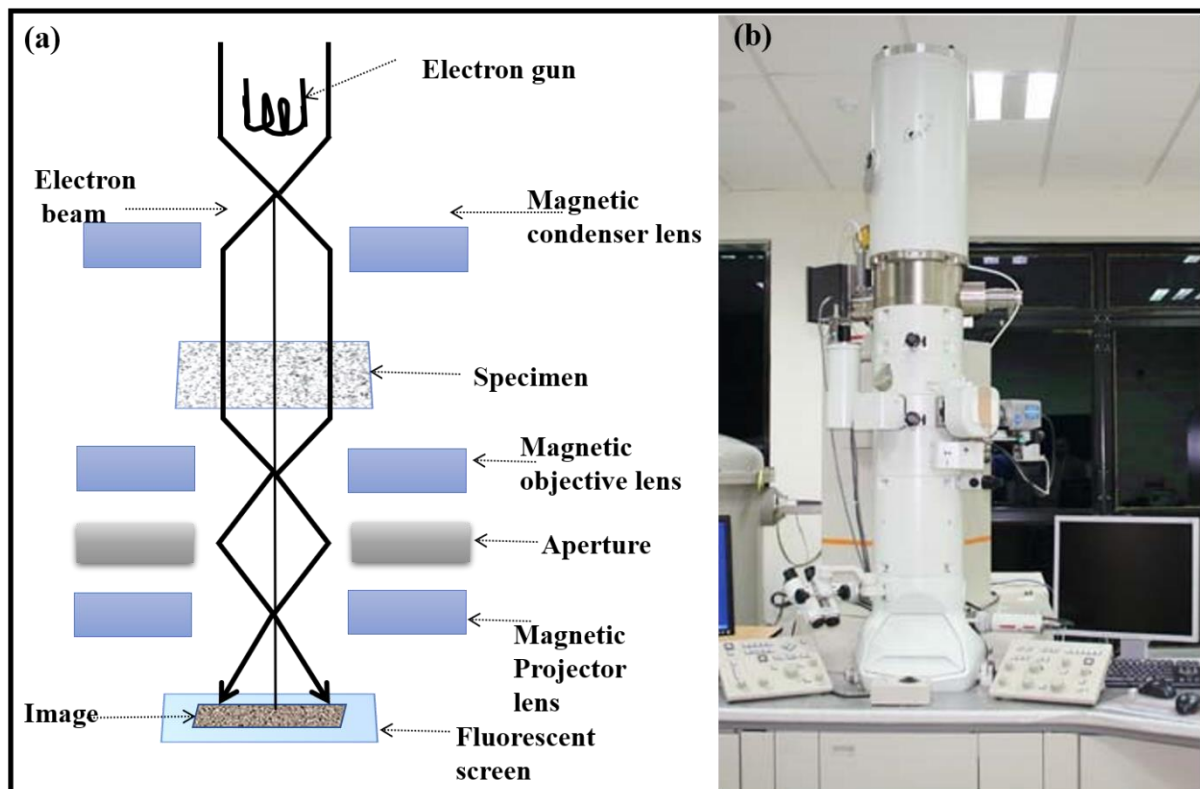


**Fig. 2.11:** Schematic diagram of TEM working principle. (b) TEM JEOL-2100F image.

In TEM instrument, electron stream generates through electron emission source and electron travel through vacuum (high voltage up to 50-150 kV) chamber. Image obtained through interaction of electron and sample in vacuum chamber and some electron either disappeared and scattered bases on the density of materials. Un-scatter electron hit the fluorescent screen at the bottom of the microscope which give shadow image of the sample (Fig. 2.11 a). Fluorescent screen used to view and focused recorded image. Darker area in the image represent the denser area of sample and light area in image due to the large number of electron beam passed through that space. In this thesis TEM JEOL-2100F (Fig. 2.10 b) instrument used for transmission electron microscope and sample was drop cast on carbon coated copper grip and dried by keeping in designator for 24 hours.

### 2.2.3.3 ATOMIC FORCE MICROSCOPE

Atomic force microscope (AFM) [Giessibl, 2003] is high resolution microscope used to get topographic image, growth profile and roughness of sample by interaction of sample and tip, these interactions depend on the force (based on Hooke's Law) between sample and tip. AFM tip used in experiment generally made up of silicon nitride with pyramidal shape while conical silicon tips used for biological sample. Tip should have only one atom to interact with the sample surface. For lateral resolution tip sharpness plays an important role while imaging higher relief surface and vertical resolution depend upon instrument vibration so it is necessary to abate instrument vibration to get maximum vertical resolution. AFM imaging based on three conventional scanning mode: non-contact, contact and tapping mode. The working of AFM shown in Fig. 2.12 (a). Instrument used in thesis for AFM imaging was Alpha 300RA WITec instrument as shown in image of Fig. 2.12 (b) and this instrument used non-contact mode for AFM images.
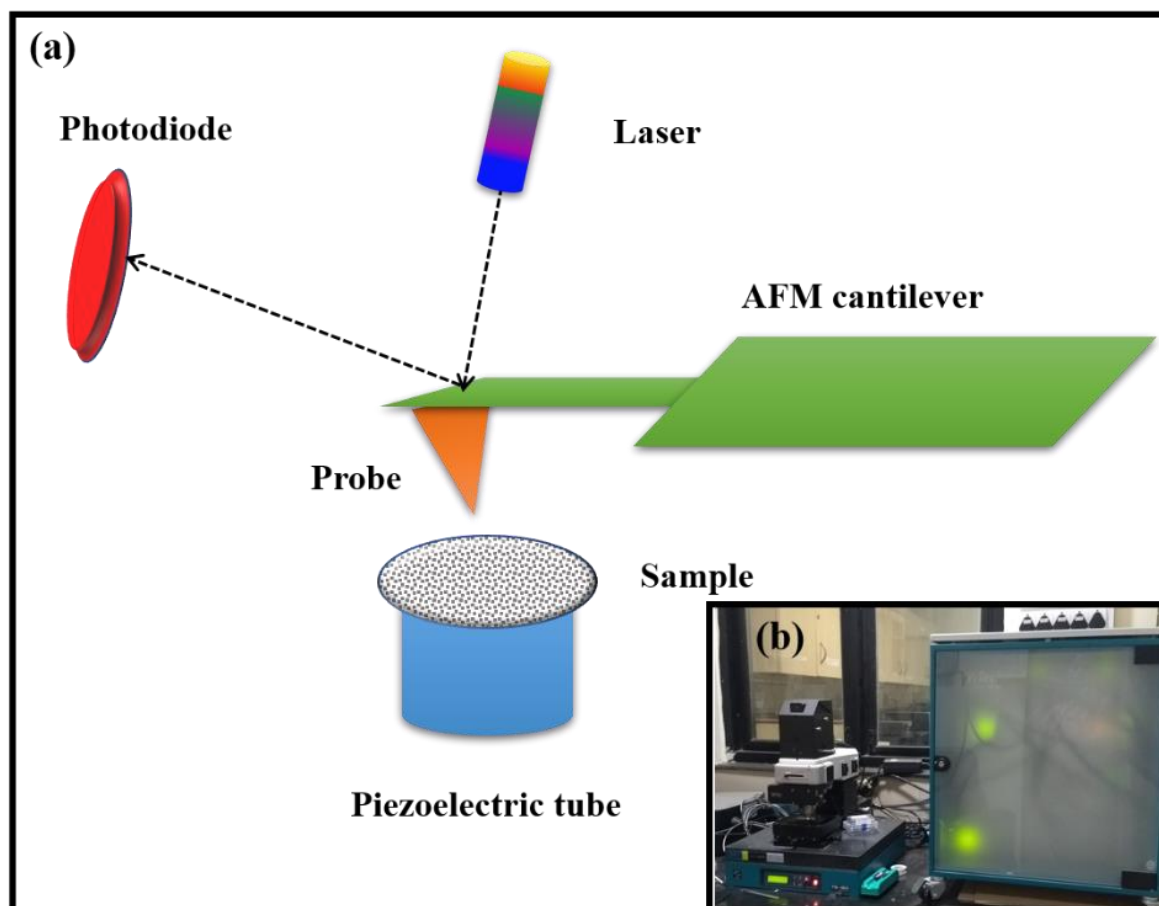
**Fig. 2.12:** (a) Working principle of AFM and (b) photo of AFM instrument, Alpha 300 RA WITec.

### 2.2.3.4 FLUORESCENCE MICROSCOPE

Fluorescence microscope [Meijering et al, 2004] is an optical microscope base on either fluorescence or phosphorescence. In this thesis fluorescence microscope used to observed visually complex coacervate samples and the instrument used for this was using 80i Nikon Instruments. The schematic of Fluorescence microscope working and physical image of fluorescence microscope shown in Fig. 2.13.
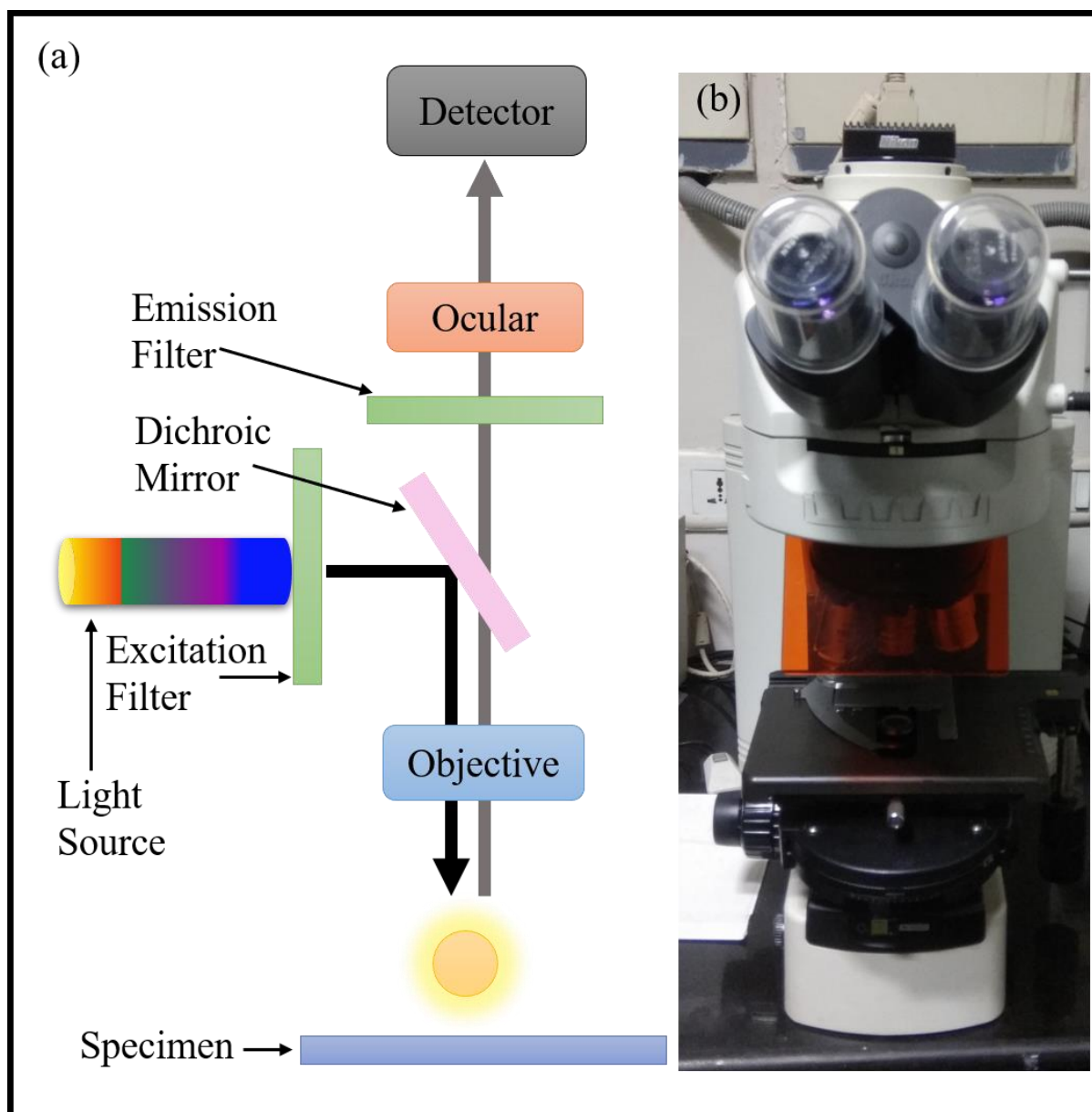
**Fig. 2.13:** (a) Schematic diagram of working of fluorescence microscope. (b) Photo of instrument, 80i Nikon fluorescence microscope

## 2.2.4 RHEOLOGY

Rheology is the study of deformation and flow behaviour of matter. Deformation and shape are very important parameter. Rheology deals with the viscoelastic properties of gel, melts and coacervates [Barnes, 2000]. Viscoelastic material are those material which has both elasticity (ability of any material to store energy in the form of deformation) and viscosity (resistance of flow and in which dissipation of deformational energy during flow) properties.
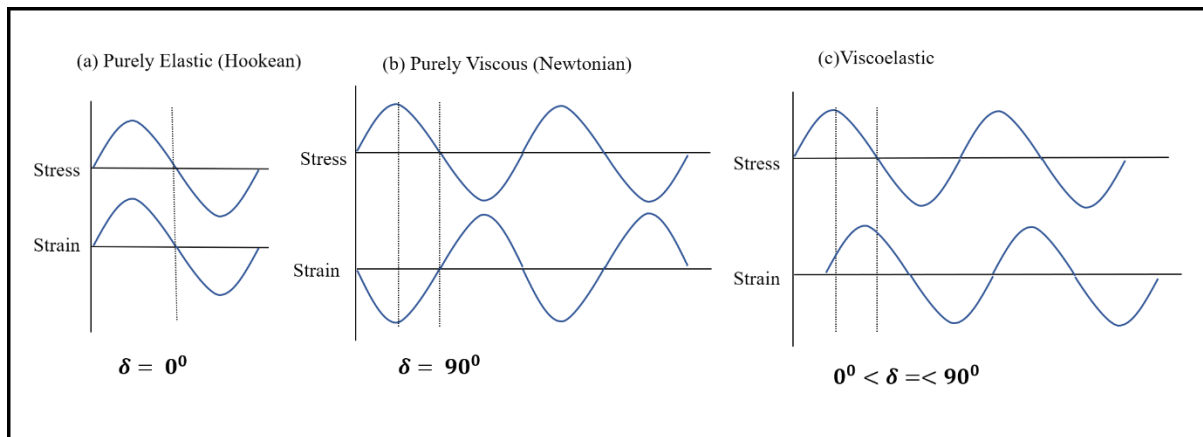
**Fig. 2.14:** How elasticity, viscosity and viscoelastic is different.

Shear applied on the fluid substance deforms continuously. Intuitively, Complex fluid do not hold Hooke's law of elasticity or Newton's law [Rudraraju, 2005].

1. Newtonian fluid

2. Non- Newtonian fluid

Newtonian fluid are fluids which follow Newton's law of flow for example water and Non-Newtonian fluid are those which don't follow the law such as paint, clay, polymers solutions etc. To study the flow and deformation stress or strain-controlled Rheometer (Fig. 2.18) is used. For different shear rates viscosity of fluids is measured. Apart from that viscoelastic properties of materials like sols, gels and coacervates are also measured.

The established Relations in rheology given as,

$$\frac{\text{Stress}}{\text{Strain}} = \text{Modulus} \tag{2.12}$$

$$\frac{\text{Stress}}{\text{Shear rate}} = \text{Viscosity} \tag{2.13}$$

In the thesis an oscillatory mode or sinusoidal mode of deformation is applied on the soft materials. The material response is measured corresponding to the applied stress or strain on

the sample. The phase angle or shift with respect of the deformation and response of the sample is monitored.

**Viscoelastic Parameters:**

Viscoelastic properties of soft material are defined by following parameters, the Complex Modulus G*: It is defined by total resistance to the deformation or of the material [De Vicente, 2012].

i.e.
$$G^* = \frac{\text{Stress}^*}{\text{Strain}}$$
(2.14)

It is mathematically given by,

$$G^* = G' + i\ G''$$
(2.15)

Where G' defines the elasticity of materials and also called as storage modulus It is the ability of soft material to store an energy.

$$G' = (\text{stress}^*/\text{strain})\ \cos\theta$$
(2.16)

G'' is viscous or loss modulus which defines ability of the material to dissipate energy.

$$G'' = (\text{stress}^*/\text{strain})\ \sin\theta$$
(2.17)

The ratio of G'' and G' is tan delta which is measure of material damping – such as vibration or sound damping and given as

$$\tan\ \delta = \frac{G''}{G'}$$
(2.18)

Typical response of $G'$ and $G''$ with respect to frequency and how it differentiate in different regions shown in Fig. 2.15.
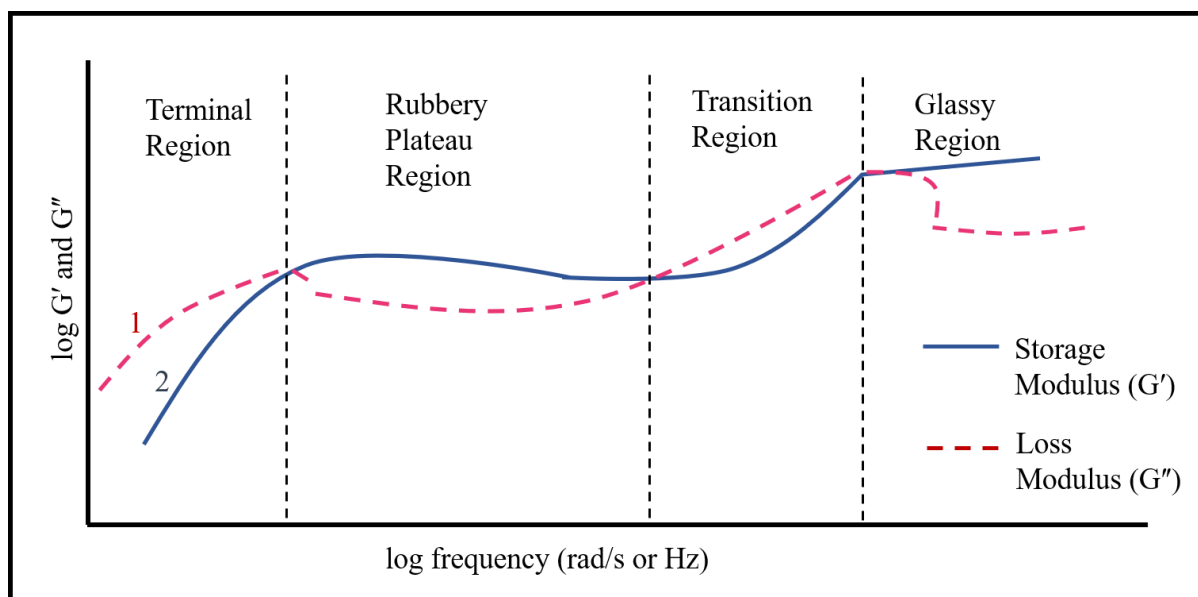
**Fig. 2.15:** Typical variation of G′ and G″ with respect to frequency and distinguish different regions.

The temperature dependence of the elastic moduli for coacervate and gel samples measured at a fixed frequency of 1 rad s$^{-1}$ using a temperature ramp of 1 $^0$C/ min. Isochronal temperature sweep protocol was used to collect this data for temperature sweep experiments. This experiment gives the characteristics thermal transitions of the sample. A typical plot of G' and G" as a function of temperature shown in Fig. 2.16.
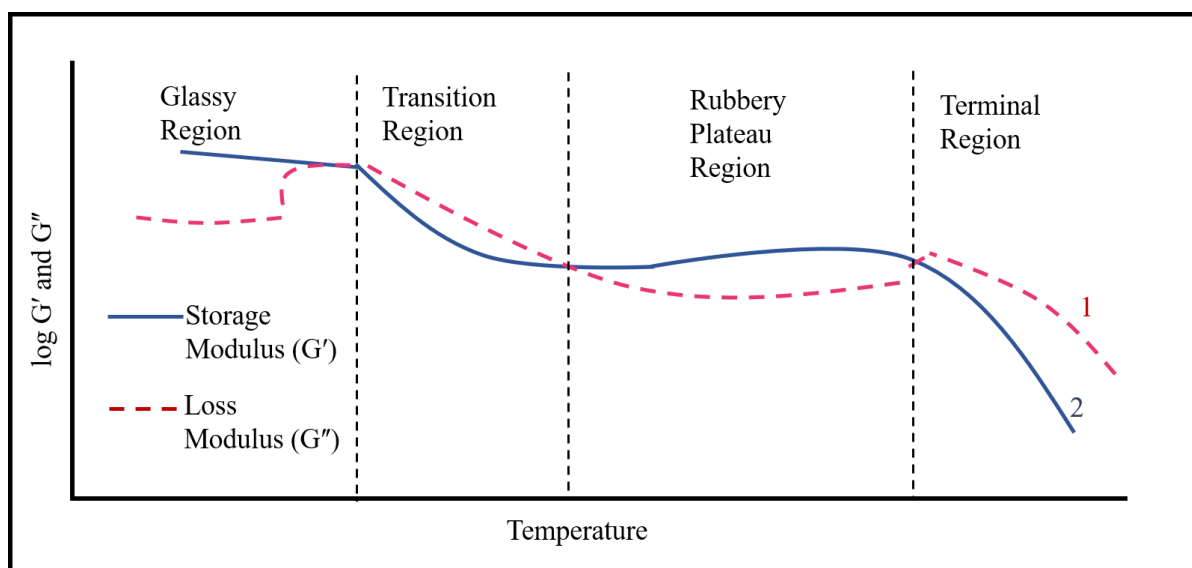


**Fig. 2.16:** Typical graph of variation of G' and G" with temperature.

In this thesis rheology experiment were performed on AR-500 (TA Instruments, UK) stress-controlled rheometer as shown in Fig. 2. 17 with cone plate $2^0$ and 40 mm diameter.
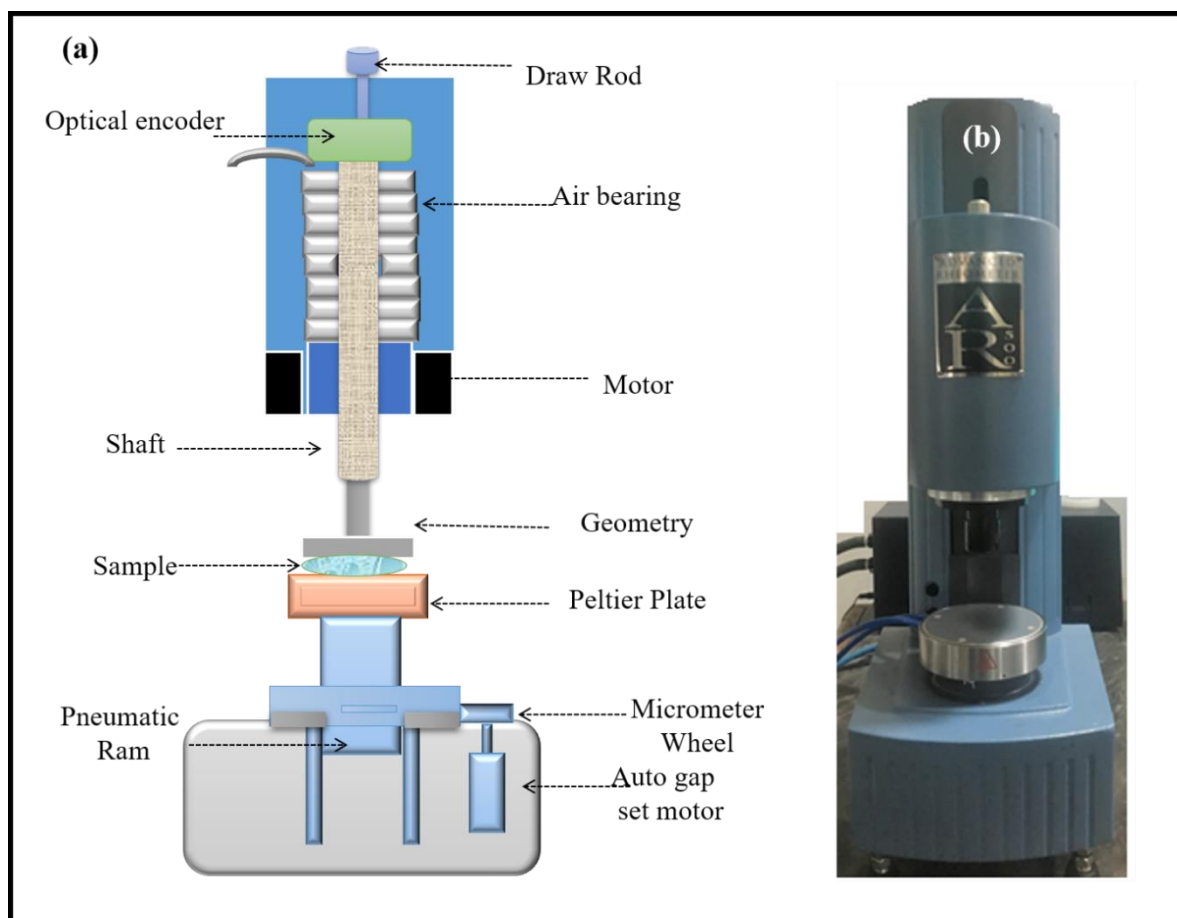


**Fig. 2.17:** (a) Schematic diagram and photo of AR-500 rheometer.

## 2.2.5 VISCOSITY

Viscosity is the resistance of a fluid to flow. When a molecule is flowing the molecule experiences experience friction due to interaction between them. Different fluids with different viscosities flow with different speed when similar force applied to them. Force required to induce movement will be larger for more viscous fluids. Viscosity is an important parameter for any process involves fluid flow. Viscosity is also help into determine how much energy required to pump out process of fluid. It also helps to determine structure of molecule such as proteins in a solution and also in determining the force required to inject a new drug

formulation. In this thesis viscometer also used to determine associative kinetics of gelation and coacervation. To probe these, I used Sine-wave Vibro SV-10 viscometer by A & D company, Japan. The schematic and physical image of Vibro SV-10 is shown in Fig. 2.18. It detects the necessary electric current to resonate the sensor plate with constant frequency 30 Hz to measure viscosity.
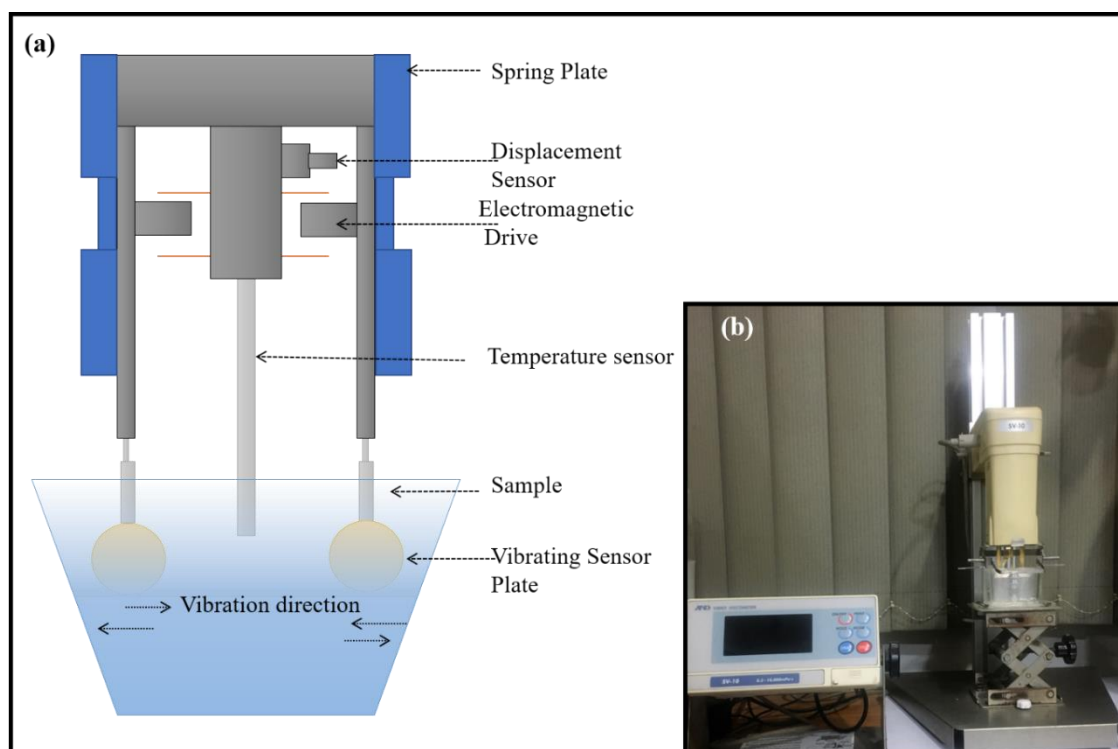


**Fig. 2.18:** (a) working schematic and (b) photo image of Vibro SV-10 viscometer.

### 2.2.6 ELECTROPHORESIS

The phenomenon of movement of charged particle under influence of electric field is called electrophoresis. When electric field applied the charged particle dispersed in solvent and move with certain velocity and potential and this measured potential is called zeta potential. The net effective charge or net surface charge on any polymer complex or colloidal solution termed as zeta potential. The magnitude of zeta potential tells about the stability of the system, particle with zeta potential above -30 mV and +30 mV considered most stable i.e. stability of

the dispersion was found to be higher while electrostatic build up is relaxed with zeta potential approaching to zero which allows aggregation. Basically, zeta potential is the quantification of the charge by measuring electrophoretic mobility which is related to the surface charge [Oshima, 1995; Hunter, 1988].

In zeta potential measurement, pH plays an important role. Isoelectric point is the point of pH at which net surface charge on the particle in the solution is zero. The distribution of net charge near the interfacial region affected by the net charge developed on particles dispersed in the solution. Near the interfacial region of charged particles, counter ions attached to oppositely charged particle and termed as Stern layer as shown in Fig. 2.19. The counter ions and the small amount of charged particle with similar polarity gets distributed diffusively from a farther distance from stern layer. Shear plane differentiate the other region from where counter ions and co-ions arranged consistently.

As we know zeta potential measurement depends upon the electric field applied between sample and the recorded particles movement due to the scattering of the particles. Henry's equation [Oshima, 1995; Smoluchowski, 1918] apply to determine zeta potential ($\zeta$) by using velocity of particle recorded and called as electrophoretic mobility ($\mu$),

$$\mu = \frac{2\varepsilon\zeta f(ka)}{3\eta}$$

where $f(ka), \varepsilon$ and $\eta$ are Henry's function with Debye length (k) and ratio of particle radius, dielectric constant and absolute zero shear velocity of the medium respectively.
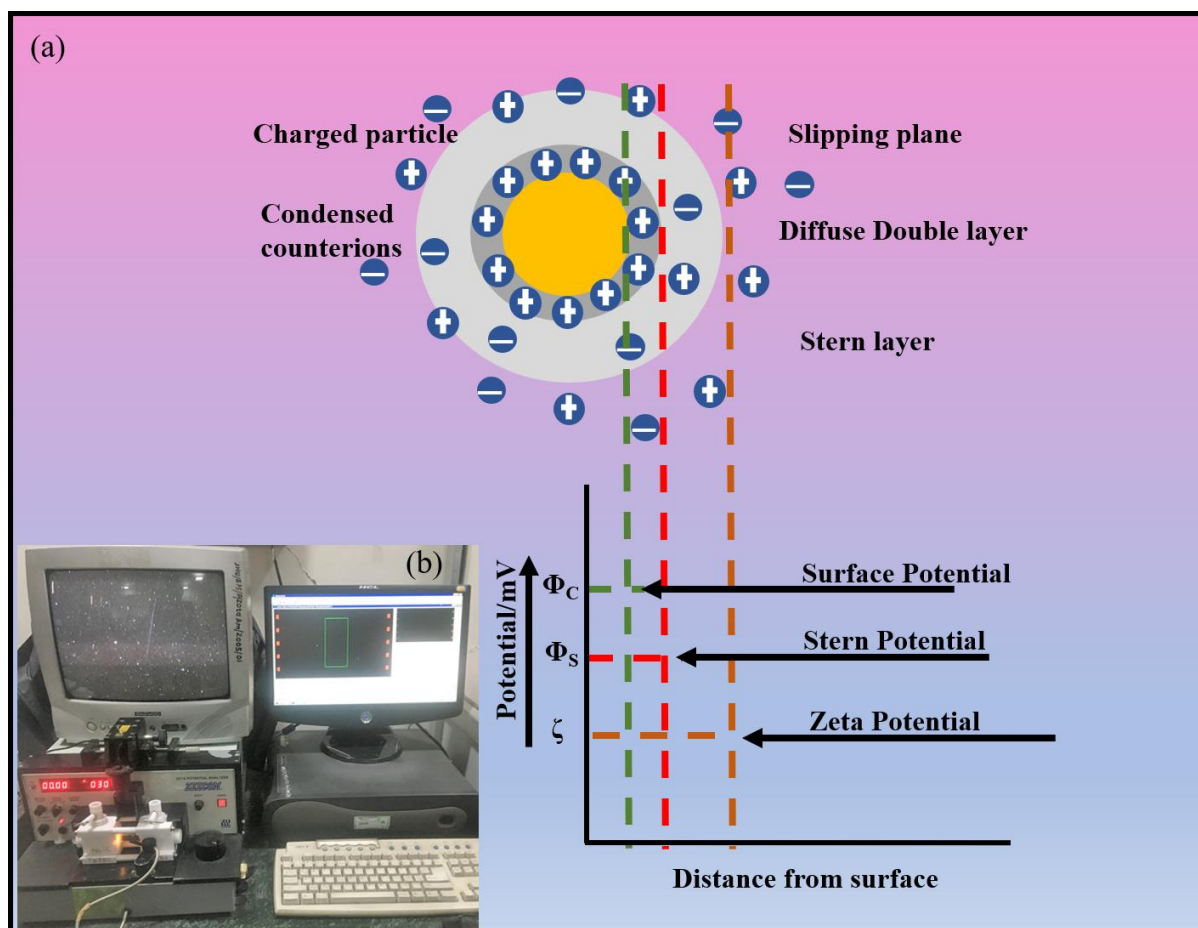
**Fig. 2.19:** (a) Double layer diagram with different potentials. (b) Zeecom, ZC-2000 image.

Instrument used in this thesis for zeta potential measurement were Zeecom, ZC-2000, Microtec, Japan as shown in Fig. 2.19 (b). It consists of molybdenum (+) and platinum (-) electrodes. The cell chamber tap on molybdenum electrode was kept open to avoid or release the air bubbles so as to reduce bubble effect on particle movement during the measurement. The requirement for sample preparation is that sample should be very diluted with deionized water so that particles don't form aggregates.

**2.2.7 REFERENCES**

1. Abou, B., Bonn, D. & Meunier, J. (2001). *Phys. Rev. E,* 64, 021510-1-6.

2. Aswal, V. K., & Goyal, P. S. (2000). Small-angle neutron scattering diffractometer at Dhruva reactor. *Current Science*, *79*(7), 947-953.

3. Barnes, H. A. (2000). *A handbook of elementary rheology*. University of Wales, Institute of Non-Newtonian Fluid Mechanics.

4. Benedek, G. B. (1968). Thermal fluctuations and Scattering of light, lectures at Brandeis Summer Institute for Theoretical Physics.

5. Berne, B. J., & Pecora, R. (2000). *Dynamic light scattering: with applications to chemistry, biology, and physics*. Courier Corporation.

6. Berne, B. J., & Pecora, R. (2000). *Dynamic light scattering: with applications to chemistry, biology, and physics*. Courier Corporation.

7. Bohidar, H. B., & Mohanty, B. (2004). Anomalous self-assembly of gelatin in ethanol-water marginal solvent. *Physical Review E*, *69*(2), 021902.

8. Boral S., & Bohidar H.B (2010). Effect of Ionic Strength on Surface-Selective Patch Binding-Induced Phase Separation and Coacervation in Similarly Charged Gelatin−Agar Molecular Systems. *The Journal of Physical Chemistry B*, 114(37), 12027-12035.

9. Brown, W. (1992). Laser light scattering in biochemistry: SE Harding, DB Sattelle and VA Bloomfield, Editors. Royal Society of Chemistry (Information Services).

10. Brown, W. (1992). Laser light scattering in biochemistry: SE Harding, DB Sattelle and VA Bloomfield, Editors. Royal Society of Chemistry (Information Services, 1992).

11. Burchard, W., Schmidt M., & Stockmayer, W.H. (1980). Macromolecular, **13**, 1264.

12. Cheng, X. X., Lui, Y., Zhou, B., Xiao, X. H., & Liu, Y. (2009). Probing the binding sites and the effect of berbamine on the structure of bovine serum albumin. *Spectrochimica Acta Part A: Molecular and Biomolecular Spectroscopy*, *72*(5), 922-928.

13. Chu, B. (1974). Laser Light Scattering Academic Press. *New York*.

14. Colthup, N.B., Daly, L.H., & Wiberley, S.E. (1975). Introduction to Infrared and Raman spectroscopy, Academic Press. Inc., New York.

15. Coviello, T., Burchard, W., Geissler, E., & Maier, D. (1997). Static and dynamic light scattering by a thermoreversible gel from Rhizobium leguminosarum 8002 exopolysaccharide. *Macromolecules*, *30*(7), 2008-2015.

16. de Gennes, P. G. (1985). Scaling concepts in polymer physics 2nd ed Cornell Univeristy Press. *Ithaca, NY*.

17. De Vicente, J. (Ed.). (2012). *Rheology*. BoD–Books on Demand.

18. Debye, P., & Bueche, A. M. (1949). Scattering by an inhomogeneous solid. *Journal of Applied Physics*, *20*(6), 518-525.

19. Djabourov M., Clark A.H., Rowlands D.W., & Ross-Murphy S.B. (1989). Small-angle x-ray scattering characterization of agarose sols and gels. *Macromolecules*, 22(1), 180-188.

20. Giessibl, F. J. (2003). Advances in atomic force microscopy. *Reviews of modern physics*, *75*(3), 949.

21. Goodhew, P. J., Humphreys, J., & Beanland, R. (2014). *Electron microscopy and analysis*. CRC Press.

22. Hunter, R. J. (1988). Zeta Potential in colloid science: Principles and applications, San Diego: Academic Press.

23. Joshi, N., Rawat, K., & Bohidar, H. B. (2016). Influence of Structure, Charge, and Concentration on the Pectin–Calcium–Surfactant Complexes. *The Journal of Physical Chemistry B*, *120*(18), 4249-4257.

24. Kantor, Y., & Webman, I. (1985). *Phys. Rev. Lett.,* 152, 1891-1894.

25. Kaushik, P., Rawat, K., & Bohidar, H. B. (2019). Heat-induced coacervation of elastin and its possible thermoreversibility. *Colloid and Polymer Science*, 1-10.

26. Kohlbrecher, J., & Wagner, W. (2000). The new SANS instrument at the Swiss spallation source SINQ. *Journal of applied crystallography*, *33*(3), 804-806.

27. Krall, A.H., & Weitz, D.A. (1998). *Phys. Rev. Lett.*, 82, 1064-1069.

28. Krall, A.H., Huang, Z., & Weitz, D.A. (1997). *Physics A*, 235, 19-37.

29. Lankchowick, J. R. (2002). *Principle of Fluorescence Spectroscopy*, 2nd edn. Kluwer Academic/Plenum, New York.

30. Li, Y., Xia, Q., Shi, K., & Huang, Q. (2011). Scaling behaviors of α-zein in acetic acid solutions. *The Journal of Physical Chemistry B*, *115*(32), 9695-9702.

31. Lovesey, S. W. (1984). Theory of neutron scattering from condensed matter.

32. Meijering, E., Jacob, M., Sarria, J. C., Steiner, P., Hirling, H., & Unser, M. (2004). Design and validation of a tool for neurite tracing and analysis in fluorescence microscopy images. *Cytometry Part A: the journal of the International Society for Analytical Cytology*, *58*(2), 167-176.

33. Ohshima, H. (1995). Electrophopretic mobility of soft particles. *Electrophoresis*, *16*(1), 1360-1363.

34. Okana, K., Wada, E., Kurita, K., & Fukuro, H. (1978). "Small-angle X-ray scattering by polymer solutions at intermediate concentrations." *Journal of Applied Crystallography* 11, no. 5, 507-510.

35. Pandey P.K., Kaushik P., Rawat K., Aswal V.K., & Bohidar H.B. (2017). Solvent hydrophobicity induced complex coacervation of dsDNA and in situ formed zein nanoparticles. *Soft Matter*, 13(38), 6784-6791.

36. Potanin, A., Rheol. J. (2004). (N. Y. N. Y). 48, 1279.

37. Pusey, P. N., & Van Megen, W. (1989). Dynamic light scattering by non-ergodic media. *Physica A: Statistical Mechanics and its Applications*, *157*(2), 705-741.

38. Ravindranath, S., & Wang, S. Q. (2008). Steady state measurements in stress plateau region of entangled polymer solutions: Controlled-rate and controlled-stress modes. *Journal of Rheology*, *52*(4), 957-980.

39. Rudraraju, V. S., & Wyandt, C. M. (2005). Rheological characterization of Microcrystalline Cellulose/Sodiumcarboxymethyl cellulose hydrogels using a controlled stress rheometer: part I. *International journal of pharmaceutics*, *292*(1-2), 53-61.

40. Rudraraju, V. S., & Wyandt, C. M. (2005). Rheology of microcrystalline cellulose and sodiumcarboxymethyl cellulose hydrogels using a controlled stress rheometer: part II. *International journal of pharmaceutics*, *292*(1-2), 63-73.

41. Smoluchowski, M. V. (1918). Attempt at a mathematical theory of coagulation kinetics colloidal solutions. *Journal of Physical Chemistry*, *92*(1), 129-168.

42. Squires, G. L. (1987). *Thermal Neutron Scattering*, Cambridge University Press, Cambridge.

43. Swinehart, D. F. (1962). The beer-lambert law. *Journal of chemical education*, *39*(7), 333.

44. Ventura, I., Jammal, J. and Bianco-Peled, H., 2013. Insights into the nanostructure of low-methoxyl Pectin–calcium gels. *Carbohydrate polymers*, *97*(2), pp.650-658.

45. Zhong Q., and M. Jin, Zein nanoparticles produced by liquid–liquid dispersion, *Food Hydrocoll.* 2009, **23**, 2380-2387.

CHAPTER 3

INTERACTION OF ZEIN NANOPARTICLES WITH DIFFERENT

POLYECTROLYTES



**OVERVIEW**

A comprehensive investigation was carried out to probe the dispersion and aggregation profile of hydrophobic protein, zein, in ethanolic solutions at pH=4 close to its isoelectric pH (=6.2). Study of the different phases resulting from interaction of in-situ formed zein nanoparticles with different polyelectrolyte using various techniques is discussed in this chapter.
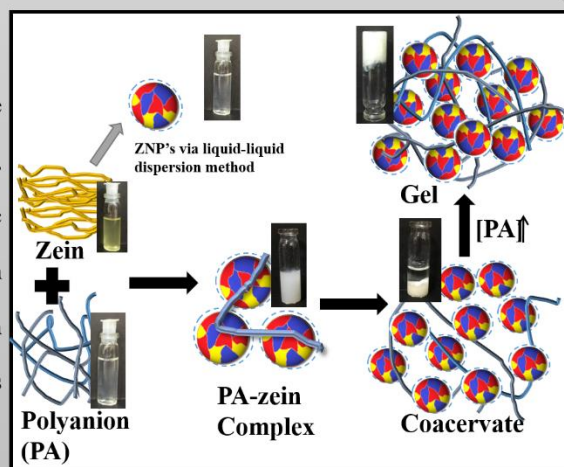
[PART-A]

## 3.1 ANOMALOUS DISPERSION AND HYDROPHOBIC AGGREGATION OF ZEIN NANOPARTICLES

### 3.1.1   MOTIVATION

The hydrophobic biopolymer zein is briefly discussed in Chapter 1. Zein has poor water solubility giving rise to a comprehensive dispersion state, which has motivated this work. In the Section 3.1 of this chapter, an extensive investigation pertaining to the dispersion phase

stability of this protein in ethanolic solution is reported. Results revealed a remarkable linear dependence of nanoparticle size and zeta potential, and its solution viscosity with ethanol content. This anomalous dispersion attribute makes this protein uniquely placed as an out of the box biomolecule.

## 3.1.2   SAMPLE PREPARATION

Maize protein zein nanoparticle was prepared by liquid-liquid dispersion method. Zein stock solution of 2% w/v was prepared by dissolving zein powder in ethanol: water (80:20) binary solvent. Then required amount of zein stock were added in double distilled water in one shot keeping final volume constant for different solvent concentration, at room temperature ($25^0$ C).

## 3.1.3. TURBIDIMITRIC TITRATION

A stock solution of 1.5 % (w/v) zein was prepared in 80:20 % (v/v) ethanol: water binary solvent at room temperature by mixing appropriate amount of protein powder in the binary solvent, and stirring it for 10 min. This clear solution had a pH of 4. This solution was titrated with water and the solution turbidity 100-%T, T being transmittance, was monitored at 400 nm continuously. This titration profile is depicted in Fig. 3.1 which is marked by four characteristic transition points in terms of the volume of alcohol present in the solution $C_{EOH}$ that corresponded to the first occurrence of turbidity at $C_{EOH-C}$=9 % (v/v), point of sharp rise in turbidity at $C_{EOH-\phi}$ =18 % (v/v) followed by observation of maximum turbidity at $C_{EOH-max}$ =35 % (v/v). Addition of more alcohol drove the system towards liquid-solid phase separation at $C_{EOH-Prep}$ = 40 % (v/v). Values of $C_{EOH-C}$, $C_{EOH-\phi}$ and $C_{EOH-Prep}$ characterized the initiation of intramolecular folding (nanoparticle formation), and intermolecular soluble aggregate formation (nanoparticle aggregates), and the subsequent insoluble micro-aggregate (microparticle) formation, respectively which was evidenced from particle size measurements done by DLS and SEM.
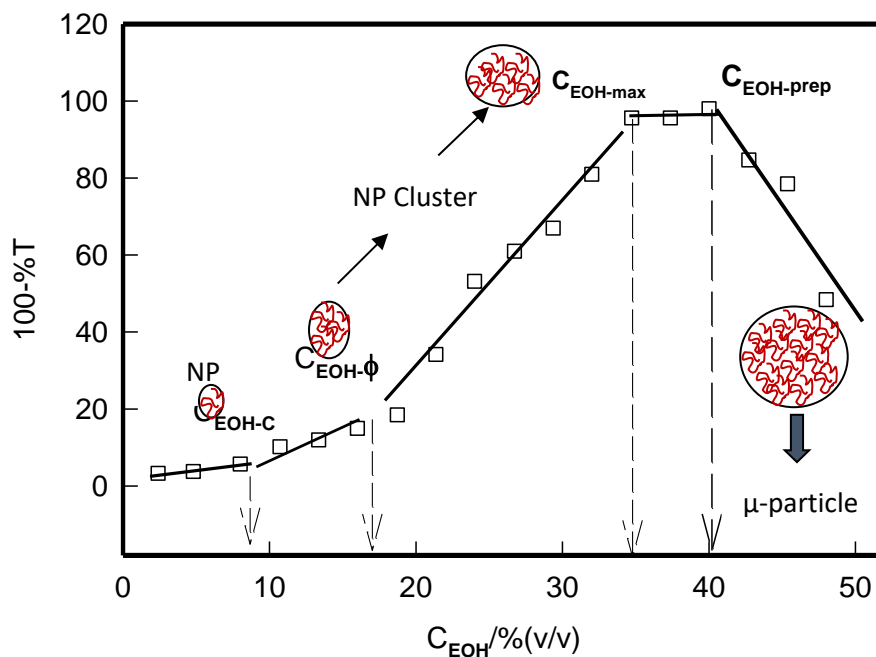
**Fig. 3.1:** Turbidity profile for zein dispersion at different ethanol concentrations measured at room temperature. Solid lines are to guide to the eye. $C_{EOH-C}$, $C_{EOH-\phi}$, $C_{EOH-max}$ and $C_{EOH-Prep}$ characterize the initiation of intramolecular folding (nanoparticle (NP) formation), and intermolecular soluble cluster formation, formation of largest size of clusters, and the subsequent insoluble micro-particle formation, respectively.

Further, these samples were monitored for changes in their solvent viscosity and electrophoretic mobility. A remarkable event was noticed here, as the ethanol concentration increased, the hydrodynamic radius of zein nanoparticles also increased from ~ 65 nm to 130 nm almost linearly (Fig. 3.2). It needs to be noted that after $C_{EOH-Prep}$ liquid-solid phase separation occurred and microparticles were precipitated from the dispersion. Thus, the largest size particles detected did not exceed, typically 130 nm (measurements were done using the supernatant). Secondly, because of increase in ethanol concentration, the zein content changed automatically (Fig. 3.2). Thus, we have a complex situation where ethanol and zein concentrations are tied up intrinsically which in turn drove protein aggregation.
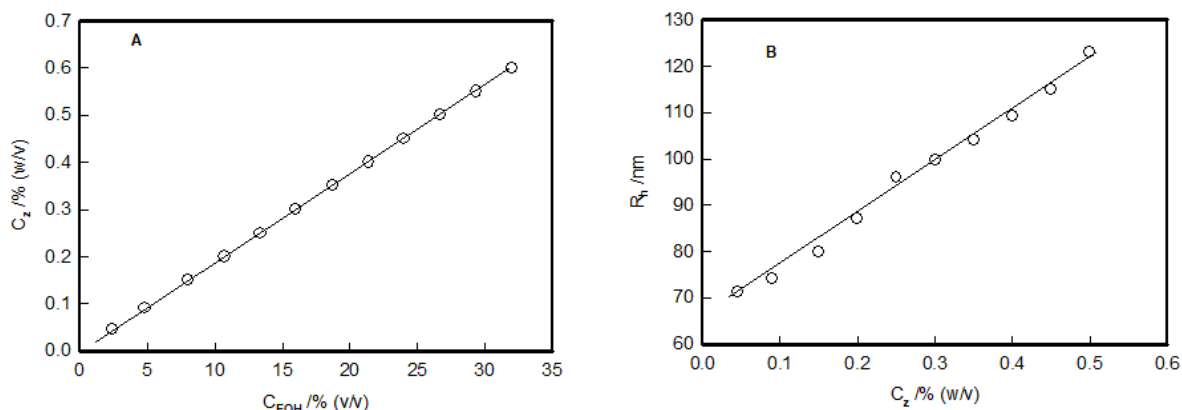
**Fig. 3.2:** Plot (A) shows simultaneous variation of zein and ethanol content, and (B) its effect on hydrodynamic radius of protein aggregates. Notice the linearity.

The three-way correlation between zein and ethanol concentration, and particle size which is depicted in Fig. 3.2. The least squares fitting of the data yielded the following relations

$$R_h(C_z) = 65 + 114C_z \tag{3.1}$$

Where $R_h$ is in nm and $C_z$ is in %, and the chi-squared value was =0.98.

And

$$C_z(C_{EOH}) = 0.02C_{EOH} \tag{3.2}$$

Thus, it was possible to predict the size of the nanoparticles either from ethanol, or protein concentration.

### 3.1.4 RESULTS AND DISCUSSION

Zein is a hydrophobic protein insoluble in water. But it is soluble in ethanolic solvent in the alcohol concentration range of 5-40 % (v/v), judged from the visual absence of suspended particulates. The ethanolic solution constitutes a marginal solvent for this protein. When a stock solution of zein was dispersed into bulk deionized water, the stock solution is sheared into small droplets due to change in the solvent environment from marginal to poor. As ethanol and water have excellent miscibility so ethanol in the dispersed droplets partitions into the bulk water, and selective solvent attrition closer to protein surface was possible. Zein becomes

insoluble and precipitates in the form of nanoparticles because the ethanol concentration in the dispersion decreases below the solubilization limit of zein. Clearly, zein nanoparticles were produced by the solvent coarsening method. During nanoparticle formation, there are three competing mechanisms: (i) stock solution breaks up into droplets by the shear force leading to intramolecular folding, (ii) solidification of zein during solvent attrition caused by interparticle clustering, and (iii) ''coalescence'' or ''partial coalescence'' of droplets in to large microparticles. We have identified the ethanol concentrations at which these phenomena occurred as $C_{EOH-C}$, $C_{EOH-\phi}$ and $C_{EOH-max}$, respectively. The relevance of these are evident from the titration profile shown in Fig. 3.1. This is further elaborated in the schematic shown in Fig. 3.3.
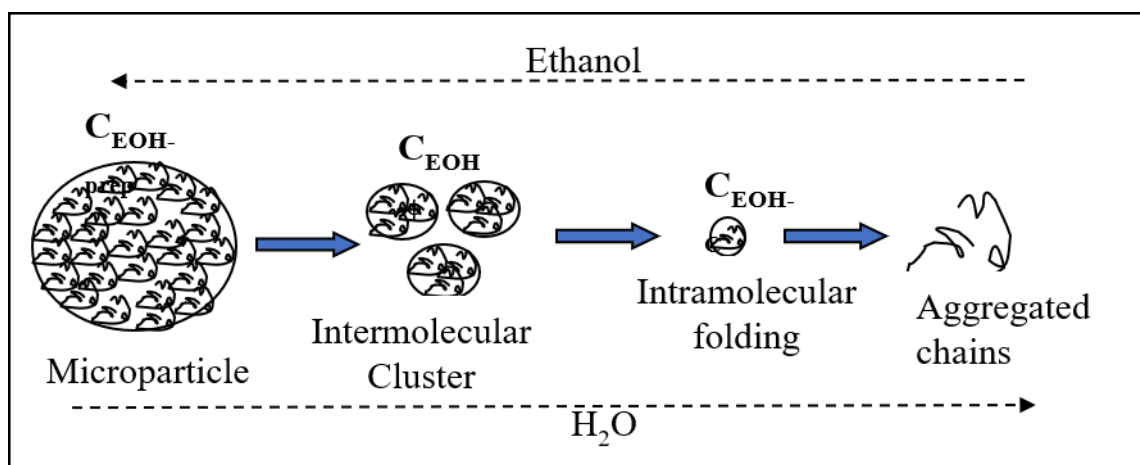


**Fig. 3.3:** Zein microparticle dispersion made in 80% (v/v) ethanolic solution get sheared into smaller nanosize clusters on exposure to water environment due to solvent coarsening followed by further dissociation of these clusters into monomeric nanoparticles. The propensity of alcohol and water hydrogen bonding on increase of water concentration reduces the solubility of zein.

It needs to be clarified that the typical size of a zein molecule should not exceed 5-6 nm (assuming it to be a sphere with a partial specific volume ~ 0.73 cc/g and molecular weight ≈ 19 kDa). In the low $C_{EOH}$ region, due to excessive depletion of water molecules near the hydrophobic surface of the protein and poor hydration provided by ethanol, the zein molecules

(chains) aggregate driven by hydrophobic interactions. Therefore, an aggregated chain is formed where the individual chains are indistinguishable. At $C_{EOH-c}$ this chain cluster collapse into a compact nanoparticle, which has been referred to as intramolecular folding. In contrast, at $C_{EOH-\phi}$ cluster aggregation is envisaged.

### 3.1.4.1 PHYSICAL PROPERTIES

Particle size of zein nanoparticles, and their polydispersity behavior in the dispersion state was measured by DLS technique using freshly prepared samples, where the ethanol concentration was varied between 5-30%. This data is presented in Fig. 3.4 (A) where excellent linearity between ethanol concentration and apparent particle size $R_h$ is manifested. The PDI values were within $0.20\pm 0.03$ in all cases. The corresponding zeta potential $\zeta$ data is depicted in Fig.3. 4(B). Here too an excellent linear dependence of zeta potential on ethanol content is noticed.

The data shown in Fig. 3.4 could be described through the following linear eqns (chi-squared >0.98)

$$R_h(C_{EOH}) = 65 + 2.13C_{EOH} \tag{3.3}$$

And

$$\zeta(C_{EOH}) = 0.75 + 19C_{EOH} \tag{3.4}$$

A comparison between eqns. (3.1) and (3.3) indicates that the slopes are identical, the consequent correlation is shown in Fig. 3.2(A). Let us peruse the relevance of eqn. (3.4). For a spherical particle of radius $R_h$, the translational diffusion coefficient $D_T$ is given by the Stokes-Einstein relation [Barnes, 1976; Bohidar, 2014]

$$D_T = \frac{K_B T}{6\pi\eta_0 R_h} \tag{3.5}$$

where $K_B$ is Boltzmann constant, T is absolute temperature, and $\eta_0$ is solvent viscosity. In the Smoluchowski formalism, such a uniformly charged particle with surface charge Q will exhibit an electrophoretic mobility $\mu$ given by [Ohshima, 1995]

$$\mu = \frac{Q}{6\pi\eta_0 R_h} \qquad (3.6)$$

Hence, one obtains

$$\frac{D_T}{\mu} = \frac{K_B T}{Q} \qquad (3.7)$$
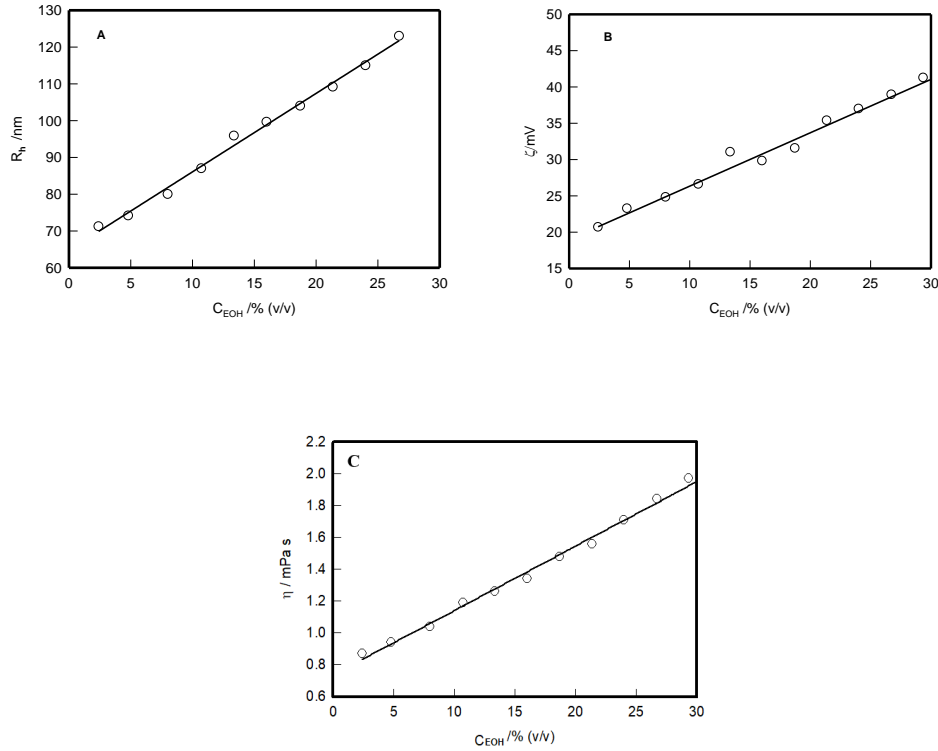


**Fig. 3.4:** Plot (A) shows variation of apparent hydrodynamic radius with ethanol content, (B) represents the same for zeta potential, and (C) for solution viscosity. Notice the linearity.

It has been shown that, to a very good approximation, the surface potential can be determined from the electrostatic potential existing at the hydrodynamic slip plane, i.e. the zeta potential. The relationship between the mobility $\mu$ and the zeta potential is then given by [Barnes, 1976; Bohidar, 2014]

$$\zeta = 4\pi \ (\mu\eta_0/\varepsilon) \qquad (3.8)$$

where $\varepsilon$ is the dielectric constant of the medium. For a given system, the ratio $(K_B T/Q)$ is constant. Hence, one has

$$D_T \sim \mu \sim \zeta \qquad (3.9)$$

This implies that

$$R_h \sim \frac{1}{\zeta} \tag{3.10}$$

Interestingly, the data shown in Fig. 3.4 implies a direct linear relationship between size and zeta potential contrary to the prediction of eqn. (3.10). Therefore, the observed behavior was anomalous. This discrepancy may be arising from the nano size effect. Smoluchowski description used here applies mostly to colloidal particles of size on the order of microns.

Fig. 3.4(C) depicts the dependence of solution viscosity $\eta$ on ethanol concentration. Here again, we noticed a remarkable linear dependence defined by (chi-squared >0.97)

$$\eta(C_{EOH}) = 0.75 + 0.04C_{EOH} \tag{3.11}$$

For a impenetrable hard sphere of molecular mass M, and radius of gyration $R_g$ the solution viscosity $\eta$ follows the universal scaling applicable for a theta solvent which is given by [Bohidar, 2014],

$$\eta \sim M^{3\upsilon-1} \sim M^{0.5}; (\upsilon = 0.5) \tag{3.12}$$

Since, $R_g \sim M^{0.5}$ (for a theta solvent), one immediately obtains

$$\eta \sim R_g \sim R_h \tag{3.13}$$

Further according to eqn. (3.3), $R_h$ is directly proportional to $C_{EOH,}$ therefore the relationship shown by eqn. (3.11) is obvious. This concludes that these particles were hard spheres in their dispersion state in ethanolic solvent, and the solvent was close to a poor solvent.

### 3.1.4.2 SURFACE MORPHOLOGY

The SEM images of some selected samples are depicted in Fig.3.5. Most nanoparticles were of spherical morphology and had diameters less than 130 nm when ethanol concentration was close to $C_{EOH-C}$ (intramolecular folding of protein molecule, Fig. 3.5(A)). While the mean size of aggregated particles was found to be close to 200 nm at $C_{EOH-\varphi}$ (inter particle clusters, Fig. 3.5(B)). Most of the particles were aggregated, and also were interconnected in this case. Physically, stock solutions are sheared to large droplets at a higher ethanol concentration that

should correspond to larger particles after zein solidification [Wang et al, 2011; Chen et al, 2015]. Increasing the concentration of protein in the droplet promotes the entanglement of its chains, which impedes droplet fission and leads to the formation of much larger aggregated particles at $C_{EOH-max}$ (Fig. 3.5(c)). Compact particles have been associated with small droplet size [Wang et al, 2011; Chen et al, 2015] and a low concentration of solutes consistent with our observations.
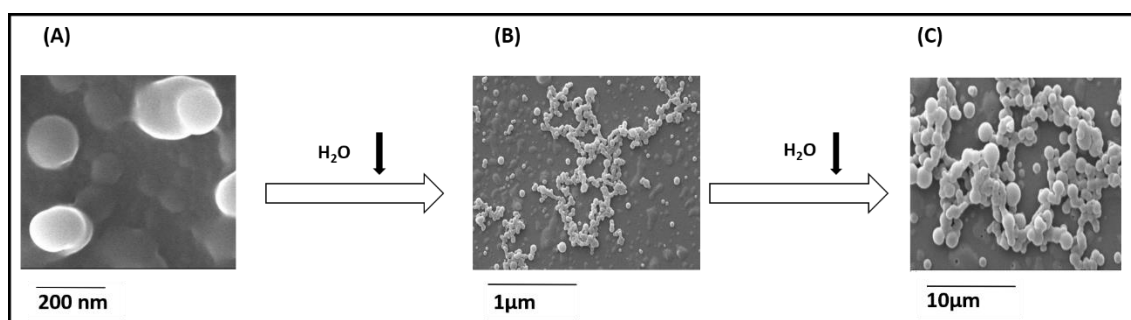


**Fig. 3.5:** SEM images showing effect of ethanol concentration on size and assembly of zein nanoparticles at $C_{EOH-C}$(A), $C_{EOH-\phi}$(B), and $C_{EOH-max}$ (C).

### 3.1.4.3 EFFECT ON SECONDARY STRUCTURE

In the next step it was felt necessary to evaluate the effect of ethanol hydration on the secondary structure of the protein. For this, the samples were probed by circular dichroism spectroscopy. This data was deconvoluted to determine their α-helix, β-sheet and random coil contents (Fig. 3.6).

A perusal of this data clearly indicated the following: (i) the helical content was about 82 % below $C_{EOH-C}$ which gradually increased to more than 95 % at $C_{EOH-\phi}$, and remained invariant thereafter, (ii) the individual contributions from β-sheet and random coil conformations remained < 10 % all throughout, and (iii) as the solvent environment became more hydrophobic (increased ethanol content) the secondary structure of the protein increased significantly. Therefore, solvent hydrophobicity induced protein folding, a conclusion, clearly evident from this data.
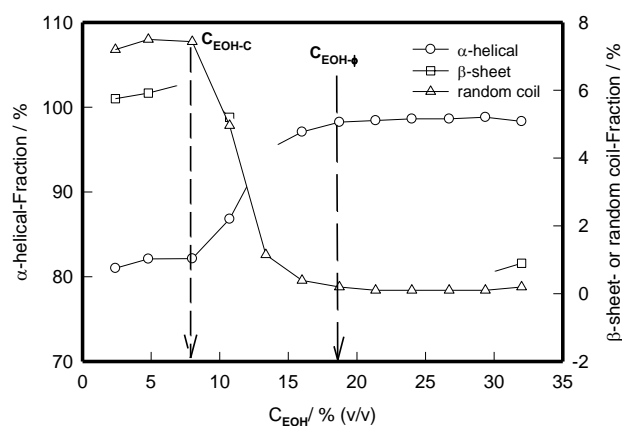
**Fig. 3.6:** Dependence of secondary structure (helicity) of the protein on ethanol concentration determined at room temperature. Solid lines tare guide to eye only.

### 3.1.4.4 HYDROPHOBIC AGGREGATION

Protein purification is an industrially challenging problem. One of the popular methods constitutes precipitation closer to the pI of the protein. For hydrophobic proteins, the challenge is deeper. For instance, hydrophobic interaction chromatography has not yet been reported as a tool for purifying these proteins, but due to their dominant hydrophobic properties, it seems an interesting option. However, the evaluation of several matrices and working conditions did not allow the separation of the mixed zeins. Instead, protein aggregation becomes a barrier due to dominant hydrophobic surfaces that often interact strongly with the support matrix. The lack of a clear profiling of hydrophobic aggregation of this protein has somewhat reduced its application potential although several mechanisms have been adopted in the past to overcome these obstacles [Wang et al, 2005; Cheng et al, 2010; Wang et al, 2010; Li et al, 2014].

It is important to note that in the solvent coarsening process used in this work, the particle morphology change could be divided into two stages: the first one is the nanoparticle formation, which is modeled as chain collapse in predominantly aqueous poor solvent environment, and the second one is the clustering of these particles in the ethanol-water binary solvent medium. The propensity of hydrophobic residues on this protein molecule requires that there is depletion

of water in its close proximity that is preferentially populated by ethanol molecules. Thus, on changing the solvent environment from poor to marginal, we noticed hydrophobic aggregation of zein particles. But, when the ethanol concentration reached ~45%, a clear liquid-solid phase separation was noticed which is due to the optimum hydrogen bonding between this alcohol and water [Waller, 1996; Bohidar et al, 2014]. In an earlier work involving polyampholyte protein gelatin B, we noticed a similar behavior with the system showing a distinctive liquid-liquid phase separation [Bohidar et al, 2014]. In the Timasheff formalism of hydrophobic solvation of proteins, a clear water depletion region closer to protein molecule was argued for [Gekko et al, 1981]. Therefore, the anomalous dispersion stability displayed by this protein owes its origin to selective hydrophobic salvation.

### 3.1.5 CONCLUSION

The coherent picture that emerged from the data in hand indicated that predominantly hydrophobic hydration provided by the presence of ethanol in the binary solvent was responsible for giving stability to the protein dispersion. When the ethanol concentration was systematically increased up to 40%, there was concomitant increase in the solvent hydrophobicity that allowed more solubility to zein. This facilitated protein aggregation. However, when the ethanol concentration reached about 40%, the maximum hydrogen bonding between the two solvents prevailed leading to poor hydration of zein clusters. This allowed the clusters to grow further in size to reach microscopic dimension, and eventual precipitation. The remarkable linearity seen between the size, zeta-potential and solution viscosity with ethanol content was anomalous. Considering the use of this unique protein in food preservation and drug delivery applications, the importance of the present study can be hardly stressed.

## 3.2 MIXING RATIO DEPENDENT COMPLEX COACERVATION VERSUS BICONTINUOUS GELATION OF PECTIN AND *IN SITU* FORMED ZEIN NANOPARTICLES

### 3.2.1 MOTIVATION

A comprehensive understanding of coacervation phenomenon in competition with gelation in complementary biopolymers will give rise to generation of a whole new class of hybrid nano-biomaterials. The importance of mapping protein-carbohydrate interaction has bearing on protein purification and downstream processing of proteins and carbohydrates, individually which motivate to study protein-polysaccharide interaction study for different phase state. So, in the section 3.2 of chapter 3, we provide a systematic, and comprehensive study of complex coacervation between pectin and zein under various conditions (ionic strength and mixing ratio) in water-ethanol binary solvent medium. In this interaction protocol, pectin was in polyanionic state while zein was used in its nanoparticle form, which were generated in situ. An array of experimental techniques, such as turbidimitry, UV-visible spectroscopy, electrophoresis, and viscometry methods were used to map the coacervation and gelation pathways. The coacervate/gel materials were characterized for their microstructure by small angle neutron scattering (SANS), and for viscoelastic properties by rheology. This work resides at the interface of nanoscience and soft matter.

### 3.2.2 SAMPLE PREPARATION

Pectin powder (3% (w/v)) was dispersed in distilled water at 40 °C which was maintained under stirring for 4 h to prepare the stock solutions which appeared lightly translucent. The pH of the stock was 4.0±0.2 which did not change upon dilution with water. Biopolymer concentrations are expressed in % (w/v), and solvent concentrations in % (v/v), unless otherwise stated. All procedures were performed at room temperature, 25 °C.

The stock solution of zein was prepared by dispersing 1.5 % (w/v) protein powder in the 80: 20 % (v/v) ethanol: water binary solvent at room temperature under stirring for 10 min; the pH of the stock was 5.4 ±0.2. This preparation had a light-yellow color. A set of solutions with varying pectin concentration was prepared by dilution of the stock solution with the required amount of water keeping the final volume the same (one-shot addition). The required amount of pectin (0.01–2 % (w/v)) from the stock solution was added to the distilled water and then the necessary amount of zein from its stock was added to this solution and stirred for 5min to create a homogeneous dispersion. This had a pH of 4.0 ± 0.2. Two sets of samples were prepared with zein concentrations of 0.1% and 0.5 % (w/v). It needs to be realized that the reaction medium was a 4 and 27 % (v/v) ethanol–water binary mixture for samples containing [zein] = 0.1 and 0.5%, respectively, and all the interactions prevailed in this milieu. Zein molecules assembled into spherical nanoparticles in situ in this dispersion by the well-known liquid–liquid dispersion method. At this stage 20 mM (50 µl ml$^{-1}$) of $CaCl_2$ from 400 mM stock was added to this mixture which led to complex coacervation (for r < 1) or gelation (for r > 1) instantaneously after $CaCl_2$ was added; the $CaCl_2$ concentration was the same in all the samples. Pectin: zein = r was 0.1 to 7.5 for 0.1% zein and 0.02 to 4 for 0.5% (w/v) zein. For a salt (NaCl) dependent study, the required amount of NaCl was added to the solvent DI water to which the required amounts of pectin, zein and $CaCl_2$ were added, from their respective stocks, in that order, followed by stirring. Note NaCl and $CaCl_2$ don't affect the solution pH. Correspondingly, the in situ formed zein nanoparticles had a size of 80 and 120 nm in the reaction medium, respectively. Therefore, one is looking at the interaction between a polyanion (pectin), and (polyampholytic) spherical nanoparticles of zein of two different sizes. Secondly, the gelation concentration of pectin is known to be close to 2% (w/v) in 20 mM $CaCl_2$ [Joshi et al, 2016]. Hence, all the experiments were performed at pectin concentrations less than its gelation value. Zeta potential, turbidity and UV-vis spectroscopy measurements were done on

specially prepared samples which had 20-fold dilution. After preparing the solution mixture (of zein, pectin, $CaCl_2$ and NaCl solutions), the pH was not adjusted which was found to remain at 4. But for the studies performed at other pHs, the solution was titrated with 0.1 M NaOH to set the pH to the desired value (say 7.4). Addition of $CaCl_2$ and NaCl did not change the solution pH. The prepared dispersions were stored in air tight borosilicate glass bottles for future use which did not exceed more than 24 h after preparation.

## 3.2.3   RESULTS AND DISCUSSION

### 3.2.3.1 EFFECT OF MIXING RATIO ON COMPLEXATION

The physical properties of both the biopolymers have been determined in the past which is summarized in Table 1. Zeta potential ($\zeta$) provides an account of the charge on the surface of the particle, and thus defines the stability of the dispersion [Ohshima, 1995]. Figure 3.7 illustrates the mixing ratio dependent zeta potential profile of pectin-zein (P-Z) complexes as function of pH (A), and ionic strength at pH 4 (B), both at r =1. For comparison the pH dependent zeta-potential profiles of the two biopolymers is included in Fig. 3.7 (A). These dispersions had to be diluted for these measurements so that the individual complexes could be isolated from the larger aggregates assuming that the net charge was unaffected by dilution. For pectin, the zeta potential was found to be negative in the entire pH region of 2-10. This was ~ -50 mV at pH $\approx$ 4-10, which decreased to -10 mV at pH $\approx$ 2. This confirmed the polyanionic nature of this biopolymer. However, zein being a polyampholyte, showed zeta potential of $\zeta$ = 40$\pm$3 mV at pH 2-4 that decreased to -30 mV at pH $\approx$ 8 with a clear pI identified at pH $\approx$ 6.2.

**Table 3.1:** Summary of physical properties of pectin in water, and zein nanoparticles in 80:20 ethanol-water solvent at pH 4.

| S.No. | Properties | Pectin [Joshi et al, 2016; Ventura, 2013] | Zein [Li, 2011; Zhong, 2009] |
|---|---|---|---|
| 1 | Molecular weight/kDa | 59-150 | 18-20 |
| 2 | Hydrodynamic Size/nm | 300 | 80-120 |
| 3 | Conformation | Stiff Chain | Sphere |
| 4 | Persistence length/nm | 10 | -- |
| 5 | pI | -- | 6.2 |
| 6 | Zeta Potential/mV | -50 | 37 |
| 7 | Polyelectrolyte nature | Polyanion | Polyampholyte |

The zeta potential data of pectin-zein (P-Z) interpolymer complexes revealed a distinct binding pattern. Between pH of 2-6, the binding interaction was predominantly electrostatic (EB) owing to the opposite polarity of the two biopolymers. The $\zeta$ value of the complex decreased gradually from +10 to -18 mV in this region which was indicative of partial charge neutralization of the pectin chain. The binding process continued in the pH region of 6-8 ($>$ pI) which is normally called "wrong side of pH" in coacervate literature [Pathak et al, 2014]. In this region the two biopolymers had similar charge polarity, therefore SPB mechanism was solely responsible to cause this association. Therefore, associative interaction leading to the interpolymer complex formation could be attributed to partial charge neutralization mechanism occurring between pectin and zein that prevailed in the pH region of 2-10. This association could be given by

$$[Z] + x[P] \rightarrow [P - Z] + (1 - x)[P] \tag{3.14}$$
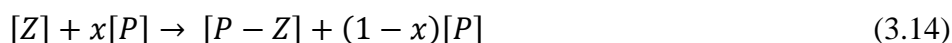
where of the available pectin content, a fraction $x$ binds to zein to yield a interpolymer complex P-Z that coexists with un-reacted pectin fraction $(1\text{-}x)$. When the zeta potential data (at pH $\approx$ 4) was used in eqn. (3.14), the value for x was found to be 1:1 (w/w). Assigning a mean

molecular weight of 100 KDa to pectin and 21 KDa to zein, x translates to, 1: 5 (approx.) implying every pectin chain was bound to 5 zein nanoparticles on an average. For r > 1, there was excess of pectin that caused gelation, and for r < 1, there was excess of zein nanoparticles in the coacervating solution as well as in its coacervate. This in turn governed the microstructure, and the viscoelastic properties of the gel/ coacervate material.

Figure 3.7(B) describes the variation of zeta potential of the P-Z complex as function of ionic strength for samples prepared at pH 4. Up to r =1 (Region-I), there was aggressive screening of the zeta potential of the complexes the value of which reduced from -10 to -6.5 mV, and for r > 1 (Region-II), there was marginal screening (-6.5 to –5.5 mV) of the same. In salt-free samples, qualitatively similar observation was made though the corresponding change in the zeta potential was less drastic. This data reinforced our earlier contention of existence of electrostatic binding between the two biopolymers at pH 4. However, the zeta potential values remained invariant of ionic strength for any given mixing ratio. Regardless, a linear dependence of zeta potential on mixing ratio was clearly noticed for all cases.
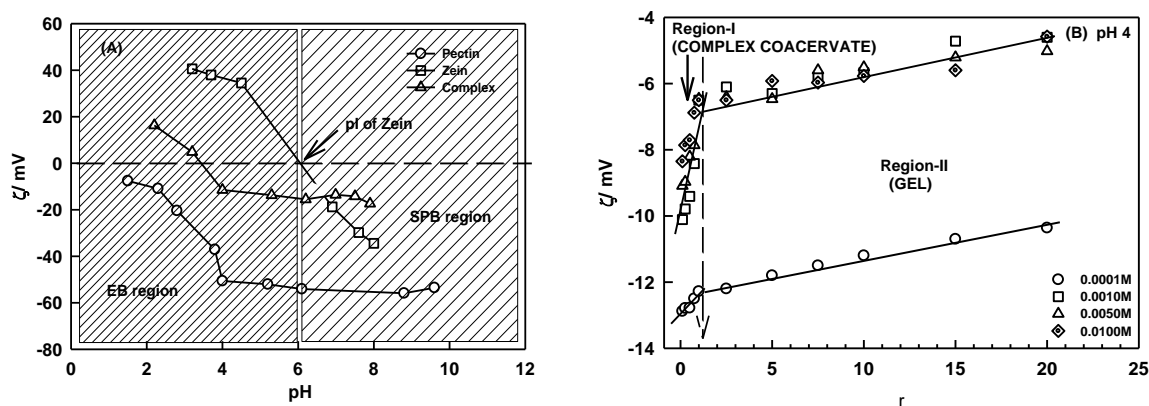


**Fig. 3.7:** (A) Zeta potential profile of pectin, zein and pectin-zein (P-Z) complex as function of pH shown for r=1:1 (w/w) sample in salt-free dispersion. Shades differentiate the electrostatic (EB) and surface patch binding (SPB) regions. (B) Effect of ionic strength on zeta potential shown as function of mixing ratio for samples prepared at pH ≈ 4.0. Solid lines are guide to the eye.

Clearly, the onset of binding would occur at pH <pI where P-Z complex begins to acquire positive charge though less than that of zein. A sharp change in zeta potential was indicative of aggressive binding due to strong electrostatic interaction between the two biopolymers.

Further increase in binding ratio, *r* for a sample maintained at pH 4, led to continuance of binding even under the mild ionic environment (I= 1-10 mM of NaCl) with the insoluble aggregates getting larger in size, but these escaped the fate of precipitation because they carry a small negative net charge (Fig. 3.7 (B)).

## 3.2.3.2 INTERMOLECULAR COMPLEX FORMATION AND COACERVATE-GEL TRANSITION

### 3.2.3.2.1 TURBIDITY

The important factors affecting the complexation of polymer-protein are pH, mixing ratio and ionic strength. Thus, turbidity measurements were performed as a function of pH for the samples having different mixing ratio and ionic strength. Turbidity of dispersions is a measure of particle size, and its concentration (number density of particles) under a given thermodynamic condition. Inter-particle associative interaction can be ascertained from the change in the turbidity parameter. The dispersion was relatively transparent before addition of zein to pectin solution at a given r. However, at pH <pI, the turbidity was found to increase with P content showing no phase separation due to similar polarity of the soluble complexes. Figure 3.8(A) illustrates the turbidity profile as function binding ratio at a given pH 4, for different zein content of the interacting solution. At this pH, the biopolymers carried opposite net charge that facilitated their associative binding *via* electrostatic interactions.

The mixing ratio dependent turbidimetric titration plot of pectin at different concentration of zein is shown in Fig. 3.8 (A). The increase in turbidity of the r<1 dispersion owed its origin to the formation of soluble interpolymer complexes, which took place below pI

of zein, due to the presence of opposite charge on the biopolymers (Region-I). So, the electrostatic interaction was found to be operative in initiating this associative binding. For a given mixing ratio, the dispersion with higher zein content displayed more turbidity. Further all dispersions with r > 1, exhibited same turbidity indicating formation of a different phase state (Region-II).
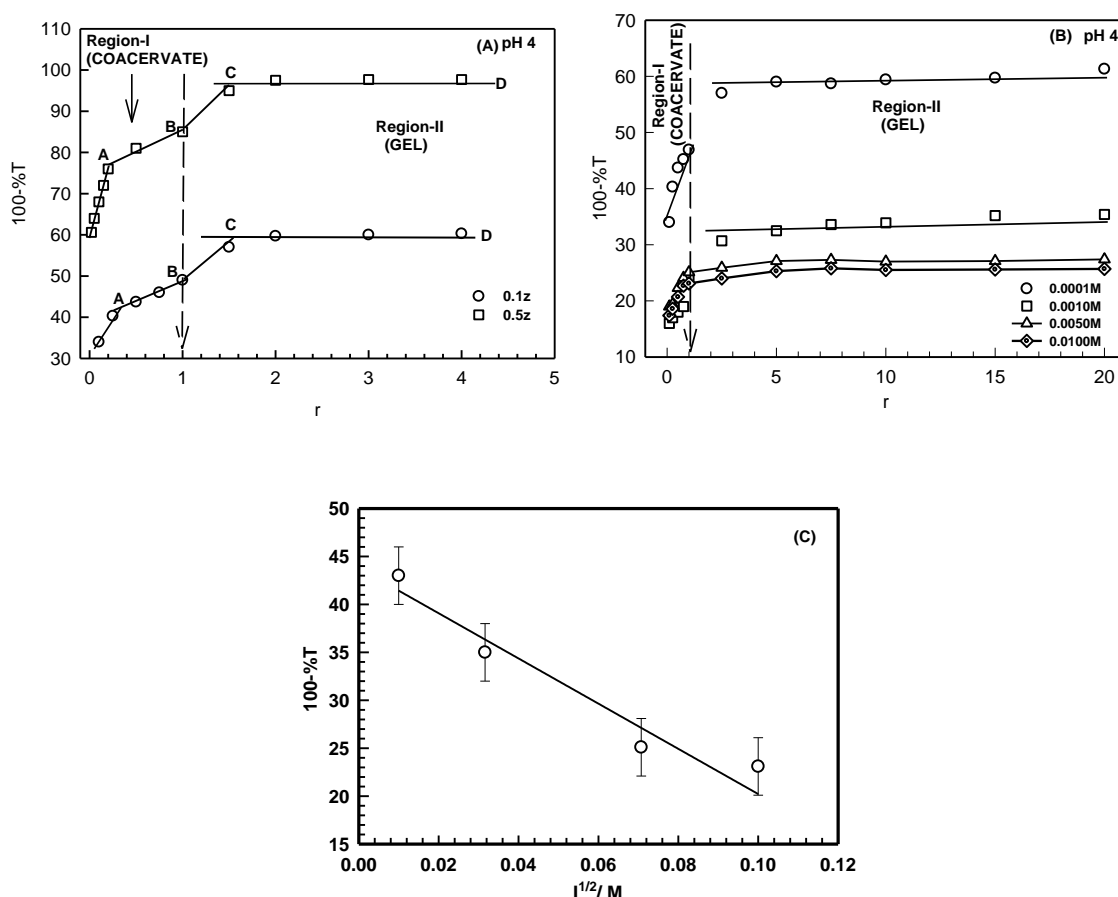


**Fig. 3.8:** Titration profiles showing change in turbidity as a function of [P] (A) without salt (at Z=0.5 and 0.1 % (w/v)) and (B) for different concentration of salt (NaCl, at 0.1 % (w/v) Z). (C) Variation of turbidity at r=1 with $I^{1/2}$ implying electrostatic nature of binding.

In the turbidity profile, the first occurrence of turbidity was noticed at low concentration of P which corresponds to the onset of formation of inter-polymer complex (A in Fig. 3.8(A)). The turbidity continued to increase with P (segment A-B in Fig. 3.8(A)) which corresponded to the formation of large soluble microscopic aggregates through Ostwald ripening. Further increase in P (r > 1) turned the coacervate dispersion into turbid gels (segment C-D in Fig.

3.8(A)). Thus, complexation on zein with addition of pectin was favored at pH=4.0±0.2 due to the complementary charge states of the two biopolymers. The supporting UV-Vis absorbance plots obtained at λ= 450 nm are shown in Fig. 3.9.
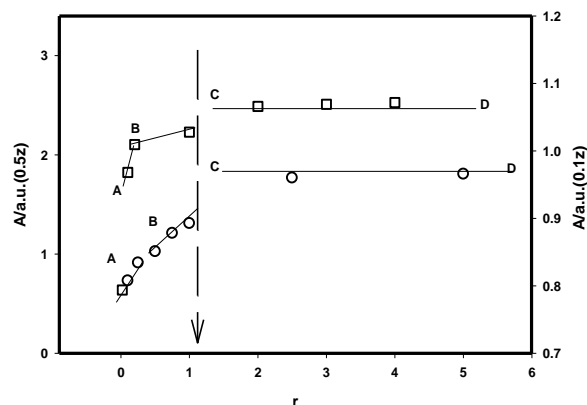


**Fig. 3.9:** Variation of absorbance of P-Z complex taken at 450 nm shown as function of mixing ratio. A-D are characteristic transition points depicting formation of complex at A, soluble complex at B, coacervate droplets at C, and gelation in the C-D region.

In a follow up experiment, the effect of solvent ionic strength was explored on the binding isotherm. Turbidity measurements were performed on the coacervating samples prepared with ionic strengths varying from I= 0.0 - 0.01 M at pH 4 which is depicted in Fig. 3.8(B). The turbidity profile remained qualitatively identical to the no-salt data except for that considerable screening in the values of turbidity was unmistakably detected. A plot of turbidity as function of $\sqrt{I}$ displayed a linear dependence (inset of Fig. 3.8(B)). To a first approximation, assuming the scattering moieties to be spherical, the interaction strength would be inversely dependent on the Debye-Huckel electrostatic screening length, and hence will linearly vary with $\sqrt{I}$, a conclusion which was supported by the data.

**3.2.3.2.2 VISCOSITY**

In order to authenticate, the observations made from turbidity data pertaining to coacervation and gelation, it was felt imperative to follow the association kinetics using an alternative method. We chose to probe these samples using steady state (30 Hz) viscosity measurements. The data is shown in Figs. 3.10(A) and (B) for the coacervating samples in salt-

free and salty environments. The viscosity versus *r* plot depicts clear transitions at points A, B and C (Fig. 3.10) corresponding to change in slope qualitatively similar to turbidity data (Figs. 3.8(A) and (B)). Considerable, reduction in viscosity was noticed in samples containing salt which clearly indicated that the interactions were Coulombic in nature. The viscosity $\eta$ of the interacting solution can be given by the most general description in the Flory-Huggins formalism as [Flory, 1953]

$$\eta(r) \cong \eta_0\left(1 + K_H^{'}\, r + K_H^{''}r^2\right) \tag{3.15}$$

Where, $r$=[P]/[Z], $K_H^{'}$is equivalent to the intrinsic viscosity [η] of the solution, and $K_H^{''}/[\eta]^2 = K_H$ is the Huggins interaction parameter. For $r <1$, eqn. (3.15) reduces to a linear form with a slope given by the intrinsic viscosity. As the size of the interpolymer complex increases, η would increase linearly, which was clearly observed in Region-I of Figs. 3.8 (A) and (B). It is not unreasonable to assume that these were mostly spherical aggregates. Points A, B and C on these plots depict specific mixing ratio values pertaining to a particular size of soluble pectin-zein complex in the coacervating solution. Thus, until point C associative association prevailed with the concomitant increase in size of the complexes.
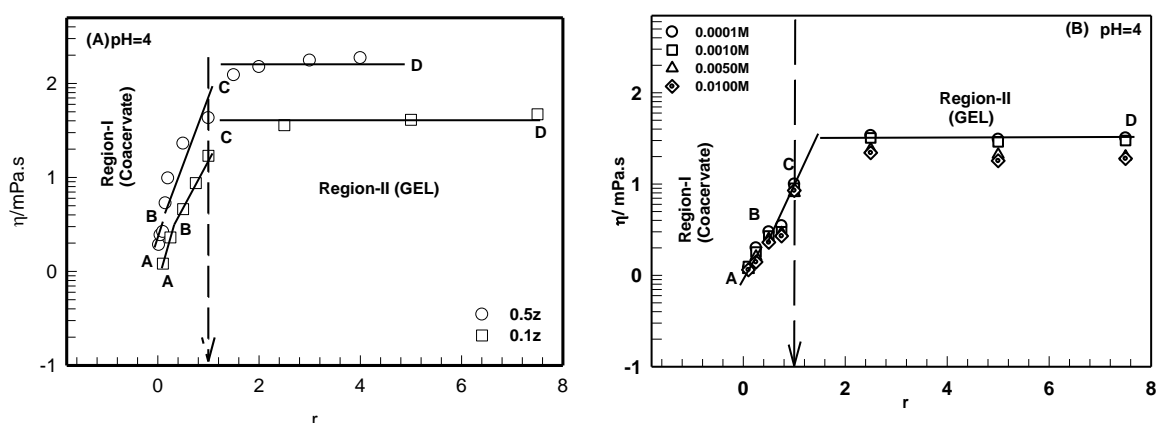


**Fig. 3.10:** (A) Variation of solution viscosity of coacervating liquid shown for various mixing ratio. (B) Effect of solution ionic strength on coacervation for zein=0.5%. Note the dotted line demarcates the coacervates from the gel regime. Solid lines are guide to the eye.

When concentration of pectin was increased further, the corresponding increase in *r* would make the quadratic term in eqn. (3.15) to dominate. Observation of a plateau in Figs. 3.10(A) and (B) implied that for *r*> 1, the samples entered a different phase state where both [η] and $K_H$ remained invariant of mixing ratio. These samples were examined for their fluid state by inverting the sample cells and noticing their non-flowing meniscus which indicated that these had transformed into gels. The depiction of higher viscosity for [zein]=0.5 % samples implied that for a given pectin concentration more viscoelasticity was generated at higher zein content. The observed plateau was indicative of the loss in fluidity of the gelling samples. Viscosity data was marginally sensitive to the variation in the ionic strength in the gelled samples. Thus, *r=1* was established as the boundary between coacervate, and gel phase of the samples, consistent with earlier discussions. Fig. 3.11 depicts the variation of viscosity and low frequency storage modulus $G_0$ as function of *r*.
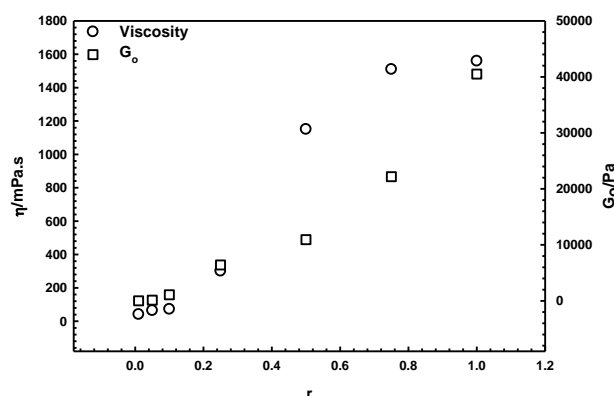


**Fig. 3.11:** Variation of viscosity and low frequency storage modulus $G_0$ of pectin-zein complex as a function of mixing ratio (or zein concentration) measured at 25 °C.

### 3.2.3.2.3 SURFACE PATCH BINDING (SPB)

After having probed the binding between pectin and zein under the pH < pI condition, where complementary net charge on the biopolymers induced associative interaction leading to coacervation for *r<1*, and gelation for *r>1*, it was felt imperative to extend the study to the "*wrong side of pH, i.e pH>pI*". Under this pH condition zein carried net negative charge,

regardless, interpolymer binding with polyanionic pectin was a reality, and associative interactions caused complex formation. The complexes were anionic, but their zeta potentials were independent of the pH in the region of 6-8. SPB has been realized in a wide range of protein-polyelectrolyte systems where the polyelectrolyte selectively binds to the oppositely charged location (segment) of the protein surface overcoming repulsion arising from similarly charged segment. Such interactions often lead to complex coacervation and liquid-liquid phase separation in complex polyelectrolyte solutions [Singh et al, 2007; Gupta et al, 2007; Pathak et al, 2016].

The turbidity and zeta potential profiles of the coacervating samples are shown in Fig. 3.12 (A) and (B). The overall picture of complex coacervation discussed earlier was noticed again though at higher ionic strength of the solution the zeta potential was found to be substantially reduced. The screening of the surface charge of the biopolymers inhibited associative electrostatic interaction between them resulting in reduction in their interpolymer complex formation efficiency that resulted in the observation of lower turbidity. However, the broader picture of coacervation to gel transition at r=1 was not disturbed. Similarly, the zeta potential and turbidity profiles at r <1, contained signature transition points as before designated as A-D, describing the initiation of formation of interpolymer complexes at A, formation of soluble complexes at B, coacervation transition at C, and gelation at C-D. The zeta potential profile could capture this feature with more finesse. Note that unlike in electrostatic binding that defined associative interactions at pH=4 (Fig. 3.8(C)), the turbidity of the interacting solution at $r=1$ did not show any dependence on $I^{1/2}$ which is a clear signature of SPB mechanism.
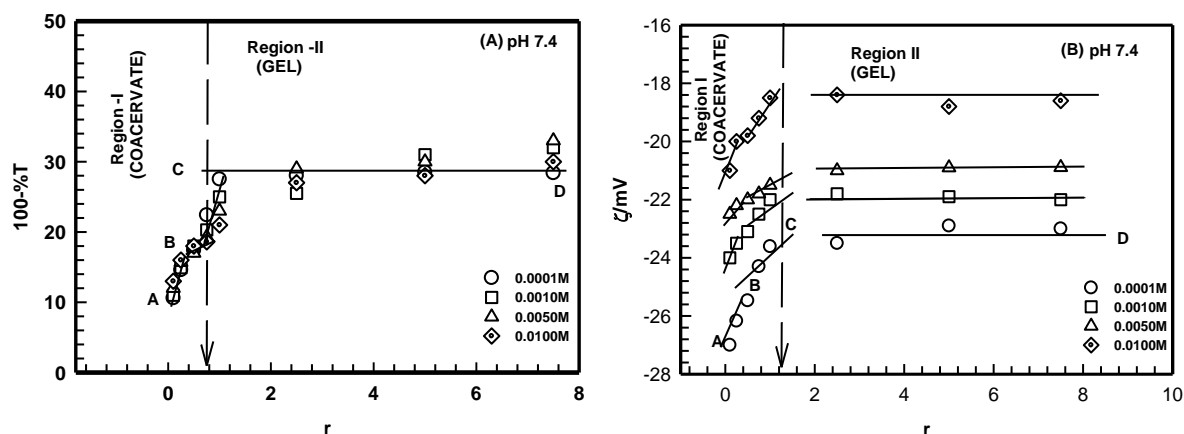
**Fig. 3.12:** Variation of (A) turbidity, and (B) zeta potential with mixing ratio shown as function of ionic strength. A-D are the transition points designating initiation of interpolymer complex formation, formation of soluble complexes, coacervation and equilibrium gel formation. Solid lines are guide to the eye. See text for details.

### 3.2.3.3 VISCOELASTIC PROPERTIES OF COACERVATES AND GELS

The samples were examined for their fluidity as function of the mixing ratio of the constituent biopolymers. Interestingly, for $r \leq 1$, all the samples were free flowing while for $r \geq 1$, these turned into gels spontaneously under ambient conditions. This was ascertained by inverting the sample cells, and observing their non-flowing meniscus which could support the weight of the material. The viscoelastic attributes of these samples were characterized by rheology. The dispersion profile of the storage (G') and loss (G") moduli of the coacervate and gel samples are shown in Fig. 3.13. In most general terms, the stress relaxations in viscoelastic materials follow a power-law behavior given by [Barnes, 2000]

$$G'(\omega) \sim \omega^{n'} \qquad \text{and} \qquad G''(\omega) \sim \omega^{n''} \tag{3.16}$$

For nascent gels, $n' \approx n''$.

Network rigidity $G_0$ is defined by the following expression

$$G_0 = \lim_{\omega \to 0} G'(\omega) \tag{3.17}$$

The scaling exponents, in the linear viscoelastic theory, assume specific values that define the viscoelastic properties of the material adequately. For a Hookean solid $n' = 0$ and for a Maxwellian liquid $n' = 2$ [Branes, 2000] which set the boundary between the solid and fluid

state of matter. When $n' \rightarrow 0$, the material gains shear modulus of elasticity and exhibits solid-like properties. Most of the viscoelastic materials (polymer melts, gels, coacervates etc.) have $n'$ values ranging between 0 and 1. In general, n′ defines elastic and n″ viscous behavior. Small n′, and n″ values attribute solid-like properties to the material while large n′ and n″ values are indicative of viscous behavior. Least-square fitting of the data to this equation yielded n′ =0.14 ± 0.02 and n″ =0.01 ± 0.01 invariant of mixing ratio for gels, and for coacervate samples the corresponding values were n' =0.24 ± 0.04 and n" = 0.02 ± 0.01. The integrity of the gels was established from the following facts: (i) $n'_{gel} < n'_{coac}$ and $n''_{coac} > n''_{gel}$, and (ii) $G'_{gel} \gg G'_{coac}$ and $G''_{gel} \ll G''_{coac}$. However, in both the cases $G' > G''$ implying even in the coacervate samples some degree of crosslinking was present which will be ascertained later.
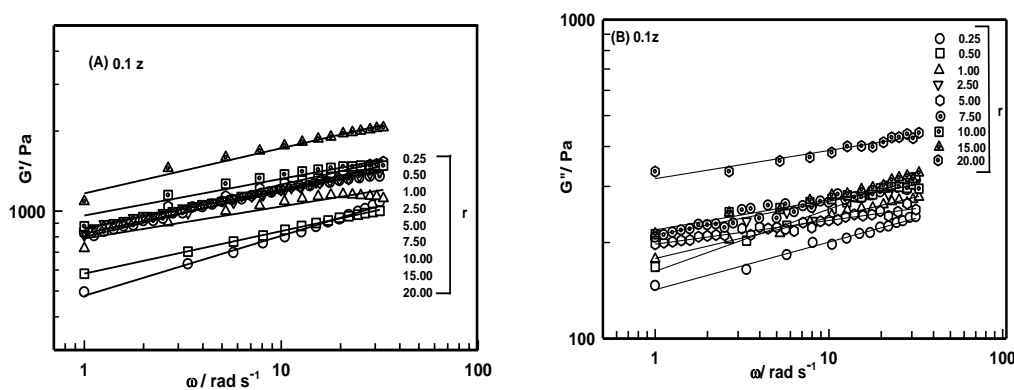


**Fig. 3.13:** Dispersion of (A) storage G′(ω), and (B) loss modulus G″(ω) of samples (coacervates and gels) as function of mixing ratio for [zein] = 0.1% preparations. The measurements were performed at 25 $^0$C at a constant oscillation stress of 6.3 Pa. Solid lines are least-squares fitting to the data.

In the case of [zein] = 0.5% samples qualitatively similar observation was made though the moduli values were typically higher by a factor of at least 10 (Fig. 3.14). Clearly, the enhanced material rigidity can be attributed to the propensity of zein nanoparticles of higher size that most likely acted as crosslink junctions.
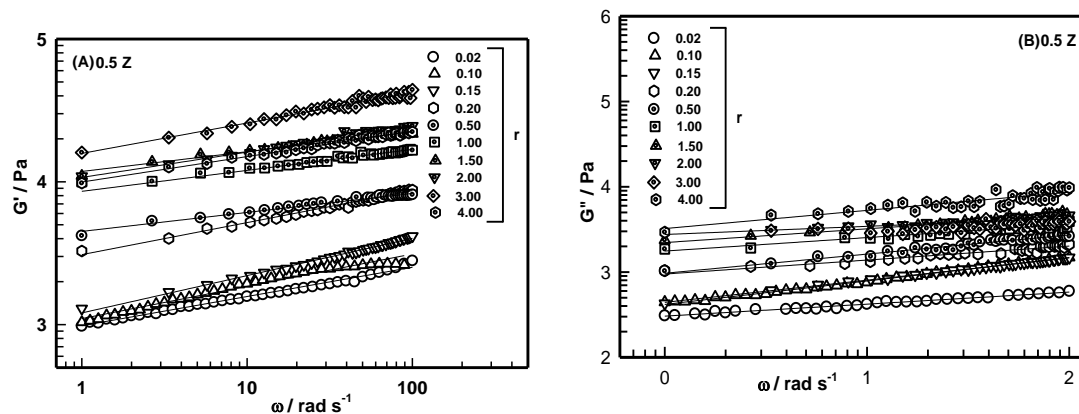
**Fig. 3.14:** Dispersion of storage G′(ω), and loss modulus G"(ω) of (A) coacervates and (B) gels samples as function of mixing ratio for [zein]=0.5% preparations. The measurements were performed at 25 $^0$C at a constant oscillation stress of 6.3 Pa. Solid lines are least-squares fitting to the data.

The $G_0$ data for various samples prepared in salt-free and salty solvents is shown in Fig. 3.15 for [zein] = 0.1 and 0.5 % preparations. It needs to be mentioned that pectin gels show rigidity modulus of $G_0 \approx 40$ Pa. Compared to this, the pectin-zein gels exhibited $G_0$ values that were at least 40 times more (Fig. 3.15(A)). Even the coacervates displayed much larger rigidity than the pectin gels. Samples prepared in presence of salt showed much lower rigidity due to screening of the interaction between the biopolymers (Fig. 3.15(B)). Further, for a given mixing ratio samples containing more zein nanoparticles produced a stronger coacervate /gel material.
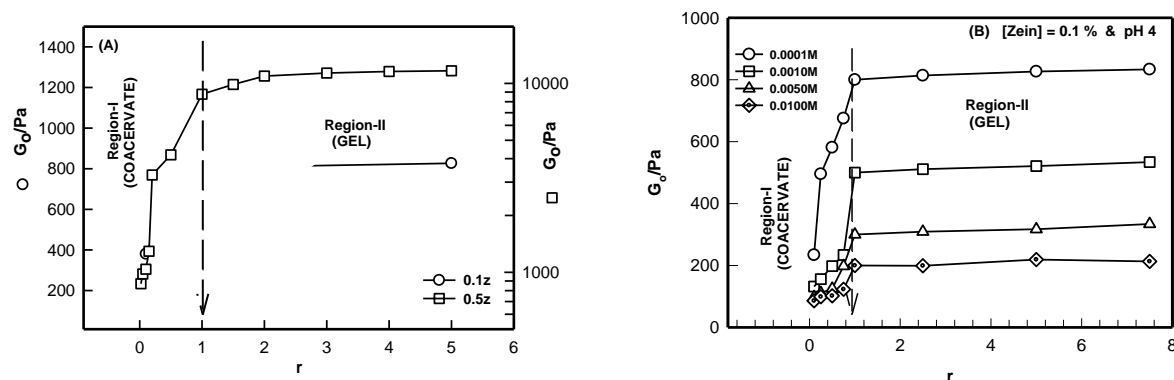


**Fig. 3.15:** Variation of low frequency rigidity modulus $G_0$ as function of mixing ratio shown for samples prepared in salt-free (A) and salty (B) solvents. Solid lines are guide to the eye.

### 3.2.3.4 CROSSLINK DENSITY

The interpolymer complex formation led to coacervation at low mixing ratio ($r < 1$), and to gelation when the mixing ratio was high ($r > 1$). At $r=1$, there was a seamless transition from the coacervate to gel phase which was driven by pectin propensity. Figures 3.7-3.10 define a point C that corresponds to complex coacervation phase for r=1 mixing ratio. The branch C-D defines the gelation regime. A pertinent question arises here, since both the coacervate and gel phases were associated with finite rigidity (storage modulus), what was their typical network density? We are basically seeking a descriptor to differentiate between the two. In gel science, normally gel fraction serves the purpose of the order parameter to describe the kinetics of gelation at microscopic level. However, gel fraction is a difficult parameter to measure. Therefore, we shall be using an alternative method to quantify the relative network density (as a descriptor) in gels compared to their preceding coacervate phase using the rheology data.

The complex coacervation can be described as follows

$$[Z] + [P] \leftrightarrow [Z - P]_{complex} + [P] \leftrightarrow [Z - P]_{Soluble\ complex} \rightarrow [Z - P]_{coac}; r \leq 1 \quad (3.18)$$

For gelation, one has

$$[Z - P]_{coac} + [P] \leftrightarrow [Z - P]_{gel}; r > 1 \quad (3.19)$$
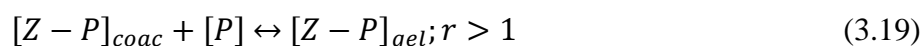
Thus, complex coacervation was a kinetic process while gelation was a thermodynamic one. Recall that formation of soluble complexes and the coalescence often precede coacervation while coacervate to gel was a single step transition. Further, it will not be incorrect to assume that the zein nanoparticles were acting as crosslinkers to pectin chains which resulted in the formation of network structures. We will be using the concept developed for rubber elasticity of crosslinked gels to estimate the crosslink density parameter. This is normally deduced from the equilibrium swelling experiments using Flory-Rehner relation [Flory, 1953]. The network density ν is approximately determined from the relation given by

$$E \approx \frac{3\rho RT}{2M_e} \tag{3.20}$$

Where E is the low deformation Young's modulus, $\rho$ is rubber density, and $M_e$ is the mean molecular weight of the polymer segment between crosslinks. Realizing, the dependence, $\rho = \nu M_e$ and the fact that $E \approx 3G_0$, eqn. (3.20) can be reduced to

$$\nu \approx \frac{2G_0}{RT} \tag{3.21}$$

The data in hand allowed us to evaluate the relative network density, $\nu_r$

$$\nu_r = \frac{\nu_{coac}}{\nu_{gel}} \approx \frac{G_{0,\ coac}}{G_{0,\ gel}} \tag{3.22}$$

The subscripts coac and gel designate the corresponding parameter of the coacervate and gel states. Realize that coacervate and gel phases are equilibrium states of condensed matter, both are free-energy driven self-assembled systems. Therefore, crosslink density which is being used as a descriptor can be replaced by the corresponding $G_0$ value under the thermodynamic premise of one equilibrium property being replaced by another. Since, we are dealing with relative values it is all the more appropriate.

Here, it was assumed that the networks were affine that allows the gel content to be described through, its rigidity modulus to a first approximation. An affine network embodies the following properties: (i) the relaxed network is isotropic, (ii) molecular level deformation is same as at the macroscopic level, (iii) volume is invariant of deformation, and (iv) network entropy is the same as sum of individual chain entropies. The variation of $\nu_r$ with mixing ratio is shown in Fig. 3.16 for the samples prepared with of [zein] = 0.1 and 0.5 % concentrations. As before, we have clear signatures of formation of interpolymer complexes at A, formation of soluble complexes at B, coacervation transition at C and gelation after C up to D. Therefore, the descriptor could capture the phenomenon of coacervation to gel transition adequately based on rheology data. Further, this process was much enhanced when zein nanoparticle content (also the size) was increased.
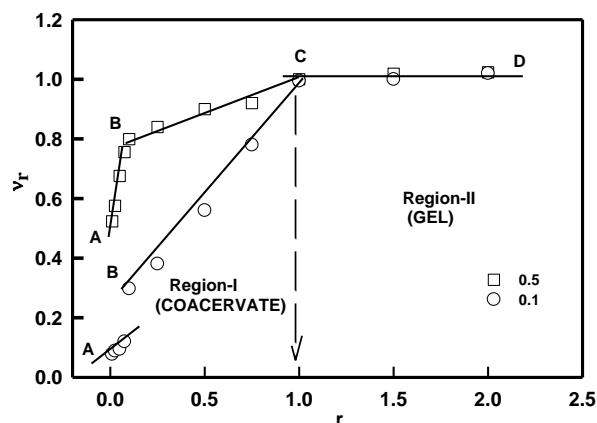
**Fig. 3.16:** Variation of crosslink density as function of mixing ratio for the two preparations with [zein]=0.1 and 0.5 %.

### 3.2.3.5 MELTING PROFILE

Figure 3.17 illustrates the temperature dependence of the elastic moduli for coacervate and gel samples measured at a fixed frequency of 1 rad s$^{-1}$ using a temperature ramp of 1 $^0$C/ min. Isochronal temperature sweep protocol was used to collect this data. The melting profile exhibited two distinct features in the representative data shown in Fig. 3.17: (i) between 20 to 56 $^0$C, the melting was gradual and incomplete (solution state could not be reached), and (ii) an abrupt rise in the storage modulus was noticed above 56 $^0$C independent of mixing ratio. The melting profile of pectin gel is depicted in Fig. 3.18.
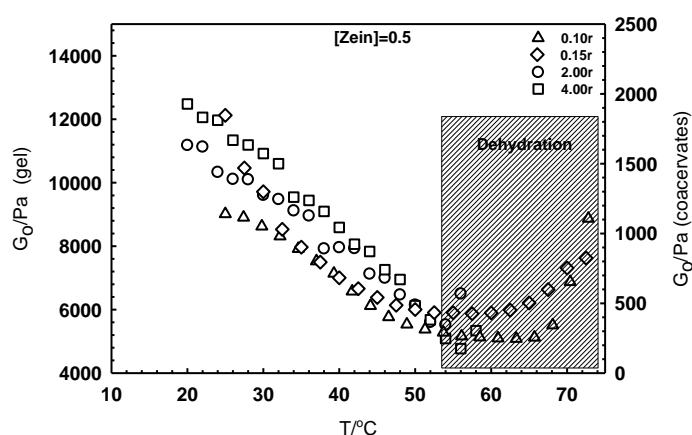


**Fig. 3.17:** Variation of low frequency storage modulus $G_0$ of samples shown as function of temperature. Melting profiles were generated by using a temperature ramp of 1 $^0$C/min. Sharp upturn in the data at 56$^0$C indicated drying of samples.

Between 20 and 56 $^0$C, the change in $G_0$ was about $\Delta G_0 = 7$ KPa which was independent of mixing ratio. This section of the data could not be fitted to the Arrhenius equation, and at 56 $^0$C the samples displayed $G_0 \approx 5$ KPa, indicating that gel to coacervate to interacting solution transition was not thermoreversible. At this stage it was felt necessary to determine what was the state of matter at 56 $^0$C. Two nascently prepared coacervate samples (r = 2 and 4) were evaluated for their thermal melting profiles. The $G_0$ values obtained were on the order of 4.5 KPa. Therefore, it is concluded that the samples were transformed from their gel to coacervate states upon melting. Since, $G_0$ is a measure of enthalpy per unit volume, in principle one can determine the enthalpy of gelation from the $\Delta G_0$ data. When these samples were heated to temperatures above 56 $^0$C significant weight loss in the samples was noticed which is attributed to loss of solvent (shaded area).
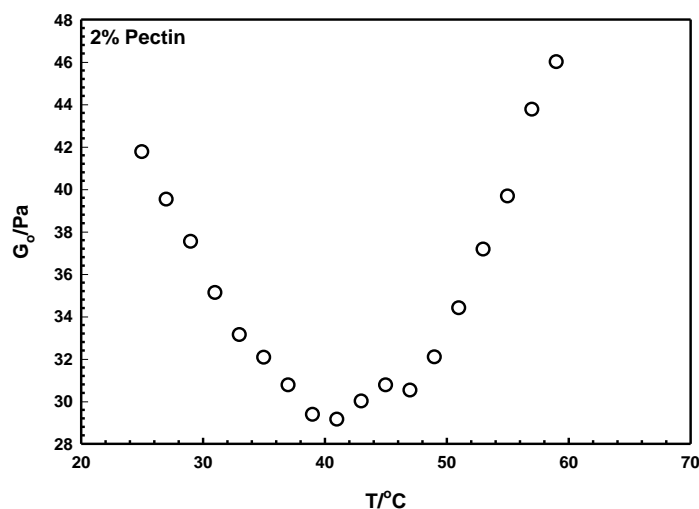


**Fig. 3.18:** Variation of low frequency storage modulus $G_0$ of 2% (w/v) pectin gel samples shown as function of temperature. Melting profiles were generated by using a temperature ramp of 1 $^0$C/min. Sharp upturn in the data at 40 $^0$C indicated drying of samples.

### 3.2.3.6 MICROSCOPIC STRUCTURE

The coacervate and gel samples were subjected to SANS studies in order to probe their internal structure. This experiment involves scattering of a monochromatic beam of neutrons from the sample and measuring the scattered neutron intensity I(q) as function of the scattering

wave vector q. Figure 3.19 depicts the SANS intensity profile, I(q) versus q data for coacervate and that of the gel samples prepared with different mixing ratios. It was found that all scattering profiles decreased as function of q. The different q-regions were separated manually after examining their $1/I(q)$ versus $q^2$, and $1/\sqrt{I(q)}$ versus $q^2$ plots. In both the coacervate and the gel system three distinct scattering regions were identified given by eqn. (3.23). A clear change in slope was noticed at $q^*$ and $q^{**}$ that separated the scattering regions (i) and (ii), and (ii) and (iii), respectively, which could be identified at 0.261 nm$^{-1}$, 0.489 nm$^{-1}$ and 0.180 nm$^{-1}$, 0.371 nm$^{-1}$ for gel and coacervate samples corresponding to [zein]=0.1 and 0.5 % preparations, respectively.
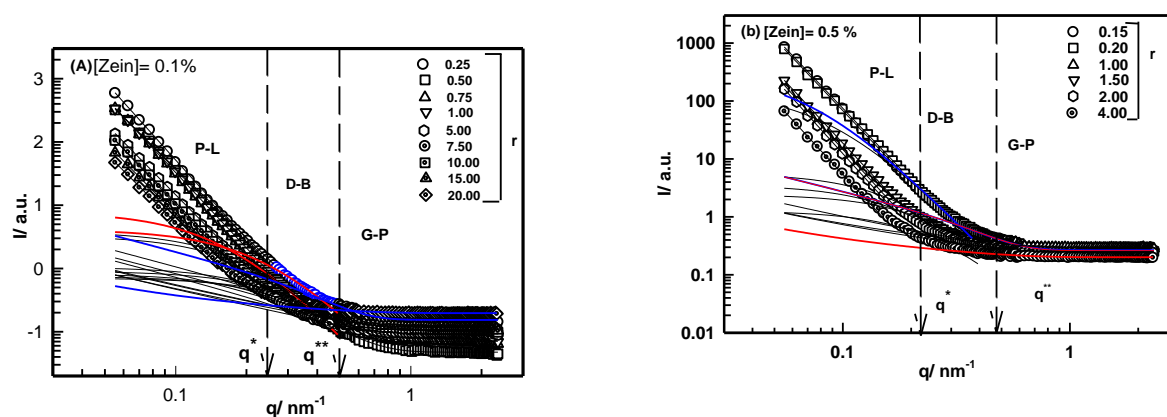


**Fig. 3.19:** Structure factor of coacervate and gel samples. (A) [zein]=0.1 %, and (B) [zein]=0.5 %. P-L, D-B and G-P represent power-law, Debye-Bueche and Guinier-Porod scattering regimes separated by $q^*$ and $q^{**}$ (arrows). Solid lines are fitting to the data. Arrows indicate the distinctive q-regions where power-law, Debye-Bueche and porod regimes prevailed. Note the dependence of these lengths on the pectin concentration (mixing ratio). The slope demarcates the coacervate and gel region. See text for details.

The SANS data were analyzed in the random phase approximation formalism in different q- regions. For both the coacervate and gel samples, the data was fitted the appropriate functions given by

$$I(q) =$$

$$
\begin{cases}
\quad I_{PL}q^{-\alpha} & (i)\,Power-law(P-L): & (0.0552 < q < 0.261\ \text{nm}^{-1}) \\
\quad \dfrac{I_{DB}}{(1+\xi^2 q^2)^2} & (ii)\,Debye-Bueche(D-B): & (0.261 < q < 0.489\ \text{nm}^{-1}) \\
\dfrac{I_{GP}}{q}\exp\left(-\dfrac{R_C^2 q^2}{2}\right) & (iii)\,Guinier-Porod(G-P): & (0.489\ \text{nm}^{-1} < q)
\end{cases}
\tag{3.23}
$$

where exponent $\alpha$ defines the geometry of the scattering moiety present in a given system. For instance, $\alpha$= 1, 2 and 4 correspond to geometrical shapes of rod, Gaussian coil, and hard sphere conformations, respectively. $\xi$ is the size of heterogeneity present in the system, and $R_c$ is the cross-sectional radius of the scattering moiety. The pre-factors ($I_{PL}$, $I_{DB}$ and $I_{P-G}$) are q-independent constants. Figure 3.19 depicts the composite plot where the various q-regions were fitted to their appropriate analytic functions.

The analysis of coacervate data gave $\alpha$=4.0±0.2, independent of mixing ratio, implying the scattering owed its origin to spherical objects present in this material. The heterogeneity size was $\xi_{Coac}$=4.0 ± 0.2 nm comparable to that of persistence length of zein which is 2.0 nm [Ventura, 2013]. Both the signature parameters $\alpha$ and $R_c$ did not reveal any dependence on pectin concentration. In contrast, coacervates had mesh size in the range of 4.0 nm and the size of inhomogeneity in gel samples was about 2 nm. Therefore, the mesh size was dependent on the mixing ratio r (Fig. 3.20).
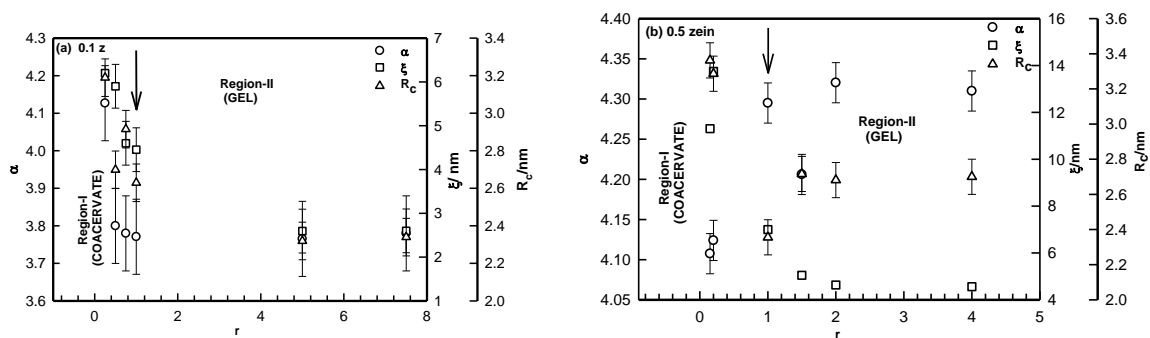


**Fig. 3.20:** Small angle neutron scattering intensity profile, fitting parameters (power-law exponent, and mesh size and cross-sectional radius) and cross-over wave vector of a P-Z (coacervate and gel) (a) 0.1 % and (b) 0.5 % (w/v) zein at various mixing ratio measured at 25 $^0$C.

It is important to note that at higher pectin concentration (r-value) the complexes carried more net charge that enabled them to strongly repel each other. Therefore, the network that was formed due to hydrogen bonding between the zein nanoparticles clad pectin chains was expected to have higher mesh size increasing with the mixing ratio. However, we observed just the opposite behavior. This discrepancy will be resolved when we discuss the hydration of the self-assembled structures later.

### 3.2.3.7 PHENOMENOLOGY OF INTERACTIONS

Two distinctive observations were made in this study. Firstly, the associative interaction driven complex coacervation was observed both at pH=4 and 7.4, while the pI of zein was 6.2. In the former case the two biopolymers had net charge of opposite polarity that facilitated their electrostatic interactions. In the latter case, the biopolymers had charge of same polarity yet coacervation was achieved. A second observation was at higher zein content stronger network was formed. The following offers a simple explanation to the aforesaid phenomena.

In the Smoluchowski description, the particle charge, Q, its zeta potential, $\zeta$, and apparent hydrodynamic radius, $R_h$ which is dispersed in a medium of dielectric constant $\varepsilon$ and Debye screening length, $\kappa$ are approximately correlated through the relation given by [Ohshima, 1950]

$$\zeta = 4\pi \left( \frac{\sigma}{\epsilon\kappa} \right) \tag{3.24}$$

Where the surface charge density is $\sigma = \frac{Q}{4\pi R_h^2}$.

Thus,

$$Q \approx \epsilon\kappa\zeta R_h^2 \tag{3.25}$$

Realize that $\kappa R_h = \alpha \geq 1$, is a condition that decides the location of the hydrodynamic slip plane where zeta potential is being observed.

Hence

$$Q \approx \alpha\varepsilon\zeta R_h \tag{3.26}$$

Correspondingly, the interpolymer interaction potential, U(r) will be given by

$$U(r) \approx \frac{1}{4\pi\varepsilon} \left( \frac{Q_P Q_Z}{r} \right) exp - (\kappa r) \tag{3.27}$$

Equation (3.27) describes the screened Coulomb interaction between pectin and zein as function of their separation, $r$. Further, $r \sim c^{-1/3}$ for a given dispersion of concentration, $c$. In our case, $Q_P$ and $Q_Z$ were constant for a given pH, therefore, the value of $U(r)$ at any $r$ can be given by

$$U \sim \varepsilon^{-1} c_z^{1/3} \tag{3.28}$$

We deal with two situations, [zein]=0.1 and 0.5 % solutions. The corresponding ethanol contents were 4 and 27 % (v/v) that corresponded to medium dielectric constant of 75 and 65, respectively. Therefore, the relative interaction potential for these two cases will be given by

$$\frac{U_{0.5}}{U_{0.1}} \approx 2 \tag{3.29}$$

This clearly implies that the samples prepared with 0.5 % zein content would be twice as reactive as 0.1 % samples at pH<pI. Such strong interactions would facilitate more crosslink density and higher gel strength. This was clearly noticed in our data that pertained to pH=4.

At pH=7.4, SPB interaction was operative and in that case the interaction potential will contain a repulsive and an attractive term where each of these will have a general form as in eqn. (3.27). Thus U(r) will be given by

$$U = \frac{Q_P}{4\pi\varepsilon} \left( \frac{Q_{Z-}}{R_-} exp - (\kappa R_-) - \frac{Q_{Z+}}{R_+} exp - (\kappa R_+) \right) \tag{3.30}$$

Here, $R_+$ and $R_-$ are the distance of the zein dipole positive and negative charge to the two ends of the pectin chain, which was negatively charged. Since, we observed coacervation even on the wrong side of pH, it will not be incorrect to argue that only one of the terms on the RHS of eqn. (3.30) was dominant in a given solvent milieu. Therefore, the condition $U_{0.5} > U_{0.1}$ would

still remain valid. It was possible to plot the interaction potentials for various zein concentrations, and solution ionic strengths. The electrostatic potentials were deeper than their SPB counter parts (data not shown) for a given solvent condition. For a given pH, the conclusion that $U_{0.5} > U_{0.1}$ qualitatively remained unchanged.
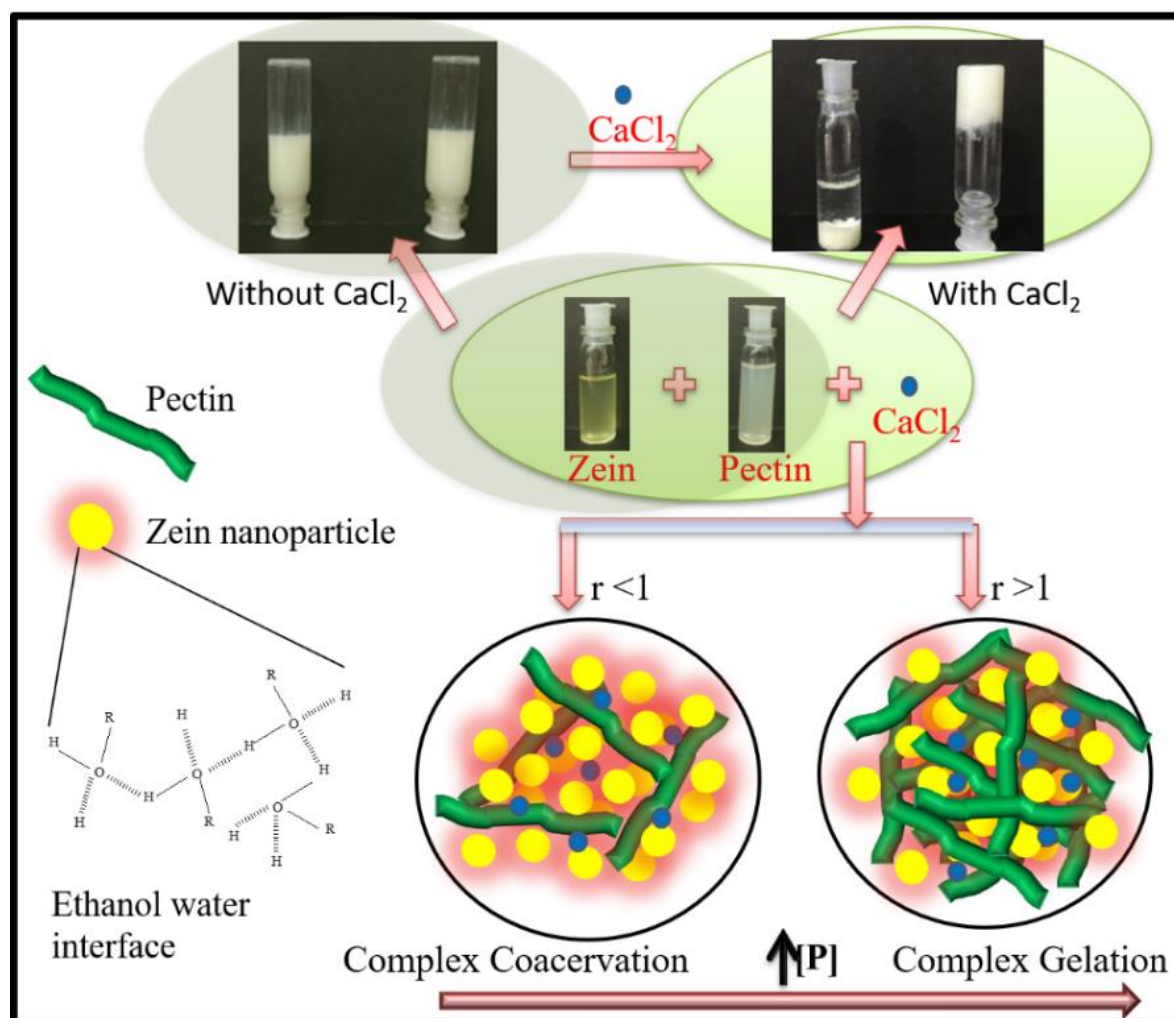


**Fig. 3.21:** Schematics model of the intermolecular binding protocol in pectin-zein interacting solution in presence of calcium ions.

A pictorial depiction of the association phenomenon is shown in Fig.3.21 and the comparison of physical characteristics of various dispersion phases of pectin-based systems is given in Table 3.2.

**Table 3.2:** Comparison of different physical characteristics of various pectin-based systems.

| Properties | P-gel | Z-P Gel (0.1z) | Z-P Coacervate (0.1z) | Z-P Gel (0.5z) | Z-P Coacervate (0.5z) |
|---|---|---|---|---|---|
| Binding type | Electrostatic/ hydrophobic | Electrostatic | Electrostatic | Electrostatic | Electrostatic |
| Go/Pa | 35±5 | 800±100 | 600±100 | 11000±1000 | 3000±1000 |
| Mesh size/nm | 50±10 | 2.5±0.5 | 5±1 | 4±1 | 12±1 |
| Viscoelastic length/nm | 50±1 | 17±0.5 | 19±1 | 8±1 | 13±3 |
| Melting temp/°C | 40±1 | -- | -- | -- | -- |
| Optical nature | Transparent | Opaque | Opaque | Opaque | Opaque |

### 3.2.4 CONCLUSION

In this section of work, we have shown that two states of soft biological matter may be created by selectively interacting a carbohydrate (pectin) with a colloidal protein (zein). The pectin polyanion selectively interacted with the *in situ* formed zein nanoparticles mostly through electrostatic interactions at low mixing ratio to cause complex coacervation for pH<pI of the protein concerned. Under similar thermodynamic conditions, formation of bicontinuous gels was observed at higher pectin to zein mixing ratio. These thermo-irreversible gels were visualized as a continuous network of pectin chains interconnected through zein nodes that served as crosslink junctions. Qualitatively, similar observation was made for samples prepared with pH>pI where surface selective patch binding dominated the interactions. However, the presence of larger crosslink nodes (zein nanoparticles size ~120 nm) facilitated higher crosslink density and that assigned more rigidity to the gels. For all other conditions remaining same, propensity of zein favoured formation of stronger gels. Crosslink density was used as a descriptor to qualitatively distinguish between the coacervates and gels. This indicated that

the internal structures of these were qualitatively very different from one another, and from that of pectin hydrogels. Therefore, the evolution of various soft matter states from the homogeneous biopolymer solutions was hierarchical in mixing ratio. A comprehensive understanding of coacervation phenomenon in competition with gelation in complementary biopolymers will give rise to generation of a whole new class of hybrid nano-biomaterials. The importance of mapping protein-carbohydrate interaction has bearing on protein purification and downstream processing of proteins and carbohydrates, individually.

## 3.3 Fluorescent Complex Coacervates of Agar and *in situ* formed Zein Nanoparticles

### 3.3.1 MOTIVATION

Fluorescent coacervate biomaterial with tunable viscoelastic properties may find applications in the real time tracking of drugs to the target, and confocal imaging of cells, and there is a paucity of fluorescent coacervates made of biomaterials the importance of present study holds sufficient promise. Which motivate to produce fluorescent coacervate for that in the section 3.3 of chapter 3 we show fluorescent zein nanoparticle interaction with agar (polysaccharide) yielding a continuous single phase coacervate. This study attempts to capture the inherent diversity of zein-polysaccharide/DNA coacervation [Kaushik et al, 2018; Pandey et al, 2017]. In order to expand the scope of the study, we report the effect of the ionic medium, pH and binding ratio on the mechanism of interpolymer complex formation and coacervation between agar and *in situ* formed zein nanoparticles at room temperature. We have found that this is a fluorescent coacervate with the luminescence emanating from the intrinsic properties of zein nanoparticles. Regardless, not many coacervates of biological origin are known to be intrinsically fluorescent and there is need to increase material capacity in this domain. Further, it is necessary to seek for a universal understanding of coacervates made of biomolecules, if any. The current report is an attempt in that direction which will be of importance to soft matter and biophysics community. We have modeled the experimental data pertaining to the interpolymer association in the framework of electrostatic theory, though DLVO model is known to describe colloidal aggregation in salty solutions [Derjaguin et al, 1964; Verwey et al, 1999] the present description adequately captured all experimental conclusions.

### 3.3.2  SAMPLE PREPARATION

Agar powder was autoclaved to make a stock solution with a concentration of 0.4 % (w/v). The zein stock solution was prepared by dispersing 2 % (w/v) of zein powder in 80:20 % (v/v) binary solvent of ethanol: water at 25°C under continuous stirring for 30 min which produced a light-yellow solution. The pH of the agar stock, zein stock, zein nanoparticle dispersion and the reacted solution were ≈ 7±0.2, 5.3±0.2, 3.8±0.2, and 5.4±0.2, respectively which did not alter upon dilution with water. A series of samples corresponding to various binding ratios were prepared by diluting of the stock solution of agar with required amount of water, while keeping the final volume same (one-shot dilution), to which desired amount of zein (from its stock) was added, and then stirred for 10 min to make a homogenous solution. Zein instantaneously turned into spherical nanoparticles *in situ* in this dispersion. It needs to be realized that samples containing [zein] =0.5 % (w/v) was in the reaction medium with effective ethanol concentration of 19 % (v/v), and concentration of agar was altered. Hydrodynamic size of zein nanoparticle formed was 120 nm. Thus, here we investigate the interaction between polyanion (agar), and *in situ* formed spherical zein nanoparticles in a 19 % (v/v) ethanolic solvent. All measurements were performed at room temperature of $25^0$C unless stated otherwise.

### 3.3.3 RESULTS AND DISCUSSION

The formation of interpolymer complexes prompting a separation of phases relies upon the physical condition of the system such as binding ratio, pH, temperature, ionic strength, and polymer charge density. It is logical to start the discussion from the molecular characterization of the constituent biopolymers.

Agar is a polyanion with a persistence length of ~6 nm while zein is polyampholyte

protein [Boral et al, 2010; Djabourov et al, 1989]. The physical properties of agar and zein are summarized in Table 3.3.

**Table 3.3:** Summary of physical properties of agar in water, zein nanoparticles in ethanol-water solvent and agar-zein complex at pH 7, 4 and 5.4 respectively. Agar-Zein data pertain to current measurements.

| S. No. | Property | Agar* | Zein** | Agar-Zein |
|--------|----------|-------|--------|-----------|
| 1 | Molecular weight/ KDa | 300 | 18-20 | --- |
| 2 | Hydrodynamic Size/ nm | 100 | 80-120 | 200-800 |
| 3 | Conformation | Stiff chain | Sphere | Sphere |
| 4 | Persistence length/nm | 6 | -- | -- |
| 5 | pI | -- | 6.2 | -- |
| 6 | Zeta potential/mV | -20 | 40 | -13 |
| 7 | Polyelectrolyte nature | Polyanion | Polyampholyte | Polyanion |

*Agar [Boral, 2010; Djabourov, 1989], **Zein [Gomez, 2012; Taylor, 2013; Zhong, 2013] and Agar-Zein (Present work).

The agar solution was titrated with zein solution under mild stirring which instantly created zein nanoparticles (NP) of opposite charge *in-situ*, and the reacting solution showed a sharp rise in solution turbidity at 400 nm while keeping the pH of the solution invariant at 5.4±0.5. All the while, the zeta potential, fluorescence, turbidity and particle size variations were monitored continuously.

### 3.3.3.1 INTERPOLYMER COMPLEX FORMATION

Binding between protein and polysaccharide may cause a conformational change in the protein molecule [Lumry et al, 1954]. Protein intrinsic fluorescence gives information about the change in the tertiary structure of the protein. Zein is fluorescent because of the presence of amino acid residues like tryptophan, phenylalanine, and tyrosine (benzene containing chromospheres) [Patel et al, 2010]. Fluorescence spectra of the agar-zein complex which is

shown in Fig. 3.22 indicates that with binding ratio fluorescence of these complexes increased till optimum binding ratio R = 0.2 was reached and beyond this the fluorescence decreased which clearly implied that of binding of agar to the zein nanoparticles caused a change in protein secondary structure for R≤0.2, a conclusion which will be proved later. The complex coacervate samples were visually observed by fluorescence microscopy using 80i Nikon Instruments which is shown in Fig. 3.23 for different mixing ratio at 40 X magnification, coacervate sample prepared at R=0.2 clearly shows maximum intensity (Fig. 3.24(a) shows 60X magnification image). The fluorescent property of coacervate was solely due to the fluorescent zein nanoparticles, because agar being a polysaccharide is non fluorescent in nature (Fig. 3.24(b)).
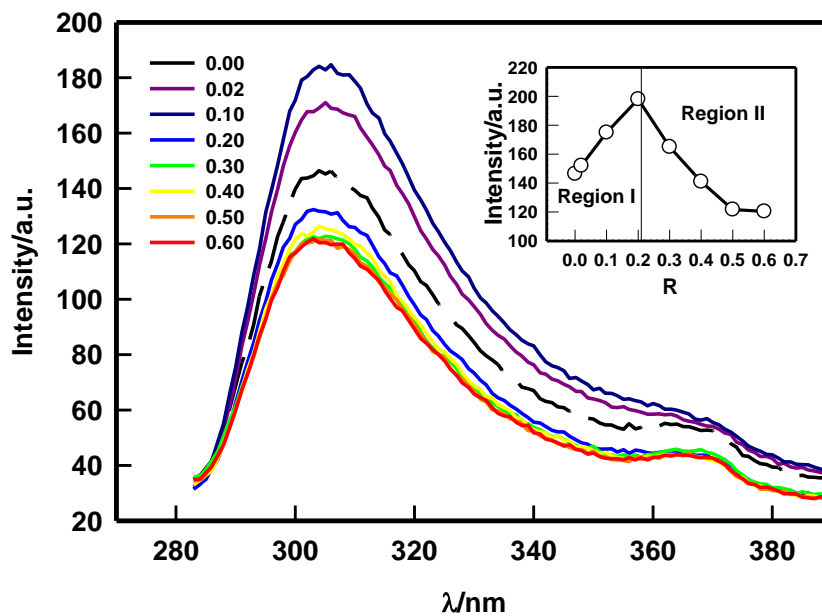


**Fig. 3.22:** Fluorescence spectra of agar-zein complexes at different binding ratio R and the inset shows the variation in emission intensity with a binding ratio at $\lambda_{em}$= 305 nm.

The complex formation was due to associative interaction between agar and zein, which in the  Regions I and II are explained by

$$X[Z] + [A] \rightarrow [A - Z]_x^{\text{Soluble}} + (1 - x)[Z] \qquad ; R < 0.2 \qquad \text{Region-I} \quad (3.31)$$

$$(1 - X)Z + [A] \rightarrow [A - z]_{1-x}^{Soluble} \qquad ; R=0.2$$

$$[A - Z]^{Soluble} + [A] \rightarrow [A - Z]_{overcharged} \qquad ; R \geq 0.2 \qquad \text{Region-II} \qquad (3.32)$$
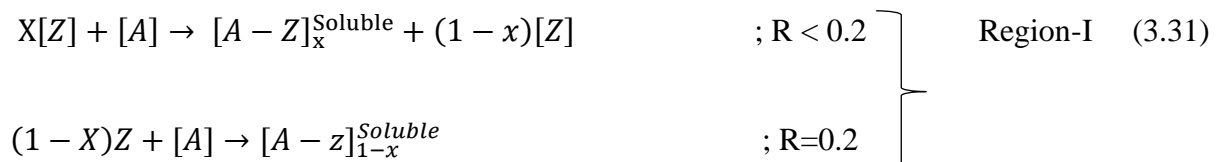
where in Region I with an increase in binding ratio the population of agar increases in the system, a fraction x of [Z] binds to [A] giving rise to increased fluorescence with the formation of soluble [A-Z] complex which coexists (1-x) fraction of unreacted zein. It will be shown later that this binding causes partial protein denaturation that exposes buried amino acid chromophores, and as a result, fluorescence emission is increased. At R = 0.2, the value of x is 1:10 (w/w) and assigning molecular weight 300 kDa to agar and 21 kDa to zein, x translates to 1:3 which implies each polymer chain was bound to 3 zein nanoparticles on the average. In Region-II, for R>0.2 the complexes continue to bind with free [A] causing large overcharged [A-Z] complexes to form. This causes the partially denatured protein surface to get covered with agar thereby burying the chromophores due to which fluorescence emission gets reduced.
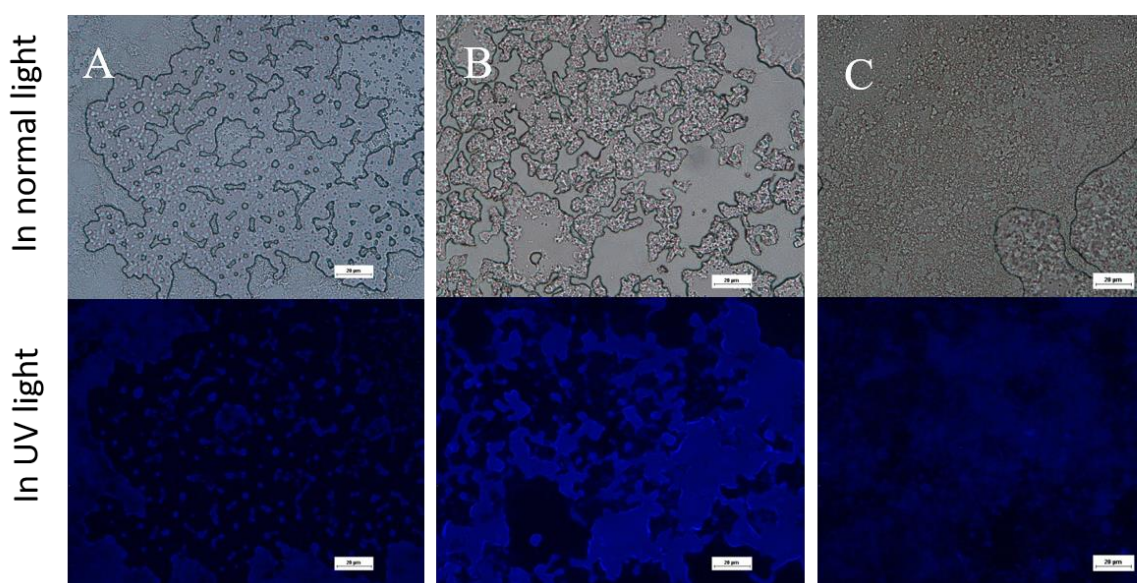


**Fig. 3.23:** Fluorescence microscopy images (magnification 40X) of complex coacervates at different mixing ratio (A) R = 0.1, (B) R = 0.2, and (C) R = 0.175 in white light (top panel) and under UV illumination (bottom panel). Notice the clear blue fluorescence emission.
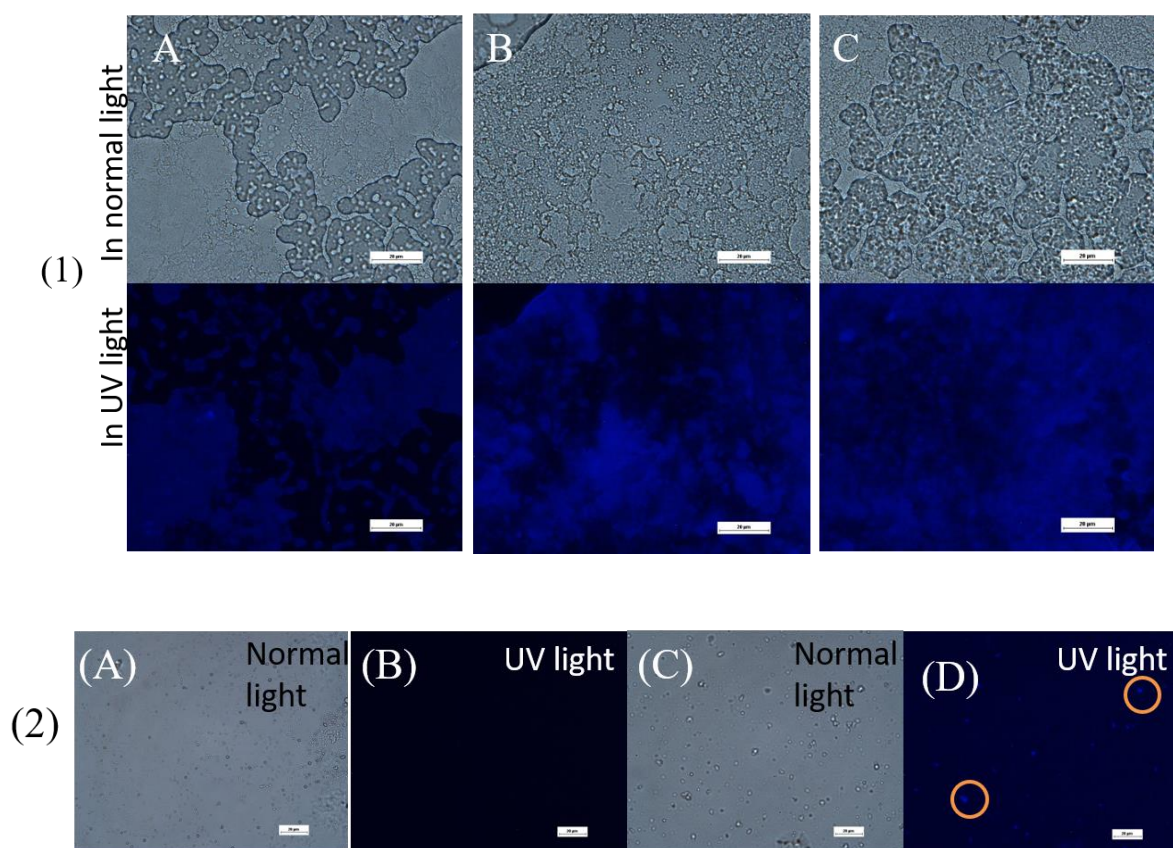
**Fig. 3.24:** (A) Fluorescence microscopy of agar-zein complex coacervates at different mixing ratio (a) R = 0.1, (b) R = 0.2, and (c) R = 0.175 in white light and blue fluorescent microscopy with magnification of 60X. (B) (a & b) Agar (0.2 %w/v) and (c & d) zein (0.5 %w/v) nanoparticle in normal and UV light.

Zeta potential ($\zeta$) is defined as the potential at the hydrodynamic slipping plane and it gives the surface charge on the molecule in the Smoluchowki model. Figure 3.25(A) represents the binding ratio dependence of zeta potential of agar-zein complexes (at R = 0.2) as a function of pH, and the data for agar and zein are included for comparison. The zeta potential for agar was observed to be negative (-20 mV) in the whole pH range of 2-10. This affirmed that agar was polyanionic in nature and zein existed as a polyampholyte with a zeta potential of 40±3 mV in the 2-4 pH range that reduced to -30 mV at pH≈8, with a clearly defined pI at 6.2. Figure 3.35(B) shows the zeta potential profile of the interpolymer complexes with the binding ratio, where the partial charge neutralization near to pI region (pH= 5.4) is clearly seen. At the pI, the protonated and deprotonated amino acids are present almost in the same ratio in a given

protein. This ascribes a characteristic charge distribution to the protein (zein) surface at a given

pH. Zein being a polyampholyte, positive patches on the surface of the zein nanoparticle tends

to binds to the negatively surface charged agar, overcoming the repulsion between similar

charge patches on zein and agar. This is the well-known surface patch bind phenomenon often

encountered in coacervates systems [Kizilay et al, 2011, Antonov et al, 2009; Park et al, 1992].
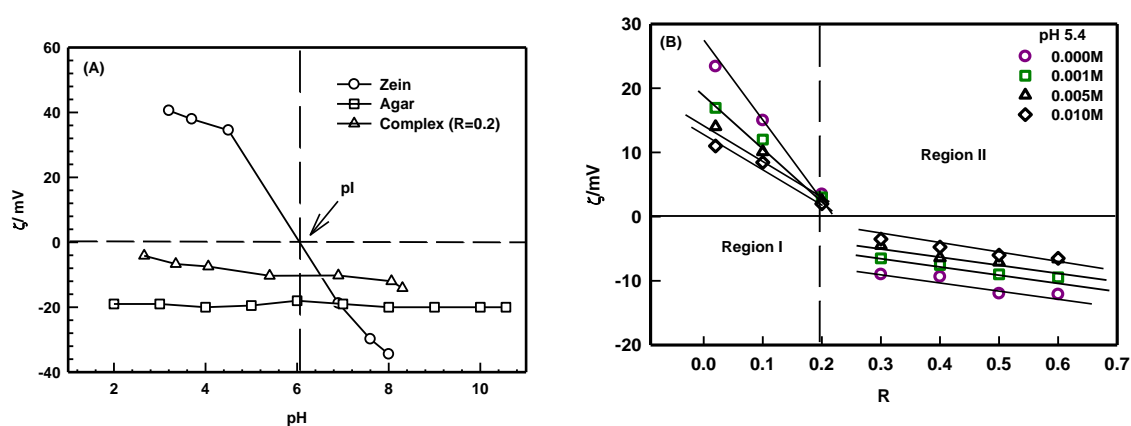


**Fig. 3.25:** (A) The variation of zeta potential with pH for zein, agar and agar-zein complex (R = 0.2) in salt-free dispersion. (B) Variation of zeta potential with the binding ratio (R) for different ionic strength for samples measured at pH≈5.4.

Zeta potential measurements were done in the ionic strength range of I = 0.0-0.01 M at

pH 5.4 (close to pI) and the data is shown Fig. 3.25 (B) which revealed the effect of counterion

binding on complexes leading to the screening of the potential at higher I for a given R. Data

clearly shows aggressive screening of surface charge of the complexes in Region I   and full

charge neutralization at R = 0.2 referring to optimum binding. Beyond this binding ratio

overcharged complexes with predominantly negative surface charge were dominant in the

dispersion (Region II). In the case of all the samples, the surface charge was observed to change

from positive to negative with the increment of agar concentration. Therefore, the role of

associative electrostatic interaction between agar and zein at pH 5.4 leading to the formation

of soluble complexes was a reality. Further, during the complex formation counterions were

released to the solvent which raised the entropy of the system facilitating aggressive binding.

### 3.3.3.2 FORMATION OF OVERCHARGED COMPLEXES AND SECONDARY STRUCTURE

The binding profile of the biopolymers is depicted in Fig. 3.26(a) is very revealing. The profile indicates two recognizable regions of association: (i) Region I which closes at R = 0.2 ([A]= 0.1% (w/v)), the turbidity increment was sharp, the zeta potential ($\zeta$) approached to charge neutralization from -23 to - 4.5 mV while turbidity increased with binding ratio and the hydrodynamic size increased in consistence with turbidity data, and (ii) in Region-II pertaining to R$\geq$0.2 turbidity, zeta potential and hydrodynamic radius all reached their plateau values. The solution turbidity remained high because of the large negative zeta potential value of the overcharged complexes. On the other hand, the particle size analysis revealed that there were two populations, one with a mean size of ~ 200 nm, and another with > 1000 nm. A time-dependent study (data not shown) revealed the abundance of the large size fraction systematically reduced in propensity (due to sedimentation) while the same of the other fraction remained unaltered. The binding profile between DNA and proteins has shown similar overcharging behavior in the past [Arfin et al, 2012; Rawat et al, 2013]. It is plausible that after the charge neutralization i.e. for R>0.2, the complexes and free agar molecules were preferentially bound through weak electrostatic forces, that produced clusters of larger size with higher zeta potential values. Thus, in order to differentiate between the bindings occurring before and after R=0.2, we shall refer to these as primary (Region I) and secondary (Region II) bindings.
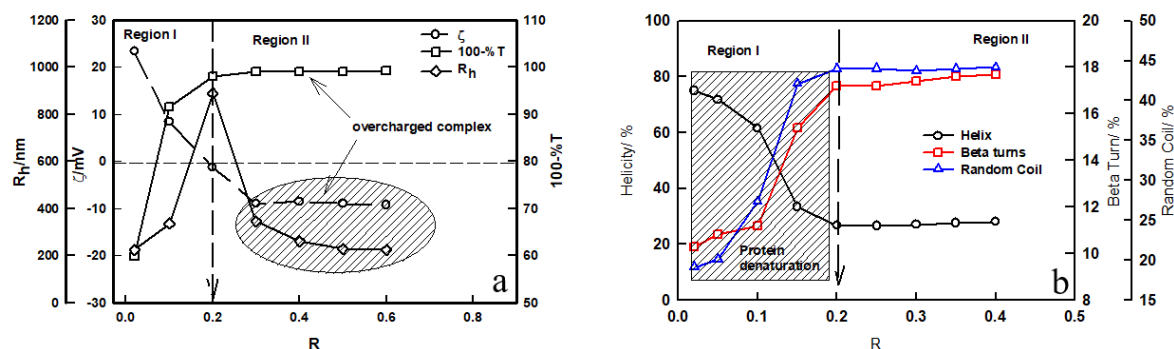
**Fig. 3.26:** (a)Variation in solution turbidity, zeta potential and hydrodynamic radius shown for different binding ratio R at [Z] = 0.5% (w/v), and pH=5.4. Notice the approach to plateau for R ≥ 0.2 which corresponds to the formation of overcharged complexes. (b) Variation of α-helix, β-sheet and random coil contents of the protein on agar concentration as a function of binding ratio determined at room temperature.

In the next step, it was felt necessary to evaluate the effect of agar on the secondary structure of the protein due to binding. For this, the samples were probed by circular dichroism spectroscopy and the profiles are shown in Fig. 3.27. This data was deconvoluted to determine their α–helix, β-sheet and random coil contents which is shown in Fig. 3.26(b) [Rawat et al, 2 012].
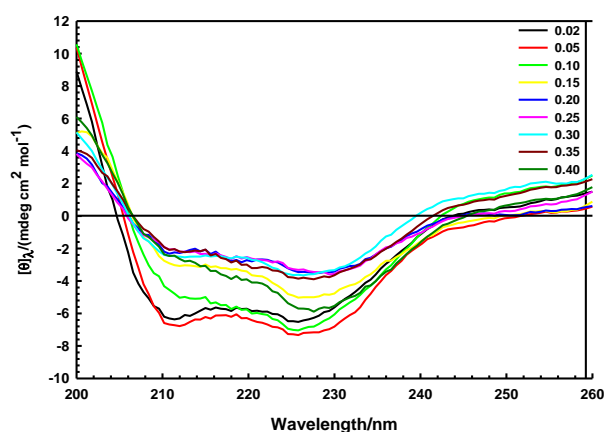


**Fig. 3.27:** Variation of circular dichroism spectra of the coacervating solutions for different R.

A perusal of this data clearly indicated the following: (i) the helical content was about 75 % for R <0.2, which gradually decreased to less than 25 % at R = 0.2, and remained invariant

thereafter. Thus, zein gradually lost its secondary structure upon binding to agar, and (ii) the individual contributions of β-sheet and random coil conformations increased till R = 0.2 and remained invariant afterward. Such an observation is consistent with the conclusion that optimum binding occurred at R = 0.2 and this caused the protein to denature.

### 3.3.3.3 EFFECT OF IONIC STRENGTH

In this study, turbidity was probed as a function of solvent ionic strength (I=0-0.1 M) at pH=5.4 in an attempt to evaluate the strength of coacervation as a function of electrostatic screening, and the data is shown in Fig. 3.28. Below R = 0.2 which we designate as Region I, turbidity decreased at higher ionic strength, I for a given R which clearly showed the role played by electrostatic screening on interpolymer complex formation. In this region, the two biopolymers exhibited aggressive associative interaction driven by electrostatic forces. Since, turbidity is a measure of size and number density of the scattering moieties, which in turn is decided by the strength of attractive forces, this data clearly implied that the interpolymer interaction was associative and electrostatic in nature. This conclusion was supported by the observation of linear dependence of turbidity on $\sqrt{I}$ which is depicted in Fig. 3.28(B). At R=0.2, the primary binding saturated, and the turbidity remained invariant of binding ratio, but the effect of electrostatic screening was continuously observed. In this region, designated as Region II, agar chains continued to bind to residual zein sites of complementary charge. However, this binding was not as aggressive as observed in Region I, which is evident from the slope of the binding profile shown in Fig. 3.28(B).

The dispersions having higher agar content (R>0.2) had more turbidity, and turbidity was invariant of R, but not of ionic strength. Zeta potential measurements revealed that the interpolymer complexes were negatively charged with the magnitude of the charge decreasing with an increase in solution ionic strength (data not shown).
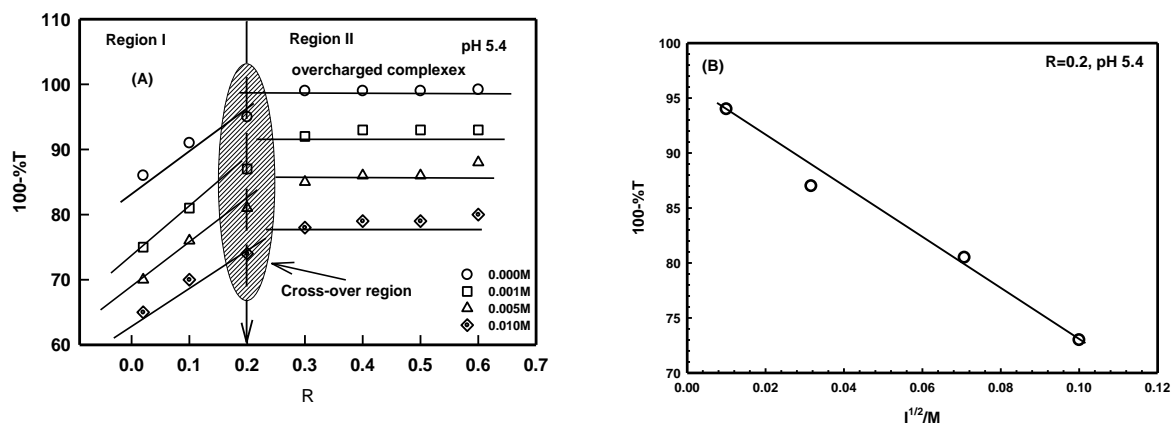
**Fig. 3.28:** (A) Effect of solution ionic strength on the turbidity of the interacting agar-zein solution shown as function of binding ratio. (B) Dependence of turbidity on the square-root of ionic strength at R=0.2. This linear dependence implies a strong electrostatic screening of interpolymer interaction. Solid lines are guided to the eye.

### 3.3.3.4 INTERACTION

The associative interaction between agar and nanoparticles of zein was modeled in the framework of DLVO theory [Derjaguin et al, 1964; Verwey et al, 1999]. In this formalism, the total potential energy, U(r) is expressed as the sum of two specific basic interactions, electrostatic $U_{elec}(r)$ and van der Waals $U_{vdW}(r)$ is given by [Vries, 2004]

$$U(r) = U_{elec}(r) + U_{vdW}(r) \tag{3.33}$$

The schematic representation of interpolymer distances and their dimensions are depicted in Fig. 3.29(A).
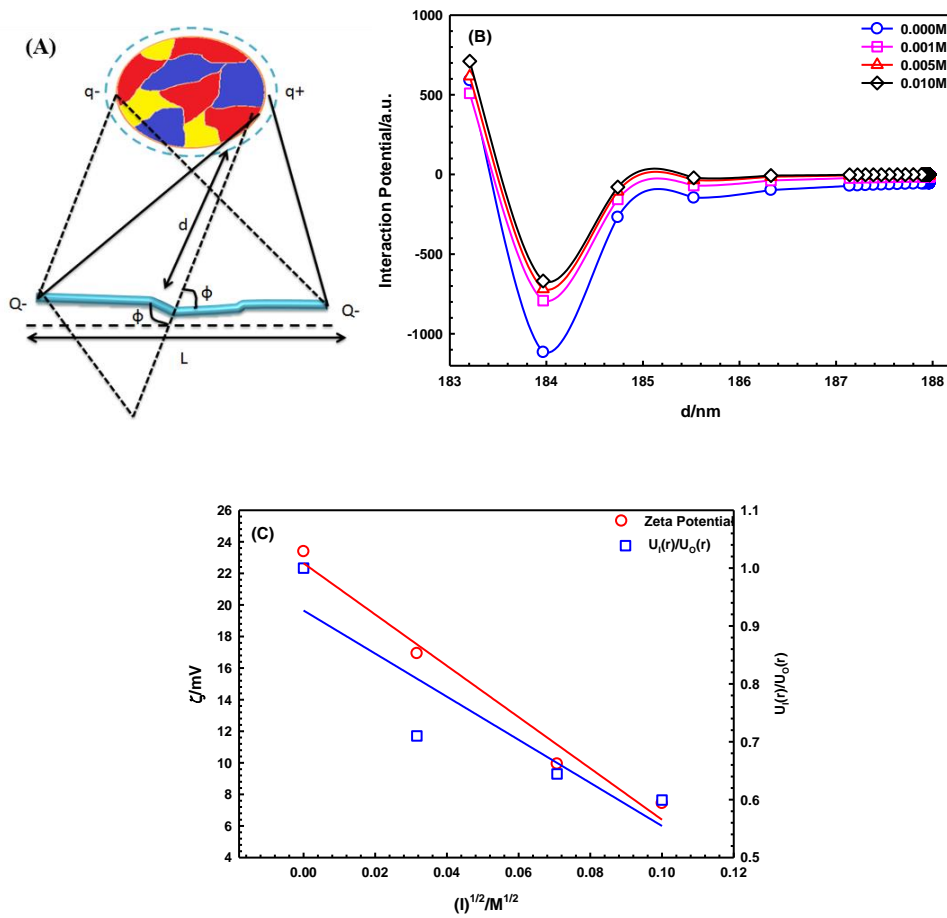
**Fig. 3.29:** (A) Geometrical representation of uniformly charged agar rod, and spherical zein particle with positive and negative charge patches, (B) variation of total interaction energy for various salt concentrations at room temperature and (C) change in zeta potential (R=0.02) and $U_I(r)/U_O(r)$ with $\sqrt{I}$ , straight lines are the least square fitted to data. The suffix I and 0 refer to the potential at finite ionic strength I and 0 respectively.

Consider agar as a uniformly charged (Q⁻ of agar at pH=5.4) finite rod of length L (L = $R_g$ √12) and as zein a polyampholyte with charge, –q and +q, each of which is the sum of contributions arising from the all deprotonated and protonated amino acid residues at pH =5.4. Electrostatic potential was calculated using the Debye-Huckel theory approximation using the geometry [Ohshima, 1995; Gögelein et al, 2008] shown in Fig. 3.29(A). This is given by

$$U_{Elec}(ij) = \frac{Q_i q_j}{4\pi \varepsilon_o \, \varepsilon_r \, r_{ij}} \ln\left(\frac{L/2 + r_{ij}}{r_{ij}}\right) e^{-k\,r_{ij}} \qquad (3.34)$$

where $r_{ij}$ is the distance between the rod and charged surface patches of a protein. So, $R_+ = r + L/2 \cos\phi$ and, $R_- = r - L/2 \cos\phi$ and, $\phi$ is the angle between charge patch of protein with respect to the rod and it varies from 0 to $\pi$. Minimization of the potential stipulated that the system was stable at $\phi = 60^0$ which yielded the optimum binding condition. Here, $\varepsilon_o$ and $\varepsilon_r$ are a vacuum and relative permittivity and $k^{-1}$ is Debye screening length, $k^{-1} = \sqrt{\frac{1000\varepsilon k_B T}{8 N_A e^2 I}}$ where $\varepsilon$, T, $k_B$, e and $N_A$ are dielectric constant of the medium, temperature, Boltzmann constant, elementary charge and Avogadro's number, respectively. Further, the mean interpolymer distance will be given by $r = \sqrt[3]{\frac{1}{N_Z + N_{Ag}}}$, with $N_Z$ and $N_{Ag}$ are approximately number density of zein and agar molecules in the dispersion which for our case will be given by $N_Z = \left(\frac{N_A}{100}\right) X \left(\frac{C_Z}{M_Z}\right)$ and $N_{Ag} = \left(\frac{N_A}{100}\right) X \left(\frac{C_{Ag}}{M_{Ag}}\right)$, where $C_{Ag}$, $M_{Ag}$, $C_Z$ and $M_Z$ are concentration (% w/v) and molecular weight of agar and zein respectively [Pathak et al, 2014; Seyrek et al, 2003; Bowman et al, 1997].

The van der Waals forces are weak so we can neglect their contribution, therefore total interaction potential is comprised of electrostatic potential only, given by

$$U(r) \sim U_{elec}(r) \tag{3.35}$$

The calculated total potential energy of interaction between agar and zein nanoparticle is shown in Fig. 6(B) for solutions of various ionic concentrations. The mean intermolecular distance was estimated to be $\approx 184$ nm. The data clearly indicated that energy minima got shallower with an increase in I, thereby implying strong electrostatic screening. Secondly, during this process, the equilibrium interpolymer separation remained largely invariant of solution ionic strength I. The normalized potential $U_I(r)/U_O(r)$ was sensitive towards iconic concentration in a manner identical to that of zeta potential, both showing $\sqrt{I}$ dependence (Fig. 3.29(C)), which is a signature of the dominance of screened Coulomb interaction. Based on this conclusion, it

was envisaged that at higher ionic strength, the coacervates would exhibit weaker electrostatic binding, lower elastic modulus and lower melting temperature. While the first two contentions were proved to be right, the dependence of melting temperature on ionic strength was just the opposite of what was expected. This will be discussed later when we deal with the viscoelastic behavior of coacervates.

### 3.3.3.5 FTIR ANALYSIS
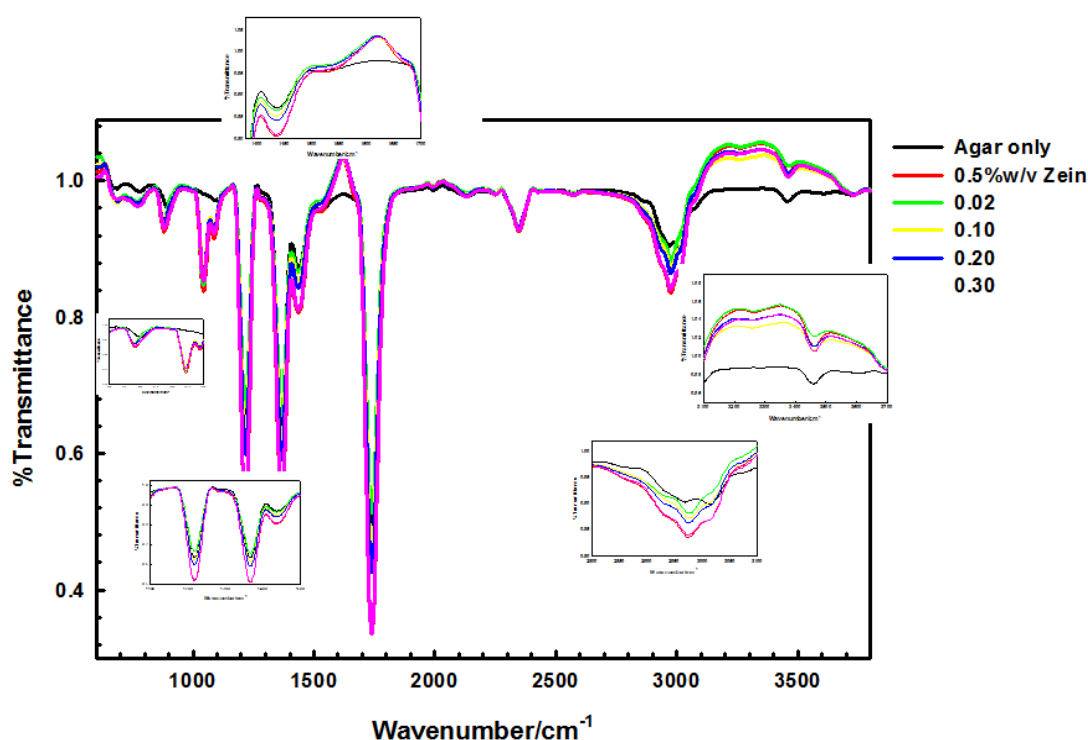


**Fig. 3.30:** FTIR data of agar (black), zein nanoparticles(red) and coacervating solutions at different R.

Fourier transform infrared spectrum of interpolymer complexes is shown in Fig. 3.30 that also includes data for biopolymers agar and zein for comparison. The N-H stretching band corresponding to the amino acids of protein emerged at 2978 (zein and complex), and 2970 and 3018 cm$^{-1}$ (agar). The O-H bond of the amino acids appeared at 3200-3500 cm$^{-1}$ (zein and complex) and 3460 cm$^{-1}$ (agar) for amide A. Amide II band represented the angular deformation vibration in N-H band appeared at 1542 cm$^{-1}$ for zein and complexes, while this

band is missing in agar. The band at 1360-1450 cm$^{-1}$ corresponded to C-H bending for agar, zein, and complex. The axial deformation vibrations of the C-N appeared at 1217 cm$^{-1}$ band for zein and complex. The band at 1044 and 1088 cm$^{-1}$ is related to stretching and vibration of C-OH of alcohol group for zein and complex while was clearly missing in agar. The stretching of =C-H bending of alcohol group emerged at 870 cm$^{-1}$ for zein and complex while for agar it was at 900 cm$^{-1}$. The bands at 3460, 2980, 1540, 1360 and 1450 cm$^{-1}$ are broadened and intensity increased with agar concentration. Similarly, 1770, 1217 and 1044 cm$^{-1}$ peaks showed an increase in with agar concentration. While for 900-800 cm$^{-1}$ intensity increased with a red shift with agar content. This data clearly indicated specific binding of agar to the amide groups of zein (mostly). These are summarized in Table-3.4.

**Table. 3.4:** Characteristics FTIR bands of agar, zein, and agar-zein coacervate samples.

| Functional Group ⟹ | O-H | N-H Amide A | N-H AmideII | C-H | C-N | C-OH | =C-H |
|---|---|---|---|---|---|---|---|
| Agar | 3460 | 2970& 3018 | ----- | 1360- 1450 | 1217 | ----- | 900 |
| Zein | 3260& 3460 | 2978 | 1542 | 1360- 1450 | 1217 | 1044& 1088 | 870 |
| Agar-Zein Complex | 3260& 3460 | 2978 | 1542 | 1360- 1450 | 1217 | 1044& 1088 | 870 |

### 3.3.3.6 SURFACE MORPHOLOGY

Surface morphology of agar-zein coacervates are clearly seen from the atomic force microscope images that provide information on the homogeneity of the complex coacervate material adsorbed onto mica surface (Fig. 3.31) [Barnes, 2000]. The height profile at R = 0.02 (Fig. 3.31A-a) showed uniform spherical zein nanoparticles with mean size of ~125 nm, while

from DLS (Fig. 3.31B) the hydrodynamic size determined was 120 nm, which are comparable. The mean size of the soluble complexes at R = 0.2 (Fig. 3.31A-b) was found to be 600 nm which again is quite similar to DLS data (700 nm). For R ≥ 0.2 the overcharged complexes had a mean size of 120 nm, these were heterogeneous and had space-filling structure. The complexes produced at R>0.2 (Fig. 3.31 (A)-c and d) were less clustered. It needs to be emphasized that for R>0.2 there was a propensity of overcharged complexes, and the possibility of large size clusters phase separating, and undergoing sedimentation cannot be ruled out. Therefore, these particular samples contained were many more individual particles of size 80-120 nm and a fewer number of larger aggregates. The size of each data point corresponds to the physical dimension of the particle.
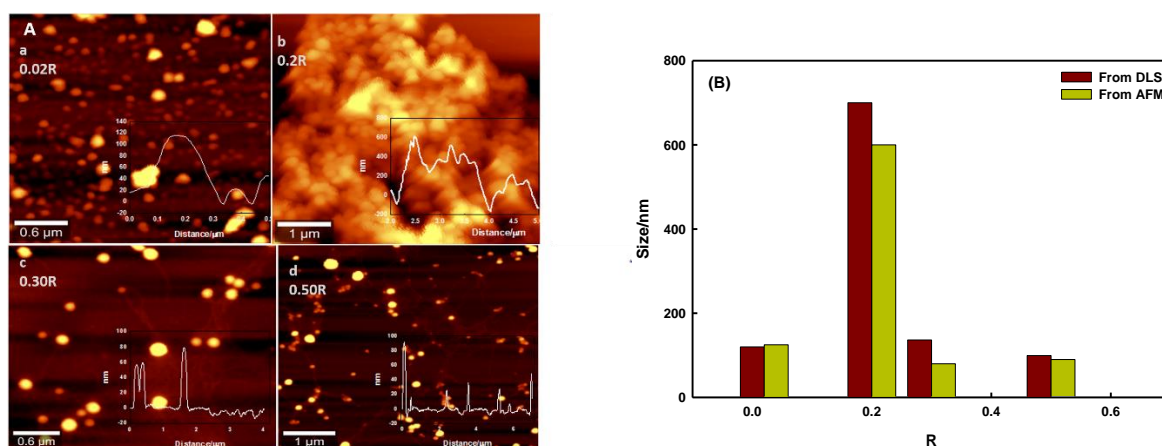


**Fig. 3.31:** (A) AFM images showing effect of agar concentration on the surface morphology of agar-zein complexes at different binding ratios: (a) R=0.02, (b) R=0.2, (c) R=0.3 and (d) R=0.5. (B) Comparison of the result from DLS and AFM.

### 3.3.3.7 CHARACTERIZATION OF COACERVATES

### 3.3.3.7.1 VISCOELASTIC PROPERTIES

In order to probe the viscoelastic profile of these coacervates rheology measurements were undertaken, and the following two distinct modes of the probe were adopted: (i) isothermal frequency and (ii) isochronal temperature sweep experiments. In the frequency

sweep studies the dispersion behavior of storage ($G'$) and loss moduli ($G''$) were examined at a constant temperature. For variable shear deformation, the elastic response of viscoelastic materials is often described by the power-law relation given by [Barnes, 2000; Singh et al, 2007]

$$G'(\omega) \sim \omega^{n'} \qquad (3.36)$$

Where $n' = 2$ for a material obeying Maxwell model, while for many viscoelastic materials (coacervates, gels etc.) [Kaushik et al, 2018] $0 \leq n' \leq 2$ with $n' = 0$ representing an ideal Hookean solid.

The measured dispersion behavior of the coacervate samples is shown in Fig. 3.32(A) and Fig. 3.33(A) in the frequency range of $\omega = 1$-$100$ rad/s. The storage modulus is a reflection of the mechanical rigidity of the material because it owes its origin to the elastic response of the material to given shear deformation. The low-frequency rigidity $G_0$ can be defined as,

$$G_0 = \lim_{\omega \to 0} G'(\omega) \qquad (3.37)$$

In the affine network model, we have shown earlier that it is possible to obtain an estimate of network density from the measured $G_0$ value [Kaushik et al, 2018].
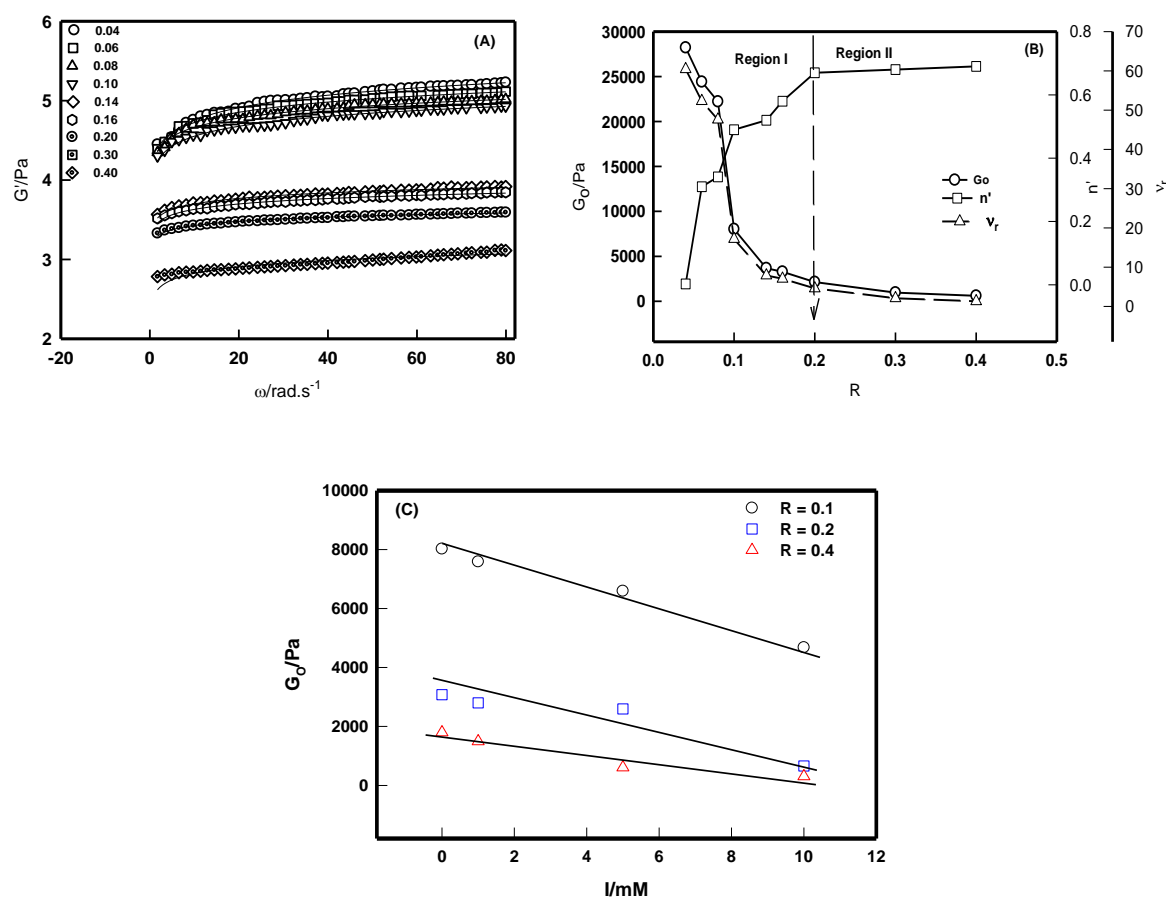
**Fig. 3.32:** (A) Variation of storage modulus G'(ω) with frequency shown for various binding ratio R. Solid lines show the least-squares fitting to the data to eqn. (3.38). (B) Change in low-frequency rigidity modulus $G_o$, n' and relative crosslink density with the binding ratio. (C) Variation of low frequency storage modulus $G_0$ with ionic strength I of the coacervate samples prepared with different binding ratio R, but at same pH=5.4. All data pertain to room temperature measurements. Solid lines are guide to the eye.

Agar is a well-known gel former, and its gel properties are well studied. Therefore, it is logical to compare the network density in the agar-zein coacervate to that of agar gel. The variation in rigidity modulus $G_o$ and relative crosslink density $v_r$ (= $v_{coac}/v_{agargel}$, $v \approx 2G_o/RT$, R is universal gas constant and T is absolute temperature) [Kaushik et al, 2018] with agar concentration is depicted in Fig. 3.32 (B). The $G_o$ value for agar-zein coacervate reduced drastically from 28 KPa to 607 Pa with R with a concomitant decrease in the value of $v_r$. This implies that at lower zein content the agar chains were able to crosslink and formed a homogeneous and strong gel-like assembly in the coacervate milieu although these were

decorated with zein nanoparticles, a situation that prevailed until the optimum binding ratio of R=0.2 was reached. Beyond that point, there was a crossover to agar gel phase because of the propensity of agar molecules. However, the disproportionately large agar population produced a heterogeneous gel with the steric hindrance provided by zein nanoparticles. The fact that the value of the power-law exponent $n'$ increased from 0.003 to 1.344, a indicating a phase transition from a rigid coacervate to soft a gel state (Fig. 3.32(B)) reinforces our contention. The viscoelastic length [Gögelein et al, 2008] $\left( \xi_{el} = \sqrt[3]{\frac{k_B T}{G_o}} \right)$ also increased which corresponded to the solid-like viscoelastic phase shown in Fig. 3.33(B). Pictorial depiction of self-assembly of agar and zein in the coacervate material is shown in Fig. 3.34.
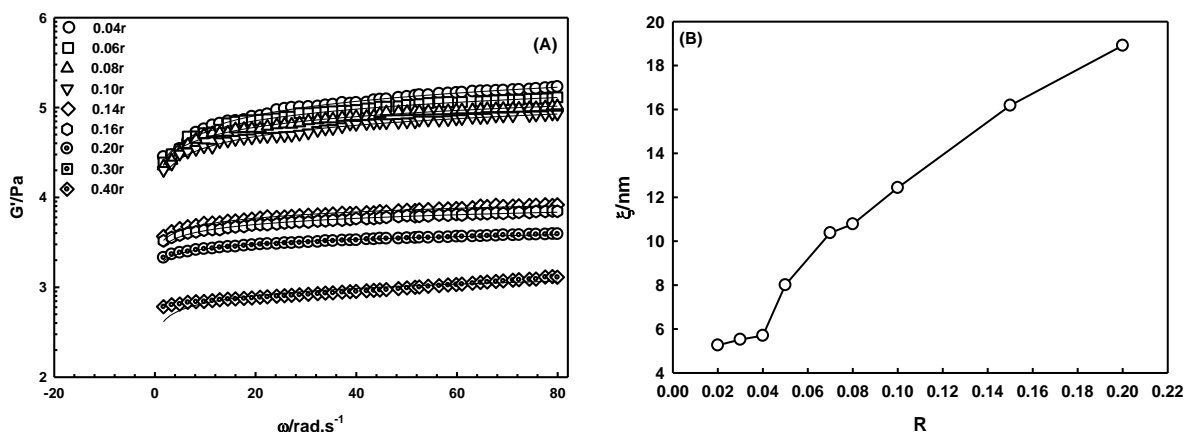


**Fig. 3.33:** (A) Dispersion of loss modulus $G''(\omega)$ of agar-zein coacervate as function of R with [Z] =0.5 %w/v. the measurements were performed at room temperature (25°C) at a constant oscillation stress of 6.3Pa. (B) Variation of viscoelastic length as function of binding ratio. Solid line is guide to eye.

Data shown in Fig. 3.32 (C) reveal two interesting features of coacervates. For a given ionic strength, I, elastic modulus decreases with binding ratio, R and for a given R it decreases with ionic strength. It is plausible that both at higher R and higher I the coacervate is in a dehydrated state which makes the material heterogeneous, and hence, poorly elastic. Salty coacervates have

shown higher elastic modulus in agar-gelatin coacervates [Boral et al, 2010]. Here, we observed the opposite behavior which may be attributed to the hydrophobic nature of zein *vis a vis* gelatin.
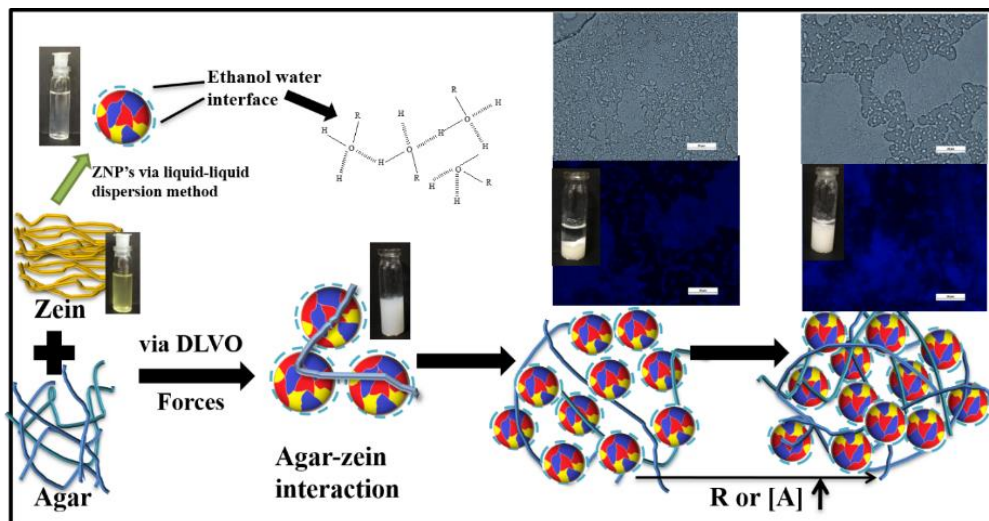


**Fig. 3.34:** Pictorial depiction of self-assembly of agar and zein in the coacervate material.

### 3.3.3.7.2 MELTING PROFILE

The melting profile of the coacervates is shown in Fig. 3.35 which was obtained from isochronal temperature sweep experiments. The data revealed two identifiable transition points which are designated as $T_{onset}$ and $T_{melt}$, and for $T > T_{melt}$ the coacervate melts into a dense liquid. A remarkable feature of this melting behavior is related to the $G_0$ values for molten samples. The samples exhibited complete melting only for samples prepared in higher ionic strength solutions. This implies that in these particular cases the complexes disentangled completely. However, the same was not true for samples prepared in low ionic strength solutions where residual entanglement of interpolymer complexes continued to persist. Further, both the $T_{onset}$ and $T_{melt}$ showed an increase with ionic strength implying stronger entanglement was facilitated at higher salt content of the sample. This can be attributed to the fact that the screened Coulomb interaction though weak would continue to facilitate inter-complex association leading to entanglements. Therefore, $T_{melt}$ varied from 56 to $68^0 C$ increasing with

the binding ratio, which basically infers to higher agar concentration of samples, and similarly, $T_{onset}$ increased from 38 to $42^0$ C in this ionic strength regime.
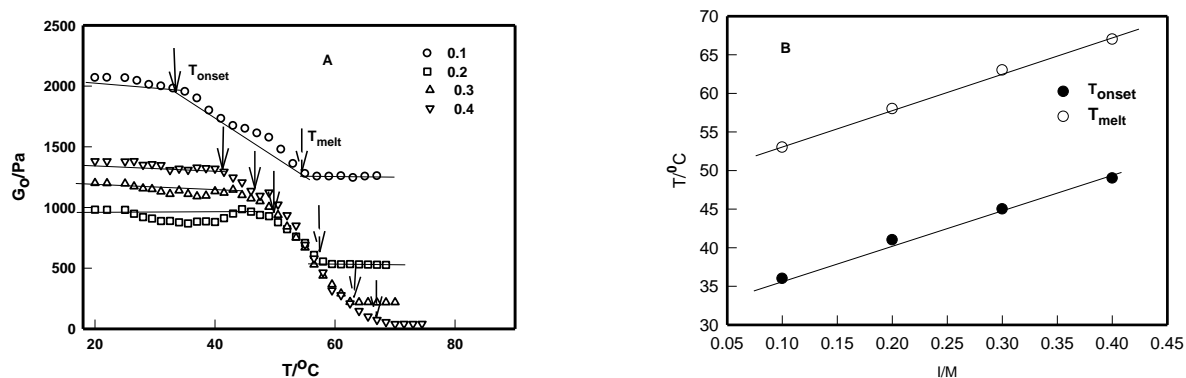


**Fig. 3.35:** Melting profiles of coacervate samples prepared (A) at different mixing ratio and (B) variation of $T_{onset}$, and $T_{melt}$ with ionic strength at R = 0.2. A temperature ramp of $1°C/min$ was used to procure the melting data. Solid lines are guided to the eye.

A relative comparison of viscoelastic properties and the internal structure of various coacervate systems is shown in Table 3.5. Perusal of this data concludes the following. Both pectin and agar are plant carbohydrates, and zein nanoparticles coacervate with these biopolymers through associative interactions. But the physical characteristic of the coacervates formed are remarkably different as far as their microstructural self-assembly is concerned which is mirrored in their viscoelastic attributes. A comparison between the two reveals that agar-zein coacervates have superior mechanical property. Therefore, complex coacervation in carbohydrates and zein solutions cannot be regarded as belonging to a universal class. Between, DNA and carbohydrates the distinction is even more sharp. Now, we have three fluorescent coacervates, namely zein-pectin, zein-DNA and zein-agar, hence we compared their luminescence intensities at their corresponding optimum ratios (See Fig. 3.36). The agar-zein sample was the most luminescent, and comparatively pectin-zein and DNA-zein samples were 40% and 80 % less bright.

**Table 3.5: Comparison between coacervation from various systems of the agar and zein.**

| S. No. | Properties | Pectin-zein* | DNA-zein** | Agar-zein |
|---|---|---|---|---|
| 1 | Interaction Type | Electrostatic | Electrostatic | Electrostatic+vdW |
| 2 | $G_o$/Pa | 3000 | 30 | 28000 |
| 3 | Mesh size ($\xi$) /nm | 12 | 2 | 14-123 |
| 4 | Viscoelastic length( $\xi_{el}$)/nm | 13 | 50 | 10 |
| 5 | Melting temperature/ $^0$C | -- | 55 | 68 |
| 6 | Optical nature | Opaque | Opaque | Opaque |

*Pectin-zein [Kaushik et al., 2018], **DNA-zein [Pandey et al., 2017] and Agar-zein (present work)
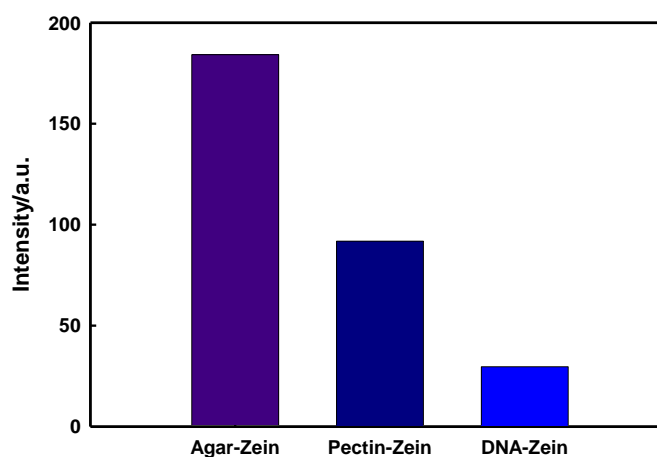


**Fig. 3.36:** Comparison of fluorescence intensity of different complex coacervates of zein with polyanions. Values refer to data at optimum binding ratio.

### 3.3.3.8 MICROSCOPIC STRUCTURE

For a better understanding of the microstructural changes occurring inside the coacervate sample as a function of binding ratio, SANS technique was used as a probe. The static structure factor profile, I(q) *vs* q for the samples was measured which clearly showed a considerable change in correlation intensity. In order to determine various physical parameters, the data was empirically treated in the following manner. First, the entire data was

fitted to $1/I(q)$ *vs* $q^2$, and $1/\sqrt{I(q)}$ *vs* $q^2$ functions which did not prove successful. In the next step, data was divided into three different q-regimes for the determination of various physical parameters on the basis of model independent best fitting functions. These were, low-q region ($4.7900e-3 \leq q \leq 0.0151$ Å$^{-1}$), intermediate q region ($0.0151 \leq q \leq 0.0438$ Å$^{-1}$) and high-q region ($q \geq 0.0438$ Å$^{-1}$).

Further, we have used the following fitting protocol to analyze the raw data: power –law in the low-q region, Debye –Bueche relation for the intermediate-q region and Guinier -Porod relation for high q-region [Gennes, 1976]. The combined function which was fitted to the structure factor data was

$$I(q) = I_{PL}(o)\, q^{-\alpha} + \frac{I_{DB}(o)}{(1+\xi^2 q^2)^2} + I_{GP}(o)exp^{-\frac{R_c^2 q^2}{2}} \right\} \quad (3.38)$$

I(q) = Power-Law + Debye-Bueche + Guinier – Porod

Here, the suffices PL, DB and GP correspond to the reference intensity of the power-law, Debye-Bueche and Guinier-Porod components. The data fitting is depicted in Fig. 3.37.
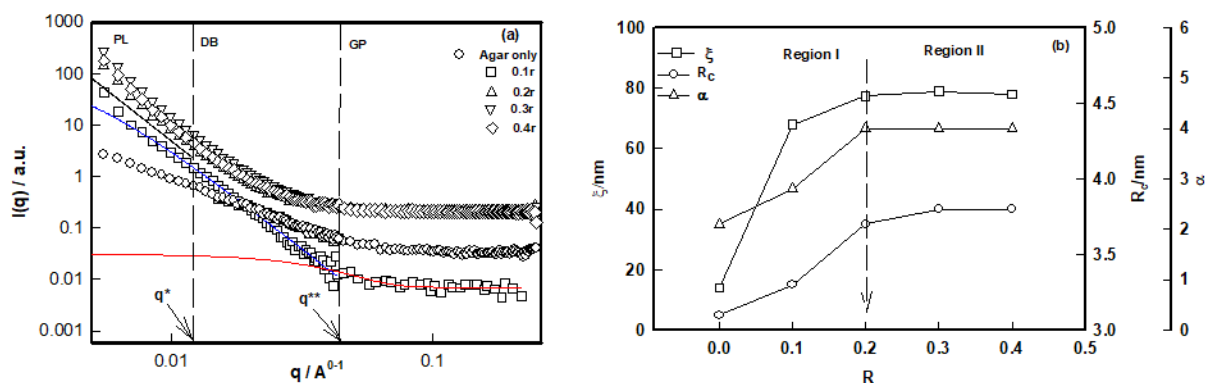


**Fig. 3.37:** (a) Static structure factor data of coacervate samples shown for various binding ratios. Dotted lines located at q* and q** divide the profile into three fitting regions: power law (PL), Debye-Bueche (D-B) and Guinier-Porod (G-P). Solid lines are fitting of the data to eqn. (3.38). (b) Variation of power-law exponent $\alpha$, mesh size $\xi$ and cross-sectional radius $R_C$ shown as a function of binding ratio. Coacervate samples were salt-free.

In the low q-region power- law fitting relation defines the scaling exponent α pertaining to the geometry of scattering center. The least square fitting of the data in the low-q region yielded α = 4±0.2, for R>0.2 which corresponds to the spherical shape of a scattering entity (mainly originating from zein nanoparticles), while at lower R, α assumed a typical value of 2.5 which is closer to a Gaussian chain description.  In the intermediate-q region, the data was fitted to Debye-Bueche relation where ξ designates the mesh size of the sample [Pathak et al, 2014]. The fitting yielded a mesh size has a value of 80 nm with was nearly invariant of mixing ratio for samples with R>0.2. It is interesting to observe that this size corresponds to the mean particle size of zein. Therefore, it will not be improper to argue that scattering moieties were mostly nanoparticles of zein. In the asymptotic region (high-q), data is defined by the Guinier-Porod function, which reveals the cross-sectional radius $R_c$ of the scattering object. The value of $R_c$ = 3.5±1.0 nm which remained invariant of the mixing ratio. We correlate this value with the cross-sectional radius of the agar strand. The coherent picture that emerges from the data analysis implies that zein nanoparticles had preferentially higher neutron scattering cross-section.

The boundary between the two Regions I and II are defined by cross-over wave vector $q^*$ and $q^{**}$ (Fig. 10(a)). These in turn yield two signature length scales $L^*$ and $L^{**}$ given by,

$$L^* = \frac{2\pi}{q^*} \text{ and } L^{**} = \frac{2\pi}{q^{**}} \tag{3.39}$$

This yields $L^* \approx 42$ nm and $L^{**} \approx 13$ nm. The typical diameter of zein nanoparticle is on the order of 120 nm, which is close to $2L^*$. Therefore, the scattering region $q<q^*$ effectively captured the scattering emanating from zein nanoparticles. The persistence length of agar is typically 6 nm which corresponds to the value of $2L^{**}$, thus for $q>q^{**}$ the neutron scattering probed the persistent regime of agar and could evaluate its cross-sectional radius $R_c$.

### 3.3.4 CONCLUSION

We have reported the synthesis and comprehensive characterization of a fluorescent complex coacervate prepared by interacting *in situ* formed zein nanoparticles with agar under ambient conditions at different binding ratio. The interpolymer complex formation involved two distinct binding regions; (i) primary soluble complexes were formed at low polymer binding ratio (R<0.2) which were mostly charge neutralized with zein showed denaturation, and (ii) residual interactions prevailed at higher binding ratio (R>0.2) yielding overcharged complexes through secondary binding. For a given binding ratio, coacervates prepared in low ionic strength solutions revealed higher storage modulus, higher network density, but lower melting temperature. At higher ionic strength, the opposite behavior was noticed. This can be explained as follows. Zein being a polyampholyte, it has both positive and negatively charged patches on its surface at any pH. Agar preferentially binds to oppositely charged patch on zein while the repulsion arising from similarly charged patch and agar remains antagonistic to this binding, thereby constantly exposing this self-assembly to strain. This will be a dominant feature when the ionic strength is low. Therefore, the coacervate material will melt at lower temperature. On the other hand, at higher ionic strength, due to the propensity of mobile counterions both the biopolymers carry very low surface charge. Here, the self-assembly is largely guided by van der Waals forces and no antagonistic forces are at play. Such a situation will lead to more homogeneity in the material, and higher melting temperature. The interpolymer complex formation was modeled in the framework of electrostatic interaction theory and results could successfully describe the experimental data. As far as the associative properties are concerned, there seem to be one universal phenomenon which is the capacity of biomolecules to form overcharged complexes which was noticed in the case of a wide range of DNA-protein coacervates including the system discussed here [Pandey et al, 2017; Arfin et al, 2012; Rawat et al, 2013; Pathak et al, 2014]. However, from the microstructure point of view

these coacervates offer considerable diversity [Mohanty et al, 2005]. Since, fluorescent coacervate biomaterial with tunable viscoelastic properties may find applications in the real time tracking of drugs to the target, and confocal imaging of cells, and there is a paucity of fluorescent coacervates made of biomaterials the importance of present study holds sufficient promise.

## 3.4 References

1. Arfin N., & Bohidar H.B. (2012). Condensation, complex coacervation, and overcharging during DNA–gelatin interactions in aqueous solutions. *The Journal of Physical Chemistry B*, 116(44), 13192-13199.

2. Barnes B.J., & Pecora R. (1976) Dynamic light scattering, Wiley Interscience, New York.

3. Barnes H. A. (2000). Handbook of Elementary Rheology. *University of Wales Press: Wales.*

4. Bohidar, H. B. (2015). *Fundamentals of polymer physics and molecular biophysics*. Cambridge University Press.

5. Bohidar, H. B., & Mohanty, B. (2004). Anomalous self-assembly of gelatin in ethanol-water marginal solvent. *Physical Review E*, *69*(2), 021902.

6. Boral S., & Bohidar H.B (2010). Effect of Ionic Strength on Surface-Selective Patch Binding-Induced Phase Separation and Coacervation in Similarly Charged Gelatin−Agar Molecular Systems. *The Journal of Physical Chemistry B*, 114(37), 12027-12035.

7. Bowman W.A., Rubinstein M., & Tan J. S. (1997). Polyelectrolyte− Gelatin Complexation: Light-Scattering Study. *Macromolecules*, 30(11), 3262-3270.

8. Chen, H., & Zhong, Q. (2015). A novel method of preparing stable zein nanoparticle dispersions for encapsulation of peppermint oil. *Food Hydrocolloids*, *43*, 593-602.

9.  Cheng, J. C., Vigil, R. D., & Fox, R. O. (2010). A competitive aggregation model for flash nanoprecipitation. *Journal of colloid and interface science*, *351*(2), 330-342.

10. De Gennes P. G. (1976). Dynamics of entangled polymer solutions. II. Inclusion of hydrodynamic interactions. *Macromolecules*, 9(4), 594-598.

11. Derjaguin B.V., & Voropayeva T.N. (1964). Surface forces and the stability of colloids and disperse systems. *Journal of Colloid Science*, 19(2), pp.113-135.

12. Djabourov M., Clark A.H., Rowlands D.W., & Ross-Murphy S.B. (1989). Small-angle x-ray scattering characterization of agarose sols and gels. *Macromolecules*, 22(1), 180-188.

13. Flory, P. J. (1953). Principles of polymer Chemistry; Cornell University. *Ithaca, New York*, *579*.

14. Gekko, K., & Timasheff, S. N. (1981). Mechanism of protein stabilization by glycerol: preferential hydration in glycerol-water mixtures. *Biochemistry*, *20*(16), 4667-4676.

15. Gögelein C., Nägele G., Tuinier R., Gibaud T., Stradner A., & Schurtenberger P.A. (2008). simple patchy colloid model for the phase behavior of lysozyme dispersions. *The Journal of Chemical Physics*, 129(8), 08B615.

16. Gomez-Estaca J., Balaguer M.P., Gavara R., & Hemandez-munoz P. (2012). Formation of zein nanoparticles by electrohydrodynamic atomization: Effect of the main processing variables and suitability for encapsulation the food coloring and active ingredient curcumin. *Food Hydrocoll,* 28, 82-91.

17. Gupta, A. N., Bohidar, H. B., & Aswal, V. K. (2007). Surface Patch Binding Induced Intermolecular Complexation and Phase Separation in Aqueous Solutions of Similarly Charged Gelatin− Chitosan Molecules. *The Journal of Physical Chemistry B*, *111*(34), 10137-10145.

18. Joshi, N., Rawat, K., & Bohidar, H. B. (2016). Characterization of microstructure, viscoelasticity, heterogeneity and ergodicity in pectin–laponite–CTAB–calcium nanocomposite hydrogels. *Carbohydrate polymers*, *136*, 242-249.

19. Joshi, N., Rawat, K., & Bohidar, H. B. (2016). Influence of Structure, Charge, and Concentration on the Pectin–Calcium–Surfactant Complexes. *The Journal of Physical Chemistry B*, *120*(18), 4249-4257.

20. Kaushik P., Rawat K., Aswal V.K., Kohlbrecher J., & Bohidar H.B. (2018). Mixing ratio dependent complex coacervation versus bicontinuous gelation of pectin with in situ formed zein nanoparticles. *Soft matter*, 14(31), 6463-6475.

21. Kizilay E., Kayitmazer A.B., & Dubin P.L. (2011). Complexation and coacervation of polyelectrolytes with oppositely charged colloids. *Advances in Colloid and Interface Science*, 167(1-2), 24-37.

22. Li, K. K., Zhang, X., Huang, Q., Yin, S. W., Yang, X. Q., Wen, Q. B., ... & Lai, F. R. (2014). Continuous preparation of zein colloidal particles by Flash NanoPrecipitation (FNP). *Journal of Food Engineering*, *127*, 103-110.

23. Li, Y., Xia, Q., Shi, K., & Huang, Q. (2011). Scaling behaviors of α-zein in acetic acid solutions. *The Journal of Physical Chemistry B*, *115*(32), 9695-9702.

24. Lumry R., & Eyring H. (1954). Conformation changes of proteins. *The Journal of Physical Chemistry*, 58(2), 110-120.

25. Mohanty B., & Bohidar H. B. (2005). Microscopic structure of gelatin coacervates, *International journal of biological macromolecules*, 36(1-2), 39-46.

26. Ohshima H. (1995). Electrophoresis of soft particles. *Advances in Colloid and Interface Science*, 62(2-3), 189-235.

27. Pandey P.K., Kaushik P., Rawat K., Aswal V.K., & Bohidar H.B. (2017). Solvent hydrophobicity induced complex coacervation of dsDNA and in situ formed zein nanoparticles. *Soft Matter*, 13(38), 6784-6791.

28. Park J.M., Muhoberac B.B., Dubin P.L., & Xia, J. (1992). Effects of protein charge heterogeneity in protein-polyelectrolyte complexation. *Macromolecules*, 25(1), 290-295.

29. Patel A., Hu Y., Tiwari J.K., & Velikov K.P. (2010). Synthesis and characterisation of zein–curcumin colloidal particles. *Soft Matter*, 6(24), 6192-6199.

30. Pathak J., Rawat K., & Bohidar H.B. (2014). Surface patch binding and mesophase separation in biopolymeric polyelectrolyte–polyampholyte solutions. *International Journal of Biological Macromolecules*, 63, 29-37.

31. Pathak, J., Rawat, K., & Bohidar, H. B. (2016). Thermo-reversibility, ergodicity and surface charge–temperature dependent phase diagram of anionic, cationic and neutral co-gels of gelatin–BSA complexes. *RSC Advances*, *6*(46), 40123-40136.

32. Rawat K., & Bohidar H.B. (2012). Universal charge quenching and stability of proteins in 1-methyl-3-alkyl (hexyl/octyl) imidazolium chloride ionic liquid solutions, *The Journal of Physical Chemistry B*, 116(36), 11065-11074.

33. Rawat K., Pathak J., & Bohidar H.B. (2013). Effect of persistence length on binding of DNA to polyions and overcharging of their intermolecular complexes in aqueous and in 1-methyl-3-octyl imidazolium chloride ionic liquid solutions. *Physical Chemistry Chemical Physics*, 15(29), 12262-12273.

34. Seyrek E., Dubin P.L., Tribet C., & Gamble E.A. (2003). Ionic strength dependence of protein-polyelectrolyte interactions. *Biomacromolecules*, 4(2), 273-282.

35. Singh S. S., H. B. Bohidar, & S. Bandyopadhyay, (2007) Study of gelatin-agar intermolecular aggregates in the supernatant of its coacervate. *Colloids Surf B Biointerfaces*, 57(1), 29-36.

**36.** Singh S.S., Aswal V.K., & Bohidar H.B. (2007). Structural studies of agar–gelatin complex coacervates by small angle neutron scattering, rheology and differential scanning calorimetry. *International journal of biological macromolecules*, 41(3), 301-307.

37. Taylor, J. D. (2013). Zein: Novel natural polymer for nanoparticle-and film-mediated gene delivery.

38. Ventura, I., Jammal, J. and Bianco-Peled, H., 2013. Insights into the nanostructure of low-methoxyl Pectin–calcium gels. *Carbohydrate polymers*, *97*(2), pp.650-658.

39. Verwey E.J.W., & Overbeek J.T.G. (1999). Theory of the stability of lyophobic colloids. *Courier Corporation*.

40. Vries R. De (2004). Monte Carlo simulations of flexible polyanions complexing with whey proteins at their isoelectric point. *The Journal of Chemical Physics*, 120(7), 3475-3481.

41. Waller R, Strang TJK (1996) Collection Forum 12:70-85.

42. Wang H-J, Lin Z-X, Liu X-M, Sheng S-Y, Wang J-Y (2005) Heparin-loaded zein microsphere film and hemocompatibility. J. Control. Release 105: 120-131.

43. Wang RX, Tian ZG, Chen LY (2011) Nano-encapsulations liberated from barley protein microparticles for oral delivery of bioactive compounds. Int. J. Pharm. 406:153-162.

44. Wang Y, Padua GW (2010) Formation of zein microphases in ethanol-water. Langmuir, 26:12897-12901.

45. Zhong Q., and M. Jin, Zein nanoparticles produced by liquid–liquid dispersion, *Food Hydrocoll.* 2009, **23**, 2380-2387.

CHAPTER 5

# PHASE STABILITY AND BEHAVIOR STUDY OF ELASTIN IN AQUEOUS AND BINARY SOLVENT: INTERACTION WITH STRONG POLYELECTROLYTE

**OVERVIEW**

This chapter described the insight of unusual dispersion and anomalous diffusion of elastin in ethanolic solution. Elastin coacervation was studied close to isoelectric point, and this thermally activated self-assembly leading to phase separation. Study of the different phase resulting from the interaction of elastin and strong polyelectrolyte using various technique.
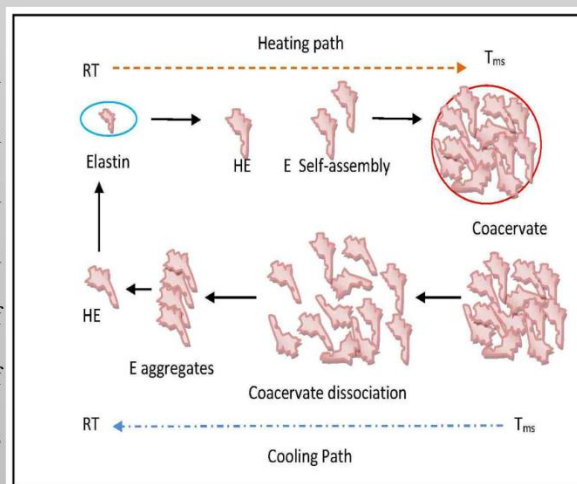


## [PART-A]

## 5.1 HYDROPHOBIC HYDRATION AND ANAMALOUS DIFFUSION OF ELASTIN IN ETHANOLIC SOLUTION

### 5.1.1 MOTIVATION

Elastin is briefly explained in Chapter 1. Elastin has found potential use in bioengineering and biomedical applications [Sell et al 2010; Zou et al, 2011; Keeley et al, 2002]. However, even with its varied application potential, fundamental questions related to its molecular assembly in different solvent environment remains poorly probed, and much less understood which comprises the main motivation of the present work. In section 5.1 of Chapter

pH RESPONSIVE DOXORUBUCIN LOADED ZEIN NANOPARTICLE CROSSLINKED

PECTIN HYDROGEL AS EFFECTIVE SITE-SPECIFIC ANTICANCER SUBSTRATES

**OVERVIEW**

This chapter describes pH-responsive hydrogels of hierarchically self-assembled protein (zein, in the form of its nanoparticles) and polysaccharide (pectin), where gelation occurs below pH 3 in the absence of crosslinkers, which we used for the encapsulation and release of anticancer drug Doxorubicin (DOX) in the cell nucleus.
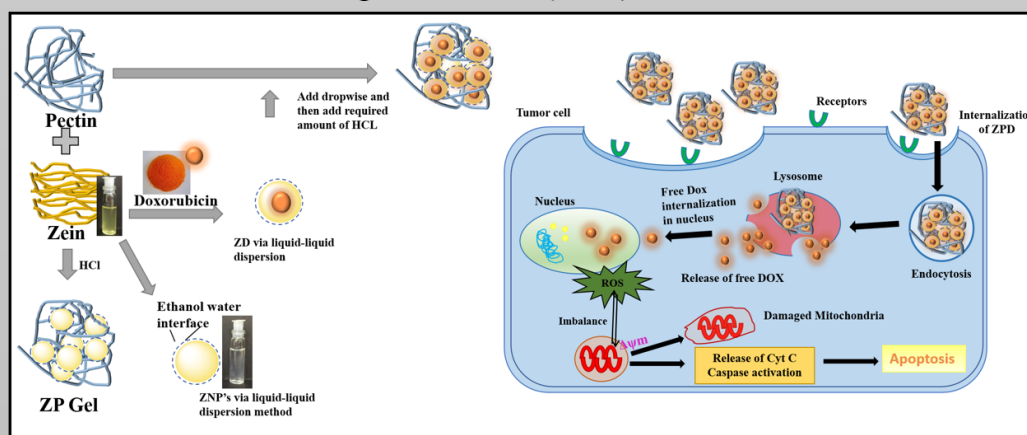


## 4.1 MOTIVATION

The effectiveness of hydrogels as a drug-delivery system has been evaluated in recent years, basically on melanoma cells.  Hydrogels of hydroxypropyl-β-cyclodextrin were encapsulated with curcumin, a water insoluble polyphenol which resulted in improved stability, solubility and permeability when targeted for melanoma treatment [Sun et al, 2014]. Likewise,

an ibuprofen-releasing hydrogel has been reported as a transdermal formulation that reduces spread of melanoma by inhibiting cellular migration [Redpath et al, 2009]. Further, hydrogels can efficiently deliver more than two therapeutic agents, thus favouring multiple target delivery which is an essential strategy to minimize drug resistance and tumour metastasis [Wang et al, 2015; Dai et al, 2015]. Doxorubicin (DOX) is a broad-spectrum anti-cancerous drug widely used in clinical treatment [Singal et al, 1998; Buzdar et al, 1985]. The generation of reactive oxygen species (ROS) by DOX in tumor cells is one of the known basis of tumor cell killing, though the exact mechanism is still not clear [Sinha et al, 1989; Gouazé et al, 2001]. However, the usage of DOX above a certain concentration is linked to cardiotoxicity with adverse effects as cardiomyopathy and heart failure [Buzdar et al, 1985]. Therefore, appropriate usage along with a regulated therapeutic approach that minimizes the release of DOX in cells is necessary. Zein has been used as a delivery system for hydrophobic drugs by co-precipitation method wherein the molecules bind to zein via hydrophobic and hydrogen bond formation. Moreover, zein is known to preserve the activity of encapsulated bio-molecule under harsh conditions while pectin counterpart provides high solubility in aqueous system [Luo et al, 2014].

In this chapter, a synergetic zein-pectin (ZP) hydrogel formulation capable of encapsulating DOX is described. As the association of DOX with some carrier molecule or its encapsulation can limit its dispersion and accumulation, thereby reducing its interaction with healthy tissues, we have used ZP hydrogels as encapsulating agent. We have systematically studied the efficacy of formed ZP hydrogel system in localization and delivery of the anti-cancerous drug, DOX. The physical characterization of the hydrogels was performed by UV-Visible, fluorescence spectroscopy, dynamic light scattering, zeta potential studies and rheological profiling. The cytotoxicity was evaluated on HeLa (cervical cancer cell line) and HEK93(endothelial cell line) via MTT and microscopy studies. The generation of ROS factors was also analyzed by treating cells with Zein-pectin Doxorubicin (ZPD) in a dose-dependent manner. The cellular uptake

and localization of ZPD was determined by confocal microscopy and alteration in cell ultrastructure was investigated by TEM. Thus, Zein-Pectin hydrogel system loaded with drug is a promising candidate that enhances drug-delivery efficiency.

## 4.2 SAMPLE PREPARATION

### 4.2.1 HYDROGEL PREPARATION

Zein (2 % w/v) powder was dissolved in a binary solvent of ethanol-distilled water (80:20 % v/v) by stirring for one hour at room temperature, $20^0$ C. Pectin (P) (3 % w/v) powder was dispersed in distilled water by continuous stirring for four hours at $40^0$ C. Zein nanoparticle (Z) was formed by liquid-liquid dispersion method. Zein-pectin complex was prepared at after its optimum binding ratio ([P]/[Z]=1) as reported earlier with some modification [Kaushik et al, 2018]. The concentrations of zein (0.5 %w/v) and pectin (1 % w/v) were kept constant in all solutions. Required amount of pectin was added to deionized water from its stock solution and then stirred to for 10 minutes to get a homogenous solution to which required amount of zein was added dropwise from its stock solution (in-situ formed zein nanoparticles) and then solution was stirred to get homogenous solution to prepare a typical sample. The pH of zein stock, pectin stock, zein nanoparticle dispersion, and zein-pectin complex dispersion were 5.3±0.2, 4.2±0.2, 3.8±0.2, and 4±0.1, respectively. Zein-pectin complex dispersion was titrated with HCl which yielded the desired hydrogel of zein-pectin (ZP) below pH 3. For the synthesis of drug loaded hydrogel, Doxorubicin (DOX) (2.7 mg) was added in the stock solution of zein and then the solution was stirred for one more hour to make a homogenous solution, which produced DOX encapsulated zein nanoparticle (ZD) by liquid-liquid dispersion method, and rest of the procedure was same as discussed earlier for the hydrogels. The hydrogel had DOX concentration of 0.0067 % (w/v).

**4.2.2 CELL CULTURE**

In this study, we used HeLa and HEK293 cell lines to analyse the cytotoxicity potential of prepared hydrogels. The cells were obtained from National Centre for Cell Science, Department of Biotechnology, Pune, India. Cell lines were cultured in RPMI-1640 medium supplemented with 10% (v/v) fetal bovine serum (FBS) and antibiotics (streptomycin 10µg/ml, penicillin 100 U/ml) and incubated in $CO_2$ (5%) incubator at 37ºC. Cell lines were sub cultured by trypsinization on attaining confluence.

**4.2.3 CELL CYTOTOXICITY ASSESSMENT ASSAYS**

**4.2.3.1 CELL PROLIFERATION/VIABILITY ASSAY**

Cellular proliferation was determined using MTT ((3-(4, 5-Dimethylthiazol-2-yl)-2, 5-diphenyltetrazolium bromide) on both HeLa and HEK293 cell lines. For this, 96 well plates were seeded with cells at a density of 5 x $10^3$ cells/ well and incubated overnight, to allow the adherence of cells. After 24-hour interval, old medium was removed and cells were supplemented with fresh medium containing varying concentration of hydrogels and further incubated for 24 hours interval. Media was removed, 30 µL of MTT (1mg/ml) was added and plate was incubated for 4 hours. On completion of incubation time, 200 µL DMSO was added after removing MTT solution. Absorbance was recorded on an ELISA plate reader at 595 nm and percentage inhibition with respect to control (cells without hydrogel) was determined from the absorbance value using the following formula [Singh et al, 2016]. All the experiments were performed in triplicates.

**4.2.3.2 DETERMINATION OF REACTIVE OXYGEN SPECIES (ROS)**

Generation of reactive oxygen species (ROS) on treating HeLa cell lines with hydrogels was analysed using 2,7-dichlorofluoresceindiacetate (DCFHDA) dye. HeLa cells were seeded at a density of $5 \times 10^5$ cell/ well and allowed to adhere for 12 hours. Cells were thereafter treated

with (DOX-loaded and WO DOX hydrogels), allowed to interact for 12 hours. On completion of treatment duration, DCFDA (10 μM) was added, incubated at 37°C for 30 minutes, lysed with alkaline and washed twice with 1X PBS (pH 7.4) and fluorescence intensity was recorded using 485 excitation and 520 nm emission on RF-5301 PC Shimadzu spectrofluorometer, Nakagyo-ku, Kyoto, Japan) [Kaur et al, 2018; Kumar et al, 2016].

## 4.2.3.3 CELLULAR UPTAKE AND CONFOCAL MICROSCOPY ANALYSIS

Doxorubicin drug is an inherently fluorescent drug, therefore we analyzed its cellular uptake and localization using laser confocal microscope (Olympus Fluo View TM FV1000) at excitation wavelength of 565 nm. The cells were treated with varying concentration (2.5, 5 and 10μL) of DOX-loaded hydrogels and incubated for 4 hours at 37°C in 5% $CO_2$ incubator. After treatments, cells were washed with 1X PBS, pH 7.4, trypsinized and centrifuged at 2000 rpm for 5 mins. The supernatant was discarded and pellet resuspensed in 1X PBS and viewed thereafter. Similar set of experiments was performed by treating HeLa cells with DOX loaded hydrogels for different time duration (30 mins, 1, 4 and 6h).

## 4.2.4 CELL MORPHOLOGY ANALYSIS

To determine the morphological changes induced by treatment of HeLa cells with hydrogels, microscopic analysis was performed. Treated cells were observed under an inverted microscope at regular time intervals for analyze morphological variations. Changes in cellular ultra-structure were determined via transmission electron microscope (JEOL-TEM-2100F) at 200 kV. For this, Hela cells were harvested after 12 hours of treatment with hydrogels (concentration) by trypsinization. Harvested cells were prefixed with 2.5% glutaraldehyde, post-fixed with 1% osmic acid followed by alcohol dehydration. The dehydrated cells were embedded in Epon 812 and cut into ultrathin sections of 70-80 nm using Ultramicrotom (Leica Ultracut—UCT).

## 4.3 RESULTS AND DISCUSSION

### 4.3.1 INTERMOLECULAR INTERACTIONS

At the outset, it was felt imperative to evaluate the characteristic properties of the precursor biopolymers and their various complexes. This was necessary to differentially place the DOX loaded zein-pectin hydrogels *vis a vis* various other complexes. This required that the zein nanoparticles (Z), pectin (P), DOX, zein-pectin complex (ZP), zein-Dox complex (ZD) and zein-pectin-DOX (ZPD) were individually profiled. Three signature physical parameters were chosen for this profiling, namely, surface charge (in terms of zeta potential, $\zeta$), size (in terms of apparent hydrodynamic radius, $R_h$) and solution turbidity (in terms of transmittance %T). While the zeta potential and hydrodynamic radius refer to the intrinsic properties, the turbidity is a measure of dispersion stability of the biopolymers or their complexes as the case may be. This data is depicted in Fig. 4.1(a), and the size histogram is shown in Fig. 4.1(b-f). The shown data pertains to solution pH=2.47 and measurements were performed on diluted (x10) samples. We have shown earlier that the optimum binding condition between zein and pectin occurred at the stoichiometric binding ratio of [P]: [Z]=1:1 [Kaushik et al, 2018]. Further, zein has a pI of 6.2 and pectin is polyanionic which stipulates that at the experimental pH=2.47, there would be attractive electrostatic interaction between the two biopolymers which is clearly noticed from the data in Fig. 4.1 [Luo et al, 2015]. The zein-pectin complex shows a zeta potential of ~10 mV, size of 100 nm and turbidity of ~ 80 % clearly implying the condensation of pectin chain on zein nanoparticle surface driven by charge neutralization. In the case of zein-pectin-DOX complexes (ZPD), we found maximum turbidity indicating the formation of large soluble complexes of apparent hydrodynamic size of ~ 300 nm and zeta potential of ~ 10 mV. A relative comparison with the zein-DOX (ZD) sample reveals that addition of pectin helped to increase the aforesaid parameters by about 10 % in turbidity, and 20% in size, but there was significant decrease in zeta potential. This decrease can be attributed

to the binding of pectin to the DOX loaded zein nanoparticles which had a larger surface area with complementary charge to that of pectin. Such a binding caused the formation of extensively charge neutralized ZPD complexes that were associated with larger size and solution turbidity. The data shown in Fig. 4.1(a) bears testimony to this. Fig. 4.1(b to f) illustrates the size histograms of various samples. Only, the ZPD sample was seen to follow a Gaussian type size distribution with a mean value of 300 nm as shown in Fig. 4.1(f). All other samples were associated with a large polydispersity. In summary, preferential binding of pectin to DOX loaded zein nanoparticles was observed which was facilitated by associative electrostatic interactions. In passing, it needs to be specified that all measurements were done at the same pH of 2.47 so there was no artifact of pH in the data reported.
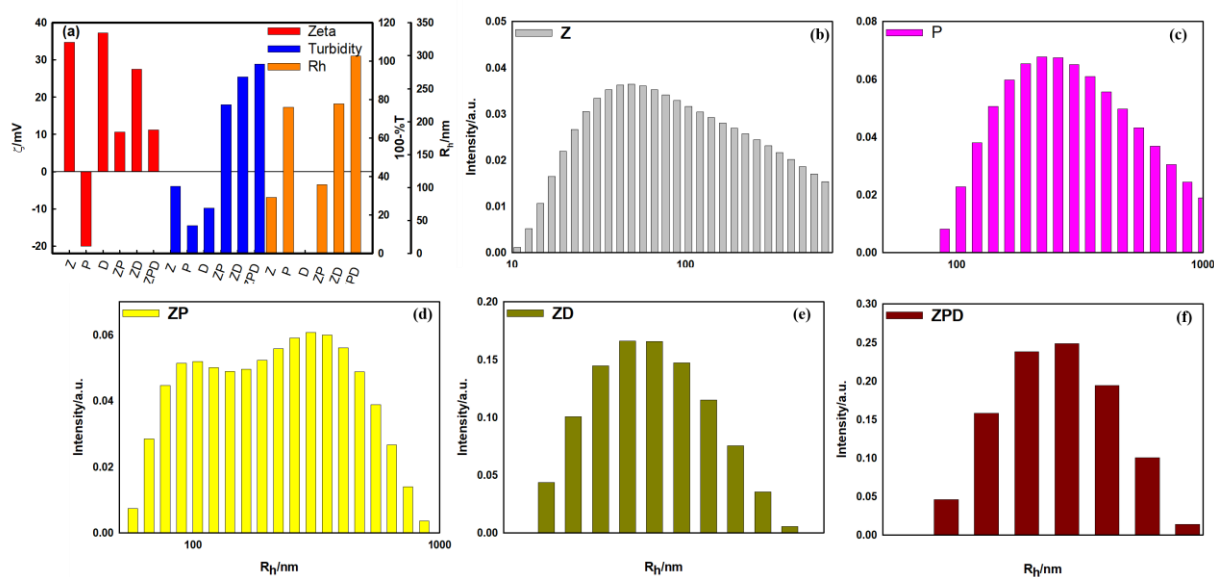


**Fig. 4.1:** Variation of **(a)** Zeta potential, turbidity and hydrodynamic radius. Size distribution histogram of **(b)** ZN, **(c)** Pectin (P), **(d)** ZP, **(e)** ZD, and **(f)** ZPD samples.

Characteristics peak of zein at 3460 and 1542 cm$^{-1}$ corresponding to -OH and the angular deformation vibration in N-H band (Amide II) respectively are shown in Fig. 4.2 which represent the presence of large amount of hydroxyl group on the surface of zein particles which was very important for DOX bonding [Victor et al, 2014; Moomand et al, 2014]. FTIR results further confirmed the entrapment of DOX in the ZP hydrogels.
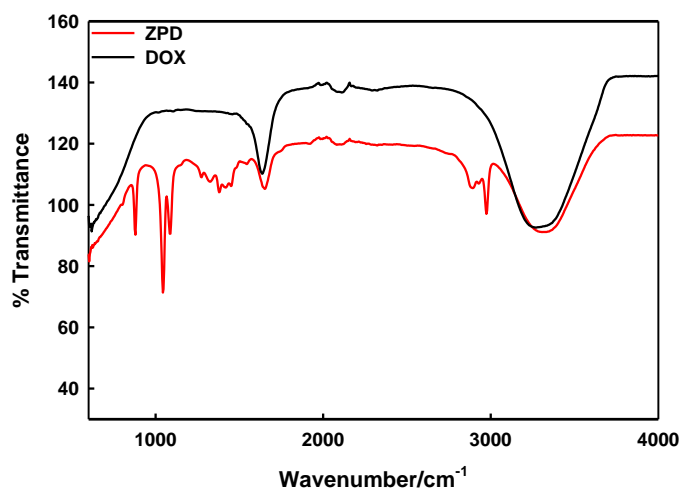
**Fig. 4.2:** FTIR of DOX, ZP, ZD, and ZPD samples. **(c)** FTIR spectroscopy of zein-pectin gel and Doxorubicin encapsulated zein pectin gel.

## 4.3.2 SOL-GEL TRANSITION
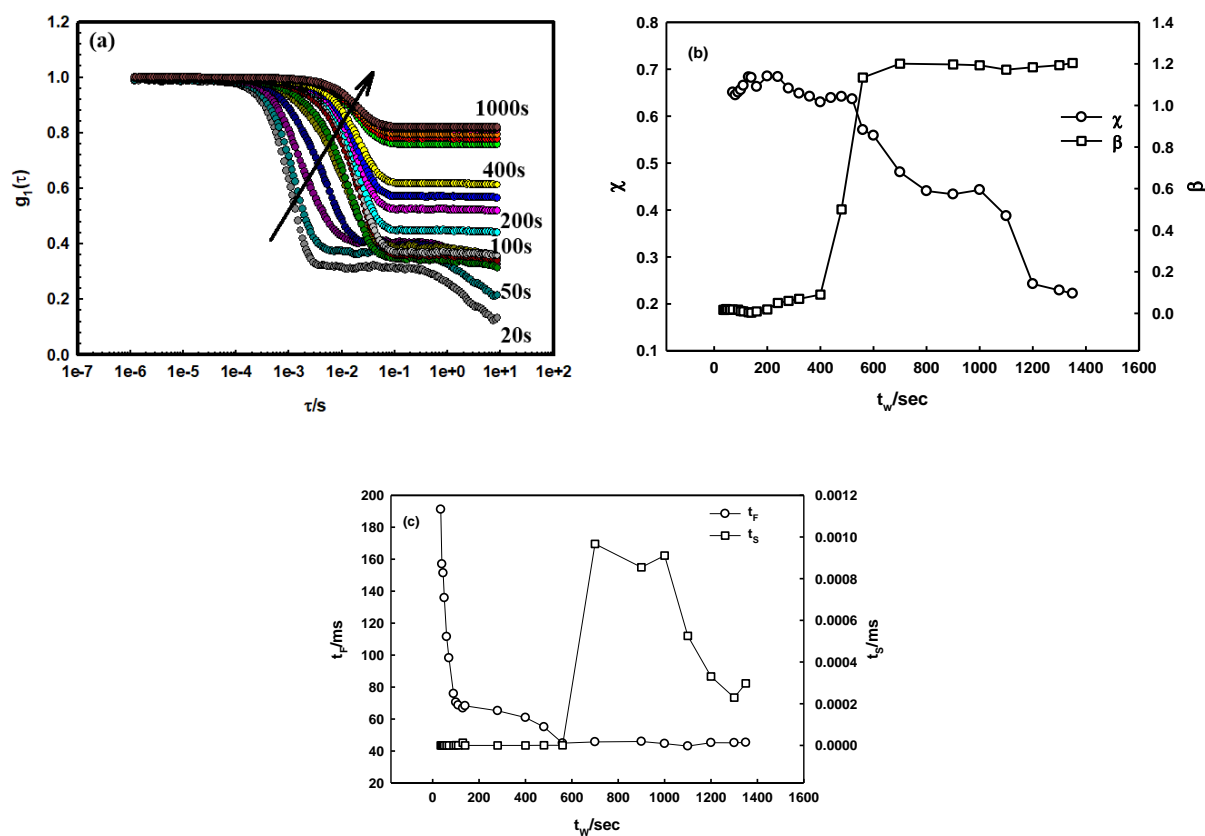


**Fig. 4.3:** (a) Time dependent dynamic structure factor, the variation of (b) ergodicity parameter ($\chi$) and stretch parameter ($\beta$) with waiting time ($t_w$) (c) fast mode ($t_F$) and slow mode ($t_S$) relaxation time of zein-pectin gel (ZP) at pH 2.47.

The pectin-zein sol prepared at pH 2.47 evolved into a gel over a period of time spontaneously. This gelation kinetics was profiled by DLS which is a non-contactual probe. The temporal variation of field autocorrelation function, also called dynamic structure factor, with waiting time $t_w$ is shown in Fig. 4.3(a). It is clearly seen from this data that at t=0 (sol state), the correlation function was fully relaxed indicating system ergodicity. With $t_w$ approaching the gelation time, $t_{gel}$, we noticed arrested dynamics leading to development of non-ergodicity in the system. A gel state is often defined as a fully arrested state with zero ergodicity.

Figure 4.3 (a) shows the time dependent variation of dynamic structure factor $g_1(q,t)$ of various samples. Network gels are often yielded $g_1(q,t)$ data that could be best described by the following function

$$g_1(q,t) = a \exp - \left(\frac{t}{t_F}\right) + (1-a)\, exp - \left(\frac{t}{t_S}\right)^{\beta} \qquad (1)$$

where a and (1-a) are the relative amplitude of the two modes, and the width of a distribution function defined by stretch parameter ($\beta$) that uniquely characterized the structure factor $g_1(q,t)$, $t_F$ and $t_S$ are the fast and slow mode relaxation time, respectively. The transition to non-ergodicity was a dynamic process that was predominantly manifested in the dynamic structure factor data. For an ergodic state, the dynamic structure factor $g_1(q,t)$ relaxes to the value 0 (at t→∞) from its initial value of 1 (t = 0). For an ergodic state, the ergodicity parameter $\chi$ or the signal to noise ratio i.e. signal modulation for $g_1(q,t)$ is given by,

$$\chi = \; g_1(q,t)_{t=0} - \; g_1(q,t)_{t\to\infty} \qquad (2)$$

Signal modulation lies between 0 to 1 for a nonergodic state due to dynamic arrest of scattering moieties and it has been seen in various soft matter systems such as in polymer and colloidal gels, glasses etc [Stauffer et al, 2014; Stauffer et al, 1982; de Arcangelis et al]. The measured $g_1(q,t)$ data was fitted to eqn. (1) to determine $t_F$, $t_S$ and $\beta$ parameters, in addition to the

ergodicity parameter χ. Gelation refers to the dynamic arrest of the zein-pectin complexes that organize to yield an interconnected gel network. A representative plot of nonergodic parameter χ and stretch exponent β are shown in Fig. 4.3(c) which reveals a transition from an ergodic to a non-ergodic state defined by an ergodicity breaking time $t_{EB}$. It is remarkable to note that both β and χ reveal identical ergodicity breaking time $t_{EB}$, which is shown in Fig. 4.3(b).
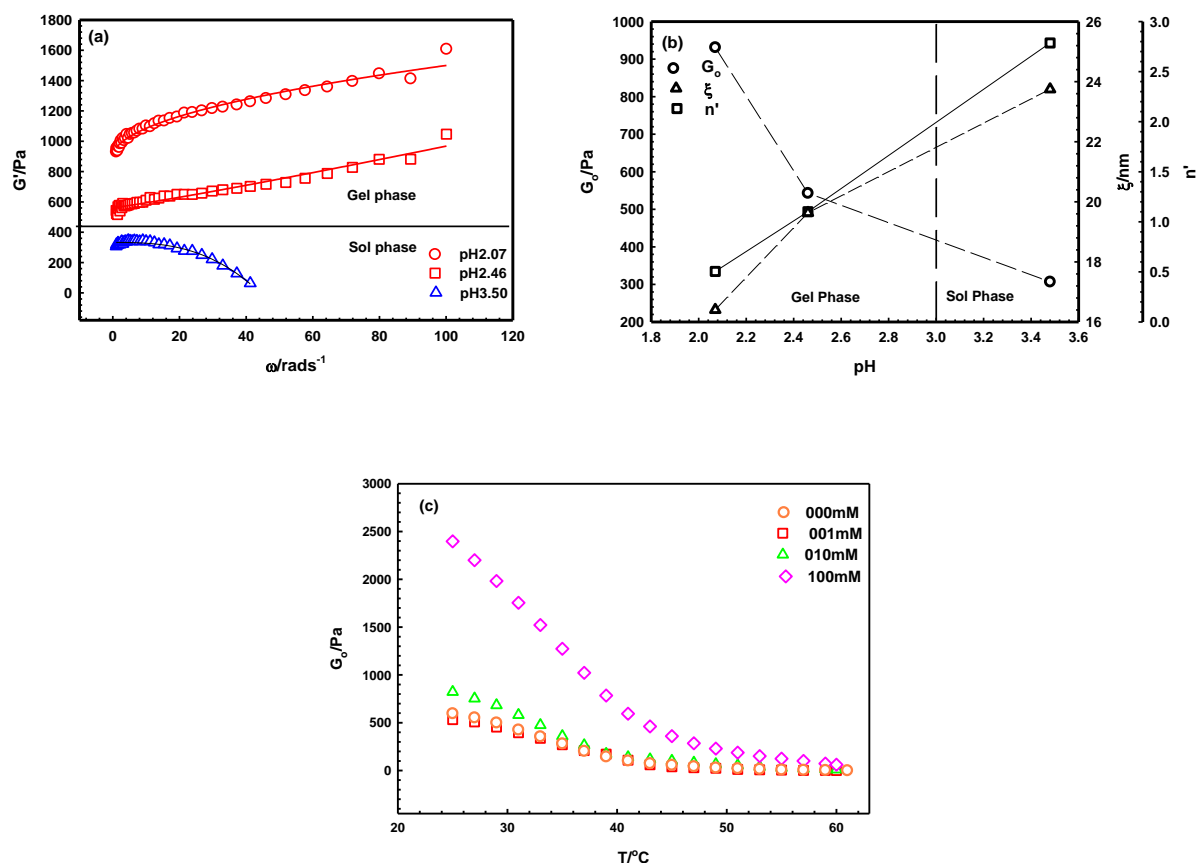


**Fig. 4.4:** (a) Variation of storage modulus of the zein-pectin complex with angular frequency at different pH. Solid lines show the least-squares fitting to the data to eqn (1). (b) variation of low-frequency rigidity, viscoelastic length and n' with pH. Sol-gel phase transition of zein pectin complex as a function of pH. (c) Variation of low frequency storage modulus with temperature for different ionic strength. Solid lines are guide to the eye.

Remarkably, the sol to gel transition occurred close to pH 3 and this was absent elsewhere. This is consistent with the data shown in Fig. 4.4 (a) and (b), where a clear sol-gel phase transition in the response to pH change was observed at the same pH. Since, this coincided with the clear development of viscoelastic properties the material entered a solid-like phase. It was felt imperative to study the viscoelastic properties of these hydrogels in order

to ascertain their rigidity and morphology both of which have a bearing on drug loading and release kinetics. Isothermal frequency sweep studies that reflected the dispersion behavior of storage (G') and loss moduli (G") were performed at room temperature which is shown in Fig. 4.4(a) and Fig. 4.4 (c) for salt dependent study. The elastic response of viscoelastic materials is often explained by a power-law relation for variable shear deformation, given by $G'(\omega) = \omega^{n'}$, where $0 \leq n' \leq 2$ for viscoelastic material with n' = 0 representing an ideal Hookean solid while n' = 2 represents an ideal viscoelastic material in Maxwell model. The low-frequency rigidity modulus $G_O$ which is a representative of gel strength is defined as $G_O = \lim_{\omega \to 0} G'(\omega)$ [Barnes et al, 2000; Gögelein et al, 2008]. In a previous report, we have made a comprehensive study of Zein-pectin complex gel in presence of a crosslinker [Kaushik et al, 2018]. But in the present case, we have not used any crosslinker and could successfully design a hydrogel by just tuning its pH as discussed in previous section. The $G_O$ value of the gel increased from 300 Pa to 1000 Pa as one approached to the more acidic region as shown in Fig. 4.4(b). The values of n' and viscoelastic length $\left( \xi_{el} = \sqrt[3]{\dfrac{k_B T}{G_O}} \right)$ reduced from 2.7 to 0.5, and 23 to 16 nm respectively, below pH 3 (Fig. 4.4(b)). The viscoelastic length is a measure of elastic energy stored in a network of size $\xi_{el}$ at temperature T [Ajji et al, 1991].

### 4.3.3 MELTING PROFILE

Another signature property of a gel is its melting temperature and profile. This information could be determined from the isochronal temperature sweep studies performed on the gel samples using the TA-100 Rheometer. This data is depicted in Fig. 4.5 (a) and its derivative in Fig. 4.5(b) which is very revealing.
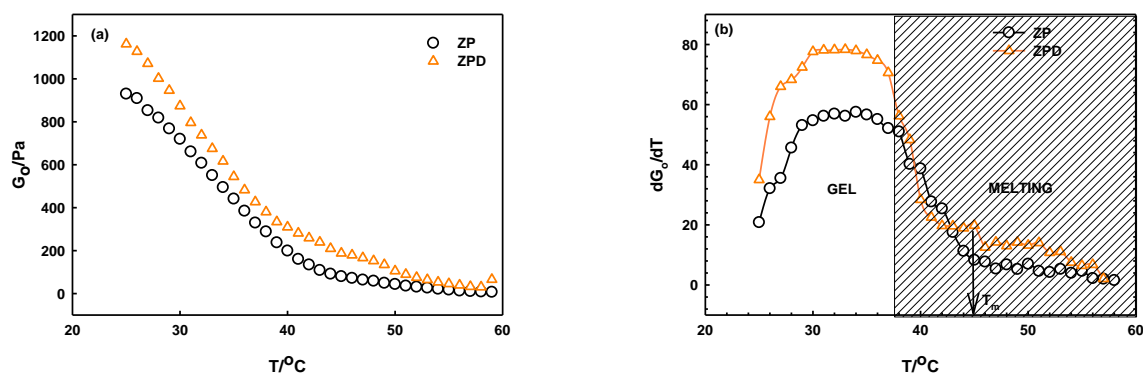
**Fig. 4.5: (a)** Variation of low frequency storage modulus and **(b)** the variation of change in low frequency storage modulus in with temperature of zein-pectin gel at different pH with and without Doxorubicin. Melting profile of zein pectin gel generated at $1^{\circ}$C/min temperature ramp. Solid lines are guide to line and arrow indicate the melting temperature.

The melting profile data revealed transition region which is designated as gel and melting, the hydrogels melts into dense liquids at this temperature. Melting temperature clearly identified from the $dG_o/dT$ *vs* T graph revealed $T_m = 46^{\circ}$C. The hydrogels samples showed complete melting after melting temperature $T_m$ which implied the presence of interconnected networks disentangled completely. Notice the $G_0$ parameter assuming very low value for molten samples. Since, these gels were used for loading of DOX, and its subsequent release, it was necessary to evaluate the changes in rheological properties, if any, after drug loading. Though, the melting profile of ZPD did not change significantly by encapsulation of Doxorubicin as is seen from Fig. 4.5(a), the gel rigidity was higher in these samples. This implies impregnation of drug strengthened the network of the hydrogel may be because of the larger surface area of DOX impregnated zein nanoparticles. Further, this observation confirmed that the drug was located inside zein nanoparticles, and not adsorbed on its outer surface.

## 4.3.4 SALT DEPENDENT STUDY
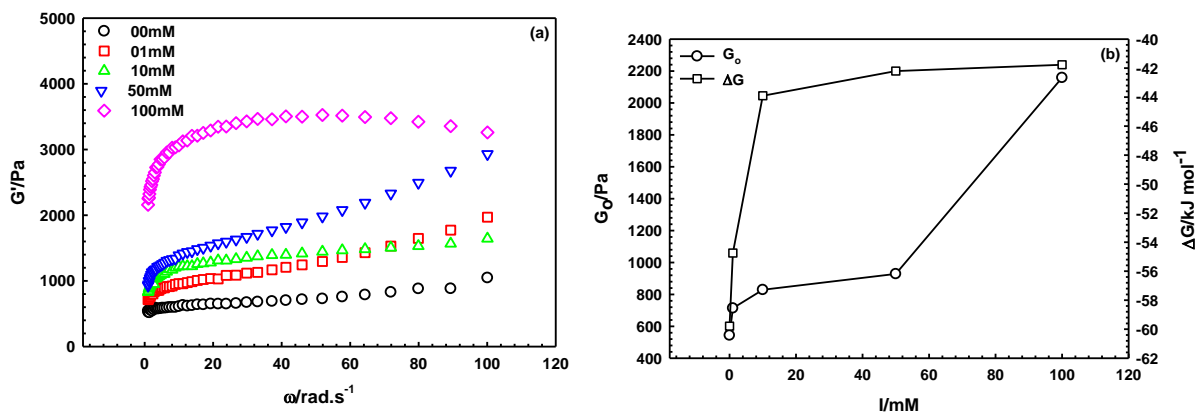


**Fig. 4.6: (a)** Variation of storage modulus with angular frequency for various salt concentration at room temperature. **(b)** Variation of low frequency modulus and Gibb's free energy with ionic concentration. Solid lines are guide to eye.

Inorganic salts are known to dehydrate soft matter systems. The loss of hydration induces reorganization of the network structure. This was probed as function of monovalent salt concentration (NaCl) in range from of $I = 10^{-4}$ to $10^{-1}$ M which yielded storage modulus profile as function of angular frequency with pH 2.47 as shown in Fig. 4.6. The low frequency modulus $G_0$ increased and Gibbs's free energy (determined from melting profile data) decreased as ionic concentration raised (see Fig. 4.6(b)). This implied the formation of constricted networks with smaller viscoelastic lengths. The pectin and zein nanoparticles compact network formation due to the strengthened hydrophobic interaction between them. Here, pectin acts as hydrophobic monomer and zein as crosslinker. The enthalpy of gelation ($\Delta G_o$) is determined by the melting profile of ZP hydrogels using Arrhenius equation is shown in Figure S2 as we know $G_O$ is a measure of enthalpy per unit volume. Pictorial depiction of self-assembly of pectin and zein in the gel material is shown in Scheme 1.
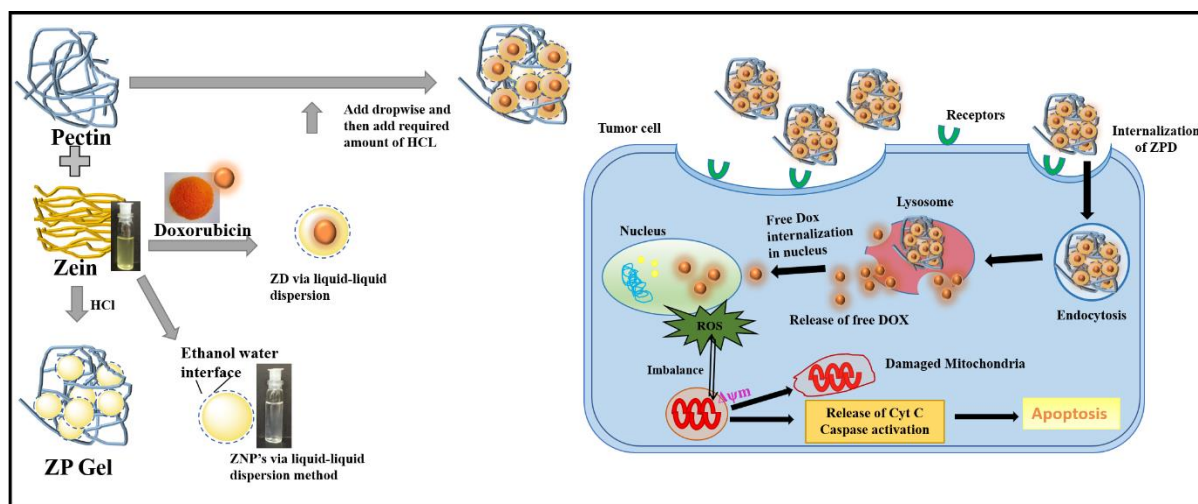
**Fig. 4.7:** Detailed illustration of the formation of ZPD hydrogels and the mode of action in HeLa cells

### 4.3.5 *IN VITRO* RELEASE PROFILE OF DOX
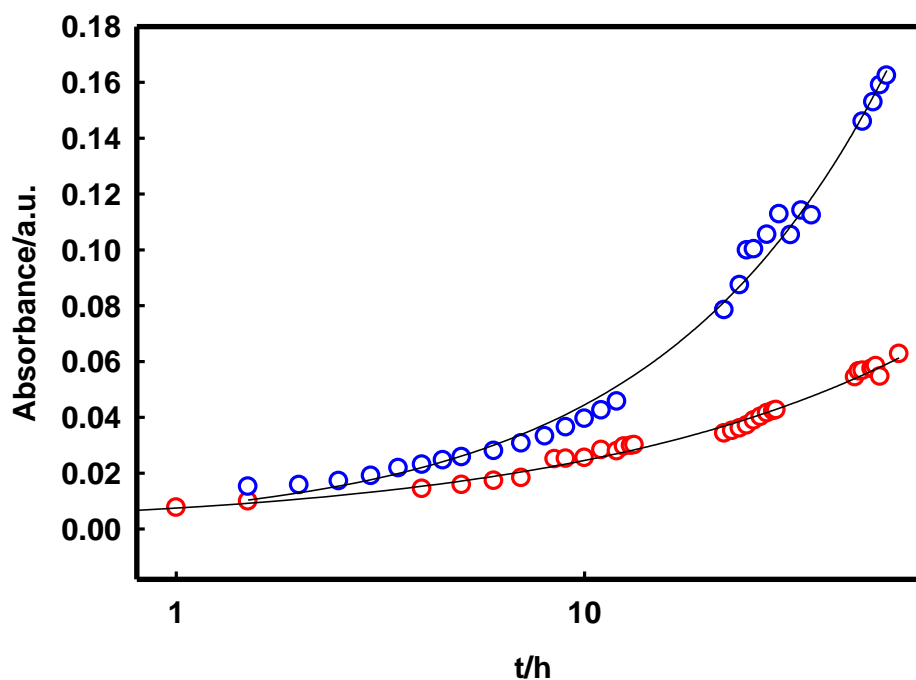


**Fig. 4.8:** release profile of DOX from ZPD at different temperature in PBS buffer solution at pH 6.4.

Drug release kinetics of the ZPD hydrogels was performed at RT (25 ºC) and 37 ºC for 3 days. The *in vitro* cumulative drug release was described by Korsmeyer- Peppas model eqn. $A = k_m t^n$ (where A, $k_m$, and n are amount of drug release, kinetic constant and diffusion

release constant) with good linearity ($r^2 = 0.98$) and n value of 0.52 indicating that the release of DOX follows first-order, anomalous or non- Fickian diffusion kinetics [Dash et al, 2010]. DOX incorporated in ZP hydrogels thus followed diffusion and swelling controlled release. Under RT condition, the release of DOX showed an initial burst followed by controlled release. The effectiveness of anticancer therapy depends on the release kinetics of drug, wherein slow and continuous release offers extended and sustained anticancer therapy.

## 4.3.6 CYTOTOXICITY AND MORPHOLOGICAL ANALYSIS

Cellular viability after treating HeLa and HEK293 cells with ZP and ZPD was analysed by MTT assay. Cell viability is taken as initial parameters to determine the bio-compatibility to the hydrogel. The optical density measured by MTT assay is a representation of the metabolic activity of the total live cell population thus providing an indirect assay of cellular proliferation and thus mitochondrial functioning [Al Faraj, 2013]. Fig. 4.9 shows the cell viability data as observed in HeLa and HEK293 cells after 24 hours of treatment. While the ZP was observed to have a minimal effect of cellular viability for both the cell lines, ZPD were selectively toxic to HeLa cells in comparison to HEK293. HeLa cells treated with ZPD showed a steady decrease in viability with increasing concentration. The $IC_{50}$ value of ZPD hydrogel was calculated to be 3.5µLfor HeLa cells. $IC_{50}$ value for all HEK293 could not be determined as the cell viability was more than 50% and as it represents the concentration of drug at which almost 50% of cells are dead. This thus signifies the comparative lower/minimal toxicity of ZP on both the cell lines, while ZPD shows selective toxicity to HeLa cells. Since, Doxorubicin is an anti-cancerous drug which mediates mitochondrial-dependent apoptosis; we hence observe a selective toxicity towards HeLa and not HEK293cells.
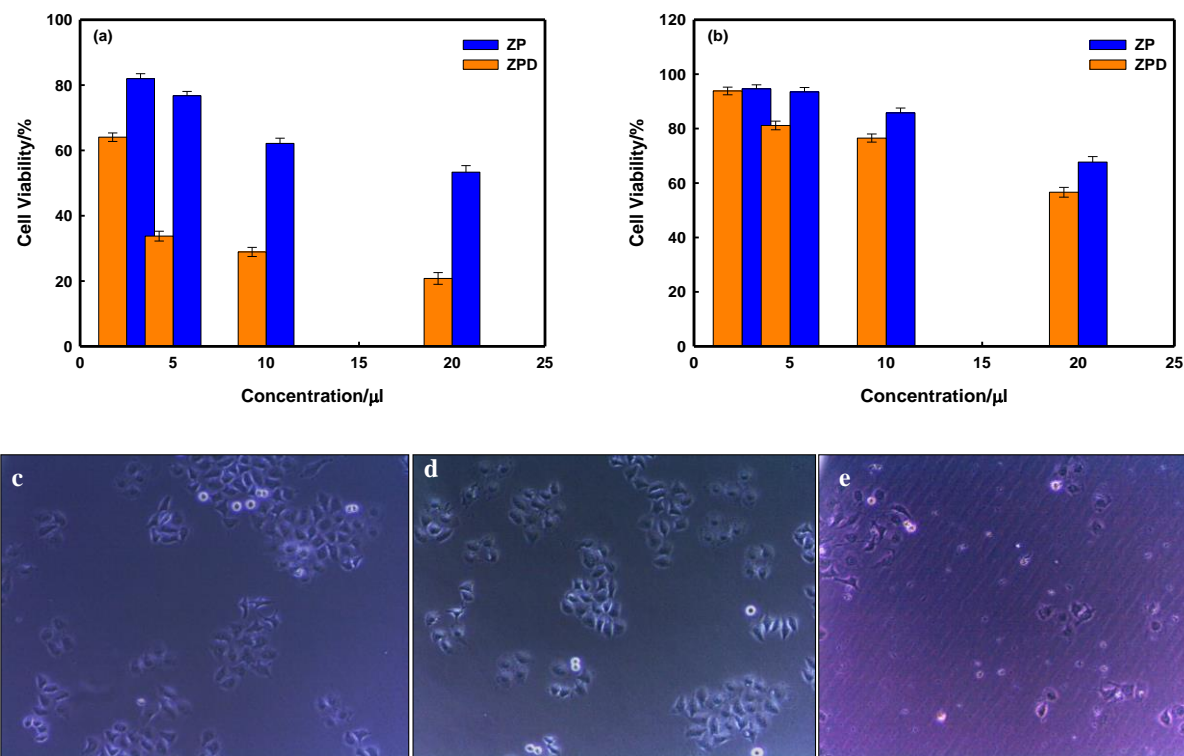
**Fig. 4.9:** Cytotoxicty of hydrogels: Effect of ZP and ZPD hydrogels on the viability of (a) Hela (b) HEK293 cell lines via MTT assay. Cell morphology analysis: (c) Control cell d) treated with ZP e) treated with ZPD hydrogels

Next, we determined morphological alterations induced by treating the hydrogels with HeLa cells for 12 hours with 5µl of hydrogel. Morphology of untreated cells and ZP treated hydrogels showed intact morphology with few dead cells compared to the ZPD. The ZPD hydrogel treated HeLa cells showed distorted outer morphology with numerous detached cells, which indicated dead cells. Moreover, significant reduction in cell density was found within 12 hours of treating cells with ZPD. The cell morphology images of control and treated cells have been shown in Fig. 4.9 (c-e). Free DOX is known to generate ROS which initiates cellular apoptosis [Gautier et al, 2012], we can thus conclude that DOX delivered via the ZP hydrogels induce intracellular apoptosis due to which a significant reduction in cell density and large number of detached cells was found.

## 4.3.7 DOX-LOADED HYDROGEL LOCALIZATION IN CELLS AND THEIR ANTIOXIDATIVE ABILITY

Free DOX is known to intercalate with DNA, inhibit topoisomerase II and thus is known to arrest cell cycle in cancerous cells at G0/G1 and G2 phase regulated by p53 [Kunznetsov et al, 2011; Gautier et al, 2012]. Additionally, a secondary mechanism wherein DOX induces the generation of ROS has also been hypothesized [Gautier et al, 2012]. For investigating the role of oxidative stress in hydrogel treated HeLa cells and corresponding apoptosis, we used the fluorescent dye $H_2DCFDA$. A significant increase in ROS activity as determined by the $2',7'$-dichlorofluorescein fluorescence signals was observed for cells treated with ZPD hydrogels after 12 hours of incubation (Fig. 4.10). However, cells treated with ZP hydrogels did not show much change in DCF fluorescence thus suggesting that DOX loaded in the hydrogels can easily penetrate cells and induce intracellular oxidative stress in cancerous cells. The penetration of hydrogels to the cell interior is assisted via the normal electrostatic interaction as the formulated hydrogels possess an inherent positive charge as already described in previous section which can easily interact with the negatively charged HeLa cells. The high level of glucose metabolism results in secretion of lactate ions. The lactate anions remove the positively charged ions thereby providing an overall negative charge on cancer cell surface [Chen et al, 2016].
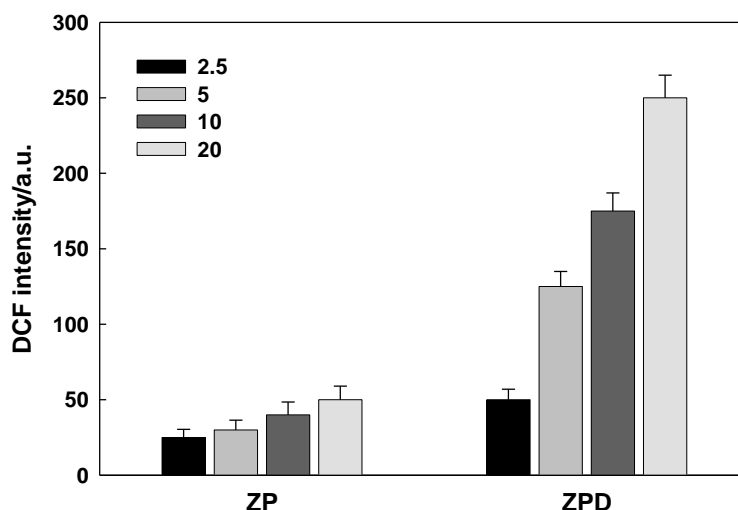
**Fig. 4.10:** Measurement of oxidative stress in hydrogel treated HeLa cells. The experiments were performed in triplicates and SD has been determined.

Cellular uptake and internalization of ZPD was monitored at regular time intervals using confocal microscope. DOX is auto-fluorescent in nature and emits light in red spectral region. To demonstrate the internalization by the HeLa cells, we treated the cells with different concentration (2.5, 5 and 10 µL) of ZPD and visualized them after 4 hours of treatment. There was a gradual increase in red coloured intensity (representing DOX) with increasing concentration of loaded hydrogel (Fig. 4.11 a-c). Thus, a direct correlation was found between DOX concentration and fluorescence intensity. Further, to understand the pathway and distribution of hydrogel in cells, confocal images were captured from the beginning of treatment. Cells were treated with 10 µLof ZPD and observed at 30 min, 1 h, 2h and 4h (Fig. 4.11 d-g). After 30 minutes of treatment, we found red fluorescence outside the cell while the cell did not show any fluorescence contributed by DOX. After 1 hour, though DOX was internalized by cells, the signal was negligible. However, after 4 hours of treatment strong signals from internalized DOX was observed from the cell cytoplasm indicating the uptake and localization of DOX. Further increase in fluorescence intensity was found at 6 hours. Moreover, we found DOX to be localized within the cell nucleus which indicates that DOX

can penetrate the cell nucleus and intercalate with DNA, which is one of the mechanisms behind DOX induced cell death. Further, internalization requires time intervals of around 4 hours which can be suggestive of the fact that DOX is released from the hydrogel assisted by acidic pH of cellular organelles and are not internalized by simple diffusion route [Du et al, 2011]. This is thus advantageous as we can modulate the early release of drug via pH dependent means which is beneficial when it comes to cancer-based therapy [Du et al, 2011].
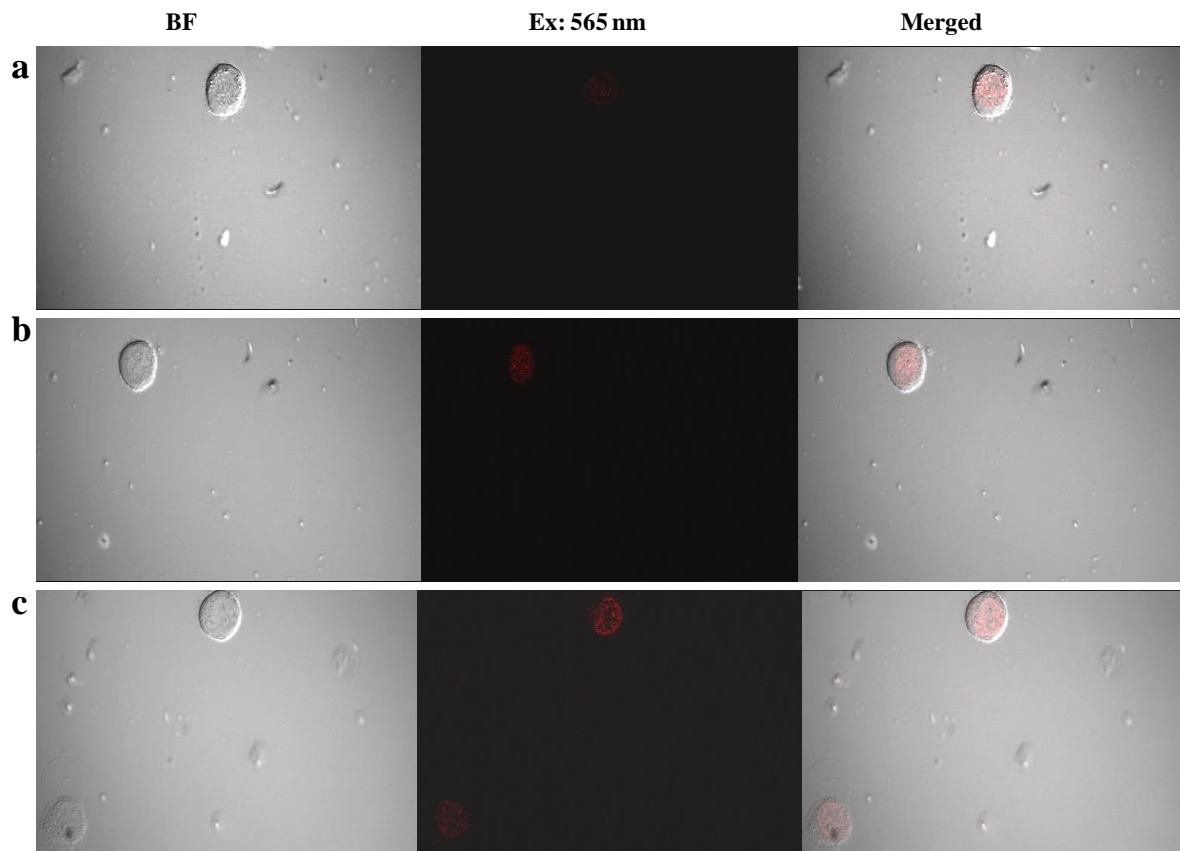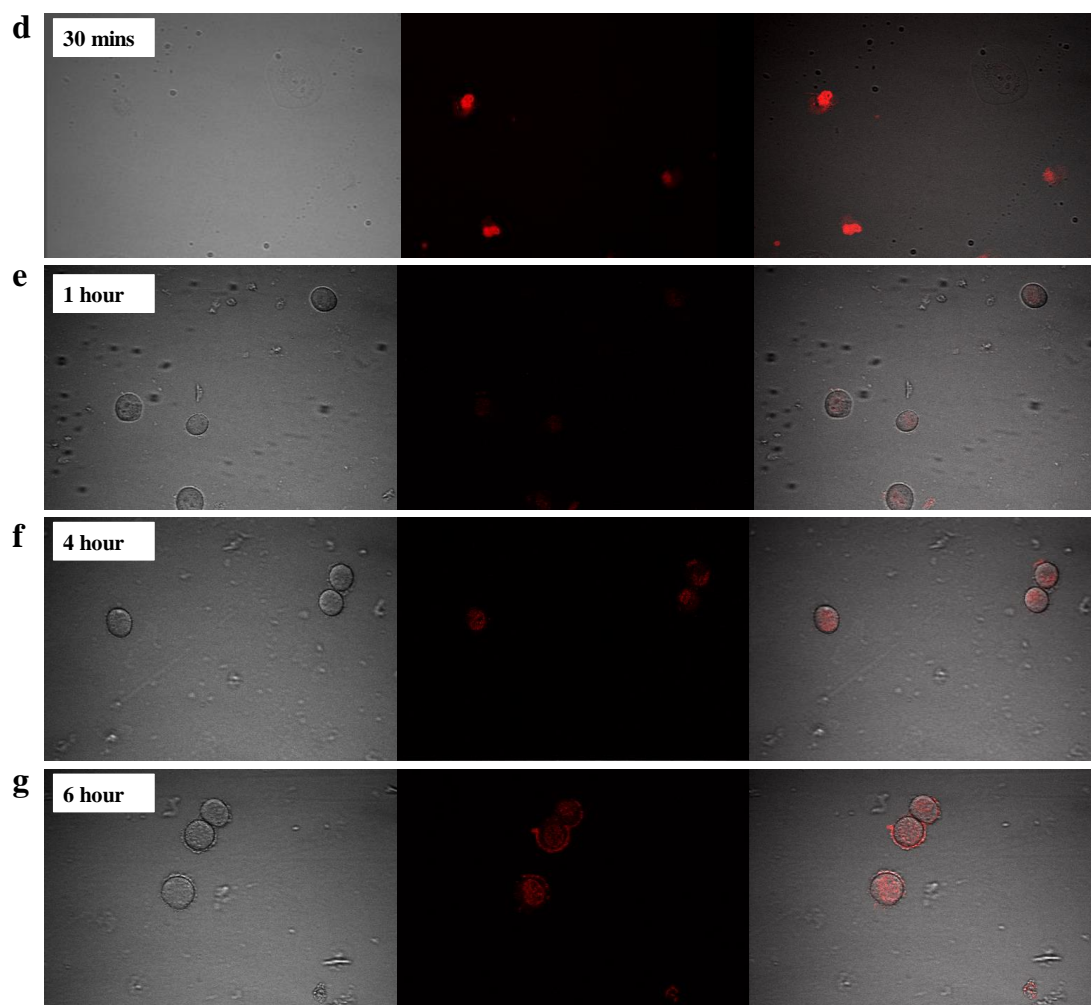
**Fig. 4.11:** Confocal Microscopy images showing Cellular uptake of ZPD after incubating HeLa cells with varying concentration of sample a) 2.5 µL b) 5 µL c) 10 µL and at different time durations d) 30 min e) 1hour f) 4-hour g) 6 hour

## 4.3.8 ULTRASTRUCTURAL CHANGES INDUCED BY DOX: TEM ANALYSIS

The transport and localization of ZPhydrogels and ZPD in HeLa cells was determined by TEM. Fig. 4.12a and b shows untreated and treated (12 hours of treatment) HeLa cells respectively. The control cells (without any treatment) did not show any evident morphological changes, with intact cell and nuclear membrane. There were abundant microvilli and mitochondria in the cells. The cells after treatment showed distinctive morphological changes with shirked cytoplasm along with marked reduction in cell volume. The cell organelles were distorted, microvilli disappeared and large liquid droplets were formed all around the cytoplasm.
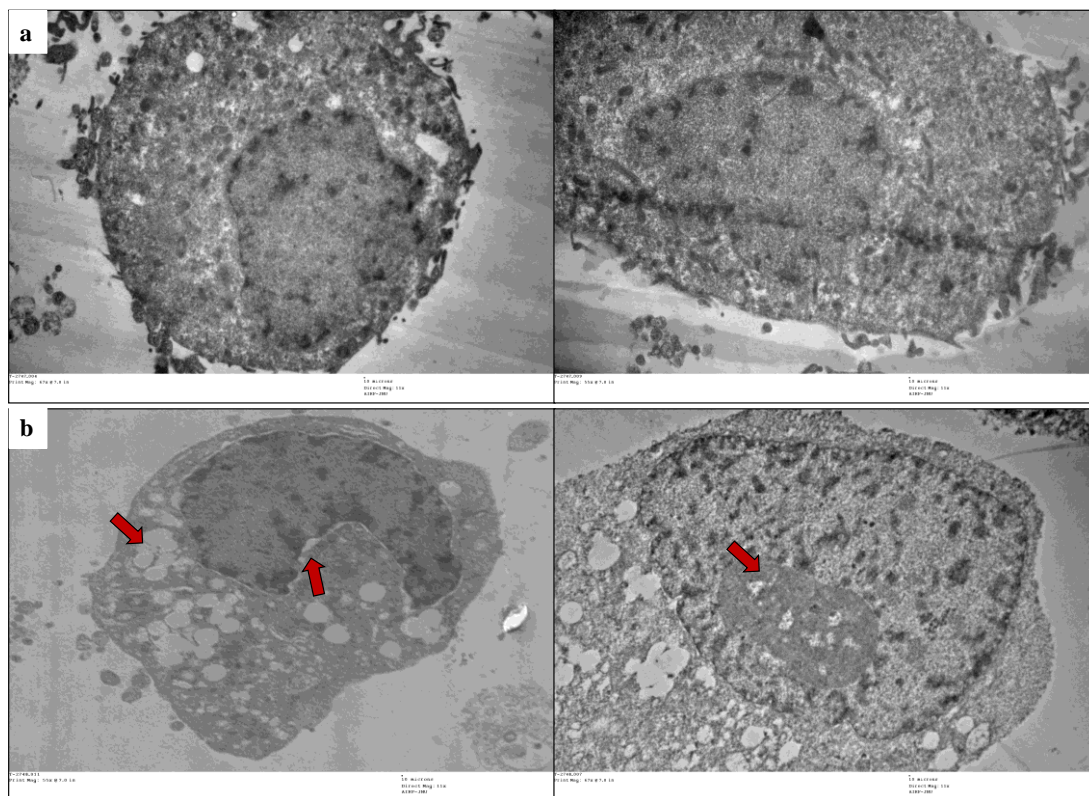
**Fig. 4.12:** TEM micrographs of a) untreated and b) treated cells showed major ultra-structural changes captured at different magnifications.

Figure 4.7 depicts a detailed illustration of the formation of ZPD hydrogels and the mode of action in HeLa cells. The larger pore size and specific receptors in cancerous cells facilitate the uptake of ZPD hydrogels by HeLa cells compared to normal cell lines [Chen et al, 2012]. Free DOX is released from ZPD hydrogels assisted by the acidic pH of the cytosolic organelles. Since, DOX is a nuclear drug, the free DOX molecules are internalized in the cell nucleus which was evident from confocal studies. This results in the generation of reactive oxygen species (ROS) leading to the imbalance in the antioxidant enzymes, formation of permeability pores via which cytochrome c is released from the mitochondria. This results in change in mitochondrial membrane potential by activation of caspases-3 which is a mainly responsible for cellular apotosis [Lewis et al, 2013]. Figure 4.7 detailed illustration of the formation of ZPD hydrogels and its toxicity effect on tumor cell (HeLa).

## 4.4 Conclusion

In summary, the study demonstrates the potential of pH-dependent ZPD hydrogel as anti-cancerous substrates for human cervical cancer cell lines demonstrated by decrease in cell viability, ROS generation and alterations in cell morphology. The prepared ZPD hydrogel favour pH dependent release of Doxorubicin to the cytosolic acidic environment of HeLa cells, thereby mediating cellular apoptosis via ROS generation. Prepared hydrogels are endowed with the advantages of controlled release, enhanced shelf-life of drug and provide an inherent environment for the drug. Thus, the results suggest that hydrogels based on inorganic materials can be used as injectable anti-cancerous agents with minimal side-effects, pH and site-specific responsiveness.

## 4.5 REFERENCE

1. Kaushik, P.; Rawat, K.; Aswal, V. K.; Kohlbrecher, J.; Bohidar, H. B. Mixing ratio dependent complex coacervation versus bicontinuous gelation of pectin with in situ formed zein nanoparticles. *Soft matter*, **2018**, *14*(31), 6463-6475.

2. Sun, Y.; Du, L.; Liu, Y.; Li, X.; Li, M.; Jin, Y.; Qian, X. Transdermal delivery of the in-situ hydrogels of curcumin and its inclusion complexes of hydroxypropyl-β-cyclodextrin for melanoma treatment. *International journal of pharmaceutics*, **2014**, *469*(1), 31-39.

3. Redpath, M.; Marques, C. M. G.; Dibden, C.; Waddon, A.; Lalla, R.; MacNeil, S. Ibuprofen and hydrogel-released ibuprofen in the reduction of inflammation-induced migration in melanoma cells. *British Journal of Dermatology*, **2009**, *161*(1), 25-33.

4. Wang, W.; Song, H.; Zhang, J.; Li, P.; Li, C.; Wang, C.; ... & Zhao, Q. An injectable, thermosensitive and multicompartment hydrogel for simultaneous encapsulation and independent release of a drug cocktail as an effective combination therapy platform. *Journal of controlled release*, **2015**, *203*, 57-66.

5. Dai, X.; Tan, C. Combination of microRNA therapeutics with small-molecule anticancer drugs: mechanism of action and co-delivery nanocarriers. *Advanced drug delivery reviews*, **2015**, *81*, 184-197.

6. Singal, P. K.; Iliskovic, N. Doxorubicin-induced cardiomyopathy. *New England Journal of Medicine*, **1998**, *339*(13), 900-905.

7. Buzdar, A. U.; Marcus, C.; Blumenschein, G. R.; Smith, T. L. Early and delayed clinical cardiotoxicity of doxorubicin. *Cancer*, **1985**, *55*(12), 2761-2765.

8. Sinha, B. K.; Mimnaugh, E. G.; Rajagopalan, S.; Myers, C. E. Adriamycin activation and oxygen free radical formation in human breast tumor cells: protective role of

glutathione peroxidase in adriamycin resistance. *Cancer research*, **1989**, *49*(14), 3844-3848.

9. Gouazé, V.; Mirault, M. E.; Carpentier, S.; Salvayre, R.; Levade, T.; Andrieu-Abadie, N. Glutathione peroxidase-1 overexpression prevents ceramide production and partially inhibits apoptosis in doxorubicin-treated human breast carcinoma cells. *Molecular pharmacology*, **2001**, *60*(3), 488-496.

10. Singh, B.; Kaur, G.; Singh, P.; Singh, K.; Kumar, B.; Vij, A.; ... Thakur, A. Nanostructured boron nitride with high water dispersibility for boron neutron capture therapy. *Scientific reports*, **2016**, *6*, 35535.

11. Kaur, S.; Sundaram, S.; Meena, R.; Rajamani, P. Stress-Generated Free Radicals Detected by Electron Paramagnetic Resonance Spectroscopy with Nitrone Spin Trap in Vicia faba Root, **2018**.

12. Kumar, S.; Meena, R.; Paulraj, R. Role of macrophage (M1 and M2) in titanium-dioxide nanoparticle-induced oxidative stress and inflammatory response in rat. *Applied biochemistry and biotechnology*, **2016**, *180*(7), 1257-1275.

13. Luo, Y.; Pan, K.; Zhong, Q. Casein/pectin nanocomplexes as potential oral delivery vehicles. *International journal of pharmaceutics*, **2015**, *486*(1-2), 59-68.

14. Victor, S. P.; Paul, W.; Jayabalan, M.; Sharma, C. P. Supramolecular hydroxyapatite complexes as theranostic near-infrared luminescent drug carriers. *CrystEngComm*, *16*(38), **2014**, 9033-9042.

15. Moomand, K.; Lim, L. T. Oxidative stability of encapsulated fish oil in electrospun zein fibres. *Food Research International*, *62*, **2014**, 523-532.

16. Stauffer, D.; Aharony, A. *Introduction to percolation theory*, **2014**, Taylor & Francis.

17. Stauffer, D.; Coniglio, A.; Adam, M. Gelation and critical phenomena. In *Polymer networks*, **1982**, (pp. 103-158). Springer, Berlin, Heidelberg.

18. de Arcangelis, L.; Del Gado, E.; Coniglio, A. Complex dynamics in gelling systems. *The European Physical Journal E*, **2002**, *9*(3), 277-282.

19. Rodd, A. B.; Dunstan, D. E.; Boger, D. V.; Schmidt, J.; Burchard, W. Heterodyne and nonergodic approach to dynamic light scattering of polymer gels: aqueous xanthan in the presence of metal ions (aluminum (III)). *Macromolecules*, **2001**, *34*(10), 3339-3352.

20. Barnes, H. A. *A handbook of elementary rheology*, **2000**, University of Wales, Institute of Non-Newtonian Fluid Mechanics.

21. Gögelein, C.; Nägele, G.; Tuinier, R.; Gibaud, T.; Stradner, A.; Schurtenberger, P. A simple patchy colloid model for the phase behavior of lysozyme dispersions. *The Journal of chemical physics*, **2008**, *129*(8), 08B615.

22. Ajji, A.; Choplin, L. Rheology and dynamics near phase separation in a polymer blend: model and scaling analysis. *Macromolecules*, **1991**, *24*(18), 5221-5223.

23. Dash, S.; Murthy, P. N.; Nath, L.; Chowdhury, P. Kinetic modeling on drug release from controlled drug delivery systems. *Acta Pol Pharm*, **2010**, *67*(3), 217-23.

24. Al Faraj, A. Preferential magnetic nanoparticle uptake by bone marrow derived macrophages sub-populations: effect of surface coating on polarization, toxicity, and in vivo MRI detection. *Journal of nanoparticle research*, **2013**, *15*(7), 1797.

25. Gautier, J.; Munnier, E.; Paillard, A.; Hervé, K.; Douziech-Eyrolles, L.; Soucé, M.; ... Chourpa, I. A pharmaceutical study of doxorubicin-loaded PEGylated nanoparticles for magnetic drug targeting. *International journal of pharmaceutics*, **2012**, *423*(1), 16-25.

26. Du, J.; Xiao-Jiao, D.; Cheng-Qiong M.; Wang, J. Tailor-Made Dual pH-Sensitive Polymer Doxorubicin Nanoparticles for Efficient Anticancer Drug Delivery. *J. Am. Chem. Soc*. **2011**, 133, 17560–17563

27. Lewis, A.; Hayashi, T.; Su, T. P.; Betenbaugh, M. J. Bcl-2 family in inter-organelle modulation of calcium signaling; roles in bioenergetics and cell survival. *Journal of bioenergetics and biomembranes*, **2014**, *46*(1), 1-15.

5 we explore the transport properties, surface charge and visco-elastic properties of elastin in the environment of varying solvent hydrophobicity (ethanol-water binary solvent). DLVO theory is used to explain the role of different forces involved in stabilizing the elastin dispersion, and to qualitatively map its self-assembly pathway.

## 5.1.2. SAMPLE PREPARATION

Different dispersions of elastin were prepared by dissolving given amount of elastin powder in binary solvent comprising of 80% (v/v) ethanol, 20% (v/v) water, and 0.7 M sodium hydroxide. The suspension was vigorously stirred for 24 hours at room temperature (25 $^0$C). Concentration of elastin was varied between 0.02 %- 1.00 % (w/v). Dispersion of 0.02% (w/v) elastin was also prepared in aqueous medium by stirring the given amount of elastin in water for 24 hrs. The pH of dispersion was set to 11 to increase the solubility. The dispersions were filtered through a 0.22 μm syringe filter to remove the insoluble fraction of the protein, if any. It was found that solubility of protein was poor in aqueous medium, but it was good in the aforesaid ethanolic solvent.

## 5.1.3   RESULTS AND DISCUSSION

Solvent tunes different polymer-solvent interactions that has serious bearing on polymer dispersion properties and its phase stability [Teraoka, 2002]. In the following section, we will explain the role played by different interactions and their effect on the stability of protein dispersion. As it was mentioned earlier elastin contains majority of hydrophobic residues in its primary structure, hence it is expected to show poor dispersibility in aqueous medium. But as the hydrophobicity of solvent is increased by introducing ethanol to the dispersion, distribution of forces changes and elastin properties reveal drastic anomaly. Fig. 5.1 shows the UV absorption spectra of the protein dispersion in aqueous, and binary solvent. It clearly shows different response of protein towards the solvent environment. In aqueous

medium protein shows absorption peak at ~200 nm, but as the hydrophobicity increased, a clear red shift was observed in the spectrum (~240 nm). The red shift indicated the presence of comparatively larger structures in the ethanolic dispersion.

### 5.1.3.1 PROTEIN MORPHOLOGY

DLS experiments were performed to understand the diffusion and internal dynamics of the protein molecules in the two solvent environments. Scattered intensity was also collected from the dispersions in the said environments (Table 5.1).
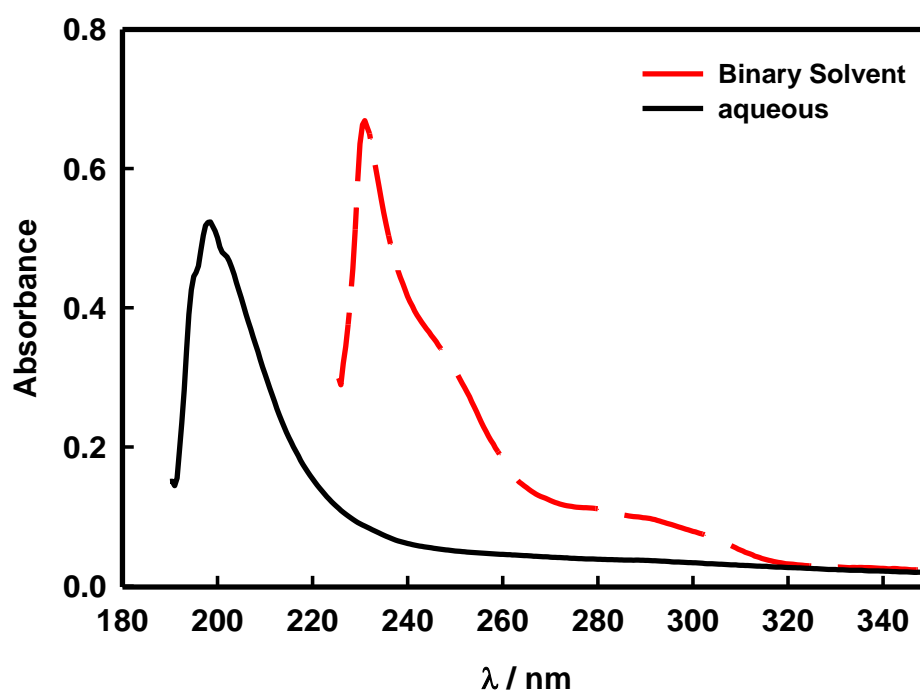


**Fig. 5.1:** UV absorption spectrum for 0.02 % (w/v) elastin dispersion in water, and water-ethanol binary solvent. The binary solvent was ethanol 80%: 20% (v/v) water mixture in the presence of 0.7M NaOH. Notice the red shift in peak absorbance.

Data in Table 5.1 show that the scattered intensity in the aqueous medium was almost half of the same in binary solvent. It was supported by the observed poor solubility of protein in aqueous medium due to the presence of fewer hydrophilic residues in the primary structure of the protein. The scattering intensity I(q) is given by [Chu, 2007]

$$I(q) = A\, C\, M\, P(q)\, S(q) \tag{5.1}$$

where A is the instrument factor, C is protein concentration, M is the molecular weight, P(q) is particle form factor, and S(q) is structure factor. The ratio of the intensity of light scattered by the two dispersions is given by

$$\frac{I_E(q)}{I_W(q)} \approx \frac{P_E(q)S_E(q)}{P_W(q)S_W(q)} \tag{5.2}$$

the suffices w and $E$ refers to the parameters related to water and ethanolic solution.

From the Table 5.1 data, we obtained

$$P_E(q)S_E(q) \cong 2\,P_W(q)S_W(q) \tag{5.3}$$

Therefore, the enhanced scattering from the binary solvent owes its origin to the combined effect of change in form, and the structure factor. While, the form factor accounts for the geometrical shape of the molecules, the structure factor defines the intermolecular interactions. Since, the measurements were performed on very dilute solutions (0.02 % (w/v)), the typical intermolecular separation was $\left(\cong \frac{CN_A}{1000M}\right)^{-1/3} \approx 350$ nm. Where $N_A$ is Avogadro's number, and M is its molecular weight. The typical radius of gyration of this molecule is about 30 nm (assuming a spherical shape, and partial specific volume $\approx$0.73 cc/g). Thus, the intermolecular separation was at least 10 times larger than the molecular size. Therefore, to a good approximation it can be assumed that S(q) $\approx$1. Hence, from eqn. (5.3), we obtain

$$P_E(q) \cong 2\,P_W(q) \tag{5.4}$$

To a good approximation, P(q) (in the Guinier approximation) for a molecule with radius of gyration $R_g$ is given by [Teraoka, 2002]

$$P(q) \approx 1 - \frac{q^2 R_g^2}{3} \tag{5.5}$$
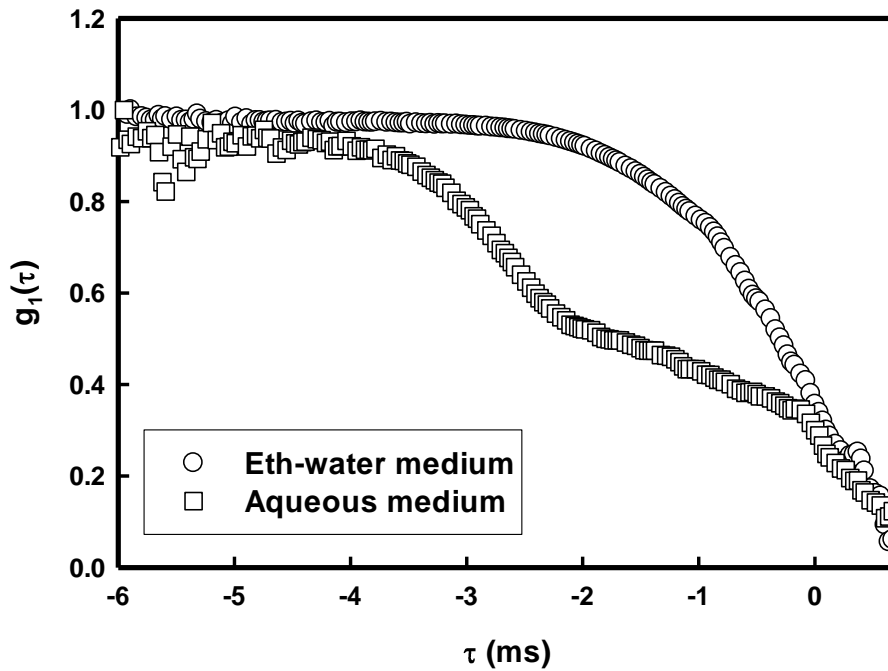
**Fig. 5.2:** Measured dynamic structure factor from 0.02% (w/v) elastin in aqueous and ethanol-water mixture dispersion.

Thus, from eqns. (5.4) and (5.5) one obtains

$$R_{gE} \approx \sqrt{2} R_{gW} \qquad (5.6)$$

This immediately implies that in ethanolic solvent elastin molecule will assume a physical size about 1.4 times larger than in aqueous medium indicating chain collapse in water, and swelling in binary mixture. Thus, the hydrophobic hydration provided by the binary solvent will facilitate the chain swelling (as shown in schematic Fig. 5.3). Note that the hydrodynamic volume increased by nearly 40-times due to the selective hydration. Since, the apparent hydrodynamic size is known it is possible to evaluate the equivalent $R_g$ values by using the relation

$$R_h = \xi R_g \qquad (5.7)$$

where $\xi$ is an empirical parameter that assumes a value of 0.875 for spheres and 0.665 for random coils.
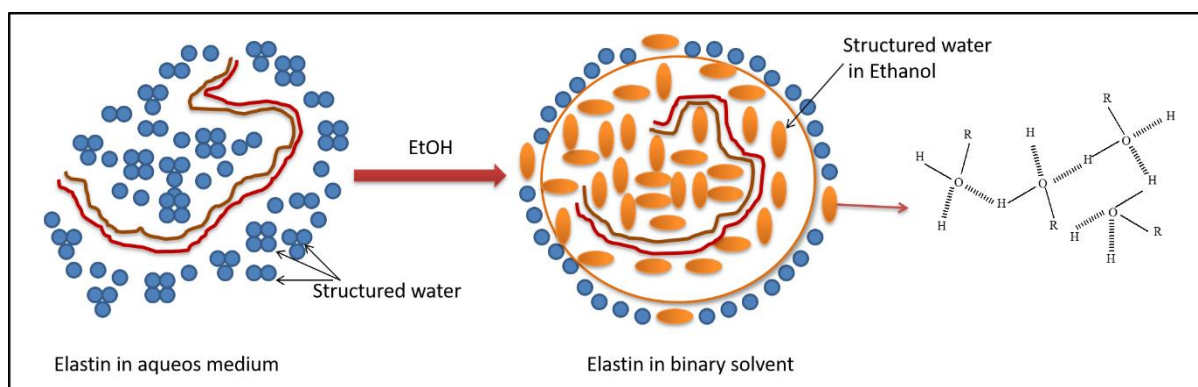
**Fig. 5.3:** Pictorial depiction of solvation of elastin molecule in aqueous and ethanol solutions. Polymer chain collapse in water and swelling in binary solvent.

Dynamic structure factor data $g_1(\tau)$ was collected from the dispersions which is shown in Fig. 5.2. It clearly indicates the sensitivity of the protein chain towards the environment provided by the solvent. The detailed description of the various interactions dominant in the environment will be discussed in latter sections. Translational diffusion coefficient D is known to be inversely proportional to particle size in free diffusion according to Stokes-Einstein relation [Chu, 2007]. For diffusion driven by Brownian dynamics $g_1(\tau)$ is given be [Chu, 2007]

$$g_1(\tau) = g_1(0)e^{-(\Gamma\tau)^\alpha} \tag{5.8}$$

with

$$D = \frac{\Gamma}{q^2} \tag{5.9}$$

where $\Gamma$ is the rate at which intensity fluctuations (arising from concentration fluctuations) in the suspension decays, and $\alpha$ defines the anomaly in the diffusion process in suspension, if any. It is unity ($\alpha=1$) for free Brownian motion (normal diffusion), and less than unity (sub diffusion) in crowded or arrested environments, like, gels, glasses or melts. The $g_1(\tau)$ data was fitted to eqn. (5.8) to yield the D values which are listed in Table 5.1. Interestingly, elastin shows two orders of magnitude smaller diffusion coefficient in binary solvent compared to water implying arrested diffusion behavior ($\alpha=0.4$) compared to the free diffusion seen in

aqueous medium ($\alpha$=0.85). Table5.1 data clearly shows a large size (apparent hydrodynamic size = 700 nm) and arrested protein diffusion in binary solvent and smaller size (= 200 nm) and normal Brownian dynamics in water. The binary solvent of ethanol-water has large solvent hydrophobicity which may be the source of complex and arrested dynamics of protein in this medium.

### 5.1.3.2 PROTEIN SURFACE CHARGE

Surface charge plays a significant role in the stability of proteins in dispersion [Ohshima, 1995]. Zeta potential $\zeta$ is the electrostatic surface potential of the protein molecule at the hydrodynamic slip plane [Bohidar, 2015]. To a very good approximation, it is directly proportional to the protein surface charge. It was measured for low protein concentration to avoid any nonlinear effects. Elastin showed an interesting transition of surface charge from negative ($\zeta$= -24 mV) in water to positive ($\zeta$= 14 mV) in ethanolic solvent which can be attributed to the hydrophobic hydration induced structural change in the biopolymer. This implies that the deprotonated residues are in a propensity in the aqueous dispersion while in the hydrophobic solvent protonated residue dominated the charge state.

### 5.1.3.3 SURFACE ACTIVE PROPERTY

Surface tension signifies the interfacial energy of the particle at the liquid-air interface in the system. It is measured as the energy required for increasing the surface area of liquid by unity. It results from an imbalance of intermolecular attractive forces at the air-liquid interface. Surface tension of elastin was found to be more in aqueous medium than in binary solvent (Table 5.1). This is because of extensive hydrogen bonding by water with ethanol.

**Table 5.1:** Comparative properties of elastin in aqueous and water-ethanol binary solvent.

| S. No. | Parameter | Water | Binary Solvent | Comment |
|---|---|---|---|---|
| 1. | Scattered Intensity/ a.u | 10,000 | 22,000 | Poor solubility in water |
| 2. | Diffusion Coefficient /cm$^2$ s$^{-1}$ | 8.14x10$^{-9}$ | 2.07x10$^{-11}$ | Slow diffusion in binary solvent |
| 3. | Diffusion anamoly ($\alpha$) | 0.85±0.07 | 0.4±0.03 | Sub diffusion dynamics in binary solvent |
| 4. | Zeta Potential/ mV | -24±2 | 14±1 | Polarity reversed in binary solvent |
| 5. | Surface Tension/ mN m$^{-1}$ | 68±2 | 25±1 | Reduced surface activity in binary solvent |
| 6. | Gibbs free energy/ KJ mol$^{-1}$ | - | -28 | - |
| 7. | Transition Temperature / K | - | 300 | - |
| 8. | Intrinsic Viscosity/ g/ml$^{-1}$ | - | 1.01 | - |
| 9. | Apparent hydrodynamic radius/nm | 200 | 700 | Chain swelling in binary solvent |

## 5.1.3.4 VISCOSITY

Viscosity of elastin was measured in aqueous and binary solvent. Fig. 5.4(A) shows the variation viscosity of elastin as a function of concentration of elastin in the two dispersions. Due to lower solubility of elastin in aqueous medium measurement was done only for one concentration of protein. Higher concentration of protein (>0.02% (w/v)) was not soluble in water. But, in the case of binary solvent, concentration of protein was varied from 0.02% to 1% (w/v). The viscosity profile clearly shows two regions: lower and higher concentration regimes (below and above 0.2% (w/v) of elastin). The protein is expected to have large intermolecular forces in the higher concentration regime
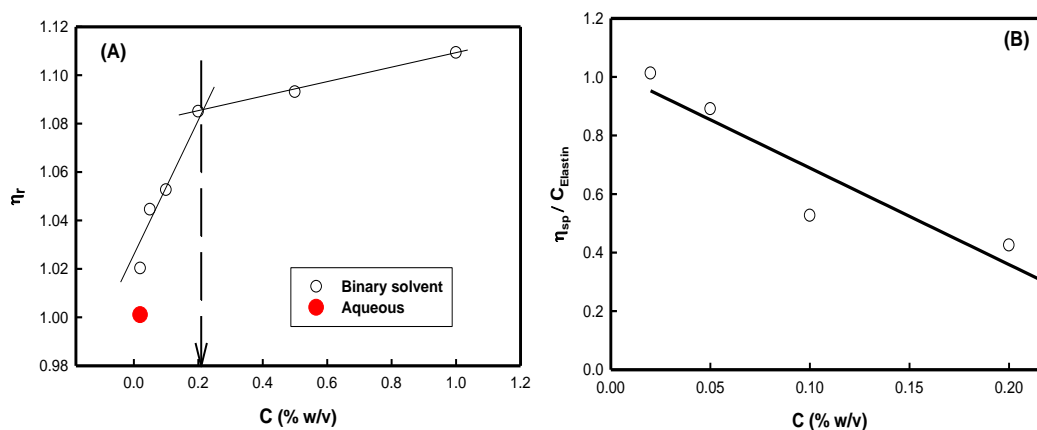
**Fig. 5.4:** (A): Variation of relative viscosity of elastin as a function of its concentration in aqueous and binary solvent. Solid lines are guide to the eye. Arrow indicates the concentration separating the two regions. (B) Solid line is linear fitting of eqn. (5.10) to specific viscosity data.

The low concentration regime was used to extract the intrinsic viscosity of the protein. Intrinsic viscosity is an important property to understand the structure and interactions in a given solvent. Specific viscosity can be defined as $\eta_{sp} = (\eta_r - 1)$ where $\eta_r$ is the relative viscosity of protein in suspension. Specific viscosity data was fitted with Huggins equation [Pawar et al, 2009] given by eqn. (5.10) to obtain intrinsic viscosity $[\eta] \approx 1.01$ ml/g, and interaction parameter $K_H \approx -3.1$ g/ml. Fitting has been shown in Fig. 5.4(B).

$$\frac{\eta_{sp}}{C} \approx [\eta] + K_H[\eta]^2 C \tag{5.10}$$

### 5.1.3.5 CONFORMATIONAL PHASE TRANSITION

These dispersions were subjected to temperature dependent viscosity studies which shows an interesting low temperature transition which is shown in Fig. 5.5. Viscosity increased sharply for T< 299 K, called a transition temperature. Variation in scattered intensity with temperature also supports presence of this transition. The transition temperature obtained from light scattering was observed at 302 K. Therefore it is reasonable to argue that mean transition temperature was (300± 2) K. This is similar to a inverse transition temperature reported for

elastin [Perticaroli et al, 2015]. Above this temperature elastin can be described as a "dynamic compact amorphous globule" [Perticaroli et al, 2015]. According to Nickels et al, hydrophobic hydration plays a significant role in tuning this inverse transition temperature. The change in intensity of scattered light is dependent on particle form factor among other parameters. At the transition temperature, a conformational phase transition of elastin is envisaged. At this temperature, hydrophobic collapse, and simultaneous expulsion of water molecules associated with the nonpolar side-chains of the protein are result of a reversal in the balance between the entropy gained upon disordering, and the enthalpy cost on removal of stabilizing interactions. Arrhenius equation was used to extract the Gibbs free energy ($\Delta G$) of the protein in binary solvent (fitting was performed above transition temperature).

Gibbs energy was determined for different concentration of protein dispersed in binary solvent. Incidently, it was found that $\Delta G$ (29±1) kJ/mol was independent of protein concentration. The array of physical data listed in Table-5.1 clearly indicates that elastin was stable in ethanolic solution through hydrophobic hydration. There was a systematic depletion of water molecules in the vicinity of elastin hydrophilic residues, ethanol molecules in turn occupied this space. Timasheff [Gekko et al, 1981] has elaborated this phenomena in details pertaining to protein dispersion in glycerol-water binary solvent. The sub-diffusion dynamics is a manifestation of this hydration process. Because, as the elastin molecule translate to a newer location, it must immediately create a new depletion region in its vicinity. Requiring a free-energy cost to be paid. This is key to the arrested dynamics.
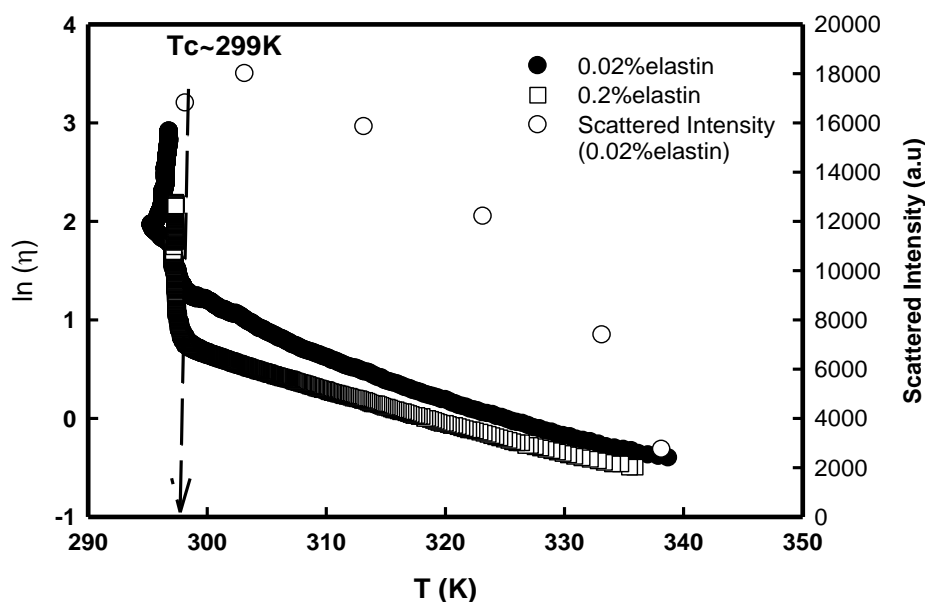
**Fig.5.5:** Variation of dispersion viscosity and scattered intensity of elastin in binary solvent as a function of temperature. Arrow indicates the transition temperature.

## 5.1.3.6 DLVO THEORY

Let us consider the system of hydrophobic protein molecules in a solvent with hydrophobicity 'f' with 'x' number of sodium ions (Sodium hydroxide was added to change the pH of dispersion in experiments). The hydrophobic parameter 'f' defines the hydrophobicity of solvent, f=1 refers to zero hydrophobicity (which can be aqueous solvent in experiments) and f=0 shows maximum hydrophobicity (which can be alcohol in experiments). In experiments, hydrophobicity of solvent was changed by introducing alcohol (ethanol) in aqueous medium. Introduction of alcohol in water introduced the hydrophobic forces in dispersion which results in the formation of water depletion region. Being hydrophobic in nature, protein molecule would prefer to reside in the water depletion region and sodium ions present in the system will provide the additional repulsive interactions. DLVO theory is one of the important theories to understand the stability of protein in the dispersion. By assuming that, protein can be treated as a colloidal particle since their sizes are in the nanometer range [Gogelein et al, 2008; Kastelic et al, 2015]. The total pair-potential between two protein

molecules can be described by the following equation [Gogelein et al, 2008; Kastelic et al, 2015]

$$U(r) = u_{LJ}(r) + u_r(r) + u_a(r)$$
(5.11)

where r is the intermolecular distance between protein molecules, $u_{LJ}(r)$ is the interaction potential between the hydrophobic domains among protein molecules. It has been assumed to be given by Lenard Jones potential (eqn. 5.12). This term explains the dominant interactions in the protein structure due to large number of hydrophobic domains. Second term of the total potential, $u_r(r)$ is the electrostatic double layer repulsive potential and the third term, $u_a(r)$ is the attractive potential due to solvent. $u_{LJ}(r)$ is given by

$$u_{LJ}(r) = 4\varepsilon \left[ \left(\frac{A}{r}\right)^{12} - \left(\frac{A}{r}\right)^6 \right]$$
(5.12)

where A represent the size of hydrophobic domains, $\varepsilon$ defines the strength of potential. The repulsive double layer potential can be described by Debye-Hückel theory [Tanford, 1967; Lekkerkerker et al, 2011] given by:

$$u_r(r) = \frac{BR}{l_B} \left[ \frac{e^{-\kappa r}}{r} \right]$$
(5.13)

where $\kappa^{-1}$ is the Debye screening length, R is the size of protein particle, quantity B can be expressed in terms of surface charge density $\sigma$ of protein as follows [Tanford, 1967; Lekkerkerker et al, 2011]

$$\frac{B}{K_B T} = \frac{8P_c^2}{1 + P_c^2}$$
(5.14)

where, $P_c = 2\pi\kappa^{-1}l_B \left| \frac{\sigma}{e} \right|$
(5.15)

with $P_c$, the number of elementary charge e on surface area $2\pi\kappa^{-1}l_B$ and screening length is defined as

$$\kappa^{-1} = \frac{1}{\sqrt{8\pi l_B I}}$$

$$(5.16)$$

where I is molar concentration of mobile ions and $l_B$ is the Bjerrum length which is defined as follows

$$l_B = \frac{e^2}{4\pi\varepsilon_0\varepsilon_r K_B T}$$

$$(5.17)$$

where $K_B$ is the Boltzmann constant, T is absolute temperature, $\varepsilon_r$ is relative dielectric constant. Attractive potential is dominated by the hydrophobic forces provided by the solvent in the system, it is given as [Iglesias et al, 2012]

$$u_a(r) = -4\pi R\kappa^{-1}\gamma(1-f)e^{-(r)/\kappa^{-1}}$$

$$(5.18)$$

where γ represents interfacial tension. Hence, total interaction potential can be given by

$$U(r) = 4\varepsilon\left[\left(\frac{\sigma}{r}\right)^{12} - \left(\frac{\sigma}{r}\right)^6\right] + \frac{BR}{l_B}\left[\frac{e^{-\kappa r}}{r}\right] - 4\pi R\kappa^{-1}\gamma(1-f)e^{-(r)/\kappa^{-1}}$$

$$(5.19)$$

The interaction potential for elastin in binary solvent (80% ethanol and 20% water) can be obtained as a function of intermolecular distance of protein using eqns. (5.11-5.19). The values of hydrophobic parameter: f is 0.2, size of protein in binary suspension obtained from DLS was 700 nm, interfacial surface tension was measured to be γ=25.4 mN/m, surface charge density of protein was obtained from measured values of zeta potential [Gekko et al, 1981] (using $\sigma = \frac{\zeta(\varepsilon\kappa)}{4\pi}$), size of hydrophobic domains (σ) has been taken as the physical size of residues ~2 nm and strength of potential ($U_0$) has been taken as ~ 20KJ/mol (order of secondary forces). Fig. 5.6 shows the variation of total interaction potential between the protein molecules in binary solvent corresponding to different ion concentration in the system. It shows that potential is highly sensitive towards the concentration of sodium ion. For low concentrations of ion (I<0.5 M), repulsive interactions were not significant to overcome the hydrophobic interaction between the protein molecules, hence no minima were observed in the total

interaction potential. Hence, it would be unfavorable to form the elastin dispersion in binary suspension at low salt concentration.
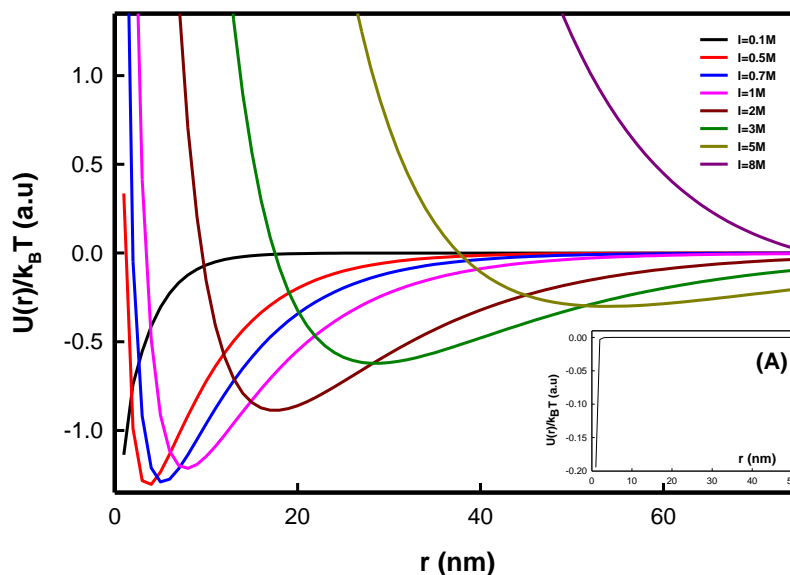


**Fig. 5.6:** Variation of total interaction potential between the protein molecules as a function of intermolecular separations for different concentration of sodium ions introduced in binary solvent. (T=298 K, f=0.2, R=700 nm, interfacial tension=35 mN/m, $\zeta$=14 mV). Inset (A) depicts the variation of total interaction potential between protein molecules as a function of intermolecular separation when protein was dispersed in aqueous medium (T=298 K, f=0.99, R=200 nm, interfacial tension=71 mN/m, $\zeta$=-24 mV).

Minima in total interaction potential of the system for I> 0.5 M signifies the balance among different interactions which favors the formation of stable dispersion of elastin. Depth of minima remains stable for 0.5 M < I > 2 M. For higher concentrations of ions depth of minima decreases, and finally disappears for I> 5 M. The effective interactions among ions become dominant for higher ion concentrations (I > 5 M), which might be the reason for the decreased depth of minima. Depth of equilibrium well (dU) was defined by energy difference between the minimum interactions in the potential well from zero (0-$U_{min}$). It was calculated for different concentration of ions in the elastin dispersions shown in Fig. 5.7. It clearly shows that depth sharply increases after I>2M and reaches zero for higher concentration of ions in the system.

After, discussing the interactions for elastin in binary solvent, consider elastin in the aqueous medium with low concentration of sodium ions. Protein would experience small repulsive, and weak attractive hydrophobic force due to solvent ($u_r/k_BT \sim 10^{-5}$ and $u_a/k_BT \sim 0$). Hydrophobic force between the hydrophobic domains of the protein molecule remains dominant ($u_{LJ}/k_BT \approx -0.2$). Hence, the total potential between the protein molecules remains attractive in nature (Fig. 5.6). This supports the low solubility of elastin in aqueous medium with low sodium ion concentration.
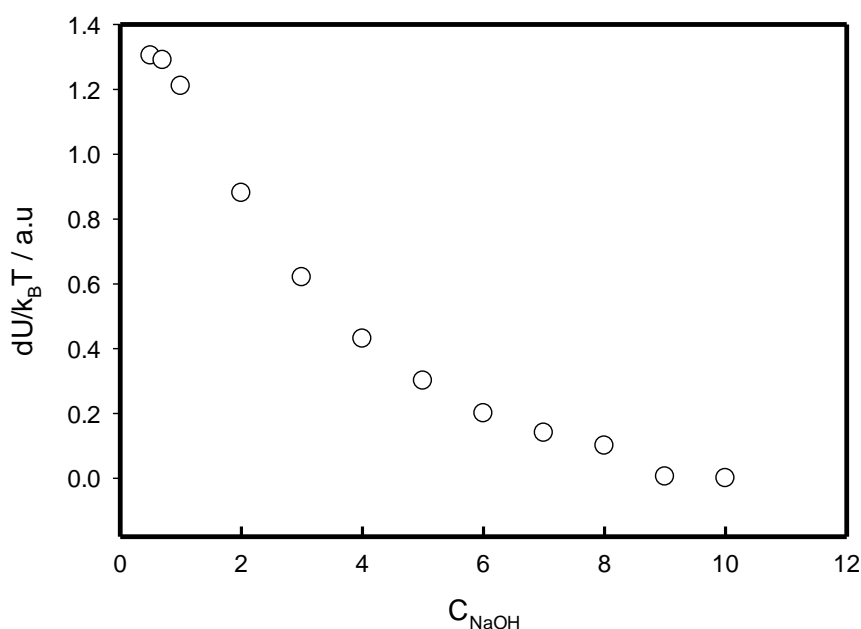


**Fig. 5.7:** Variation of depth of minima (from zero) as a function of different concentration of sodium ions introduced. Note that depth drops sharply after I>2M.

### 5.1.4   CONCLUSION

Organization of structural protein, elastin was deeply explored in aqueous and binary solvent of ethanol and water. Binary solvent introduces the hydrophobic forces in the dispersion medium and create cage-like open structures, in which hydrophobic protein molecule resides. Light scattering showed that protein molecules undergo slow and anomalous diffusion in binary solvent as compared to normal Brownian motion of molecule in aqueous medium. Anomalous diffusion is due to restricted or limited motion of protein molecule in

cage-like structures. It has been further supported by the observed red shift in the UV spectrum of the protein molecules in binary solvent as compared to aqueous medium. Electrophoresis measurement shows an interesting flip in the net surface charge of protein molecule, from positive to negative as the hydrophobicity of solvent decreases as the molecule transits from binary solvent to aqueous medium. It was observed that protein shows an interesting transition temperature at 299 K. Protein molecule above the transition temperature in binary solvent is rich in hydrophobic forces with little hydrogen bonding. DLVO theory explained the organization of this hydrophobic protein in the binary solvent. It was found that concentration of sodium ions should lie in the range of $0.5 < I > 2$ M for the best dispersion stability of elastin. Also, model predicted that hydrophobic interaction among protein molecule dominates over other interactions in aqueous solvent, which supports the instability or low solubility of elastin in aqueous medium.

## 5. 2 HEAT INDUCED COACERVATION OF ELASTIN AND ITS POSSIBLE THERMOREVERSIBILITY

### 5.2.1 MOTIVATION

The phenomenon of complex coacervation has been observed in a variety of complementary polyelectrolyte systems [Jong, 1935; Dubin et al, 2018; Cooper et al, 2005; Pathak et al, 2017]. Associative interaction between oppositely charged polyions often leads to the formation of soluble interpolymer complexes which may in turn coalesce to yield macroscopic coacervate droplets [Elhassan et al, 2018; Danielsen et al, 2018; Kizilay et al, 2011]. In the coacervate family, it is rare to find coacervation transition in unicomplex polyampholyte systems driven by temperature. Temperature-induced coacervation is not very common because solubility increases with temperature in most polyelectrolyte solutions. Elastin coacervation has drawn much attention in the past and it has been mostly recognized that the insoluble fraction of elastin, tropoelastin, is mostly responsible for causing coacervation. In section 5.1 of Chapter 5 we try to give find out: how thermoreversible is elastin coacervation? This is one area which has not received much attention in the past, and in the literature, there is the paucity of information on this. Since, tissue engineering involves multiple cycles of rupture and regeneration of tropoelastin self-assembly, the importance of exploration thermodynamic reversibility of elastin coacervate can be hardly stressed that motivate this work.

### 5.2.2 SAMPLE PREPARATION

Elastin dispersion 0.1% (w/v) was prepared by dissolving biopolymer powder in deionized water at 25°C under constant stirring for 4 h which produced a homogeneous and optically clear solution with a very light-yellow color. For salty samples, the required amount of NaCl (10 – 100 mM) was added to the solvent water and stirred for 5 minutes to which

elastin powder was added and stirred for 4 h at room temperature. For pH dependent study, the pH of each solution was adjusted as per experimental requirement using 0.1 M HCl or 0.1 M NaOH solution. All the solutions appeared optically clear and transparent after preparation. The prepared dispersions were stored in air tight borosilicate glass bottles at 4ºC for future use which in any case did not exceed 48 h. Each experiment was repeated four times to ascertain data reproducibility and the reported values are averages.

## 5.2.3 RESULTS AND DISCUSSION

### 5.2.3.1 CHARACTERIZATION OF ELASTIN

Since elastin is a heterogeneous biopolymer with much of its physicochemical properties dependent on the source and method of its extraction, it is necessary to first validate its physical properties. In the literature, elastin protein from various sources has been used for the coacervation studies, but there had been rarely any attempt to fully characterize the biopolymer prior to its use. We avoided this shortcoming in the present study. As the first step, we performed a pH titration of the salt-free elastin solution at room temperature and measured the solution turbidity, hydrodynamic radius ($R_h$), and zeta potential ($\zeta$) of the biopolymer (Fig. 5.8).

As expected, the turbidity and particle size increased until the isoelectric pH, pI=4.5±0.3 was reached where the zeta potential recorded almost zero value. The zeta potential remained in the range of +25 to -25 mV corresponding to the pH region 2.5 to 9. The mean hydrodynamic radius increased from 100 to 900 nm as pI was approached, and for pH>pI this value slowly decreased to 100 nm. If this plot is converted to a symmetry plot about the variable (pH-pI) (See Fig. 5.9), it depicts not a perfect symmetry of elastin charge state about its isoelectric pH. This implies that the fraction of protonated and deprotonated residues was quantitatively different at a given pH. However, this had a remarkable bearing on the average aggregate size of elastin. Below, pI the average aggregate size was much larger implying more

exposure of hydrophobic domains (Region-I). This aspect was probed more intensely by looking at the pH-dependent particle size histogram (Fig. 5.10).
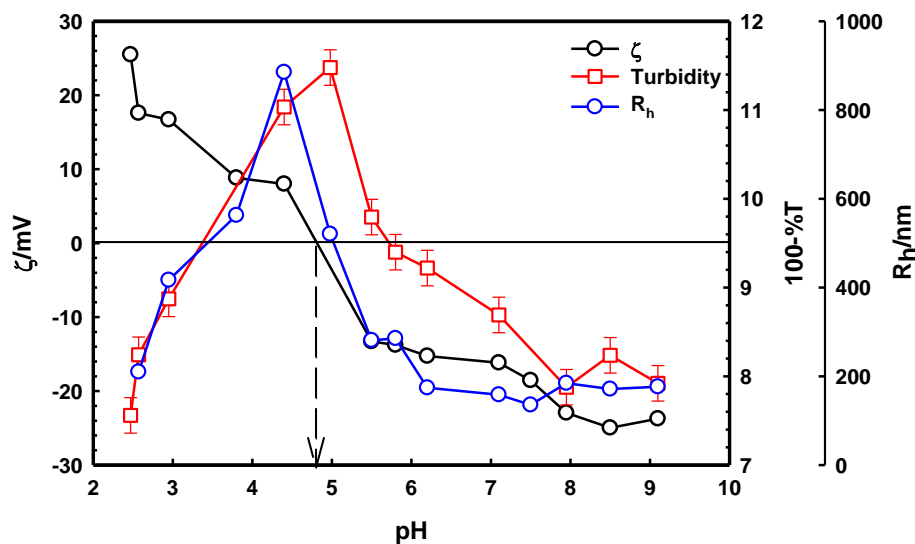


**Fig. 5.8:** Variation of solution turbidity (100-%T), mean hydrodynamic radius ($R_{h1}$), and zeta potential as a function of pH measured at room temperature $25^0$ C.
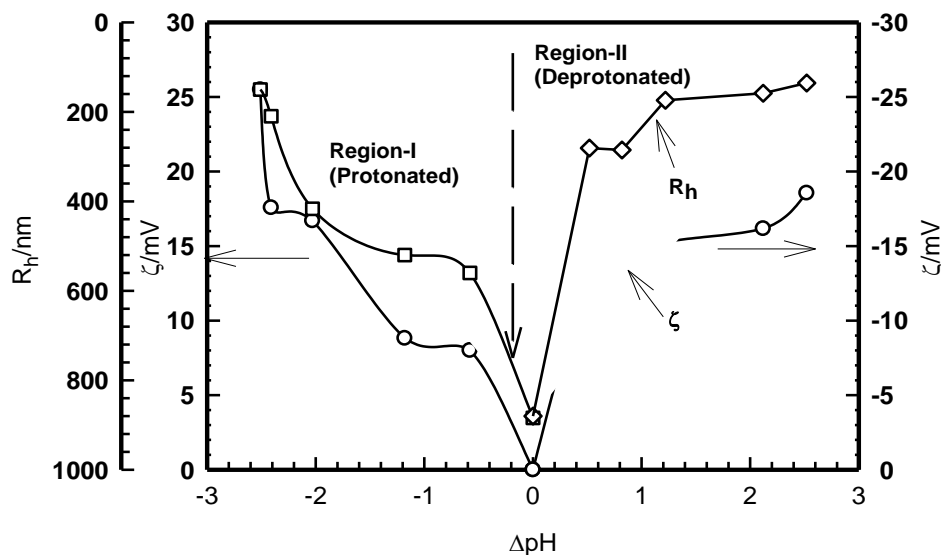


**Fig. 5.9:** Symmetry plot showing a variation of zeta potential and mean size about pI of elastin ($\Delta$pH = pH-pI). Notice the higher size of the aggregates when elastin was in its protonated state.
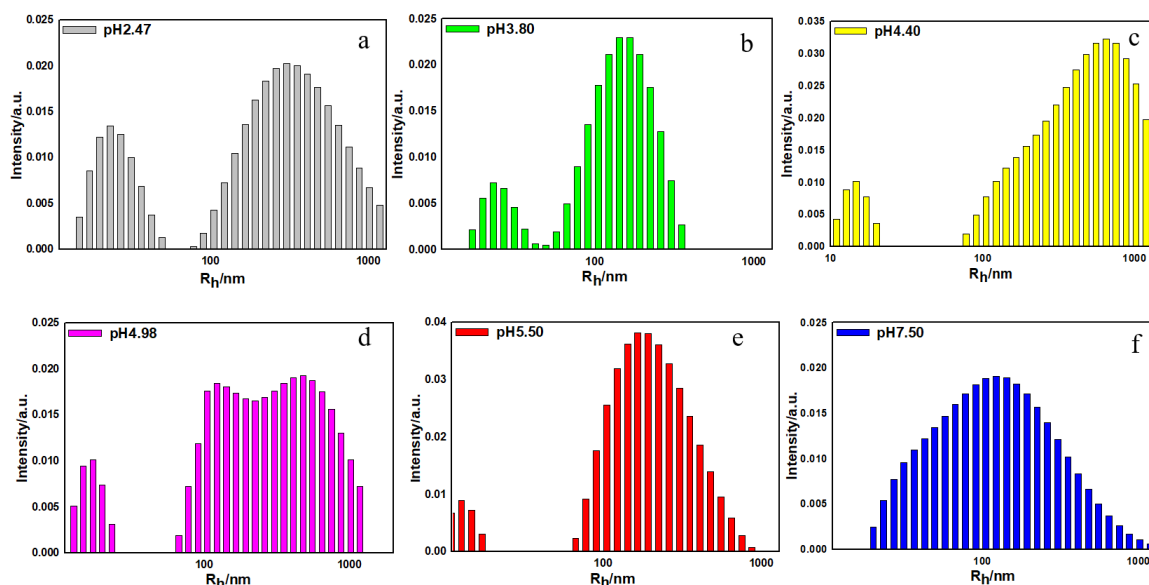
**Fig. 5.10:** Particle size histogram is shown as a function of pH of the solution evaluated at room temperature.
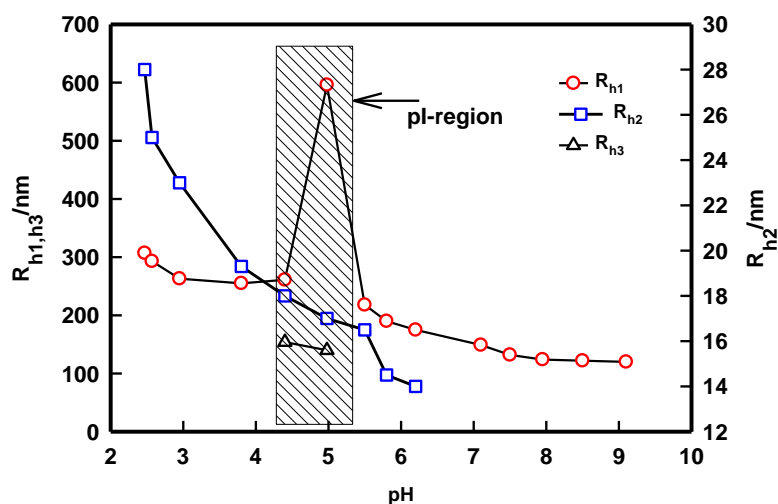


**Fig. 5.11:** Mean hydrodynamic radius shown as a function of solution pH. Note that close to pI-region, there are three populations present in the dispersion.

From the size histogram data shown in Fig. 5.10, bimodal particle size distribution was noticed in the pH region between $\approx 2$ to 4 (Fig. 5.10(a) and (b)), and 5.5 to 6.2 (Fig. 5.10 (e)). Beyond pH=6.2, there was only unimodal distribution (Fig. 5.10 (f)). Remarkably, in the region pI$\pm$0.5, there were three distinct populations in the size distribution (see Fig. 5.10 (d)). The dominant fraction had a mean size of $R_{h1}$ =300 nm that shot up to 600 nm at pI, and eventually reduced to 150 nm for pH>7. The second fraction had a mean size of $R_{h2}$= 28 nm at pH=2

which gradually decreased to 14 nm at pH =6. Interestingly, a third fraction was noticed only near the pI region that had a mean size of 150 nm. For pH>6, the particle size histogram was unimodal. Numerous studies have attributed self-assembly to the hydrophobic aggregation. Thus, for pH<pI, the observed higher aggregate size was clearly due to the abundance of intermolecular hydrophobic forces, which at pH=pI reached a maximum (Figs. 5.8 and 5.11). The coherent picture that emerged from this data revealed that the pH≈pI region (shaded region of Fig.5.11) was the most coacervate-rich zone compared to the rest of the pH domains. Further, between pH<pI and pH>pI regions, the former had more propensity of intermolecular hydrophobic interactions, and hence, was more prone to coacervate.

### 5.2.3.2 COACERVATION

The representative temperature dependent turbidity profiles of three salt-free elastin solutions at different pH depicted in Fig. 5.12. Temperature dependent experiments were done up to 60°C in order to avoid possible heat induced denaturation of the protein at a higher temperature. The data clearly shows the sample prepared with pH=4.7 (close to pI) undergoing unicomplex formation that resulted in the coacervation at $T_C$. The other two samples did not reveal similar behavior although the pH<pI sample exhibited marginally higher turbidity compared to the pH>pI sample (Fig. 5.12 (A)). The turbidity and UV-Vis absorbance profiles depicted qualitatively identical trend for the coacervating sample (Fig. 5.12 (B)). From the change in the slope ( $\frac{d(100-\%T)}{dT}$ $vs$ $T$ graph, Fig. 5.12 (C)) data it was possible to identify three distinct temperatures where observable changes in the turbidity occurred. These temperatures are identified as onset of self-assembly $T_{os}$, coacervation transition $T_C$ and mesophase separation temperature $T_{ms}$.
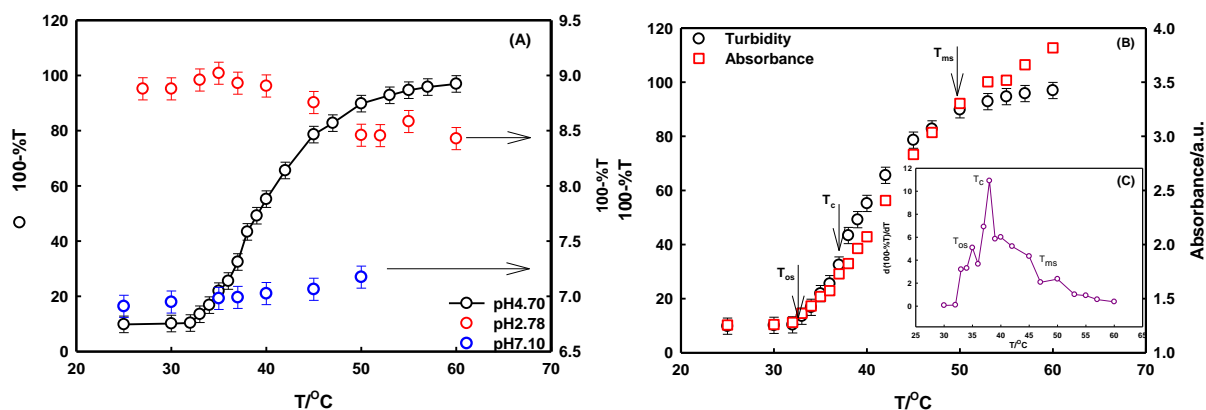
**Fig. 5.12:** (A)Temperature dependent turbidity profiles of three samples of elastin prepared at pH close to pI, pH<pI and pH>pI. The one at pH=4.7 undergoes coacervation while the other two samples mostly remain stable to temperature variation. (B) shows turbidity *vs* T that identifies the transition temperatures $T_{os}$, $T_C$ and $T_{ms}$, and in (C) and $\frac{d(100-\%T)}{dT}$ $vs T$ is shown that reveals clear peaks representing aforesaid temperatures. These data are from salt-free solutions. Onset of associative self-assembly occurs at $T_{os}$, coacervation transition at $T_C$ and mesophase separation at $T_{ms}$. See text for details.

The coacervation phenomenon was probed as a function of monovalent salt concentration (NaCl) in the range from $10^{-4}$ to $10^{-1}$ M (data not shown) which yielded turbidity profiles similar to the one shown for the pH=4.7 sample (Fig. 5.12). This data was changed to the derivative plot of $\frac{d(100-\%T)}{dT}$ $vs T$ which is depicted in Fig. 5.13. The peak in this plot corresponds to the coacervation temperature $T_C$ and shifts to lower temperature at higher salt concentration and similar behavior was found for the other two transition temperatures too. The dependence of $T_c$, $T_{os}$ and $T_{ms}$ with different salt concentration is shown in Fig. 5.14 which is revealing. Between $10^{-4}$ to $4 \times 10^{-2}$ M NaCl the $T_C$ value changed by almost $5^0$ C making the coacervation process highly temperature tunable. Since, the process of coacervation is preceded by self-assembly of elastin which in turn is governed by how much of the protein is exposed, and is available for self-association. This implies salt induced unfolding of this protein in the concerned salt content region, and occurrence of maximum of this at 40 mM NaCl concentration.
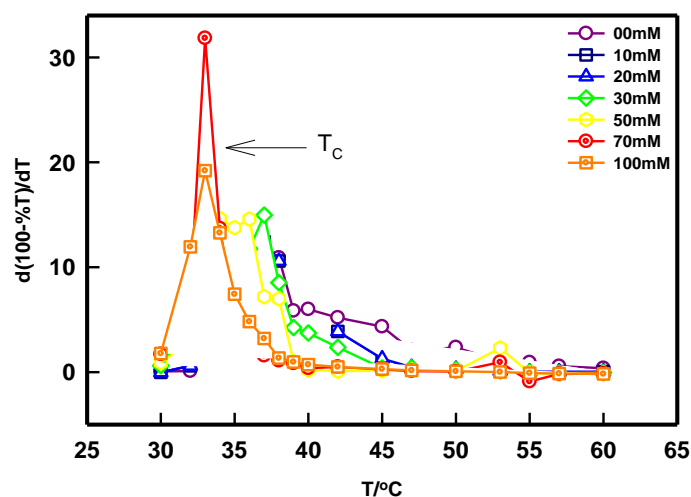
**Fig. 5.13:** Plot of $\frac{d(100-\%T)}{dT}$ $vs\ T$ shown for samples prepared with different salt concentrations. The peaks indicate coacervation temperature $T_C$, and it shifts to lower temperature at higher salt concentration.
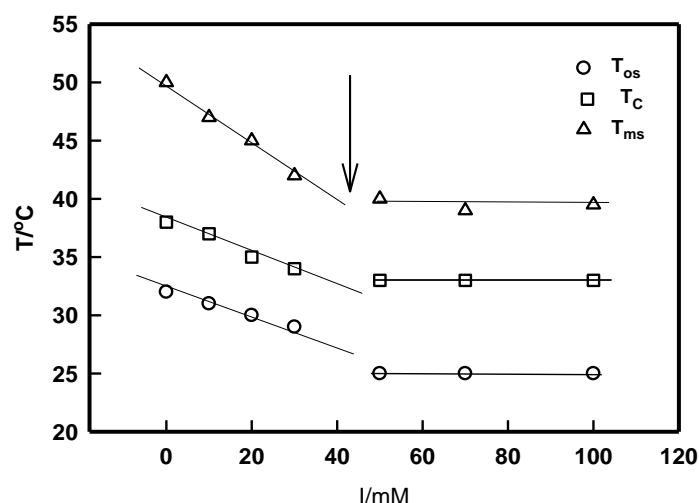


**Fig. 5.14:** Dependence of onset of self-assembly, coacervation and mesophase separation temperatures, $T_{os}$, $T_C$ and $T_{ms}$ respectively shown as a function of NaCl concentration of the coacervating elastin solution. Notice the shifting of $T_C$ by as much as $5^0$ C making the process highly temperature tunable. No significant dependence was found for [NaCl] > 40 mM.

### 5.2.3.3 THERMO-REVERSIBILITY OF COACERVATES

After probing the thermally activated coacervation in elastin solutions it was felt imperative to examine the thermoreversibility of the coacervates. Fig. 5.15 (A) depicts this behavior for salt-free solutions and (B) for salty preparations monitored through their turbidity profiles. The ABCD heating path characterizes the coacervation transition while DEFG

defines the behavior on temperature reversal in Fig. 5.15 (A) (cooling path). These heating-cooling profiles were identical in salty solutions too. However, two major differences were noticed: (i) the area under the loop (heating-cooling curves) decreased for higher salt concentrations (horizontal arrows in Fig. 5.15 (B)), and (ii) the remnant turbidity (turbidity at room temperature, vertical arrows in Fig. 5.15 (B)) was more for solutions with higher salt concentrations. What will happen if a sample is subjected to two heating-cooling cycles? Fig. 5.15 (C) data provides an answer to this question clearly. Some clear observations are made from this data: (i) the hysteresis loop area diminished significantly in the second cycle indicating thermoreversibility, and (ii) the remnant turbidity was almost zero implying the oligomeric state of elastin at room temperature remained unaltered.
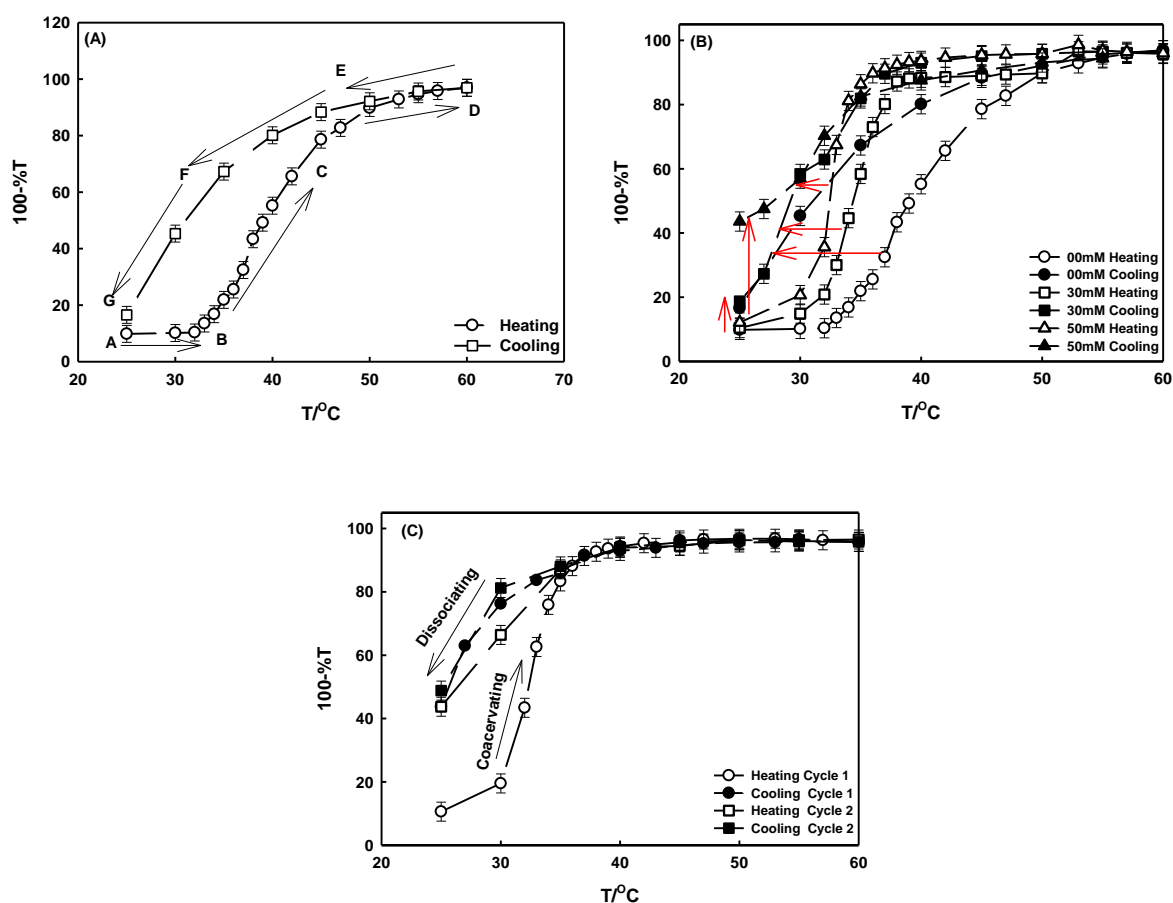


**Fig. 5.15:** (A) Turbidity profile of salt-free, and (B) for salty elastin solutions. Notice the bigger hysteresis loops in low-salt containing samples (horizontal arrow) and more remnant turbidity for higher-salt containing samples (vertical arrow). (C) second cycle heating-cooling diagram reveals reversibility to a large extent (I=70 mM).

In Fig. 5.16, the area under the turbidity hysteresis loop (data from Fig. 5.15) is plotted as a function of salt concentration along with the remnant turbidity. The self-assembly of elastin is a fully hydrophobic driven process and we have already shown in Fig. 5.14 that at higher salt concentration coacervation occurred at a much lower temperature. Thus, more hydrophobic sites were available for interaction at higher salt containing elastin solutions. Thus, the presence of salt facilitated the unfolding of elastin which enabled exposure of hydrophobic sites that were buried inside the core of the native elastin at room temperature. For a given ionic strength of the coacervating solution, as the temperature was raised from room temperature (RT) to $T_C$, more of elastin denatured revealing the hydrophobic sites to enable their associative interaction with their neighboring binding partners. When the temperature was reversed from $T_C$ to RT, first the coacervate got dissociated into individual elastin oligomers and further into smaller oligomers of the protein. This dissociation was more aggressive in salty solutions which enabled the elastin molecules to refold as it approached RT. However, the experimental data (Fig. 5.15) suggest that there was always a remnant fraction of small elastin aggregates even at RT that prevented complete refolding of elastin. This conjecture is depicted in Fig. 5.17 clearly.
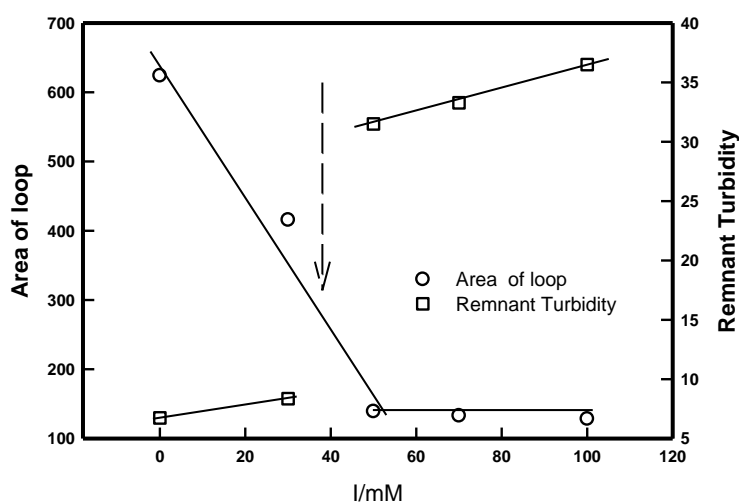


**Fig. 5.16:** The area under the heating-cooling curve loop (Fig. 5.15) and the remnant tropoelastin aggregates plotted as a function of the ionic strength of the coacervating solution.
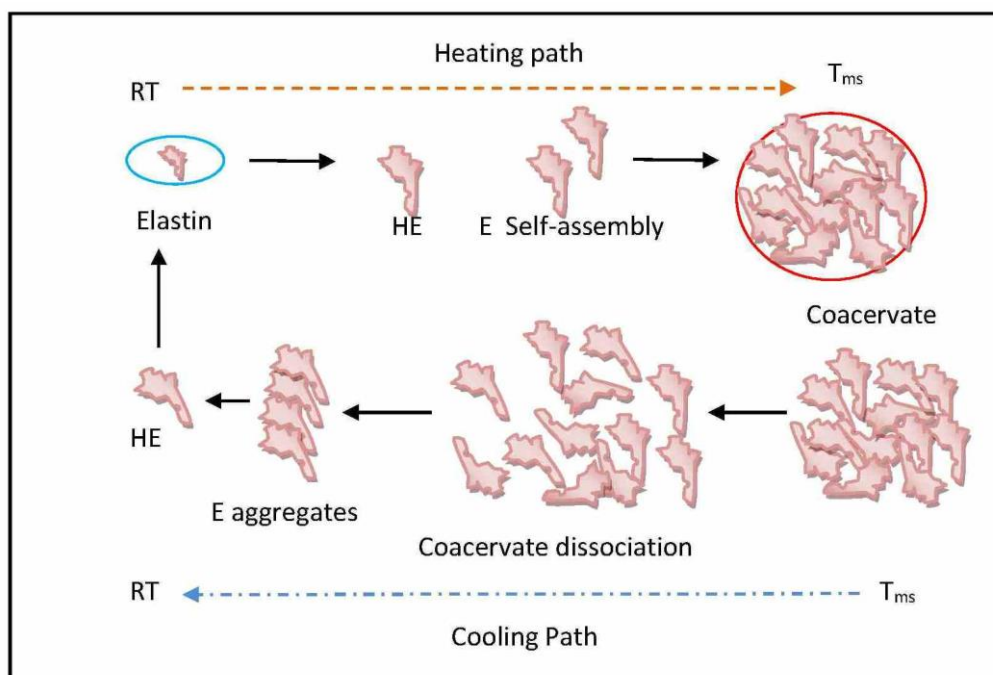
**Fig. 5.17:** Representative depiction of thermo-reversibility of elastin (E) coacervation. The hydrophobic motifs of elastin self-assemble (HE) to form soluble unicomplexes that coalesce to form coacervate droplets prior to mesophase separation. Legends: RT is room temperature, E is elastin, HE is the elastin with hydrophobic parts exposed, and $T_{ms}$ is mesophase separation temperature.

### 5.2.3.4 PHENOMENOLOGY OF THERMO-REVERSIBILITY

First, it is necessary to understand the molecular structure of elastin. Elastin (E) is constituted by linking together many small soluble precursor tropoelastin (TE) molecules of typical molecular weight of 50-70 kDa to generate the large insoluble complex. Each tropoelastin typically consists of a sequence of 36 small domains, each weighing about 2 kDa. The molecular structure consists of alternating hydrophobic and hydrophilic domains.

Tropoelastin self-assembles at physiological temperature due to the interaction between hydrophobic motifs that confer elasticity to the structure and also lead to β-turn formations. This process is thermodynamically controlled and does not require protein cleavage. The hydrophobic domains are highly stretchable from 20 to 160 nm. Baldock et al [Baldock et al, 2011] have shown that the mean persistence length of TE is 0.36 nm and it has a contour length of $166 \pm 49$ nm. TE monomer has a hydrodynamic radius of 5.09 nm and radius of gyration of

6.2 nm that ascribes an elongated conformation to this molecule. This molecule has Young's modulus of about 3 kPa [Baldock et al, 2011; Graham et al, 2004].

Clarke et al have argued the disadvantages in the use of $\alpha$-elastin as a descriptor for the tropoelastin coacervation. Because $\alpha$-elastin is derived from elastin partly hydrolyzed with oxalic acid, it consists mostly of hydrophobic elastin fragments that are heterogeneous and crosslinked. Tropoelastin, on the other hand consists of alternate domain structures [Clarke et al, 2006]. It has been further shown that unlike most proteins that show denaturation with increased temperature and become less ordered, elastin polypeptides appear to get more ordered eventually leading to the process of coacervation. This process has been described for tropoelastin, $\alpha$-elastin, and synthetic polypeptides mimicking the hydrophobic domain sequences [Bellingham et al, 2001]. Jamieson et al have shown that coacervation in the elastin system is not a second-order phase transition. The protein hydrolysates exist in the cold solution as monomeric $\alpha$-fragments, which on warming to higher temperature form isotropic and stable aggregates preferentially at pH values near the isoelectric point [Jamieson et al, 1973].

In general terms, the coacervation pathway can be qualitatively visualized through a set of equilibrium steps given by

$$[E]_N \leftrightarrow [HE]_x + [E]_{1-x} \tag{5.20}$$

$$[HE]_{n-1} + [HE] \leftrightarrow [E]_{agg} \tag{5.21}$$

$$[E]_{agg} + [E]_{agg} \leftrightarrow [E]_{ms} \tag{5.22}$$

First, a fraction $x$ of available elastin molecules[E] do undergo partial heat induced structural change to expose the hydrophobic fragments of elastin [HE] which in turn associates with an existing oligomer $[HE]_{n-1}$ to generate an elastin aggregate $[E]_{agg}$. $[E]_N$ and $[HE]_x$ represents the concentration of native elastin and hydrophobic fragment of elastin respectively. In the final stage at $T_C$ these aggregates coalesce to form the coacervate mesophase $[E]_{ms}$. The dissociation pathway can be described as follows

$$[E]_{ms} \leftrightarrow [E]_{agg} \leftrightarrow [HE]_{olig} \leftrightarrow [E]_{1-x} + [HE]_x \qquad (5.23)$$
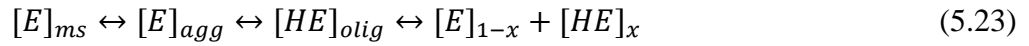
which can be approximated to a pseudo two-step process given by

$$[E]_{ms} \leftrightarrow [E]_{RT} \qquad (5.24)$$

when $[E]_{RT}=[E]$, it is fully reversible, and in the case of partial reversibility ($[E]$-$[E]_{RT}$) will describe the remnant fraction of aggregated elastin that does not permit restoration of elastin to its native state (vertical arrows in Fig. 5.15 (B)). Further, we treat $[E]_{ms}$ is the coacervate phase made of self-assembled elastin units. Equations (5.20) to (5.24) are a qualitative representation of kinetics of coacervation pathway. It cannot be claimed that all the $[E]_{agg}$ turned into $[E]_{ms}$. However, in order to provide a thermodynamic description of the coacervation process, it was presumed that it involved a complete transformation of aggregates to mesophase.

However, as far as the dissociation process is concerned, the above-mentioned multiple step reaction can be simply described through an equilibrium constant $K_{eq}$ involving an approximate two-step process where $[E]_{ms}$ dissociates to approach $[E]_{RT}$ during the cooling cycle (eqn. (5.24)). Thus, to first-approximation

$$K_{eq} = \frac{[E]_{RT}}{[E]_{ms}} \approx \frac{(100-\%T)_{RT}}{(100-\%T)_{ms}} \qquad (5.25)$$

The solution turbidity depends on particle density (equivalent to concentration) among other things. Therefore, to first approximation turbidity can be assumed to be directly proportional to particle concentration assuming that particle form factors do not change. Thus, the concentration of $[E]_{RT}$ and $[E]_{ms}$ was assumed to be proportional to the turbidity of that phase. Such simplification will facilitate quantitative estimation of the free-energy of coacervation $\Delta G$ using Arrhenius description which is given by

$$K_{eq} = \exp(-\Delta G/RT) \qquad (5.26)$$

The temperature dependent turbidity profiles shown in Fig. 5.15 (B) were fitted to eqn. (5.26) to determine the corresponding $\Delta G$ values and the results are plotted in Fig. 5.18.
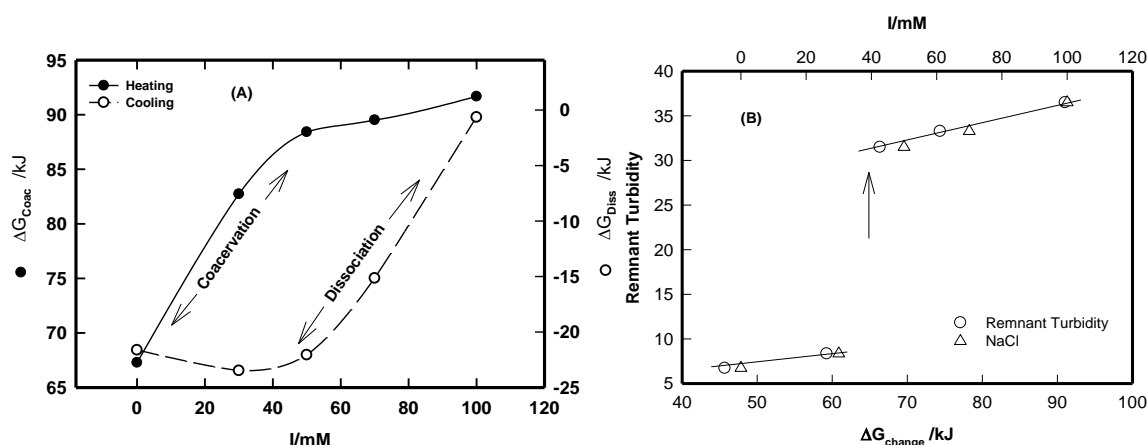
**Fig. 5.18:** (A) Variation of coacervation and dissociation free energy, $\Delta G_{coa}$ and $\Delta G_{Diss}$ with the ionic strength of the sample. (B) Dependence of remnant turbidity on free energy difference $\Delta G_{change} = (\Delta G_{coa} - |\Delta G_{Diss}|)$.

The heating path involved an activation free-energy $\Delta G_{coa}$ (coacervation free energy) while the same for the cooling path it was $\Delta G_{Diss}$ (dissociation free energy). The data shown in Fig. 5.18 implies that the unicomplex formation through hydrophobic association of TE leading to coacervation was a thermally activated process. On the contrary, on cooling, these self-assembled complexes dissociated to their oligomer state spontaneously facilitated by free-energy gain. The free-energy change, $\Delta G_{change} = (\Delta G_{coa} - |\Delta G_{Diss}|)$ is in fact identical to the remnant [E] oligomer content (remnant turbidity at RT). Therefore, their linear dependence with a positive slope is indicative of the fact that elastin solutions in salty environment undergo thermally activated self-assembly which on temperature reversal remain trapped in a partially unfolded state giving rise to an intrinsically disordered protein, IDP-like situation.

## 5.2.3.5 SECONDARY STRUCTURE
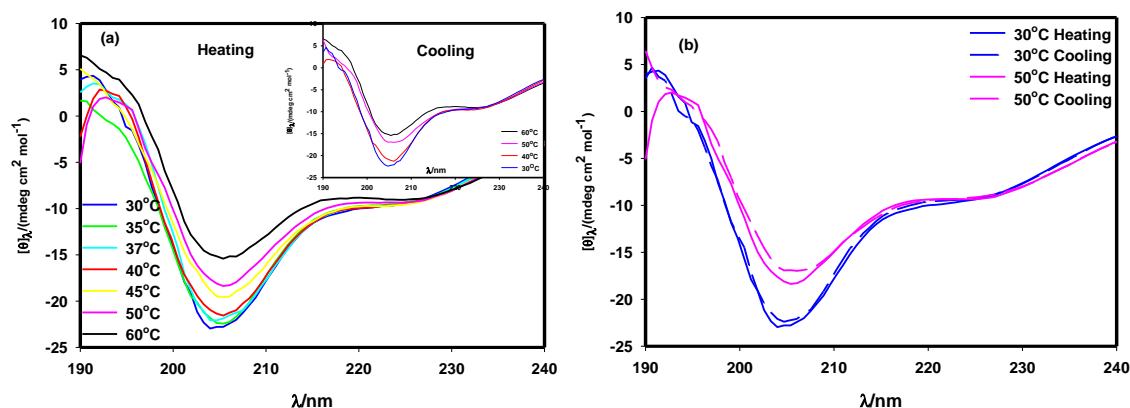


**Fig. 5.19:** Variation of circular dichroism spectra of elastin (a) heating and inset cooling cycle (b) comparison with heating cooling for 30 and 50 $^\text{O}$C in salt-free solution.

The secondary structure of elastin in coacervate samples were monitored for heating and cooling cycle using Circular Dichroism measurements in the temperature range of 30 to 60$^0$ C (Fig. 5.19(A)). The spectra show two prominent peaks one positive band at 195 nm, and one negative band at 205 nm, and a minor negative band at 225 nm. Figure 5.19(a) clearly shows molecular ellipticity of these bands reduced with a rise in temperature indicating a decrease in helicity. In addition, the spectra clearly showed that elastin exhibited thermoreversible change as shown in the insets. There was a small hysteresis in CD spectra of elastin in heating and cooling cycle data consistent with the same noticed in turbidity. Therefore, it can be argued that there was a loss in secondary structure (helix component) of elastin with the rise in temperature and the consequent possible formation of intrinsically disordered protein-like structures cannot be ruled out [Kjaergaard et al, 2010]. This conclusion was utilized in arriving at a molecular level schematic shown in Fig. 5.17 and the eqns (5.20-5.23). For a given temperature the two profiles do overlap to a good extent (Fig. 5.19). This indicated that at the molecular level the secondary structure opened up during heating and *vice a versa*. Since the hydrophobic moieties of proteins reside inside the core of the molecule to minimize the free-energy of the structures when in contact with water, it is logical to argue that

at a given temperature a partially denatured structure of the elastin molecule will exist revealing only a portion of its hydrophobic moiety, which is qualitatively referred to as HE in this work. It needs to be emphasized that what we have proposed in this model is at best a conjecture based on data in hand.

### 5.2.4 CONCLUSION

We performed an extensive study to map the pH-dependent physical properties of the elastin molecule and found that the zeta potential was not completely symmetric about its isoelectric pH. The protonated molecules were found to be in an aggregated state with a mean size that was much larger than their deprotonated counterparts. The particle size histogram revealed considerable aggregation in the pH= pI±0.5 region making this zone fertile for coacervation. The coacervation kinetics of elastin precursor tropoelastin was mapped as a function of solution ionic strength. This mesophase separation was found to be strongly temperature dependent and the coacervation temperature could be lowered by as much as $5^0$ C from its initial value of $38^0$ C (for salt-free sample). The samples were subjected to heating-cooling cycles that produced hysteresis loops with loop area decreasing with ionic strength which implied larger thermo-reversibility of salty coacervates. However, at room temperature the heat-cool cycled sample did reveal the presence of monomeric TE molecules only for salt-free samples, but in all other samples there was clear evidence of the existence of a remnant fraction of aggregated elastin molecules. The size of this remnant aggregates increased with the ionic strength of the samples. Estimation of free-energy of the coacervation and the dissociation processes revealed that coacervate dissociation was free-energy driven while the elastin self-assembly leading to coacervation was hydrophobic and thermally activated. This study attempts to provide an understanding to the phenomenon thermoreversibity of elastin coacervates which remains poorly explored hither to.

## 5.3 COMPLEX COACERVATION BETWEEN DSDNA AND VERY WEEKLY CHARGED PROTEIN ELASTIN IN AQUEOUS AND SALTY SOLUTIONS

### 5.3.1 MOTIVATION

DNA-protein interaction plays a key role in many biological processes like DNA replication, recombination, repair, transcription, packaging of chromosomal DNA, and gene expression. In DNA-protein interaction, protein can act as catalyst and enzyme for biochemical reactions which motivate this work what kind of interactions and forces are involved in protein-DNA binding. In this part of chapter 5, a detailed study that probed the interaction between elastin and 2000 base pair ds DNA in salt-free and salty aqueous solutions at room temperature. The binding profile indicated the following dependence on elastin concentration: DNA condensation ($C_{ELASTIN} = 0.2\%$ (w/v)), and formation and growth of DNA –Elastin soluble complexes ($0.2 \leq C_{ELASTIN} \leq 0.5\%$ (w/v)) followed by complex coacervation.

### 5.3.2 SAMPLE PREPARATION

The DNA stock solution was prepared by dissolving DNA (0.2% (w/v)) in double distilled deionized water at room temperature for an hour (pH= 6.5). A 5% (w/v) elastin stock was prepared by dissolving elastin powder in double distilled deionized water at room temperature for half hour (pH= 4.0). Both the solutions appeared optically clear and transparent after preparation. Samples for the experiments were prepared by mixing previously prepared elastin and DNA solutions (pH = 4.4 to 5.3) at the required mixing ratio. In all the samples the elastin concentration was maintained at 0.05 % (w/v) while titrating with the stock solution of DNA (0.2% (w/v)) and final DNA concentration in the solution were kept $C_{DNA} = 0.14 \times 10^{-3}$ to $6.33 \times 10^{-3}$ (w/v). These samples were stored in air tight borosilicate glass vials for further analysis, which in all instances, did not exceed 24 hours after preparation. All procedures were performed at room temperature 25 $^0$C unless otherwise mentioned.

### 5.3.3 RESULT AND DISCUSSION

### 5.3.3.1 PRIMARY BINDING: CONDENSATION OF DNA (r < 0.01)

Complex formation and coacervation can be understood on the basis of mixing ratio. The formation of complexes and coacervate can be defined in this section is as follows: Mixing ratio for the samples is defined as r,

$$\text{r} = \frac{[DNA]}{[E]} = \frac{[C_{DNA}]}{[C_E]} \tag{1}$$

In the present case [DNA] was varied and [E] was kept fixed. The interaction between DNA and elastin divide in three distinct regions divide (Fig. 5.20) by mixing ratio as follow:

(a) $r_c$ is the mixing ratio from where the associative interaction ensues which results in a soluble complex formation.

(b) $r_\phi$ is the mixing ration where complexes coalesce to result in liquid –liquid phase separation leading to coacervation

(c) $r_{prep}$ is at which large insoluble complexes drives the solution to liquid-solid phase separation.

At $r_c$, the possibility of free elastin attached to the DNA leads the formation elastin–DNA interpolymer complexes. The pHs of the Elastin–DNA mixed solutions were close to that of DNA solution. At this pH, the zeta potentials of Elastin and DNA were measured to be 7.2 and -55 mV, respectively, which would facilitate their associative interaction via electrostatic forces, and in a salt-free environment, in particular, leading to the formation of soluble interpolymer primary complexes. The data in Fig. 5.20 and 5.21 clearly indicate such binding, which was evident from the fact that the zeta potential complex vary (from 6.65 to -33.5 mV) during this interaction with a concomitant increase in its apparent hydrodynamic size (from 130 to 2000 nm). The size of complex decreases with further increase in DNA concentration due to rise in the content of insoluble complexes. The corresponding scattering intensity varied

from $1.2 \times 10^5$ to $2.4 \times 10^5$ because of dominant scattering emits from the large size complexes which eventually phase seperated and intensuty decrees to $1.8 \times 10^4$ due to precipitaion. In our experiments, a large amount of elastin was required for the DNA condensation and its total charge neutralization.
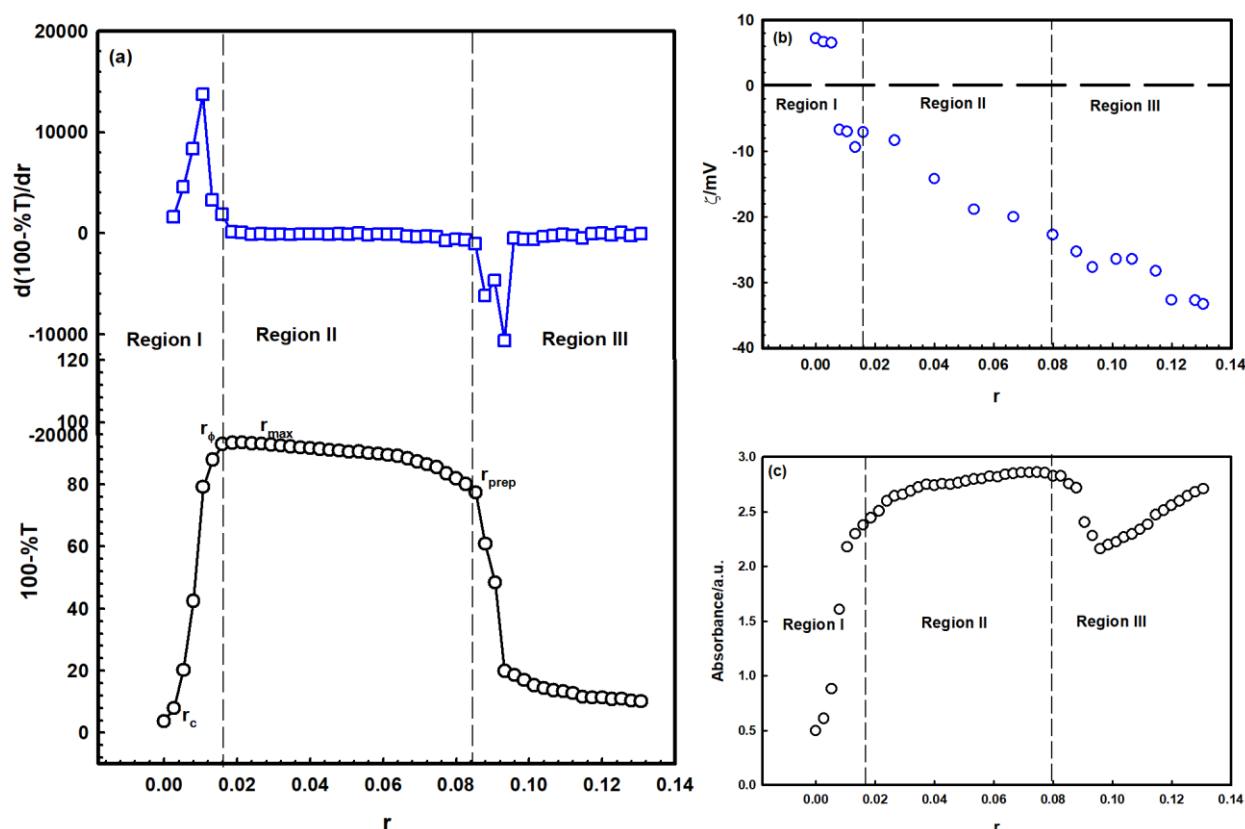


**Fig. 5.20:** (a) Variation of turbidity and d(100-%T)/dt with a mixing ratio for DNA: elastin. The optimum mixing ratio is $r_\phi = 0.01$, $r_{max}$ is corresponding to the point where saturation in turbidity takes place and $r_{prep}$ is corresponding to the ration from where precipitation takes place in the elastin complex. Spikes in the derivative plot corresponding to turbidity plot clearly shows the regions of mixing ratio $r_\phi$ and $r_{prep}$ precipitation in the system. Variation of (b) zeta potential and (c) absorbance (at $\lambda = 260$ nm) with respect to mixing ratio.

This phenomenon can be understood from the data shown in Figs. 5.20 and 5.21. Variation of zeta potential ($\xi$), solution turbidity (100-%T), hydrodynamic radius ($R_h$) and absorbance are shown for different samples. Elastin concentration was fixed at 0.05% (w/v). Notice the sharp change in slope at r ~ 0.0.01. The top row photographs depict the growth in turbidity as DNA concentration was increased. Firstly, because of the high charge ratio (DNA:

Elastin ≈ 7.5), more DNA was required to bind and charge neutralize the Elastin. Secondly, because of the large and rod-like the structure of DNA, Elastin will feel steric hindrance while attaching to incoming DNA molecules. The elastin has a net charge is close to 8 mV compared to -60 mV for DNA. In this mechanism, the positively charged elastin will preferentially bind to polyanionic DNA. This interaction, which was electrostatic in nature, was supported by the zeta potential data which depicted total charge neutralization of the Elastin–DNA complex upon addition of DNA in Region-I. This can be referred to as primary binding. The inter-polymer complex formation in Region-II can be described as follows

$$[\text{Elastin}] + (1\text{-}x)\,[\text{DNA}] = [\text{Elastin–DNA}]_C + x[\text{DNA}] \tag{2}$$

Of the available DNA, a fraction (1-x) was bound to Elastin to yield the Elastin–DNA primary complex, and the remaining fraction x was available as free in the dispersion. Elastin–DNA complex in the dispersion as free protein. Thus, the nucleic acid condensation was due to the combined effect of binding of DNA strand to the Elastin. Thus, the condensation was a result of charge neutralization of the Elastin protein.

## 5.3.3.2 SECONDARY BINDING IN ELASTIN (COMPLEX COACERVATION (0.01 < r < 0.09)

The data are shown in Fig. 5.21 reveals a signature change in their histogram and mean size profiles from $r_\phi$ to $r_{prep}$. However, the solution turbidity does change significantly, and then get saturated. The zeta potential of the complex changes -8 mV to -29 mV (Fig. 5.20(b)) viz. more charge neutralization, and the apparent hydrodynamic size also increases (400 nm to 2400 nm). The behavior of the coacervating system in Region-II can be visualized as follows. The existing interpolymer primary complexes that were only partially charge neutralized, as stated in the previous section, continued to attract more DNA for further binding and as a consequence, the turbidity and zeta potential kept increasing called as secondary binding. This

dispersion had a population of Elastin–DNA complexes, and free DNA. The physical size of the complexes was larger than DNA. It needs to be emphasized that the secondary binding was achieved at saturated plateau $0.01 < r_{max} < 0.08$ shown at Fig. 5.20.
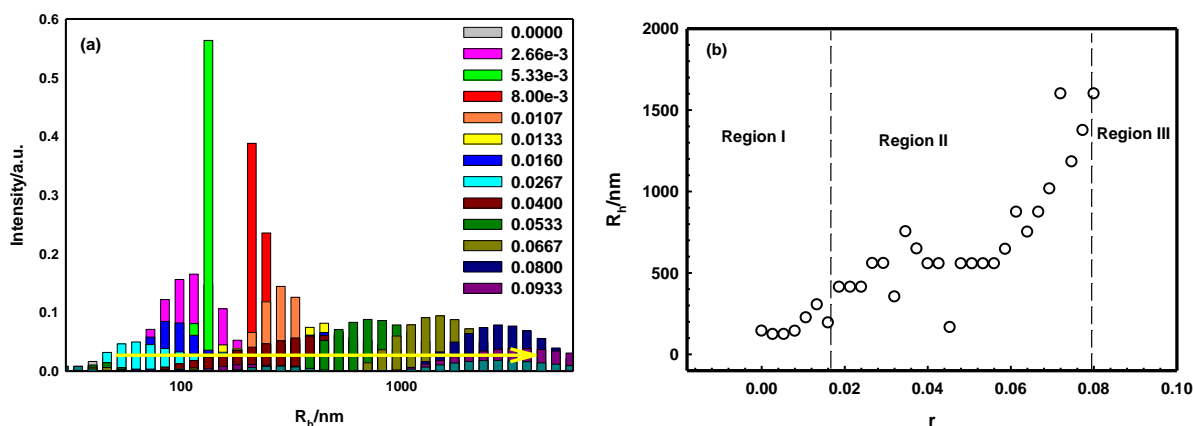


**Fig. 5.21:** (a) Variation of size histogram for ELASTIN: elastin at different mixing ratio and (b) Variation of hydrodynamic ration with mixing ratio r.

### 5.3.3.3 PRECIPITATION ($r_{prep} > 0.09$)

Interestingly, the turbidity, size, absorbance and scattering intensity decreased like in many other coacervating systems, because of the large soluble complexes.

### 5.3.3.4 STATIC STRUCTURE FACTOR
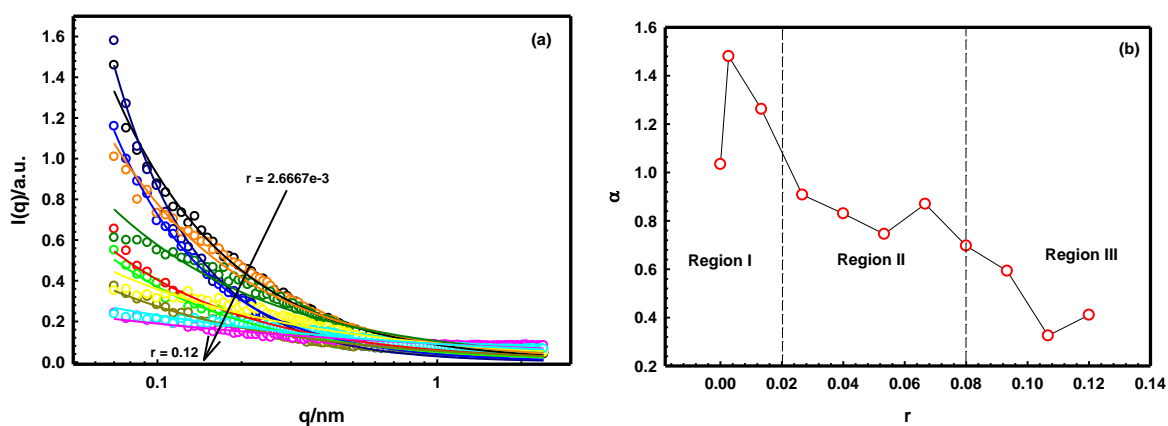


**Fig. 5.22:** (a) Structure factor data, I(q) vs q for complexes at different mixing ratio (b) Variation of α with mixing ratio.

The complexes were examined for microstructure information by SANS. The SANS data revealed the microscopic structure of the material under consideration over a length scale of a few nanometers. These samples were subjected to SANS studies to determine their underlying microscopic structures. The static structure factor data is depicted in Fig. 5.22 for various mixing ratio. The scattering profiles show the SANS data could be described by excellent least-squares fitting to the power-law function. The I(q) vs q profiles depicted convey information about the structure factor of the complex. The data were fitted to power-law.

$$I(q) = I(0)q^{-\alpha} \tag{2}$$

where the exponent $\alpha$ defined by eqn. 2 owes its origin to the geometry of the scattering moiety in a given system. For instance, $\alpha = 1, 1.7, 2,$ and $4$ correspond to geometrical shapes of the rod, diffusion-limited cluster (DLA), Gaussian coil, and sphere, respectively. For self-similar objects, this exponent is equivalent to the mass fractal dimension of the object. The analysis of SANS data from coacervate yielded $\alpha = 0.8 \pm 0.4$ for all the samples. For the rod-like the structure it is known that $\alpha = 1.0 \pm 0.5$. Thus, it is plausible that the coacervate composed has rod-like structures (a reflection of DNA) at room temperature.

### 5.3.3.5 SALT-DEPENDENT STUDY

Further to study the type of interaction salt dependent study was performed. Fixed concentration of elastin was taken in different salt NaCl (0 M to 0.1 M) concentration, then different amount of DNA was mixed in this salt mediated elastin solution. DNA interact with the remaining binding sites of Elastin. As mixing ratio r increases for particular salt concentration turbidity of sample increases till 0.02 ratio, then turbidity decreased (Fig. 5.23(a)) because of salt mediated salting out within the system. Initially empty binding sites of elastin was occupied by DNA (till r~ 0.02) and then due to salt occupancy within the system it

does not allow DNA to bind with elastin. We found that turbidity of the solution decreases, as salt concentration increased for particular mixing ratio.
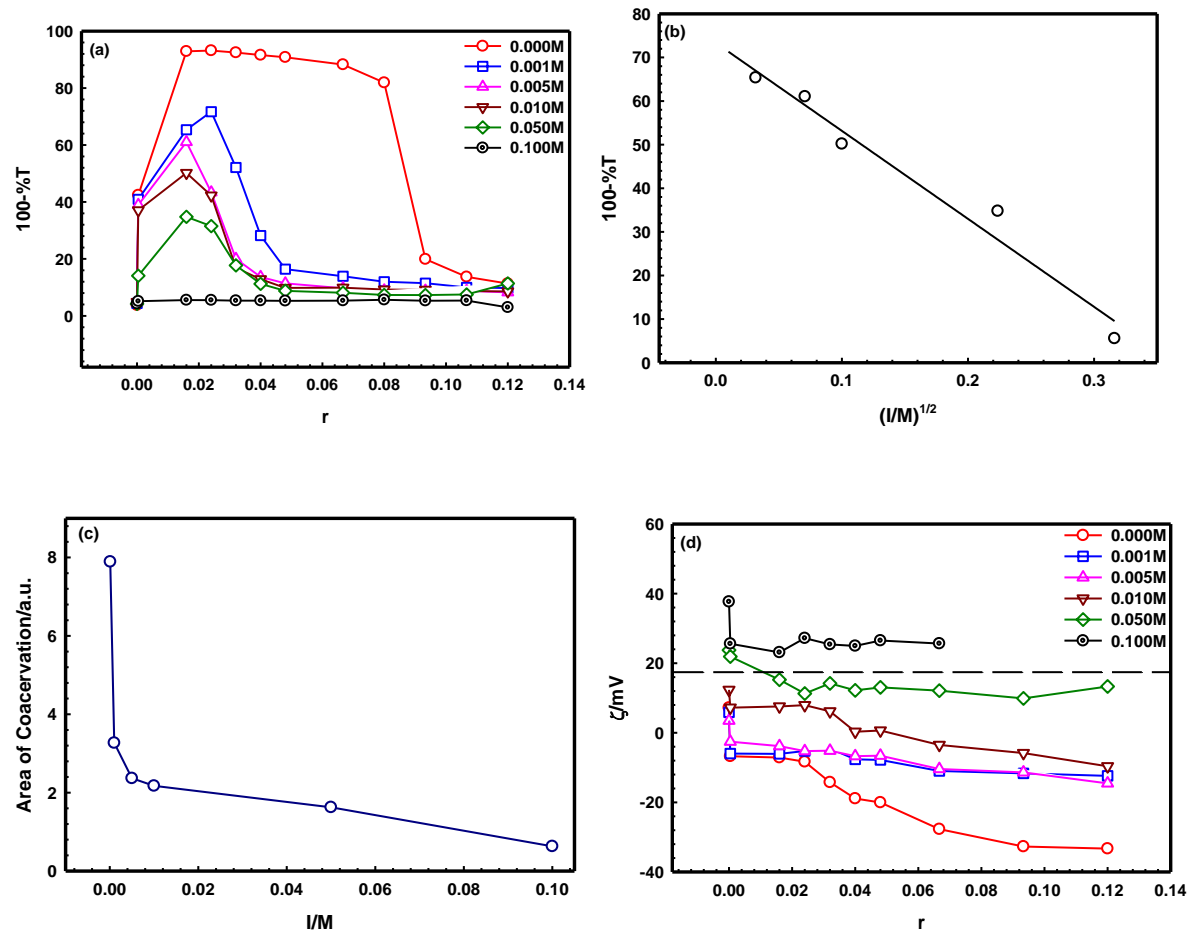


**Fig. 5.23:** (a) Variation of turbidity with mixing ration for different salt concentrations. (b) Variation of turbidity with square root of ionic concentration for r = 0.2, (c) Turbidity-peak area of coacervate samples at different ionic concentration, and (d) variation of zata potential of the complex with mixing ration for different salt concentrations.

Fig. 5.23(b) clearly depicts that turbidity of the solution is decreasing with square root of ionic concentration. Therefore, with rise in salt concentration coacervation yield or area of coacervation evaluated from the Fig. 5.23(a) decreased (Fig. 5.23(c). Zeta potential also revealed that as mixing ratio increased for particular salt concentration first zeta potential decreased till 0.02 optimum mixing ratio then it gets saturated because of total over charge within the system. As salt concentration increases further then zeta potential of the solution

decreases or approach to charge neutralization which also suggested that salt mediated screening has the coacervation process. This whole process between salt mediated elastin–DNA solution indicated the presence of electrostatic binding between elastin and DNA.

## 5.3.4 CONCLUSION

We evaluated that elastin and DNA complex formation leads coacervation process. The interaction was studied via turbidity, zeta, DLS and SANS measurement which revealed it to be strongly hierarchical, with distinct binding regions. Region I showed DNA-Elastin primary binding for $r < 0.02$ and size of complex increases, Region II ($0.02 < r < 0.08$ indicated secondary binding where total charged is neutralized and come to saturation, turbidity become very high ($\sim 90\%$) and size remains constant in this region, which resulted in the appearance of soluble complexes and initiation of coacervation. Region III ($0.08 < r < 0.12$ revealed growth of insoluble complexes with large sizes followed by precipitation. The binding profile of DNA-elastin complex coacervation decreased with monovalent salt concentration. Small angle neutron scattering (SANS) data of coacervates indicated rod like structure of scattering moiety. Salt mediated study revealed that the interaction of hydrophobic protein elastin with DNA is electrostatic in nature.

## 5.4 REFERENCES

1. Baldock, C., Oberhauser, A. F., Ma, L., Lammie, D., Siegler, V., Mithieux, S. M., ... & Rogers, S. (2011). Shape of tropoelastin, the highly extensible protein that controls human tissue elasticity. *Proceedings of the National Academy of Sciences*, *108*(11), 4322-4327.
2. Bellingham, C. M., Woodhouse, K. A., Robson, P., Rothstein, S. J., & Keeley, F. W. (2001). Self-aggregation characteristics of recombinantly expressed human elastin polypeptides. *Biochimica et Biophysica Acta (BBA)-Protein Structure and Molecular Enzymology*, *1550*(1), 6-19.

3. Bohidar, H. B. (2015). *Fundamentals of polymer physics and molecular biophysics*. Cambridge University Press.

4. Chu, B. (2007). *Laser light scattering: basic principles and practice*. Courier Corporation.

5. Clarke, A. W., Arnspang, E. C., Mithieux, S. M., Korkmaz, E., Braet, F., & Weiss, A. S. (2006). Tropoelastin massively associates during coacervation to form quantized protein spheres. *Biochemistry*, *45*(33), 9989-9996.

6. Cooper, C. L., Dubin, P. L., Kayitmazer, A. B., & Turksen, S. (2005). Polyelectrolyte–protein complexes. *Current opinion in colloid & interface science*, *10*(1-2), 52-78.

7. Danielsen, S., Delaney, K., & Fredrickson, G. (2018). Small ion effects on self-coacervation phenomena in block polyampholytes. In *APS Meeting Abstracts*.

8. De Jong, H. B., & Bonner, J. (1935). Phosphatide auto-complex coacervates as ionic systems and their relation to the protoplasmic membrane. *Protoplasma*, *24*(1), 198-218.

9. Dubin, P., & Stewart, R. J. (2018). Complex coacervation. *Soft matter*, *14*(3), 329-330.

10. Elhassan, M. S., Oguntoyinbo, S. I., Taylor, J., & Taylor, J. R. (2018). Formation and properties of viscoelastic masses made from kafirin by a process of simple coacervation from solution in glacial acetic acid using water. *Food chemistry*, *239*, 333-342.

11. Gekko, K., & Timasheff, S. N. (1981). Mechanism of protein stabilization by glycerol: preferential hydration in glycerol-water mixtures. *Biochemistry*, *20*(16), 4667-4676.

12. Gogelein, C., Nagele, G., Tuinier, R., Gibaud, T., Stradner, A., & Schurtenberger, P. (2008). *J. Chem. Phys.*, 129, 085102(1-12).

13. Graham, J. S., Vomund, A. N., Phillips, C. L., & Grandbois, M. (2004). Structural changes in human type I collagen fibrils investigated by force spectroscopy. *Experimental cell research*, *299*(2), 335-342.

14. Jamieson, A. M., Downs, C. E., & Walton, A. G. (1972). Studies of elastin coacervation by quasielastic light scattering. *Biochimica et Biophysica Acta (BBA)-Protein Structure*, *271*(1), 34-47.

15. Kastelic, M., Kalyuzhnyi, Y. V., Hribar-Lee, B., Dill, K. A., & Vlachy, V. (2015). Protein aggregation in salt solutions. *Proceedings of the National Academy of Sciences*, *112*(21), 6766-6770.

16. Keeley, F. W., Bellingham, C. M., & Woodhouse, K. A. (2002). Elastin as a self–organizing biomaterial: use of recombinantly expressed human elastin polypeptides as a model for investigations of structure and self–assembly of elastin. *Philosophical

*Transactions of the Royal Society of London. Series B: Biological Sciences*, *357*(1418), 185-189.

17. Kizilay, E., Kayitmazer, A. B., & Dubin, P. L. (2011). Complexation and coacervation of polyelectrolytes with oppositely charged colloids. *Advances in colloid and interface science*, *167*(1-2), 24-37.

18. Kjaergaard, M., Nørholm, A. B., Hendus–Altenburger, R., Pedersen, S. F., Poulsen, F. M., & Kragelund, B. B. (2010). Temperature-dependent structural changes in intrinsically disordered proteins: Formation of α–helices or loss of polyproline II. *Protein Science*, *19*(8), 1555-1564.

19. Lekkerkerker, H. N., & Tuinier, R. (2011). *Colloids and the depletion interaction* (Vol. 833). Springer.

20. Ohshima, H. (1995). Electrophoresis of soft particles. *Advances in colloid and interface science*, *62*(2-3), 189-235.

21. Pathak, J., Priyadarshini, E., Rawat, K., & Bohidar, H. B. (2017). Complex coacervation in charge complementary biopolymers: Electrostatic versus surface patch binding. *Advances in colloid and interface science*, *250*, 40-53.

22. Pawar, N. & Bohidar, H. B. (2009). *J. Chem.Phy.*, 131, 045103(1-10).

23. Perticaroli, S., Ehlers, G., Jalarvo, N., Katsaras, J., & Nickels, J. D. (2015). Elasticity and inverse temperature transition in elastin. *The journal of physical chemistry letters*, *6*(20), 4018-4025.

24. Sánchez-Iglesias, A., Grzelczak, M., Altantzis, T., Goris, B., Perez-Juste, J., Bals, S., & Liz-Marzán, L. M. (2012). Hydrophobic interactions modulate self-assembly of nanoparticles. *ACS nano*, *6*(12), 11059-11065.

25. Sell, S. A., Wolfe, P. S., Garg, K., McCool, J. M., Rodriguez, I. A., & Bowlin, G. L. (2010). The use of natural polymers in tissue engineering: a focus on electrospun extracellular matrix analogues. *Polymers*, *2*(4), 522-553.

26. Swanson, J. P., Monteleone, L. R., Haso, F., Costanzo, P. J., Liu, T., & Joy, A. (2015). A library of thermoresponsive, coacervate-forming biodegradable polyesters. *Macromolecules*, *48*(12), 3834-3842.

27. Tanford, C., (1967). Physical Chemistry of Macromolecules, *John Wiley, New York*, USA.

28. Teraoka, A. A., & Teraoka, I. (2002). *Polymer solutions: an introduction to physical properties*. John Wiley & Sons.

29. Zou, Y., & Zhang, Y. (2011). The orthotropic viscoelastic behavior of aortic elastin. *Biomechanics and modeling in mechanobiology*, *10*(5), 613-625.

# CHAPTER 6

## SUMMARY

### 6.1 SUMMARY OF THE THESIS

Chapter 3 discuss a comprehensive investigation was carried out to probe the dispersion and aggregation profile of nitrogen deficient hydrophobic protein, zein, in ethanolic solutions at pH=4 close to its isoelectric pH (=6.2). Morphology of zein nanoparticles and their hydrophobically driven aggregation can be controlled solely by tuning the solvent hydrophobicity. Hydrophobic hydration provided by the presence of ethanol in the binary solvent was responsible for giving stability to the protein dispersion. Study of the different phases resulting from interaction of in-situ formed zein nanoparticles with different polyanion (pectin and agar) using various techniques is discussed in this chapter and summarize in table 6.1.

**Table 6.1:** Comparison of different physical characteristics of different polyanion with in-situ formed zein nanoparticle.

| S. No. | Properties | Pectin-zein | Agar-zein |
|--------|-----------|-------------|-----------|
| 1 | Interaction Type | Electrostatic | Electrostatic + vdW |
| 2 | Phase | Bicontinuous (Coacervate & Gel) | Moncontinuous (Coacervate) |
| 3 | Optimum binding/R | 1 | 0.2 |
| 4 | $G_o$/Pa | 3000 (Coacervate) & 11000 (Gel) | 28000 |
| 5 | Viscoelastic length ( $\xi_{el}$)/nm | 13 | 10 |
| 6 | Melting temperature/ $^0$C | -- | 68 |
| 8 | Mesh size ($\xi$) /nm | 12 | 14-123 |
| 9 | Fluorescence Intensity/a.u. | 180 | 90 |
| 10 | Optical nature | Opaque | Opaque |

*R = [Polyanion]/[Z]

Chapter 4 discusses the pH-dependent Zein-pectin Doxorubicin encapsulated hydrogel prepared and used as anti-cancerous substrates for human cervical cancer cell lines demonstrated by decrease in cell viability, ROS generation and alterations in cell morphology. The prepared ZPD hydrogel favour pH dependent release of Doxorubicin to the cytosolic acidic environment of HeLa cells, thereby mediating cellular apoptosis via ROS generation. Prepared hydrogels are endowed with the advantages of controlled release, enhanced shelf-life of drug and provide an inherent environment for the drug. Thus, the results suggest that hydrogels based on inorganic materials can be used as injectable anti-cancerous agents with minimal side-effects, pH and site-specific responsiveness.

Chapter 5 discusses the organization of structural protein, elastin (insoluble) was deeply explored in aqueous and binary solvent of ethanol and water. Binary solvent introduces the hydrophobic forces in the dispersion medium and create cage-like open structures, in which hydrophobic protein molecule resides. It was found that concentration of sodium ions should lie in the range of $0.5 < I > 2$ M for the best dispersion stability of elastin. Model predicted that hydrophobic interaction among protein molecule dominates over other interactions in aqueous solvent, which supports the instability or low solubility of elastin in aqueous medium. Then the coacervation kinetics of elastin (soluble) precursor tropoelastin was mapped as a function of solution ionic strength. This mesophase separation was found to be strongly temperature dependent. The samples were subjected to heating-cooling cycles that produced hysteresis loops with loop area decreasing with ionic strength which implied larger thermo-reversibility of salty coacervates. However, at room temperature the heat-cool cycled sample did reveal the presence of monomeric TE molecules only for salt-free samples, but in all other samples there was clear evidence of the existence of a remnant fraction of aggregated elastin molecules. Estimation of free-energy of the coacervation and the dissociation processes revealed that

coacervate dissociation was free-energy driven while the elastin self-assembly leading to coacervation was hydrophobic and thermally activated. The interaction of elastin with strong polyelectrolyte (DNA) leads to coacervation. Interaction revealed it to be strongly hierarchical, with distinct binding regions. Region I showed DNA-Elastin primary binding for $r < 0.02$ and size of complex increases, Region II ($0.02 < r < 0.08$ indicated secondary binding where total charged is neutralized and come to saturation, turbidity become very high (~ 90%) and size remains constant in this region, which resulted in the appearance of soluble complexes and initiation of coacervation. Region III ($0.08 < r < 0.12$ revealed growth of insoluble complexes with large sizes followed by precipitation. The binding profile of DNA-elastin complex coacervation decreased with monovalent salt concentration. Small angle neutron scattering (SANS) data of coacervates indicated rod like structure of scattering moiety. Salt mediated study revealed that the interaction of hydrophobic protein elastin with DNA is electrostatic in nature.

## 6.2 WORK IN PROGRESS

### 6.2.1 SURFACTANTS INTERACTION WITH ELASTIN PROTEIN

Protein has three-dimensional structure and have marginally stability and can disturb by minor perturb forces, cause formation of non-native protein aggregation and biological activity loss. Protein surfactant interaction widely studied to understand the structural change and stability of the protein. Elastin interaction with different charged surfactant like cationic (C-TAB and D-TAB), anionic (Sodium dodecyl sulphate) and neutral (Tx-100) studied using different characterization techniques. Preliminary experiments were done for this problem.

### 6.2.2 ELASTIN INTERACTION WITH WEAK POLYELECTROLYTE AGAR

In this thesis we discussed the interaction of elastin with strong polyelectrolyte (DNA), that make chaos what the interaction profile for very weekly charged protein elastin with weak

polyanion agar. To understand this problem titration profile of turbidity has been done to know the optimum binding.

**6.3 FUTURE PLAN**

During the period of this thesis work, I encountered few problems that can be studied to enhance the basic understanding of interpolymer interaction complexation in biopolymer.

1. Protein-polyelectrolyte interaction at interface.

2. Theoretical model for better understanding of these complexe, coacervate and gel system.

## LIST OF PUBLICATIONS:

1. **Priyanka Kaushik**, Kamla Rawat, Vinod Kumar Aswal, Joachim Kohlbrecher, and Himadri B. Bohidar. "Mixing ratio dependent complex coacervation versus bicontinuous gelation of pectin with in situ formed zein nanoparticles." *Soft matter* 14, no. 31 (2018): 6463-6475. **(I.F. = 3.798)**

2. **Priyanka Kaushik,** K. Rawat, and H. B. Bohidar. "Heat-induced coacervation of elastin and its possible thermo-reversibility." *Colloid and Polymer Science*: 1-10. **(I.F. = 1.906)**

3. Nisha Pawar, **Priyanka Kaushik**, and H. B. Bohidar. "Hydrophobic hydration and anomalous diffusion of elastin in an ethanolic solution." *Physical Chemistry Chemical Physics* 19, no. 21 (2017): 13994-14000. **(I.F. = 3.567)**

4. **\*\***Pankaj Kumar Pandey, **Priyanka Kaushik**, Kamla Rawat, V. K. Aswal, and H. B. Bohidar. "Solvent hydrophobicity induced complex coacervation of dsDNA and in situ formed zein nanoparticles." *Soft matter* 13, no. 38 (2017): 6784-6791. **(I.F. = 3.798)**

5. **\*\***Pankaj Kumar Pandey, **Priyanka Kaushik**, Kamla Rawat, and H. B. Bohidar. "Effect of organic and inorganic salt environment on the complex coacervation of in situ formed protein nanoparticles and DNA." *International journal of biological macromolecules* 122 (2019): 1290-1296. **(I.F. = 4.784)**

6. **Priyanka Kaushik**, K. Rawat, V.K. Aswal, J. Kohlbrecher and H.B. Bohidar; "Fluorescent complex coacervates of agar and *in situ* formed zein nanoparticles: Role of electrostatic forces." (*Communicated*).

7. **Priyanka Kaushik**, Eepshita Priyadarshani, R. Paulraj and H.B. Bohidar; pH responsive doxorubicin loaded zein nanoparticle crosslinked pectin hydrogel as effective site-specific aniti-cancerous substrate. (*Communicated*).

**Under Preparation:**

1. **Priyanka Kaushik**, P. Pandey, V.K. Aswal and H.B. Bohidar; Complex coacervation between dsDNA and very weekly charged protein elastin in aqueous and salty solutions.

2. **Priyanka Kaushik**, Eepshita Priyadarshani, R. Paulraj and H.B. Bohidar; Comparision how the morphology and size of the protein (zein) change property and can use for various application.

3. **Priyanka Kaushik**, P. Pandey, V.K. Aswal and H.B. Bohidar; Elastin interaction with weekly charged polyelectrolyte agar.

4. **Priyanka Kaushik** and H.B. Bohidar; Surfactants interaction with elastin protein.

**\*\***Not part of thesis.

## CONFERENCES AND WORKSHOP:

1. Participated in National Conference on '**Interdisciplinary Approaches in Chemical Sciences IACS -2015'** on 16th December, 2015 at Centre for interdisciplinary Research in Basic Sciences Jamia Millia Islamia, New Delhi, Jawaharlal Nehru University, New Delhi, India

2. Participated in National Seminar on '**Recent Trends in nano-Bio interface'** on 18th December, 2015 at Special Centre for Nano sciences, Jawaharlal Nehru University, New Delhi, India

3. Participated in National seminar on **'Advances in Polymer science and Technology (POLY-2016)'**on March 9-10,2016 organized jointly by Prof. Sukumar Maiti Polymer Award Foundations & Special Centre for Nano sciences, Jawaharlal Nehru University, New Delhi, India

4. Poster presentation **SPS, JNU March Meeting**, 18-19 March 2016.

5. Poster presentation in **National Seminar on Biophysics (Biophysika 2017)** on 16th march 2017 organized by CIRBSC, S. Ramanujan Block, Jamia Milia Islamia, New Delhi-110025, India.

6. Participated in **National Science Day** organized by DST and Jawaharlal Nehru University, New Delhi, India on 28th febuary,2017.

7. Poster Presentation in '**International Conference on Nano biotechnology'** held  on February 5-6, 2018 at CIRBSC, S. Ramanujan Block, Jamia Milia Islamia, New Delhi-110025, India.

8. Poster Presentation in **"soft and active matter"** during 11th -17th February 2018.